

DTIC FILE COPY

1

GL-TR-90-0333
ENVIRONMENTAL RESEARCH PAPERS, NO. 1074

AD-A230 519

Proceedings of the 8th Annual DARPA/AFGL Seismic
Research Symposium, 6-8 May 1986

Editors:

JAMES F. LEWKOWICZ
JEANNE M. McPHETRES



3 December 1990

DTIC
ELECTE
JAN 07 1991
S B D



Approved for public release; distribution unlimited.




EARTH SCIENCES DIVISION PROJECT 2309
GEOPHYSICS LABORATORY
HANSCOM AFB, MA 01731-5000

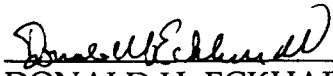
91 1 4 001

"This technical report has been reviewed and is approved for publication."

FOR THE COMMANDER



JAMES F. LEWKOWICZ
Branch Chief
Solid Earth Geophysics Branch
Earth Sciences Division



DONALD H. ECKHARDT
Director
Earth Sciences Division

This report has been reviewed by the ESD Public Affairs Office (PA) and is releasable to the National Technical Information Service (NTIS).

Qualified requestors may obtain additional copies from the Defense Technical Information Center. All others should apply to the National Technical Information Service.

If your address has changed, or if you wish to be removed from the mailing list, or if the addressee is no longer employed by your organization, please notify GL/IMA, Hanscom AFB, MA 01731-5000. This will assist us in maintaining a current mailing list.

Do not return copies of this report unless contractual obligations or notices on a specific document requires that it be returned.

3December 1990

Scientific, Interim

Proceedings of the 8th Annual DARPA/AFGL Seismic
Research Symposium, 6-8 May 1986

PE 61102F
PR 2309
TA G2
WU 06

Editors: James F. Lewkowicz
Jeanne M. McPhetres

Air Force Geophysics Laboratory, AFSC
AFGL/LWH
Hanscom AFB, MA 01731-5000

GL-TR-90-0333
ERP, No. 1074

DARPA/GSD
1400 Wilson Boulevard
Arlington, VA 22209-2308

This research was supported by DARPA under PE 61101E and 62714E.

Approved for Public Release; distribution unlimited

These proceedings contain papers presented at the Eighth Annual Defense Advanced Research Projects Agency/Air Force Geophysics Laboratory (DARPA/AFGL) Seismic Research Symposium held 6-8 May 1986, in Colorado Springs, Colorado. In its capacity as a Technical Agent, the AFGL's Solid Earth Geophysics Branch (LWH) manages the DARPA Geophysical Sciences Division's (GSD) basic research program in seismology. The scientific objective of this program is to improve the Air Force's capability to seismically detect, locate, identify and estimate the yield of underground nuclear explosions. The purpose of this symposium, which is organized annually by LWH, is to provide the GSD staff an opportunity to review the research accomplished during the preceding year and outline areas of investigation for the coming year. For the researchers, it provides a forum for the exchange of scientific information, as well as occasions to meet personally with the GSD and LWH staff to discuss individual projects, ideas and results. In addition, the technical presentations serve as a means to

underground nuclear explosion, seismic waves, regional
seismology arrays, yield estimation, source coupling

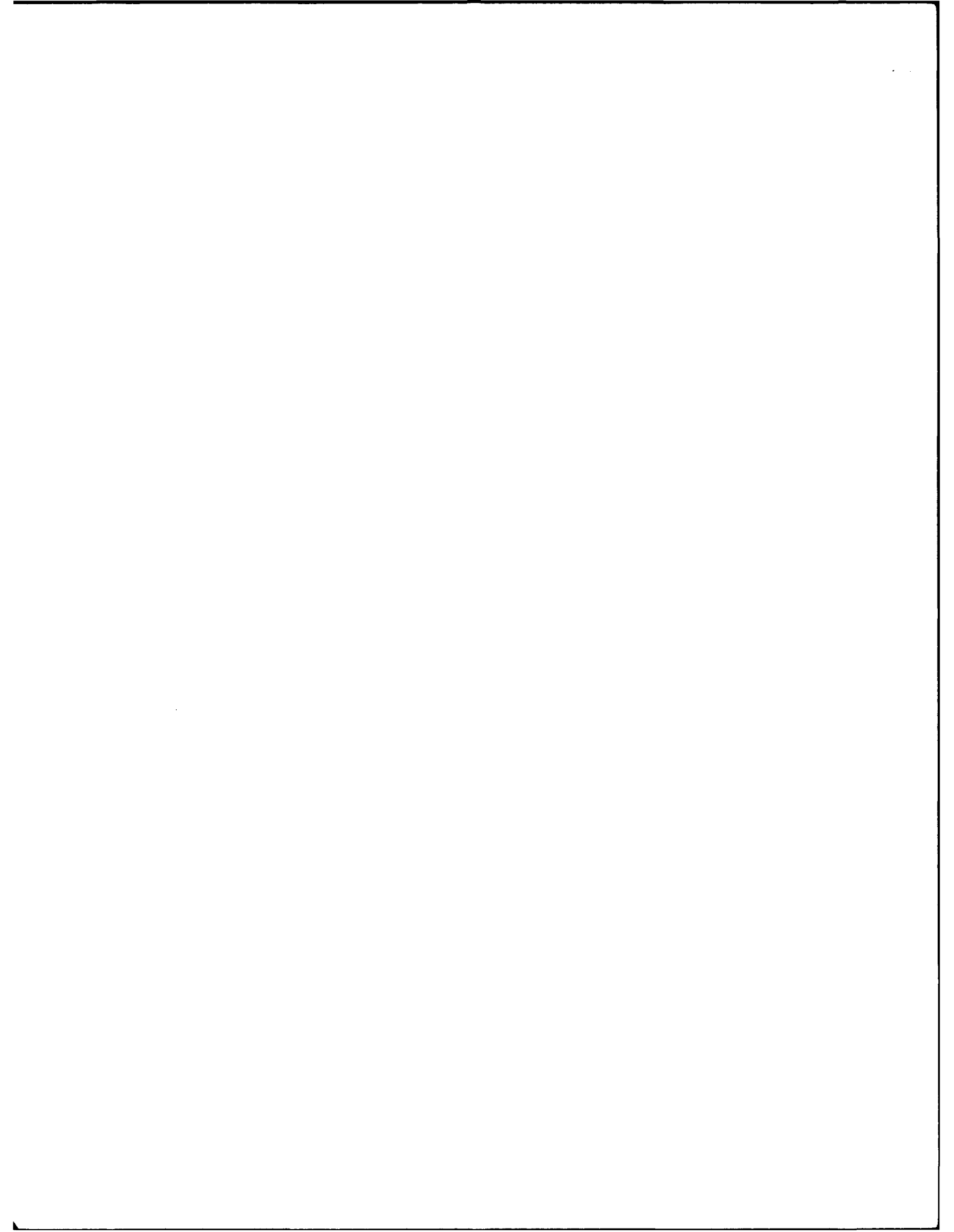
226

UNCLASSIFIED

UNCLASSIFIED

UNCLASSIFIED

UL



inform representatives from other Government agencies about advances in seismic monitoring research, technologies and techniques as part of the important process of technology transition. The papers include studies on regional seismic wave propagation, attenuation and scattering, array processing and seismic techniques of yield estimation.

Accession For	
NTIS GRA&I	<input checked="checked" type="checkbox"/>
DTIC TAB	<input type="checkbox"/>
Unannounced	<input type="checkbox"/>
Justification	
By	
Distribution/	
Availability Codes	
Dist	All and/or Special
A-1	



<u>CONTENTS</u>	<u>PAGE</u>
Resolution of Source Functions and Structure from Near-field Data, J. S. Barker, R. W. Burger and L. J. Burdick	1
Seismic Wave Propagation in a Laterally Heterogeneous Crust M. Bouchon and M. Campillo	10
Modeling Explosions using 2-D Numerical Methods Donald V. Helmberger, Richard Stead, and John Vidale	18
Modeling Lg Propagation Across Crust-mantle Transition Zones and Evaluating Surface Wave Path Corrections Janice Regan, Peter Glover and David G. Harkrider	27
Geophysical Investigations at Ahute Mesa, NV John F. Ferguson	36
Regional Studies with Broadband Data T.V. McEvilly and L.R. Johnson	44
Determination of Source Function for a Seismic Swarm P. Mechler and F. Riviere	52
The Damage Mechanics of Brittle Solids in Compression C.G. Sammis and M.F. Ashy	66
Sources Spectra Determination for a Recent Seismic Crisis in the East Part of France J. L. Plantet and B. Massinon	86
Focussing and Defocussing of Body Waves by Three-Dimensional Structure in Source and Receiver Regions Vernon F. Cormier	94
Regional Event Detection Using The NORESS Array F. Ringdal	102
The Nature of Teleseismic P Coda at NORESS Anton M. Dainty and M. Nafi Toksoz	110
Propagation Characteristics of Regional Phases and NORESS Real Time Processing Performance S. Mykkeltveit and T. Kvaerna	117
Wavefield Decomposition using ML-probabilities in Modelling Single-site 3-component Records: Practical Applications on Locations of Events and Scattering A. Christoffersson, E.S. Husebye, S.F. Ingate and B.O. Ruud	125
Observational and Theoretical Studies of Regional Wave Propagation C.A. Langston, A. Lakhtakia, V.K. Varadan and V.V. Varadan	133

<u>CONTENTS</u>	<u>PAGE</u>
Source Characterization and Yield Estimation from Lg and P-Coda Measurements Douglas R. Baumgardt	141
The Tectonic Release Signature at Regional Distances Terry C. Wallace	150
Lg Magnitudes of Selected shagan River, East Kazakhstan Explosions Otto W. Nuttli	159
Analysis of Teleseismic P Wave Amplitude and Coda Variations for Underground Explosions Thorne Lay, Christopher Lynnes and Joan Welc	167
Comparison of Matched Filters to Time-Variable Filters for Amplitude Determination of Normal Modes in Surface Wave Analysis D.R. Russell and H.-J. Hwang	175
Anelastic Properties of the Crust and Upper Mantle in Stable and Tectonically Active Regions H.-J. Hwang and B. J. Mitchell	183
P Wave Attenuation, m_b Bias and the Threshold Test Ban Treaty Thomas C. Bache, Steven R. Bratt, and Lolitia B. Bache	194
Synthetic P_n / S_n Phases and the Frequency Dependence of Q of Oceanic Lithosphere Thomas Sereno and John Orcutt	202
Surface Wave Synthesis for Laterally Heterogenous Spherical Earth Models Keiiti Aki, Ta-liang Teng and John Faulkner	210
Regional Distribution of Apparent Attenuation in the Center of France M. Campillo	216
LIST OF ATTENDEES	221

Resolution of Source Functions and Structure from Near-field Data

J. S. Barker, R. W. Burger and L. J. Burdick
Woodward-Clyde Consultants, 566 El Dorado St., Pasadena, CA 91101

INTRODUCTION

An important problem in nuclear explosion seismology is the accurate determination of the reduced displacement potential (RDP). This paper summarizes the results of three studies concerning the determination of the RDP from near-field data, and implications for teleseismic attenuation estimates.

THE FORM OF THE RDP

Two representations of the RDP are currently in use, differing principally in their high-frequency asymptotic behavior and in their scaling with yield. The displacement spectra derived from these RDPs for the Pahute Mesa event HALFBEAK are shown in Figure 1. At high frequencies, the Mueller-Murphy (1971, M-M) spectrum falls off as f^{-2} , whereas the Helmberger-Hadley (1981, H-H) spectrum falls off as f^{-3} . In the 1-5 Hz band resolvable with near-field data, however, the two spectra are virtually indistinguishable. This is perhaps to be expected, since both formalisms were derived by fitting near-field data within this band. A comparison of the spectral slopes and the spectral ratio of these source functions (Figure 1) indicates that they diverge significantly only above about 5 Hz and below 1 Hz.

Comparisons of elastic generalized ray synthetic seismograms computed for both RDP representations with observed near-field data are given in Barker et al (1986), but a typical example is shown in Figure 2. Shown at the top is the observed vertical velocity waveform from the event BOXCAR recorded at a range of 10 km. Shown in the dashed line is the H-H synthetic using parameters determined by Barker et al (1985), and in the dotted line is the M-M synthetic scaled to the announced yield of 1300 kt. The first peak amplitude and frequency content of the M-M synthetic are too high to match the

observations. Shown below the time-domain velocity waveforms are the amplitude spectra for the window indicated above the traces. Only those portions of the spectra from 1-10 Hz have been displayed. Once again, from 1-5 Hz, the two synthetic spectra are virtually identical and differ from the observed spectrum mostly due to later, unmodeled arrivals in the window. Above 5 Hz, the M-M spectrum is enhanced relative to the observations, while the H-H spectrum continues to track the data.

Since the elastic M-M synthetic is too rich in high frequency energy to satisfy the observations, we investigated whether the effects of local anelastic attenuation could improve the fit. Figure 3 shows a comparison in the time and frequency domains between elastic H-H and M-M synthetics and M-M convolved with a Futterman (1962) average attenuation operator for a Q of 100 (MMQ). The synthetics are computed for a 1000 kt source at 10 km, similar to the BOXCAR comparison shown in Figure 2. The value of $Q=100$ brings the first peak amplitude of the MMQ synthetic into agreement with the H-H amplitude, and has the desired effect of depressing the high-frequency spectral amplitudes. Barker et al (1986) indicate that Q values as high as 100 are too high for the M-M synthetics to match observations at shorter ranges. We conclude that with a moderate level of local anelastic attenuation, the M-M source representation is indistinguishable from the elastic H-H source, but that a range-dependent, or more precisely, a depth-dependent attenuation model must be specified before the M-M synthetics can be used with near-field data.

IMPLICATIONS FOR TELESEISMIC ATTENUATION ESTIMATES

It is apparent from Figure 1 that the spectral amplitudes of the H-H and M-M sources are significantly different in the 0.5-2 Hz band in which teleseismic, short-period P waves are observed. Within this band, the scaling relations result in the M-M source having higher absolute amplitudes than the H-H source. Thus, the former requires higher t^* values to match observed teleseismic amplitudes. The figure also shows that out to about 4 Hz, the two

spectra have comparable spectral roll-off. The more rapid decay of the H-H source occurs only above 4 Hz. We have used the near-field results to model the amplitudes and periods of teleseismic, short-period waveforms in order to determine estimates of teleseismic attenuation. Both frequency-independent (Futterman, 1962) and frequency-dependent (Minster, 1978) models were considered. Details of the study may be found in Burger et al (1986), but an overview is given in Figure 4. Shown are various source amplitude spectra (multiplied by f^2) convolved with attenuation operators. The top curve is the model inferred by Der et al (1985) based on matching the teleseismic spectral shape in the 0.5-4 Hz band using a VSB source and a t^* of 0.34 s. The other curves result from short-period P-wave modeling, and include the H-H source with a Minster Q operator with $t^*=1.0$ s and $TAU_m=0.044$ s (H M), the M-M source with Minster Q parameters $t^*=1.25$ s and $TAU_m=0.051$ s (M M), the H-H source with a Futterman t^* of 0.79 s (H F) and the M-M source with Futterman t^* of 0.99 s (M F). It is immediately apparent that the Der et al (1985) model does not fit the time-domain amplitudes near 1 Hz. Similarly, both the H-H and M-M sources with the Futterman attenuation operator have spectral fall-off inconsistent with the data modeled by Der et al (1985). However, both of these source models with the frequency-dependent Minster Q operator match both the time-domain amplitudes and spectral fall-off, within a reasonable scatter in the data.

THE EFFECT OF LOCAL STRUCTURE

The determination of source parameters from near-field data is sensitive to errors or inadequacies in the assumed local velocity structure model. For example, Stump and Johnson (1984) obtained time-varying moment tensors for three events, interpreting the deviatoric parts in terms of non-isotropic source radiation. These may just as well have resulted from purely isotropic sources but inaccurate Green's functions. In order to quantify and account for these tradeoffs, we have developed a simultaneous inversion for the

parameters of the explosion source and the velocity structure models. Figure 5 shows the results of a test inversion using a synthetic data set. The synthetic data were generated for a 2-gradient model approximating the Pahute Mesa model of Hartzell et al (1983). In the inversion, the structure parameters are the gradient, the velocity at the top of the layer, and the depth to the top of the layer. The gradient is discretized into a plane-layered model based on a critical wavelength, and synthetics are computed using asymptotic generalized ray theory. For this case, the source is represented by the parameters of the H-H source (holding the B parameter constant at 1.0). The residuals are the normalized cross-correlation coefficient (a measure of waveform fit), the difference of normalization factors (a measure of amplitude) and the time lag to the peak of correlation (a measure of travel time). Partial derivatives are computed numerically by perturbing each of the starting parameters, and a linearized generalized inverse is solved. The results are listed in Table 1. For the first five iterations, only the parameters of the source and upper gradient layer were allowed to vary. The waveforms in Figure 5 indicate rapid convergence to the upper gradient, but details of waveforms at farther stations are not well modeled, and the source parameters are still unresolved. The parameters of the lower gradient could not be resolved using only stations out to 12 km. However, when artificial data out to 20 km was included, these parameters approach their correct values in iterations 6-10. The parameter resolution matrix from the inversion indicates the extent to which source and structure parameters trade-off as a function of iteration. In addition, with an estimate of the variance of the residuals using real data, error ellipsoids for the inversion parameters may be formed and used to evaluate the quality of the solution.

REFERENCES

- Barker, J. S., S. H. Hartzell, L. J. Burdick and D. V. Helmberger (1985). Effective source functions for underground nuclear tests at Pahute Mesa from near-field modeling, Final Technical Report WCCP-R-85-01, Woodward-Clyde Consultants, Pasadena.
- Barker, J. S., L. J. Burdick and T. C. Wallace (1986). Analysis of near-field seismic waveforms from underground nuclear explosions, Scientific Report No. 1, AFGL-TR-85-0321, Woodward-Clyde Consultants, Pasadena.
- Burger, R. W., T. Lay and L. J. Burdick (1986). Estimates of Q and yield for teleseismic P waves from Pahute Mesa nuclear explosions, in preparation.
- Der, Z., T. McElfresh, R. Wagner and J. Burnetti (1985). Spectral characterization of P waves from nuclear explosions and yield estimation, Bull. Seismol. Soc. Am., 75, 379-390.
- Futterman, W. I. (1966). Dispersive body waves, J. Geophys. Res., 67, 5279-5291.
- Hartzell, S. H., L. J. Burdick and T. Lay (1983). Effective source functions for Pahute Mesa nuclear tests, Final Technical Report WCCP-R-83-3, Woodward-Clyde Consultants, Pasadena.
- Helmberger, D. V. and D. M. Hadley (1981). Seismic source functions and attenuation from local and teleseismic observations of the NTS events JORUM and HANDLEY, Bull. Seismol. Soc. Am., 71, 51-67.
- Minster, J. B. (1978). Transient and impulse responses of a one dimensional linearly attenuating medium; Part I. Analytic results, Geophys. J., 52, 479-501.
- Mueller, R. A. and J. R. Murphy (1971). Seismic characteristics of underground nuclear detonations. Part I. Seismic spectrum scaling, Bull. Seismol. Soc. Am., 67, 1675-1692.
- Stump, B. W. and L. R. Johnson (1984). Near-field source characterization of contained nuclear explosions in tuff, Bull. Seismol. Soc. Am., 74, 1-26.
- von Seggern, D. and R. Blandford (1972). Source time functions and spectra for underground nuclear explosions, Geophys. J., 31, 83-97.

Table 1 - Inversion Results

Iteration	XSI	K	V_1	Gr_1	Gr_2	Z_2
Start	2.000	9.000	2.000	0.500	-	-
1	1.328	6.702	2.501	0.633	-	-
2	1.329	6.708	2.537	0.777	-	-
5	1.270	6.370	2.450	0.890	0.890	2.000
7	0.838	6.225	2.445	0.889	0.488	2.557
10	0.906	6.243	2.450	0.889	0.389	2.680
Data	1.000	7.000	2.500	0.830	0.200	3.000

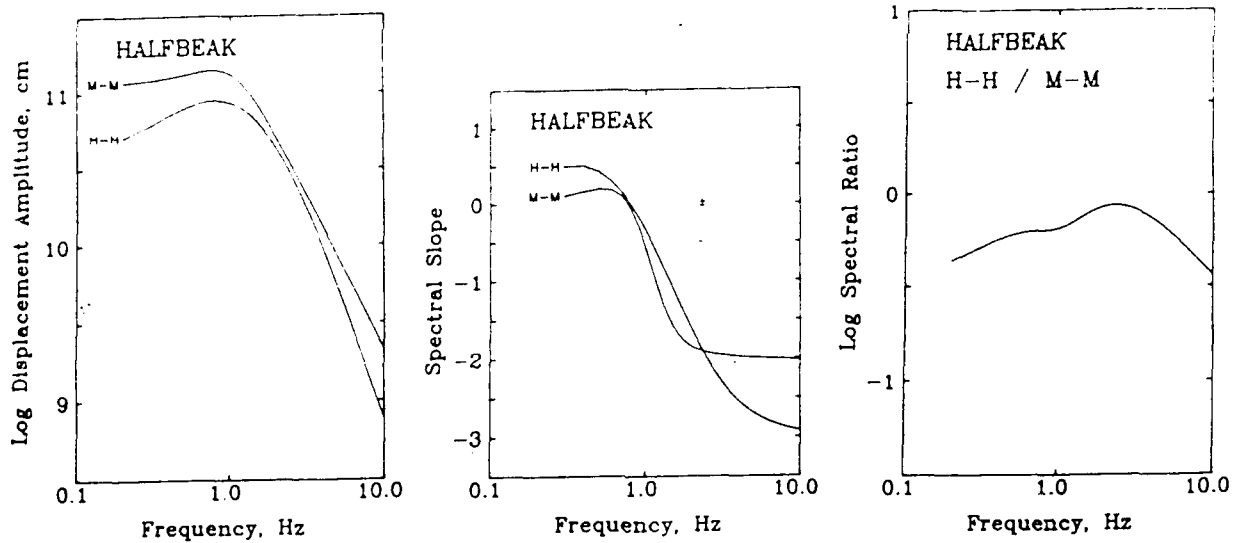


Figure 1. (Left) Predicted source displacement spectra for HALFBEAK. The Mueller-Murphy source models are based on the announced yield. The Helmberger-Hadley are based on the near field modeling results of Barker et al. (1985). (Center) Spectral slopes of the displacement spectra versus frequency. (Right) The spectral ratio of the two source models.

BOXCAR S-34 UV 10.40 KM
SIGNAL WINDOW 2.70 TO 4.70 SEC

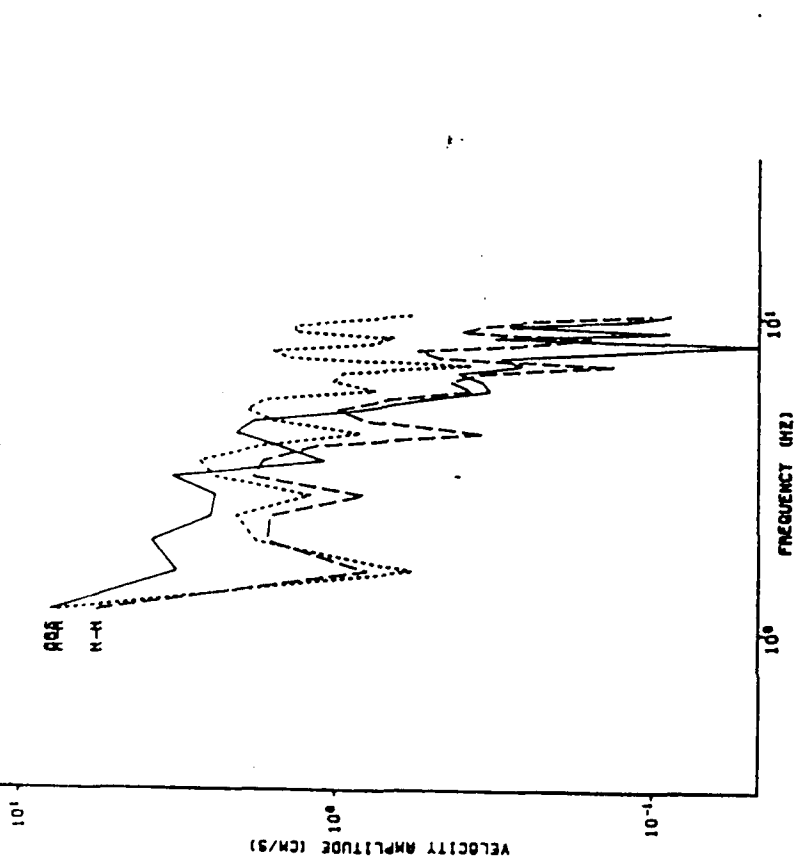
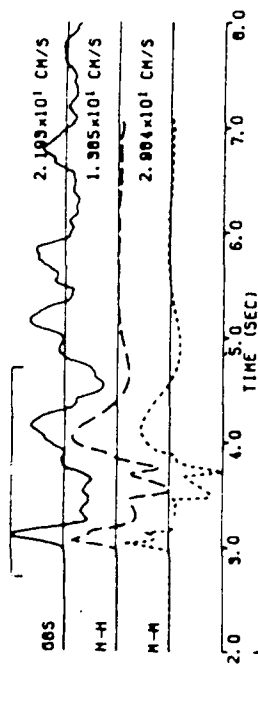


Figure 2. A comparison of the observed (solid line) versus predicted (Mueller-Murphy dotted line or Helmlinger-Hadley dashed line) near field P wave velocity spectra for BOXCAR. The original observed and synthetic time series are shown at the top with the trace amplitudes indicated. The positioning and length of the signal window is indicated at the very top.

1000 KT SYNTHETICS AT 10 KM
SIGNAL WINDOW 2.50 TO 6.50 SEC

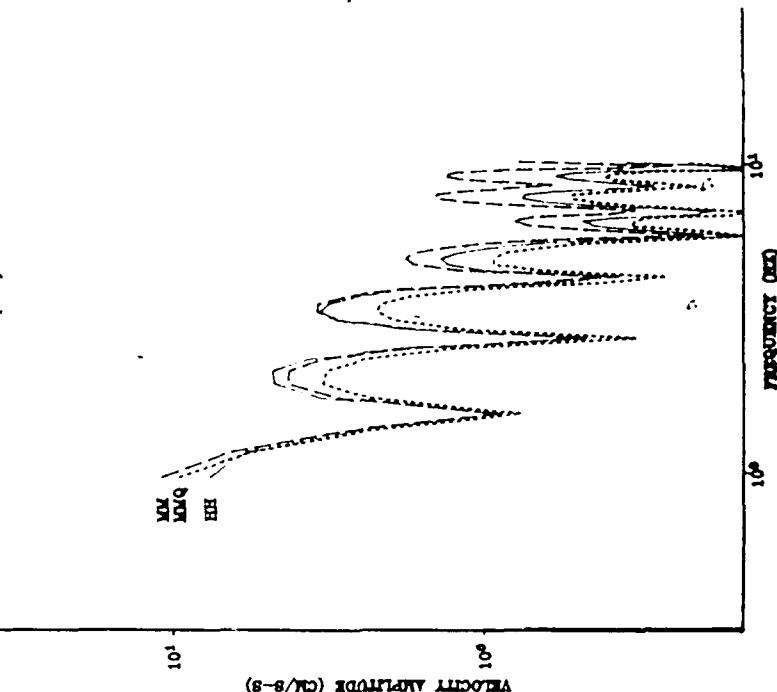
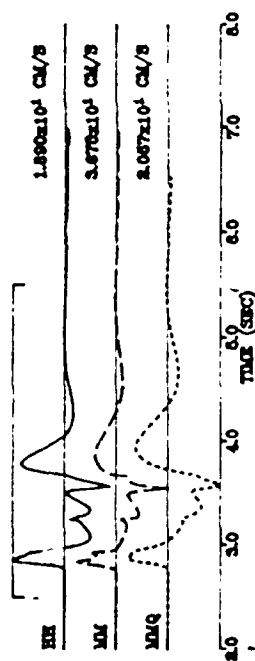


Figure 3. A comparison of the theoretical spectra for Mueller-Murphy (long dash) and Helmlinger-Hadley (solid line) sources at 10 km. in an elastic crust for 1000 kt. The short dash line is the Mueller-Murphy spectrum corrected assuming an average crustal Q of 100.

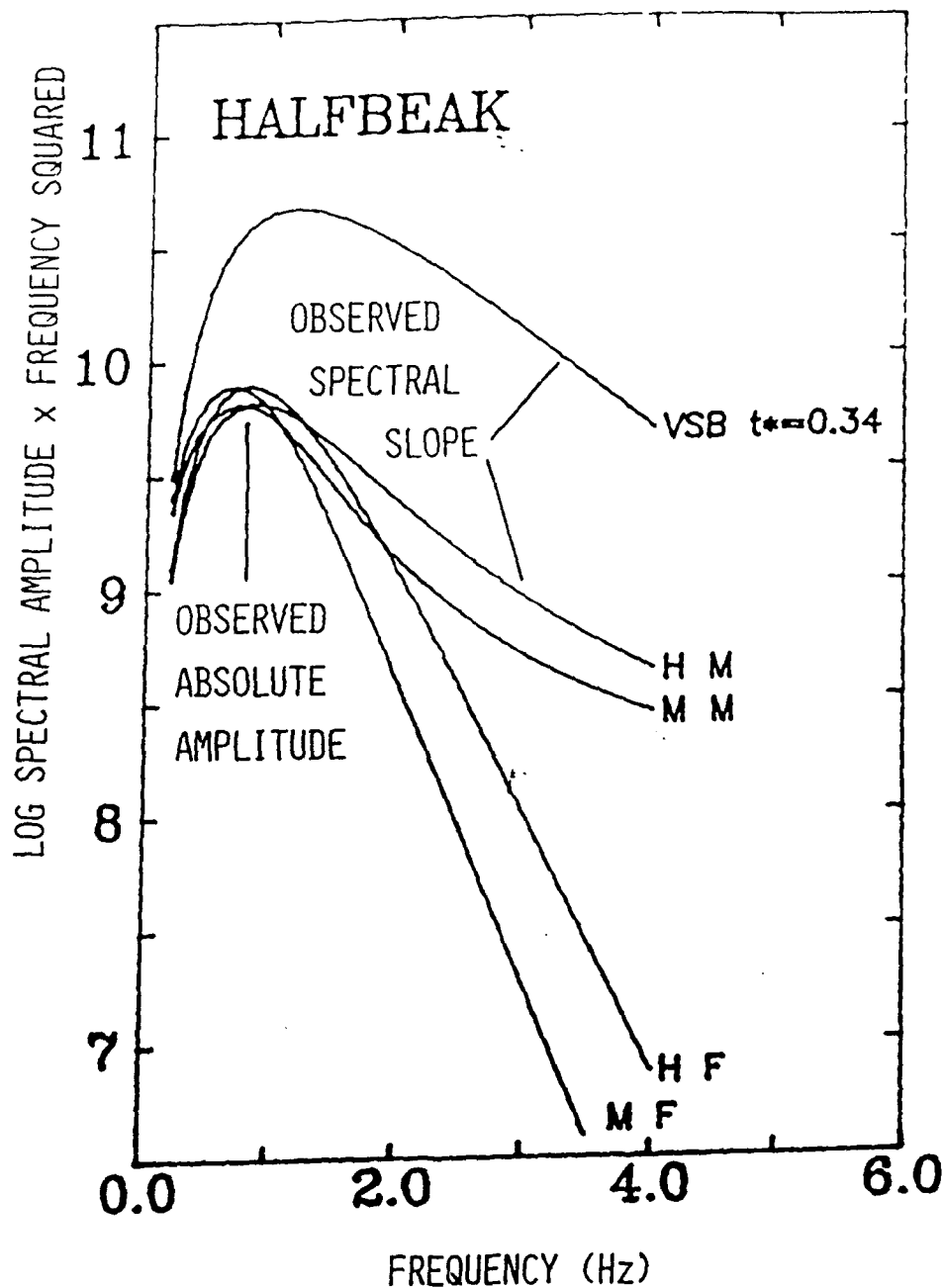


Figure 4. A comparison of the theoretical spectra for the Helmberger-Hadley and Mueller-Murphy sources convolved with the Futterman and Minster Q operators to the spectrum preferred by Der et al. (1986) for Pahute Mesa (von Seggern and Blandford source with Futterman Q operator, $t^*=0.34$).

Test Inversion for Source and Structure

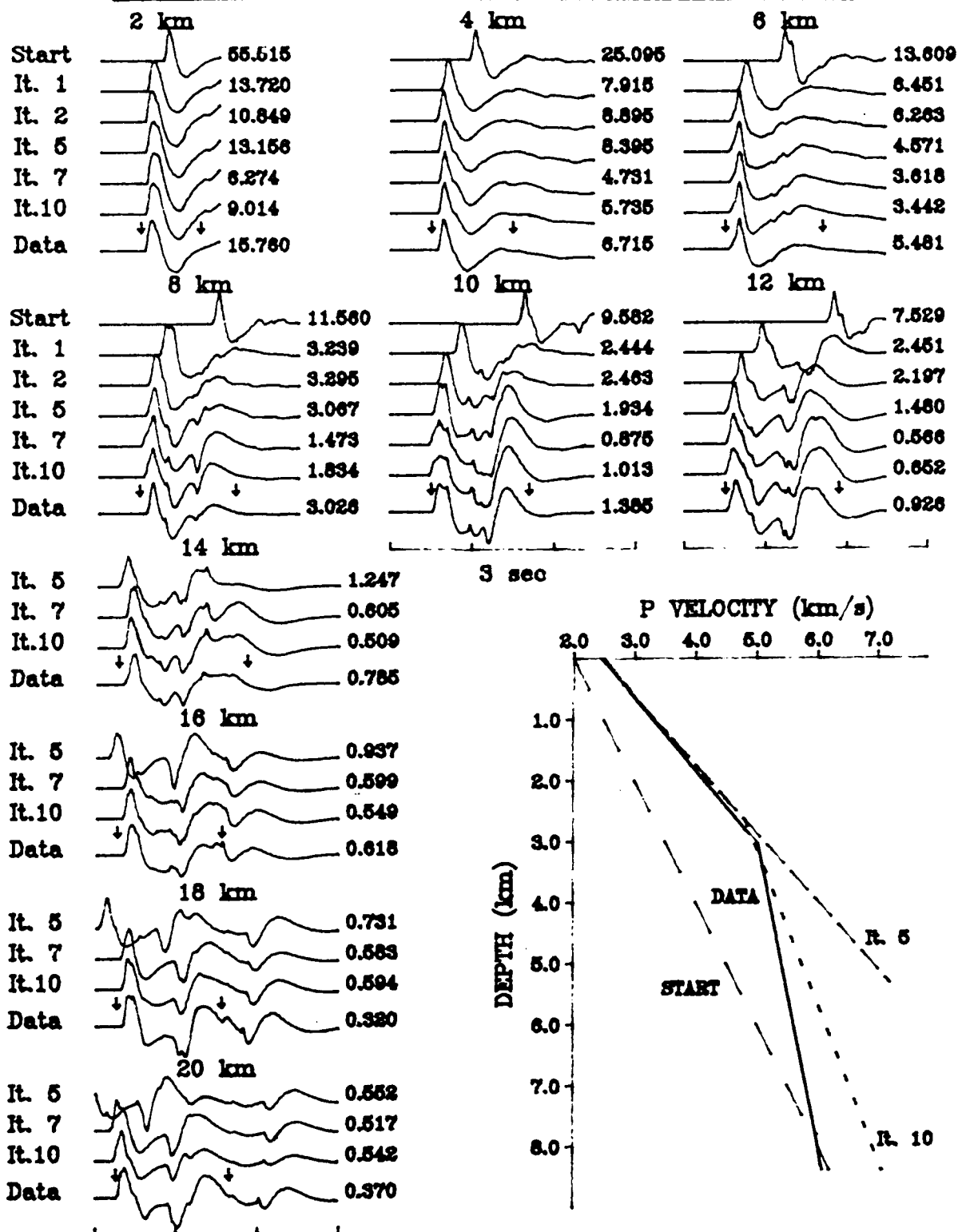


Figure 5. Inversion waveforms and structure model results. The starting model and results of selected iterations are shown and compared with the synthetic data set. For the first 5 iterations only receivers to 12 km were included. For iterations 6-10, the inclusion of receivers to 20 km allowed the lower gradient to be resolved. Arrows indicate the time windows, and peak amplitudes are shown.

AFGL / DARPA Seismic Research Symposium

U. S. Air Force Academy

Colorado Springs- 6-8 May 1986

Paper Tittle : Propagation of Lg waves through a laterally
heterogeneous crust

Paper authors : M. Bouchon and M. Campillo - Radiomana

Grant n° 85 0033

Introduction

The method used in that study is derived from the discret waves numbers method. It has been used to characterize the effects of different large scale heterogeneities on the Lg waves propagation.

Two types of effect have been studied.

First, the effects due to Moho irregularities. The Lg waves train is a superposition of reflected S waves trapped within the crust. Consequently any variation of the Moho depth might affect the waves guide quality and leads to some apparent strong attenuation zone for Lg waves.

Second, we look at the effects of sedimentary basins on the Lg waves propagation path.

The study is limited to the SH in two dimensions. Irregularities dimensions are selected to fit the situations met in central part of France for which general attenuation features have been studied (Campillo , Plantet and Bouchon 1985).

I Variation of the Moho depth

The crust model is given in Figure 1. Computations have been made for seismic sources at 10 km depth, located at 0, 50, 100, 150 and 200 km from the Moho irregularity.

Figure 2 shows maximum amplitude variations for Lg waves versus distance, for a planar crust mode (thick solid line) and for a crust model with irregularity at these previous distances.

In the irregularity vicinities, steepen reflectors bring strong amplitude variations.

On the contrary, at larger distances, no important and systematic differences are seen between a Moho without or with irregularity.

This points out that any Moho ascent should commonly bring limited attenuation effects on Lg waves.

II Sedimentary basin

We look now at the influence of a thickened sedimentary layer or a sedimentary basin as described in Figure 3 on Lg waves at the same distances from the irregularity (as describe in Figure 1) seismic sources are always at 10 km depth.

The synthetic seismograms are presented in Figure 4 for various distances from 0 to 290 km, every 10 km, for both a planar crust (upper seismograms) and a thickened sedimentary layer at the top of the crust (lower seismograms).

Clearly seen is the formation of a Love wave in the case of a sedimentary basin. As superficial layers are propagation structures which strongly affect Love waves., the converted Lg waves to Love waves energy will be rapidly dissipated.

Within the sedimentary basin itself, classical amplification phenomena might happen.

These two rough synthetic examples suggest to verify their conclusions for some real cases.

Conclusion

These results pointed out the importance of graben zones for Lg waves propagation. Nevertheless, at this stage of the study we do not possess any separation tool between two types of phenomena which could create attenuation :

- small scale diffraction (or scattering)
- large scale geometrical effect.

A study of frequency dependancy for Q should help in the interpretation of our data.

On the other hand, developments of numerical simulation methods encourage us to investigate more complex zones in order to interpret the quasi-extinction phenomena of Lg waves we have observed along peculiar paths.

Figure 1 : crust model with Moho irregularity - the star is the seismic source - seismograms are built at various distances.

Figure 2 : maximum amplitudes of Lg waves versus distance (2D).

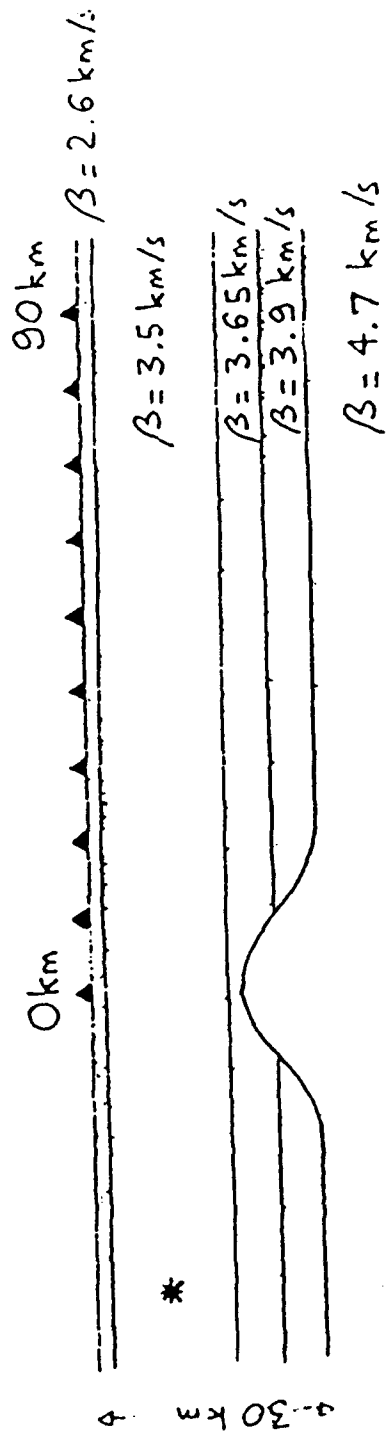
Figure 3 : crust model with a sedimentary basin

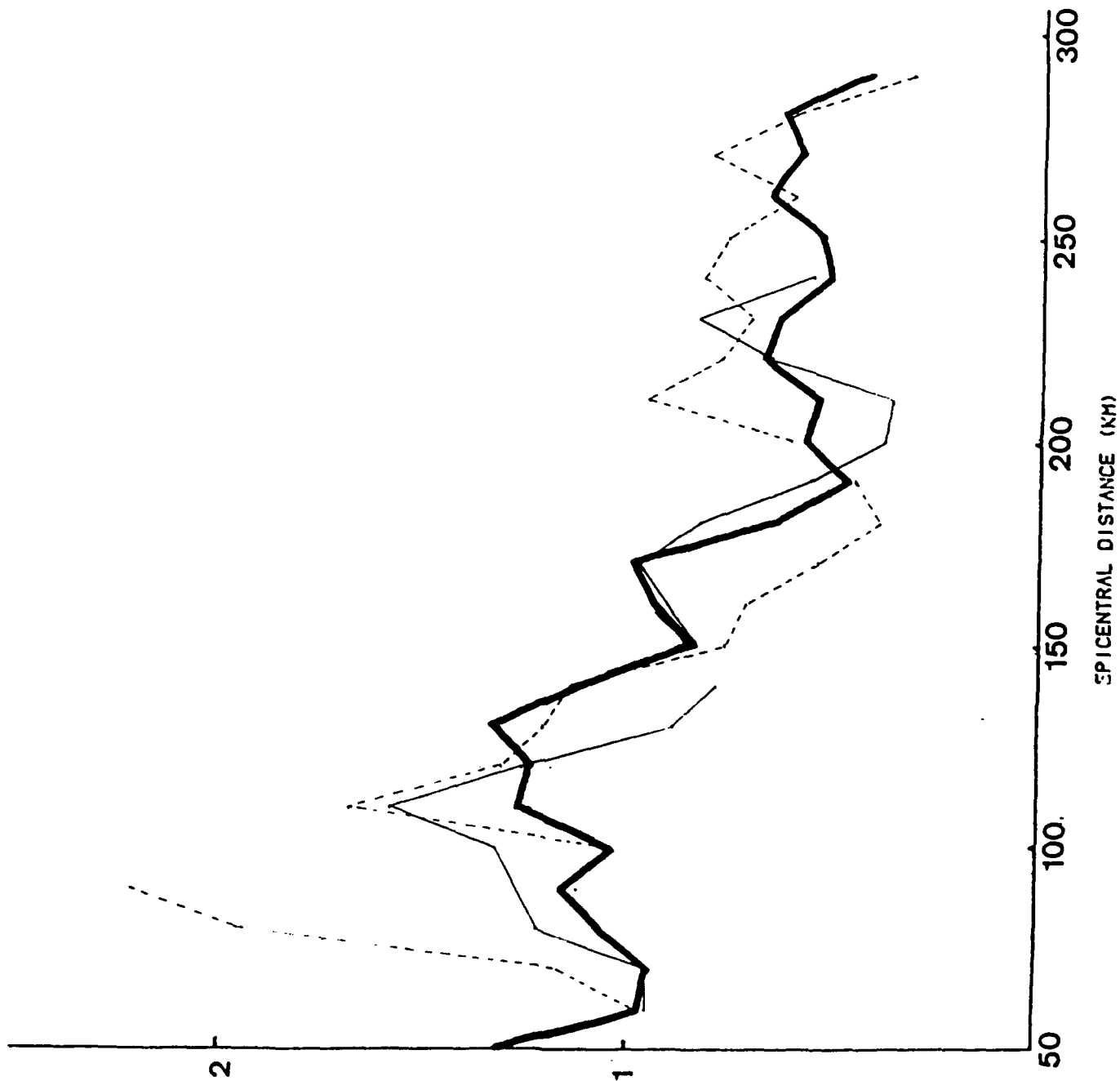
Figure 4 : synthetics obtained with a planar crust model (high) and with a sedimentary irregularity (low)

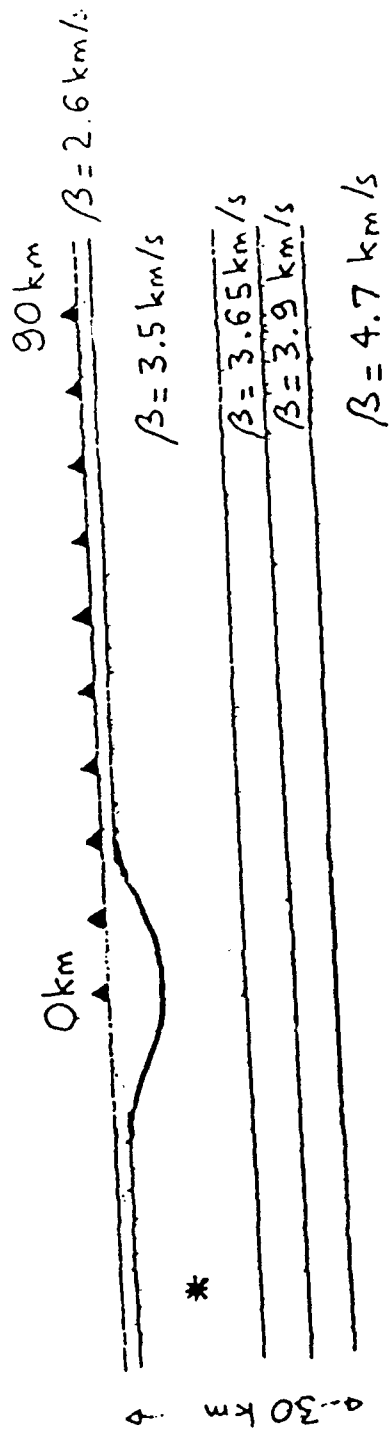
Figure 5 : Rays paths used to build up a map of Q_0 factor for France

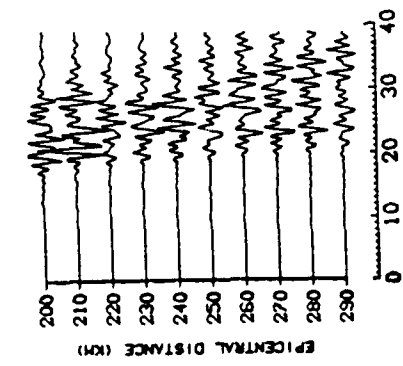
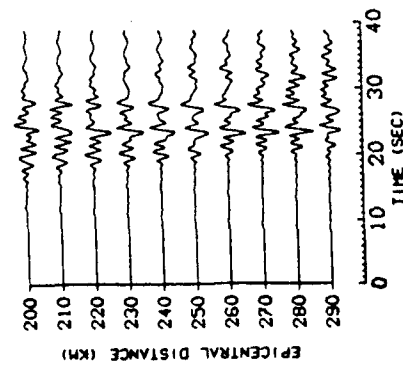
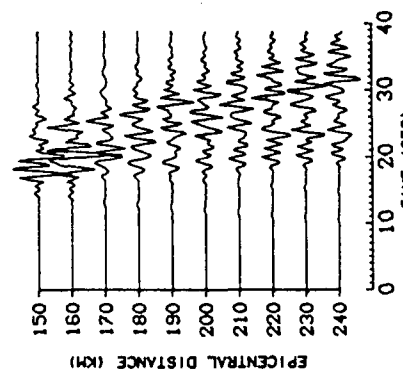
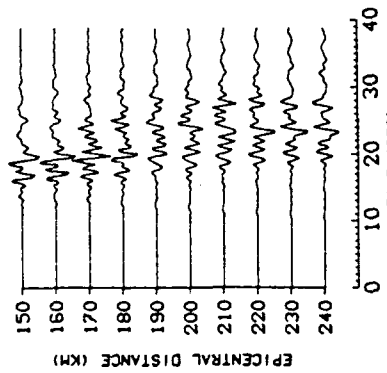
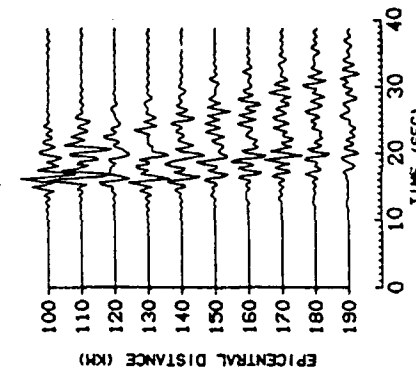
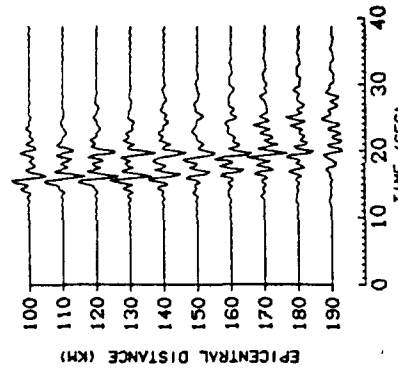
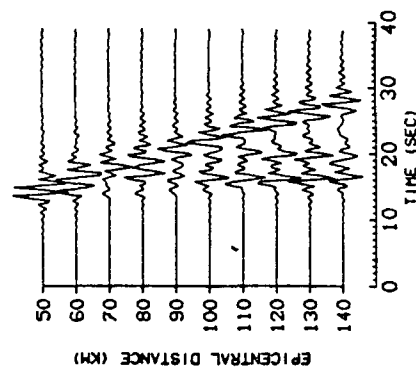
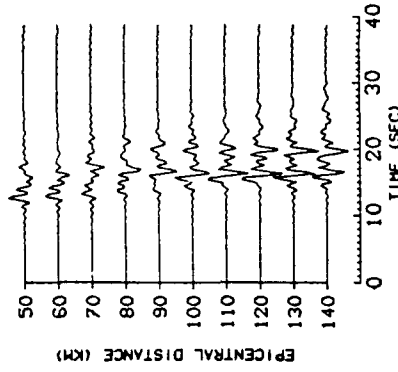
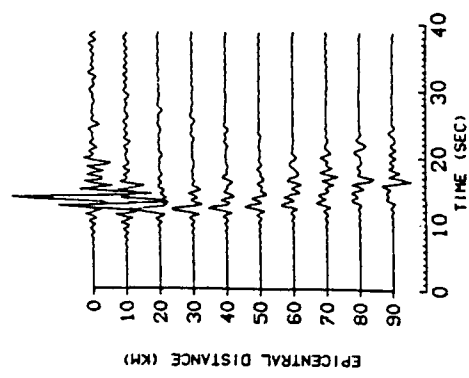
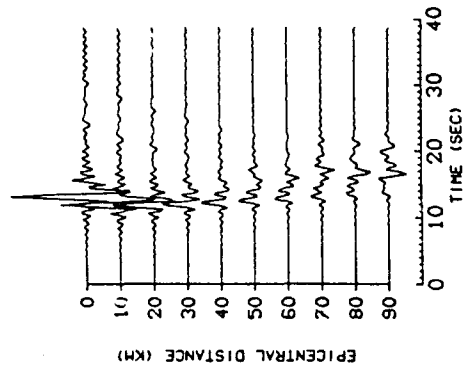
Figure 6 : Map of confidence index

Figure 7 : Map of France (Center) for Q factor at 1 Hz









AFGL/DARPA REVIEW OF NUCLEAR TEST MONITORING BASIC RESEARCH
U.S. AIR FORCE ACADEMY, 6-8 MAY 1986

Modeling Explosions Using 2-D Numerical Methods

Donald V. Helmberger, Richard Stead and John Vidale
Seismological Laboratory
California Institute of Technology

Introduction

It is well known that yield versus m_b plots often show geographical correlations, for example see Lay et. al (1984). Some of this variation could be caused by depth effects and, perhaps, tectonic release. Another possibility is scattered Rayleigh waves. Alewine has shown that many shots near the edge of Yucca Flats and Pahute Caldera have enhanced m_b 's. Stead and Helmberger (1985) argue that this effect may be due to scattered Rayleigh waves. Blandford and his colleagues have suggested this complexity earlier with respect to in-coming signals and reciprocity arguments. We will briefly discuss a rather simplified model of the phenomena for Yucca Flats.

Basin geometry can have several effects on seismic wave propagation. For example, the angle of basin termination can have a strong attenuating effect on surface waves crossing this boundary. At Yucca Flats the basin terminates at relatively shallow dips, probably less than 30° , which causes energy to leak out the bottom. Figure 1 shows the observed strong motions for the FLASK event as recorded on the vertical component. All three components are available and particle motion plots indicate that the larger period secondary arrivals are Rayleigh waves. Note their relative reduction in amplitude at the western hard

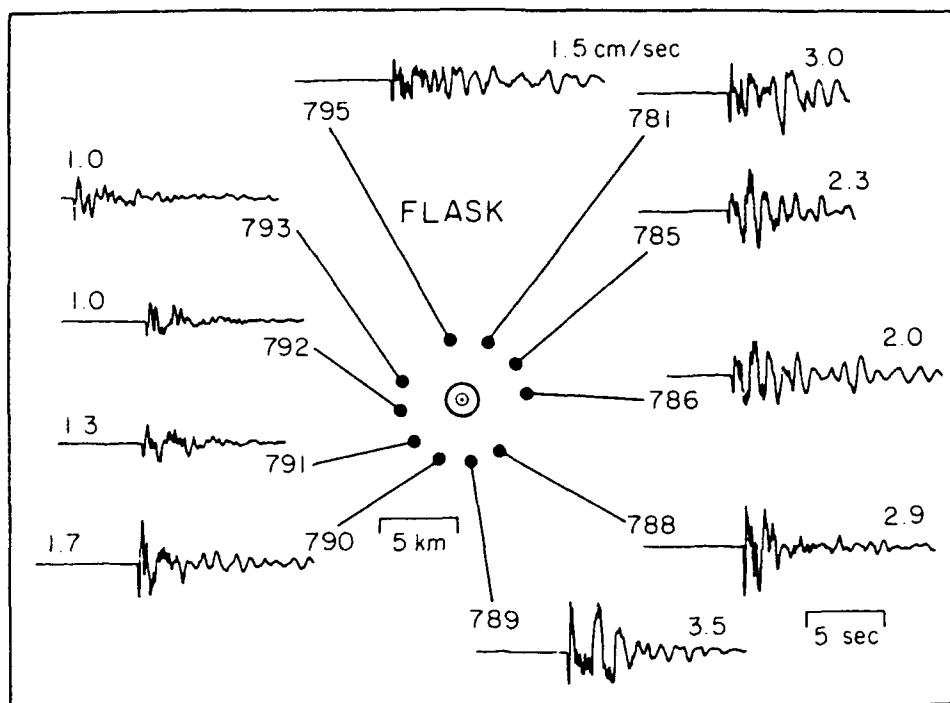


Figure 1. Vertical components of the strong-motion records at roughly 3 km with peak amplitudes indicated above each trace. Note the strong reduction in amplitudes towards the west.

From the Laplace transform of the 2-d wave equation in cylindrical coordinates, Green's transformation gives the result

$$\bar{u}(P) = \frac{-1}{2\pi} \int_{\Gamma} \left[\bar{u} \frac{\partial}{\partial n} K_0 \left(\frac{sr}{\alpha} \right) - K_0 \left(\frac{sr}{\alpha} \right) \frac{\partial \bar{u}}{\partial n} \right] dl.$$

Using the approximate form of K_0 ,

$$\bar{u}(P) = \frac{\sqrt{\alpha}}{2\sqrt{2\pi}} \int_{\Gamma} \frac{1}{\sqrt{sr}} e^{-\frac{sr}{\alpha}} \left[\bar{u} \left(\frac{s}{\alpha} + \frac{1}{2r} \right) \frac{\partial r}{\partial n} + \frac{\partial \bar{u}}{\partial n} \right] dl.$$

Inverting to the time domain,

$$u(P) = \frac{\sqrt{\alpha}}{2\sqrt{2\pi}} \int_{\Gamma} \frac{1}{\sqrt{r}} \left[\frac{1}{\sqrt{t}} * \left(\frac{\partial u}{\partial n}(r, t) + \frac{1}{2r} \frac{\partial r}{\partial n} u(r, t) + \frac{1}{\alpha} \frac{\partial r}{\partial n} \frac{\partial u}{\partial t}(r, t) \right) \right] dl$$

where $\tau = \text{retarded time} = t - \frac{r}{\alpha}$.

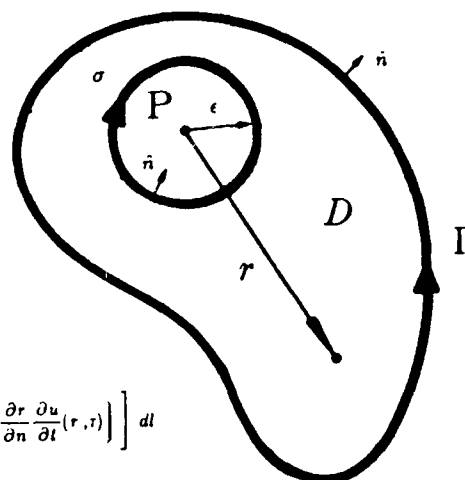


Figure 2. Diagram indicating the enclosed two-dimensional surface and corresponding integral representation.

rock sites. The important problem, then, is that assuming the surface wave energy is generated isotropically from the source, where does the energy go and does it leave as P and/or S waves? Part of it may appear in teleseismic body wave coda as suggested earlier. There are two important observations which can be noted. The first is that there are large complicating arrivals following the P and pP phases for most Yucca events. The second is that for those events showing the complications, the later phases vary greatly as a function of source position.

Approach

In order to model the teleseismic records using a complex source region, we derive a representation theorem similar to Kirchhoff integration, see Scott and Helmberger (1985). We will begin with a simple 2-D Kirchhoff method outlined in Figure 2, where K_0 is the modified Bessel function. The summation procedure is similar to that discussed earlier except that we need only sum over a line of elements.

An application of this technique to an idealized cross-section, taken from NTS is given in Figures 3 and 4. Note that the receivers are arranged from roughly the location of the Yucca Fault across the Valley and onto hard rock. The simplified cross-section of Yucca Flat produces the surface waves shown in the accelerograms of Figure 3. As above, these are computed using a two-dimensional finite difference method and include a Von Seggern-Blandford RDP source with a K of 12 and B of 1. These accelerograms were produced using the asymmetric source of

Surface Wave Synthetics (Accelerograms)

Figure 1 displays a comparison of seismic waveforms for three different cases: Flat Layer Case, Source 1 (East), and Source 4 (West). The waveforms are stacked vertically for each case, representing depths from 0.47 km to 4.26 km. A vertical bracket on the left indicates a depth of 1.2 km. A horizontal bracket at the bottom right indicates a time scale of 5 seconds. The waveforms show varying degrees of complexity and amplitude, with the Flat Layer Case showing the most complex and highest amplitude signals, and the Source 4 (West) case showing the simplest and lowest amplitude signals.

21

Vidale and Helmberger (1986), discussed in the next section. The receivers remain fixed for all three cases, and the easternmost station in each case is the first receiver immediately to the west of the source. The first case is a flat layer geometry with the same velocities as the simplified cross-section and is included for comparison. Comparing Source 1 and the flat layer geometry shows an increase in surface wave frequency and greater amplitude decrease as the waves pass into hard rock across the boundary. Source 4 demonstrates well the drop in surface wave amplitude when crossing this boundary as is observed for many Yucca events.

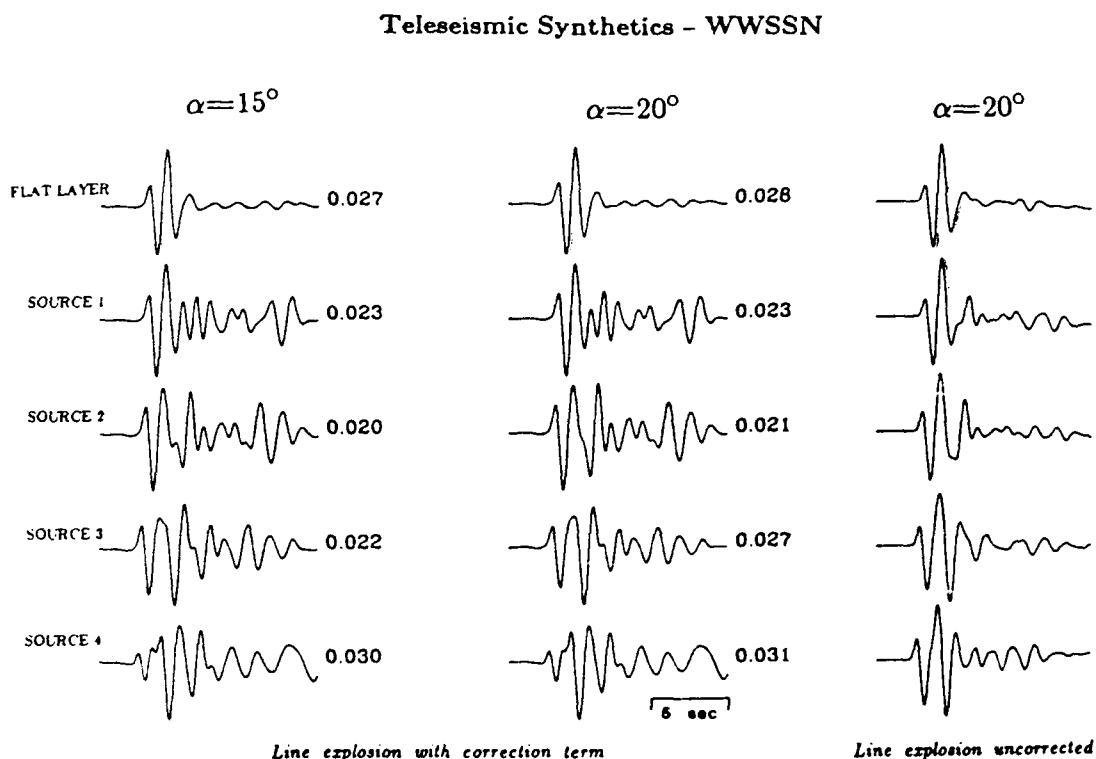


Figure 4. Comparison of teleseismic synthetics obtained from propagating the signals out the bottom of the model via Kirchhoff. Note the strong secondary arrival associated with case 4.

The teleseismic synthetics of Figure 4 are computed using the two-dimensional Kirchhoff method. Once again the flat layer case is included for comparison. The record sections show the variation in the waveforms as the source is moved across the basin. The most interesting observation is that moving the source one kilometer in the basin is much more important than varying the take-off angle five degrees. Also shown is a comparison with a symmetric explosion demonstrating the importance of the correction mentioned above.

Correction Factor for Explosions in 2-D Numerical Grids

We will show that the amount of energy leaving the source region at an angle θ with the vertical in the 2-D grid may be approximated by the amount of energy in the point source case multiplied by $\sqrt{\sin \theta}$. The additional $\sqrt{\sin \theta}$ in the point source or three-dimensional solution can be explained in terms of geometrical spreading as is shown in Figure 5a and 5b. The energy with takeoff angle i between i_0 and $i_0 + di_0$ for the point source becomes

$$E_p \propto \frac{(2\pi \sin i_0 r)}{2\pi r^2} r di_0$$

or

$$E_p \propto \sin i_0 di_0$$

while for the line-source $E_L \propto di_0$

Since energy is proportional to the square of the amplitude we obtain the $\sqrt{\sin \theta}$ dependence.

If we use an isotropic explosion as the source in the 2-D

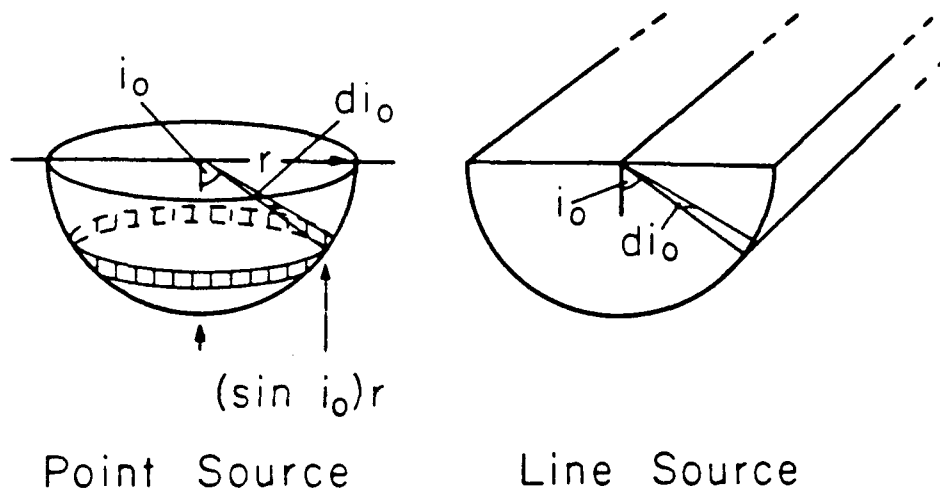


Figure 5. Diagrams showing energy with takeoff angle i in the range $i_0 < i < i_0 + di$ for a point source and for a line source. The energy varies as \sin for the point source case but does not vary as a function of θ for the line source case.

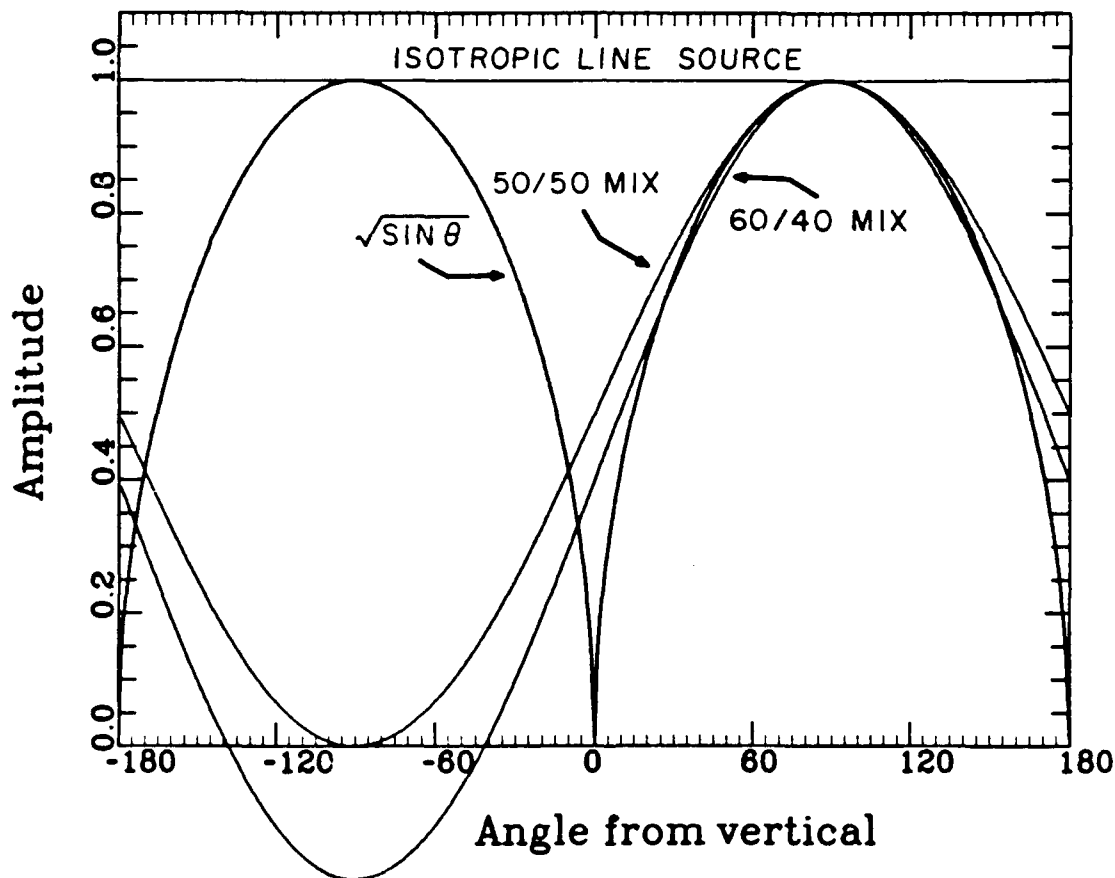


Figure 6. Comparison of radiation pattern for corrected and uncorrected line sources. The level line shows the isotropic radiation pattern which results from an uncorrected explosive line source. The $\sin \theta$ curve shows the best radiation pattern to simulate an explosive point source. The two sinusoidal curves show the result of mixing a line source force with a line source explosion with 50%/50% and 60%/40% weighting. The mixed sources are meant to be accurate in the range $\theta = +20^\circ$ to $+160^\circ$.

grid, each arrival in a record may have a different take-off angle θ , but we can only correct for a constant $\sqrt{\sin \theta}$. The result is that the importance of vertically as opposed to horizontally traveling energy is overemphasized in the line source compared to the point source case.

One might ask why not simply multiply the isotropic source by $\sqrt{\sin \theta}$. Such a source does not satisfy the 2-D elastic wave equation, unfortunately, and will not maintain the $\sqrt{\sin \theta}$ radiation pattern once the energy leaves the source region, primarily due to the cusp in the $\sqrt{\sin \theta}$ at $\theta = 0^\circ$.

The source functions we have found which are solutions to the 2-D elastic wave equation have radiation patterns of $\sin^n \theta \cos^m \theta$, where we may choose n and m . An isotropic line source explosion, for example, is the solution with $n = m = 0$, and the dislocation sources have $n + m = 2$ (Vidale and Helmberger, 1986). Also, because of the asymptotic nature of our solutions, the compressional and shear parts of the source separate. The correction we introduce is to add the compressional component of the horizontally-directed force term ($n = 1$ and $m = 0$) to the explosive source that decreases the amplitude of energy leaving the source vertically, but leaves unchanged the amplitude of energy going horizontally out the side.

By judiciously mixing the explosive and force terms, we can modify the vertical radiation pattern of the explosion to mimic the $\sqrt{\sin \theta}$ we desire. Figure 6 shows the radiation patterns that result from using 100% explosion, 50% explosion mixed with 50%

force, and 40% explosion mixed with 60% force. These cases are compared with the $\sqrt{\sin \theta}$ and isotropic line source radiation patterns. Energy that leaves the source at angles near $\theta = 90^\circ$ is not affected by the correction, but energy at angles near $\theta = 0^\circ$ is markedly affected. The mix of explosive and force source expressions determines where in the radiation pattern the source is most accurate. The 50%/50% mix is most accurate near $\theta = 90^\circ$ and the 60%/40% mix is less accurate near $\theta = 90^\circ$, but is also accurate near $\theta = 30^\circ$, as may be seen in Figure 6. It is clear from Figure 6 that only energy leaving the source at positive angles may be modeled with this corrected source.

Recommendations

Line-source calculations to generate point-source spreading with proper radiation patterns looks quite promising. However, the problem is truly 3-dimensional and we plan to perform some full scale checks in the near-future. The final objective, of course, is relating the above synthetics to actual data for known geology and the proper geometries.

MODELING L_g PROPAGATION ACROSS CRUST-MANTLE TRANSITION ZONES AND EVALUATING SURFACE WAVE PATH CORRECTIONS

Janice Regan, Peter Glover, and David G. Harkrider

Seismological Laboratory, California Institute of Technology,
Pasadena, California, 91125

INTRODUCTION

Finite element forms of the seismic Representation Theorem (RT) have been developed to allow modeling of teleseismic L_g waves crossing continental margins, or other heterogeneities. The accuracy of this formulation and the efficiency of an absorbing boundary condition designed to reduce computation time have been previously established. Initial calculations of L_g wave propagation through transition regions have been verified and extended by a numerical experiment which studied the effects of different lengths of transition regions on the L_g waves traversing them. The FE calculations are driven by specifying the displacement time histories at a column of nodes which represent the boundary between the laterally homogeneous region and the transition zone. These time histories can be calculated using standard techniques when the source is separated from the margin by long continental paths. Alternatively, they can be input from other FE calculations. Both of these approaches are used in the results reported here. The first approach, will be referred to as the hybrid method. The time histories used as FE input for the hybrid calculations described below are L_g mode sum displacement time histories calculated at .5 km vertical spacing down a grid edge at a distance $\alpha = 1500$ km from a 8 km deep source. The FE calculation propagates the energy through the remaining portion of the path, a distance β , to the receivers located at distance δ . We should point out however that our technique is only valid for waves propagating at normal incidence.

Recent estimates of explosion moments using surface waves are made using surface wave path corrections based on a modification of a two dimensional approximation of normal incident surface waves crossing slowly varying transition zones. Similar to this correction, the Gaussian beam approximation for surface waves also conserves lateral energy flux. In addition it includes the effect of lateral heterogeneity on geometrical or optical spreading. Since neither technique was intended for generating path corrections for surface waves generated by sources in limited source regions with possibly sharp boundaries, such as low velocity basins, it is important to test their validity. This was done by comparing synthetic Rayleigh waves calculated by these techniques with those obtained from hybrid finite-element codes coupled to analytic teleseismic modal propagator codes.

L_g ACCOMPLISHMENTS

An initial test of the effects of a transition region on the propagation of L_g mode sum seismograms used a pair of 20 km transitions of the type shown in Figure 1. The results of this test, outlined below, indicated that a numerical experiment to quantify the dependence of L_g attenuation across transition regions on the structure of those transition regions, could give some significant insights into where and why L_g disappears when it interacts with oceanic structures. The initial test results also describe the common properties observed for all transitions studied. Energy reflected back from the transition zone toward the source is clearly visible. The energy impinging on the crust to water sloping boundary is mostly reflected. The passage of the L_g wave through the forward transition region effected the distribution of energy with depth. Since no energy is transmitted into the water layer, the remaining energy must be concentrated by the sloping boundary into the oceanic crustal layer. Thus, the amplitudes in the oceanic crustal layer at the end of the transition are larger than the amplitudes between 5 km and ten km depth at the beginning of the transition. The difference is maximum at a depth of 5km and decreases with depth, suggesting that some energy is traveling down the sloping surface into the oceanic crustal layer. The energy incident on the sloping crust to mantle boundary seems to be primarily transmitted. Conversely, for the reverse transition, the energy traveling in the oceanic crustal layer spreads into the entire continental crustal layer reducing the amplitudes at any particular depth. Most of the energy incident on the sloping mantle to crust boundary is reflected. As the wavefront goes through the continent to ocean transition surface displacement history amplitudes increase as the crustal thickness decreases. When the wavetrain propagates through the oceanic structure surface amplitudes decay with distance, rapidly at first, and then more slowly. Furthermore, as the wavefront passes through the oceanic to continental transition a rapid decay in amplitude is observed. After the L_g wave reenters the continental structure amplitude decay continues for a short distance while the waveform and amplitude stabilize.

A study of the effects of the length of simple transition regions on the attenuation of SH type L_g mode sum seismograms passing through them has yielded some interesting results. In order to discuss these results the models must first be described and the methods of analysis explained. Two classes of transition models were considered. An example of each class is illustrated in Figure 1. Calculations were performed for four individual models from each class, for a continental crustal layer over a mantle half space, and for an oceanic crustal layer over a mantle half space. The difference between individual transition models was the length of the transition region, or the horizontal distance between points B and D shown in Figure 1. As the length of the transition increases the angle that the the ocean to crust boundary or crust to ocean boundary makes with the horizontal (ϕ_{oc} or ϕ_{co} in Figure 1) varies between 3° and 90° , and the angle the the crust to mantle boundary or the mantle to crust boundary makes with

the horizontal (ϕ_{mc} or ϕ_{cm} in Figure 1) varies from 12° to 90° . The differences in slope of the boundaries and the different elastic properties of the layers the separate indicate that different behavior should be expected along those two boundaries. The initial model discussed previously used a transition length of 20 km. Real ocean to continent type transitions occur over lengths of order 100 km. Limiting FE computation time per model to approximately one cpu day imposed an upper limit of 100 km on the length of the transition. Thus, the lengths used for this investigation were a step transition (0 km), 25 km, 50 km, and 100 km. For each model seismograms were recorded at intervals of approximately 5 km along the surface. Figure 2 shows the RMS surface amplitudes calculated over the first 60 seconds of seismogram for each of the receivers along the surface of the 50 km transition. Seismograms were also recorded, with vertical spacing of 2.5 km, at several distances. Depth sections were recorded at distances A through E (Figure 1) for all models. For the 100 km transitions additional sections were recorded midway between B and C and midway between C and D. For the 50 km forward transition an additional depth section with vertical spacing of .5 km was recorded 25km beyond the end of the transition. This section was used as input for later calculations.

The first class of models are of continent to ocean, or 'forward' transitions. Each 'forward' transition model uses the same set of input data, or forcing functions. In each case the leftmost column of nodes of the forward transition FE grid are constrained to move with the displacement time histories specified by the driving functions. In each forward transition model the transition region is characterized by a continuous rate of thinning of the crustal layer between the thirty two km thick continental crust at the beginning of the transition region and the 5 km oceanic crust, overlain by 5 km of water, at the end of the transition region. The mode sum forcing functions are also used as input to a reference model of a thirty two km continental layer over a mantle half space. Depth sections at A and B (see Figure 1a) were subtracted from depth sections recorded after the same distance of FE propagation in the continental reference model. These differences give the wave reflected back from the transition region.

The second class of models are of ocean to continent, or 'reverse' transitions. The driving functions for the 'reverse' transition tests are recorded during the 50 km 'forward' transition calculation. They consist of a depth section of hybrid seismograms recorded 25 km past the oceanic end of the 50 km forward transition, which corresponds to a distance of 1755 km from the source. The vertical spacing within the depth section is .5 km. The reverse transition driving functions are also used as input to an oceanic reference model of a 5 km crustal layer over a mantle half space. Each reverse transition is modeled as a smooth increase in thickness of the crustal layer between a 5 km thick oceanic crust, overlain by 5 km of ocean, at the beginning of the transition and a 32 km continental crust at the end of the transition.

The 'forward' transition tests illustrate several properties that change with the length or slope of the transition model. At the crust to water boundary the amplitude of the waveform reflected back into the continental layer, that is back toward the source, decreases as the length of the transition increases. A similar effect of much smaller magnitude is observed along the crust to mantle boundary. The difference in the magnitudes of the effects at these two boundaries can be explained by the difference in velocity contrast across them and the difference in the angles ϕ_{mc} and ϕ_{co} . Although no energy is transmitted into the water layer, not all energy impinging on the water layer is reflected. Instead some of the energy is concentrated by the transition into the oceanic crustal layer. The amount of concentrated energy, increases as the length of the transition increases (Figure 3). Concentrated energy is observed as an increase in amplitude of seismograms in the oceanic crustal layer with respect to the amplitudes of seismograms at the same depth, between 5 km and 10 km, in the continental crustal layer at the beginning of the transition. Due to the transmission of energy across the crust to mantle boundary, detection of a similar concentrating effect associated with this boundary will require more detailed analysis of the calculated results. Amplitudes in the mantle layer within the transition region are maximum immediately below the crust to mantle transition and decay nearly exponentially with depth below the boundary. The amplitude of the transmitted seismograms below the oceanic crustal layer, at the oceanic end of the transition, decrease as the length of the transition increases. Figure 2 shows that the seismogram amplitudes at the surface of the crustal layer show a general increase as one passes through the transition, however, this increase does not appear to be monotonic. The variation in surface amplitude within the transition zone has similar pattern for all lengths of transitions, but the width of the oscillations scale as the width of the transition region. This is illustrated in Figure 3, which shows a sketch of the variation in the behavior of RMS amplitudes with distance along the surface for each transition length.

The 'reverse' transition tests have not been as extensively studied. However, it is clear that a longer transition is much more effective at reducing surface amplitudes. Examination of Figures 2 and 3 show that the surface amplitude decay across the transition is monotonic for the reverse transition, and that the surface amplitude vs. distance relation along the oceanic portion of the path is oscillatory. This oscillatory behavior is also observed for the oceanic reference model calculation, where it is superimposed upon a slow decrease in amplitude. The amplitude distributions with depth indicate that energy is being channeled down into the mantle by the reverse transition. The amount channeled energy seems to increase as the length of the transition increases. The amplitudes below the crustal layer of the transition region do not die off as strongly with depth as they do in the 'forward' transition case. It appears that it is in the 'reverse' transition and the propagation through the intermediate oceanic layer that causes the attenuation of L_g type waves when they travel across a mixed path containing an oceanic region.

The length of the intermediate oceanic path between the continent to ocean and the ocean to continent transition is also being investigated. Calculations for three distances have been done using multiple FE calculations to go from the edge of the first transition model to the receiver. Due to computational limits, the lengths of these intermediate paths are short, but definitely within the range of interest. Lengths of 30, 70, and 120 km, have been used. For the shortest paths energy transmitted in to the mantle layer has little time to dissipate out of the calculation before much of it passes back into the crustal layer as it travels through the reverse transition. This implies that there may be a critical distance where enough of the energy has been lost by propagation through the oceanic structure that L_g would essentially disappear due to dilution caused by propagation through the reverse transition region. Further analysis of completed calculations, and additional calculations are needed to establish whether this is true, and to quantify any such effect. In particular a coupling method to pass the FE results back into the mode sum calculations is nearing completion. This will allow consideration of longer paths, and easier determination of shorter paths.

SURFACE WAVE PATH CORRECTION ACCOMPLISHMENTS

The source region medium is a cylinder with a radius of 1.8 km and extends from the free surface down to a depth of 1.8 km. The source cylinder is embedded in a half space of the same elastic properties as that of the upper part of the propagating medium. The RT surface, over which the propagation Green's functions are integrated, surrounded the plug at a distance of 0.3 km into the half space of propagation material. The RT surface is composed of 11 nodes or rings per side with a spacing of 0.2 km. The propagation model is CIT109, which is based on western US observations and has a 14 km thick upper crust. The three elastic materials used in the source medium cylinder are characteristic of the shot point properties at three NTS areas; Climax Stock, Pahute Mesa and Yucca Flat. The seismic velocities, densities and other material properties for the source media are given in the following table.

Material Properties of Source Region Models						
SOURCE MODEL (S)	α km/s	β km/s	ρ gm/cm ³	$\frac{\mu_{CIT}}{\mu_S}$	$\frac{(\lambda+2\mu)_{CIT}}{(\lambda+2\mu)_S}$	α^2/β^2
YUCCA	2.35	1.30	1.86	10.7	10.2	3.27
PAHUTE	4.00	1.90	2.30	4.06	2.86	4.43
CLIMAX	5.33	2.78	2.67	1.63	1.39	3.68
CIT109	6.20	3.51	2.74	1.00	1.00	3.12

In order to demonstrate that modeling an explosion by applying a stress glut at two elements along the the vertical axis was sufficient, we made an RT calculation in which the source medium was the same as the surrounding medium. We then calculated its analytic Rayleigh wave analog, a point explosion at a

depth of 0.4 km in the CIT109 model. The time domain records of both calculations as seen through a long period WWSSN instrument at 3000 km were essentially indistinguishable. The maximum error was less than 2 %.

Previous reports have focused on time domain comparisons between RT and CLEF. Since the phase of the CLEF calculation is not used to estimate the explosion and tectonic release moments, we will restrict this report to comparisons of amplitude spectra and spectral ratios. In Figure 4a, we show the spectra and spectral ratios of the analytic and RT synthetics for the pure CIT109 model with the WWSSN-LP instrument. The calculation frequency range is 0 to 2.5 hz. The agreement between the two calculations is excellent out to the roll-off frequency of the cosine filter which was applied to the finite element forcing functions before their decimation to 0.2 second time steps. The original finite element time step was considerably smaller, by nearly a factor of 13.

In this figure, we only spectra out to 0.2 hz. This frequency range gives the best detail of the frequencies of interest in estimating seismic moments using surface wave path corrections. At periods greater than 50 seconds, the RT calculation has larger amplitudes than the analytic or exact synthetic. This can be considered the long period upper limit to the accuracy of the RT calculations.

In the rest of Figure 4, we display the spectra and spectral ratios of RT calculations for the three source media and their CLEF approximations. The agreement between RT and CLEF spectra is good especially considering the rational behind the approximations. The three cases all show the same character in that CLEF spectra is smaller than RT at long periods and greater at higher frequencies. The cross-over is somewhere between 20 and 10 seconds period.

In Figure 5 a and b, we show the spectra of the RT model of Yucca with a lateral and vertical transition zone out to 0.2 hz and 1.0 hz respectively. It is compared with its CLEF analogue. Beyond 0.2 hz, the CLEF approximation becomes increasingly bad. This is true of all the models with the CLEF approximation having higher frequency content. Because of the small vertical extent of the inhomogeneous source region relative to the wavelengths of the surface waves, the difference between the spectra of CLEF and GBSW is negligible for periods greater than two to four seconds. This is shown in Figure 5 c for the Yucca models. At higher frequencies, the GBSW approximation has less frequency content out to 1.0 hz as shown in Figure 5 d.

In Figures 6 and 7, we show the CLEF and GBSW approximations out to 1.0 hz compared to the RT models discussed above. The CLEF comparisons are on the left and the GBSW comparisons are on the right of each figure. In every model calculated, the GBSW outperforms the CLEF approximation and never has less frequency content than the RT model.

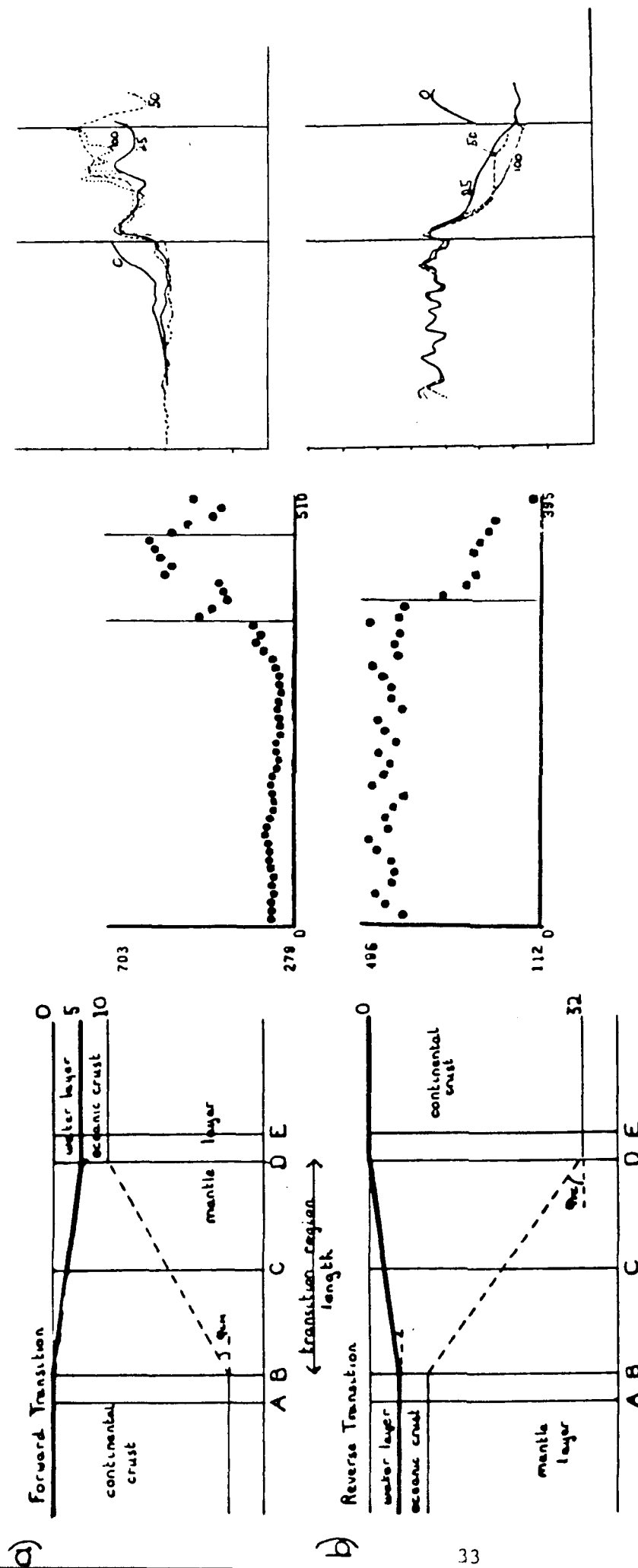


Figure 2) Sample profile of surface amplitudes. Upper curve shows amplitudes of surface seismograms as a function of distance along the surface of the forward transition model. Lower curve shows analogous amplitudes for the reverse transition model. Vertical lines indicate the limits of the transition region.

Figure 3. Variation of surface amplitude along the surface of each transition. The upper sketch shows the variation in RMS amplitude (60s) along the surface of each forward transition model. The lower sketch shows the amplitude (50s RMS) distance relation of surface amplitudes for each reverse transition. Amplitude is recorded as the y coordinate. The distance scale is not uniform along the whole axis. The two vertical lines indicate the limits of the transition region. Outside the transition region the scale is uniform. Within the transition region distances are plotted with respect to an origin at the beginning of the transition region, as fractions of the transition length. All data points lie on the indicated line except for some scatter in the 100 km transition results.

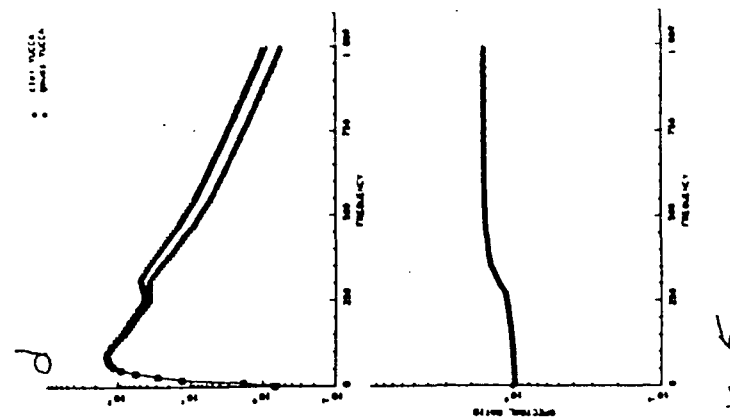
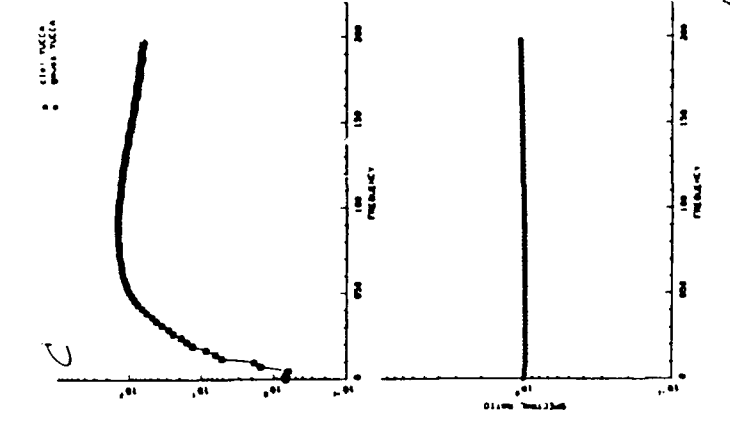
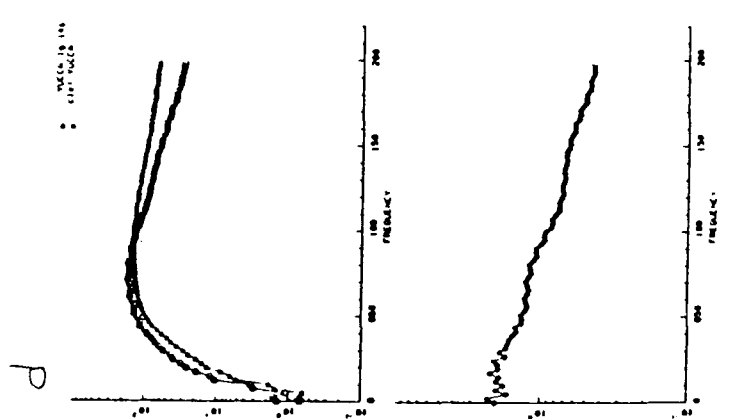
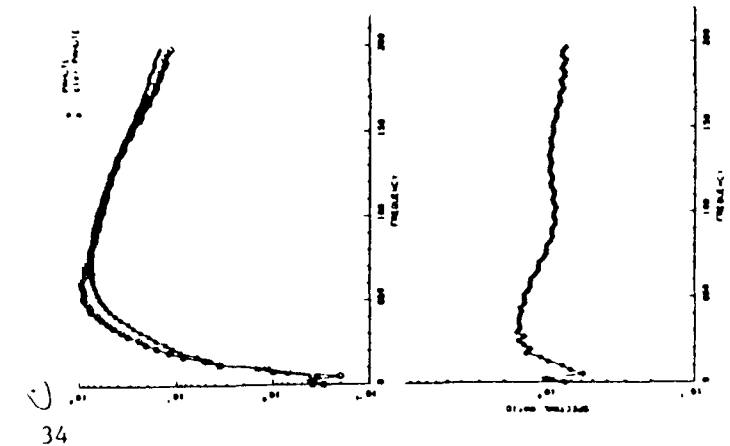
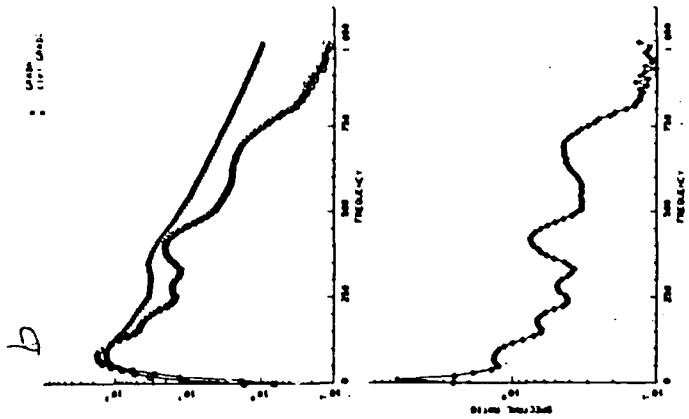
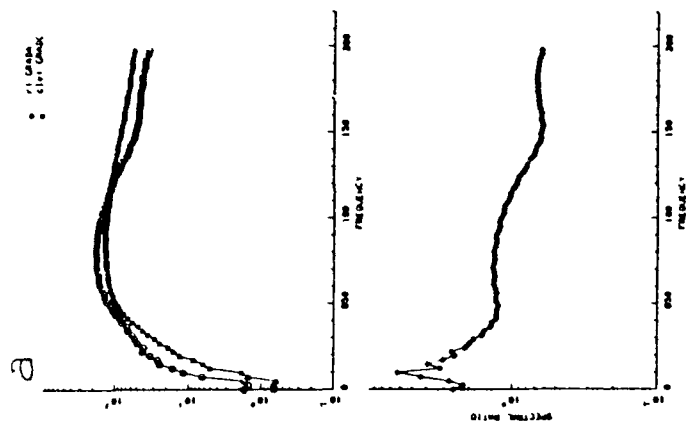
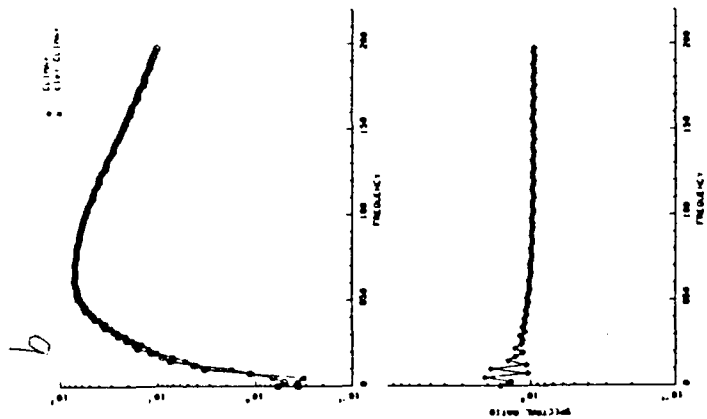
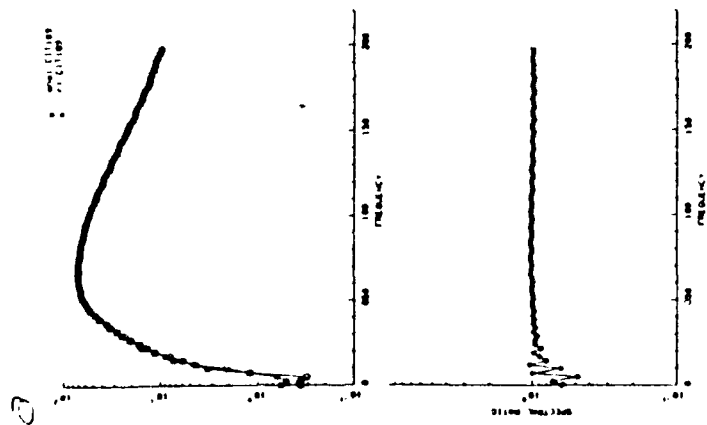


Figure 5

Figure 4

GEOPHYSICAL INVESTIGATIONS AT PAHUTE MESA, NV

JOHN F. FERGUSON

THE UNIVERSITY OF TEXAS AT DALLAS

This paper is a progress report, midway through a two year study of the shallow (<5 km) geophysical structure under Pahute Mesa, NV and its effect on teleseismic observations of events at that site. Topics to be discussed include the geophysical properties as deduced from well logs, new gravity stations acquired in June 1985, models of the Bouguer gravity for the Silent Canyon Caldera and a seismic reflection - refraction experiment to be conducted in May and June of 1986.

Both uphole P-wave velocity surveys and either density or borehole gravity logs were available in holes U19af, Ue19z, U19x, U19ak, U19ae and U19ab. Locations for these holes are shown in Figure 1. The geologic formations can be geophysically clustered into four units as follows. 1) Tuffs - low density and velocity. 2) Lavas - high density and velocity. 3) Rainer Mesa tuff (Tmr) - high density and low velocity. 4) Peralkaline rocks of the Silent Canyon Caldera - high density and velocity, which constitutes the geophysical "basement". The tuffs have been characterized by linear density and velocity functions as illustrated in Figure 2. Below the water table, at about 700 m, the gradient decreases to $0.42 \text{ gm/cm}^3/\text{km}$, with similar behavior in velocity also expected.

Prior to 1985 the gravity data base for the Pahute Mesa - Timber Mt. area consisted of 3200 stations obtained by the USGS in the early 1960's. Elevation control was based on poor maps and barometric altitudes. The station density was generally 1 or 2 $/\text{km}^2$. In June of 1985 UTD obtained 300 new stations on traverses

along roads at 300 m intervals. The elevation control was by EDM, so that the new data is approximately an order of magnitude more accurate than the old. Near the southeast margin of the Silent Canyon Caldera, two-dimensional coverage was obtained. In Figure 3 the 1985 traverses are shaded over the station locations. The old and new data agree well in areas of overlap. The Bouguer anomaly was computed for the merged data with a density of 2.0 gm/cm^3 and terrain corrections were applied using digital topographic data. The resulting Bouguer anomaly is contoured in Figure 4.

The 25 mGal residual anomaly can be modeled as a low density (with linear density function) surface inclusion of volcanic fill in the high density Silent Canyon collapse structure. The high density Tmr and lava units are well controlled by boreholes and their effect can be stripped from the data. The Silent Canyon interface is more sparsely controlled, but can be estimated by inversion using a modification of Oldenburg's (1974) method. The regional gravity anomaly is simultaneously estimated by a least squares fit to borehole constraints. As an example the profile B-B' on Figure 4 is presented in Figure 5. The Tmr is shown by the dashed pattern and the lava unit (Tra) is presented with the cuneform pattern. The Silent Canyon basement is stippled. Excellent agreement is found at four boreholes near the profile. The estimated regional shows a small "high", which may correspond to the deep crustal high velocity anomaly noted by previous investigators (Taylor, 1983).

In May and June of 1986 a seismic reflection - refraction

experiment will be performed at Pahute Mesa by UTD in cooperation with Los Alamos National Laboratory and the USGS refraction group at Menlo Park, CA. Seventeen high explosive shots will be fired in outcropping Silent Canyon basement at the location indicated in Figure 4 and recorded on the line crossing the southeast caldera margin and trending northwest for 15 km. Up to 70 Dinoseis shots will be recorded at near offsets. A 24 channel, floating point recording system will be used with 60 m geophone group interval and 1400 m spreads with 50% overlap.

The USGS (Hoffman and Mooney, 1984) has had considerable success with a combined refraction and gravity interpretation at the Crater Flat Caldera, to the south of Pahute Mesa. The model presented in Figure 6 was derived from data that are more sparse than the Pahute Mesa experiment, but with much longer offsets (out to 40 km) for deeper crustal penetration. The 1986 experiment will map the Silent Canyon basement and shallow structures in the tuffs and lavas filling the caldera. It may be possible to record reflections from as deep as 5 km, which could be associated with Paleozoic units and Tertiary or Mesozoic intrusives.

In the future it would be possible to extend the depth range of the model by recording nuclear tests at Pahute Mesa, Rainer Mesa and Yucca Flat with event recorders on the same profile. This concept is illustrated in Figure 7. Detailed knowledge of the shallow structure at Pahute Mesa gained in 1986 and previously for Rainer Mesa and Yucca Flat will permit interpretation of the far offset data for mid-crustal structure.

I would like to acknowledge the contributions of students at

UTD to this project and especially Sharon Reamer for her part in the gravity investigations. Much of this study would have been impossible without the support of personnel at Los Alamos National Laboratory. Allen Cogbill, Rick Warren, Jack House and Don Collins of Los Alamos deserve special recognition.

REFERENCES

Hoffman, L. R., (1984), A seismic study of Yucca Mountain and vicinity, southern Nevada; data report and preliminary results, USGS Open-File Report 83-588, Menlo Park, CA.

Oldenburg, D. W., (1974), The inversion and interpretation of gravity anomalies, *Geophys.*, v 39, p 526-536.

Taylor, S. R., (1983), Three-dimensional crust and upper mantle structure at the Nevada Test Site, *J. Geophys. Res.*, v 88, p2220-2232.

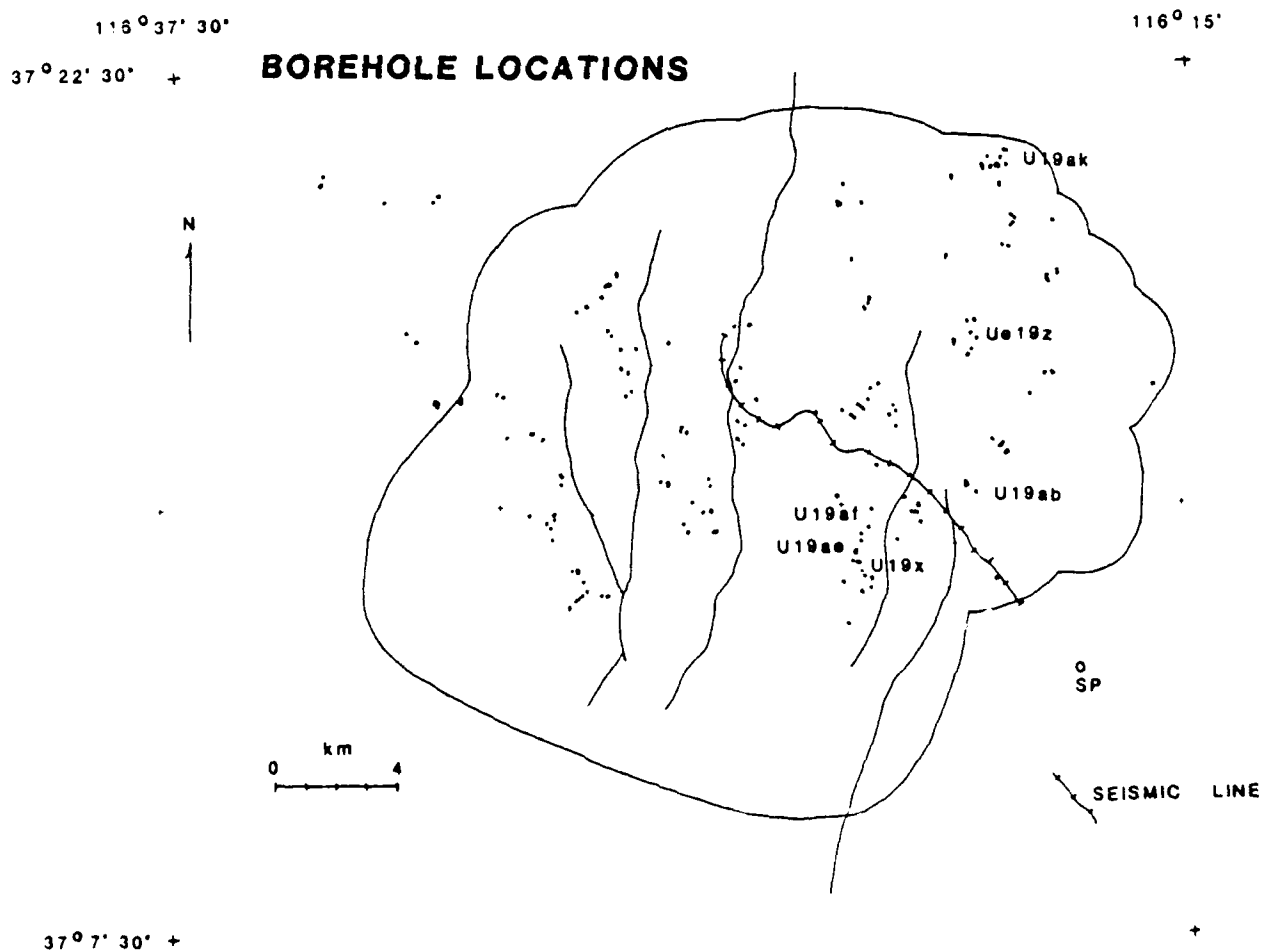
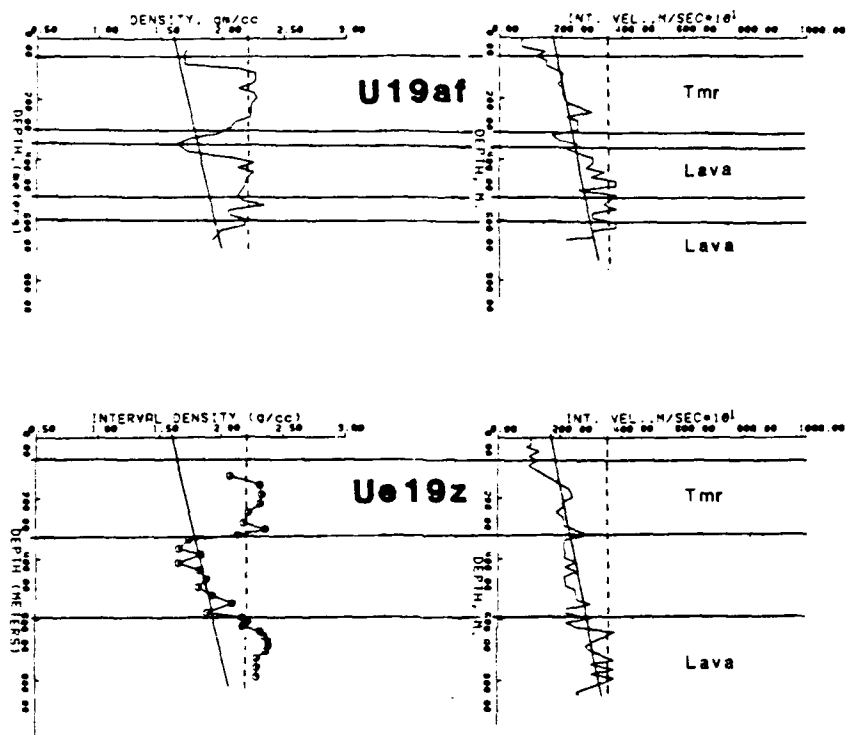


Figure 1



Velocity:

Tuffs-

$$v(z) = 1.70 + 2.15 z \text{ km/sec}$$

Lavas-

$$v(z) = 3.50 \text{ km/sec}$$

z in km

Density:

Tuffs (excluding Tmr)-

$$\rho(z) = 1.51 + 0.74 z \text{ gm/cm}^3$$

Lavas and Tmr-

$$\rho(z) = 2.20 \text{ gm/cm}^3$$

PAHUTE MESA GEOPHYSICAL LOGS

Figure 2

GRAVITY STATION LOCATIONS

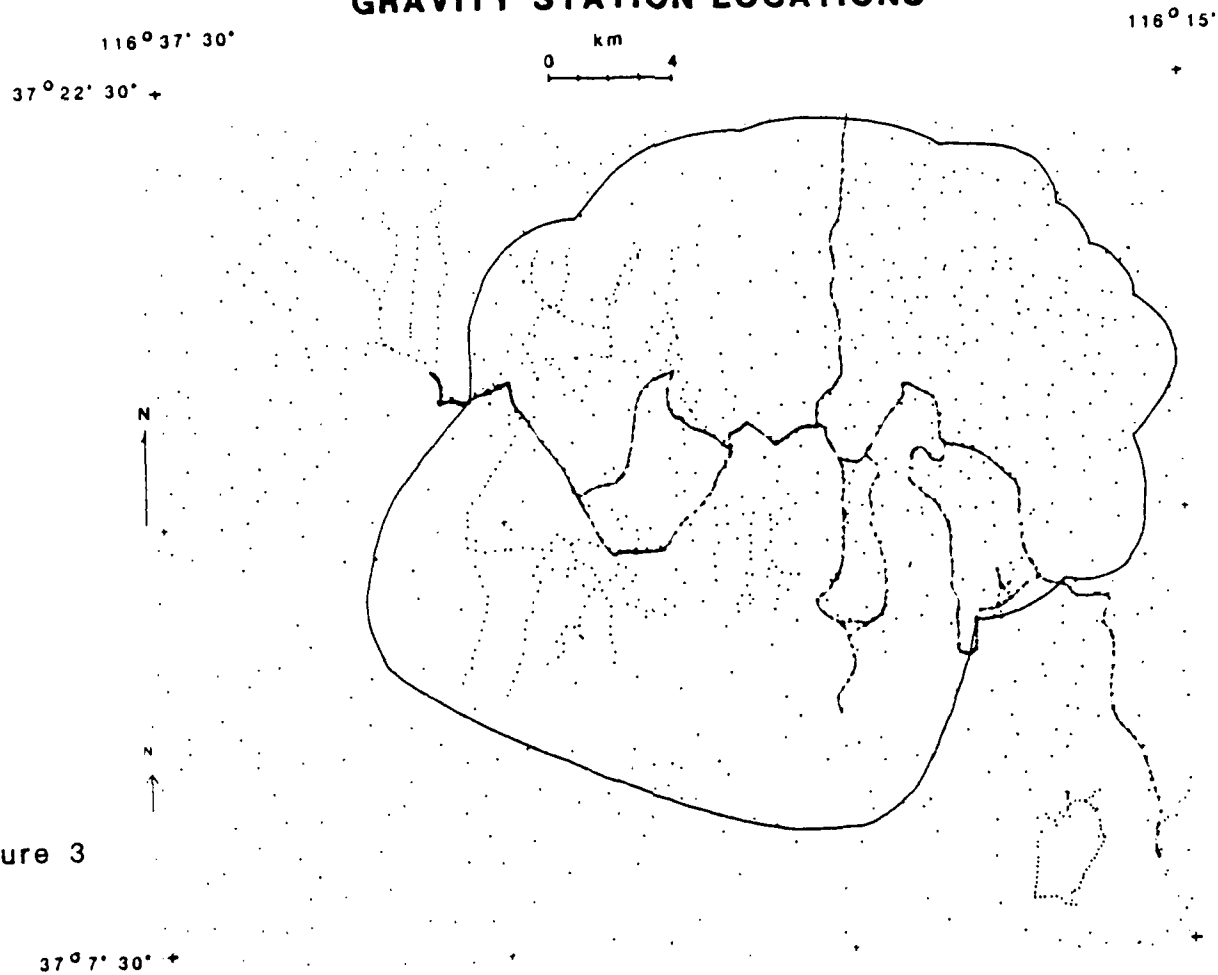


Figure 3

BOUGUER GRAVITY ANOMALY

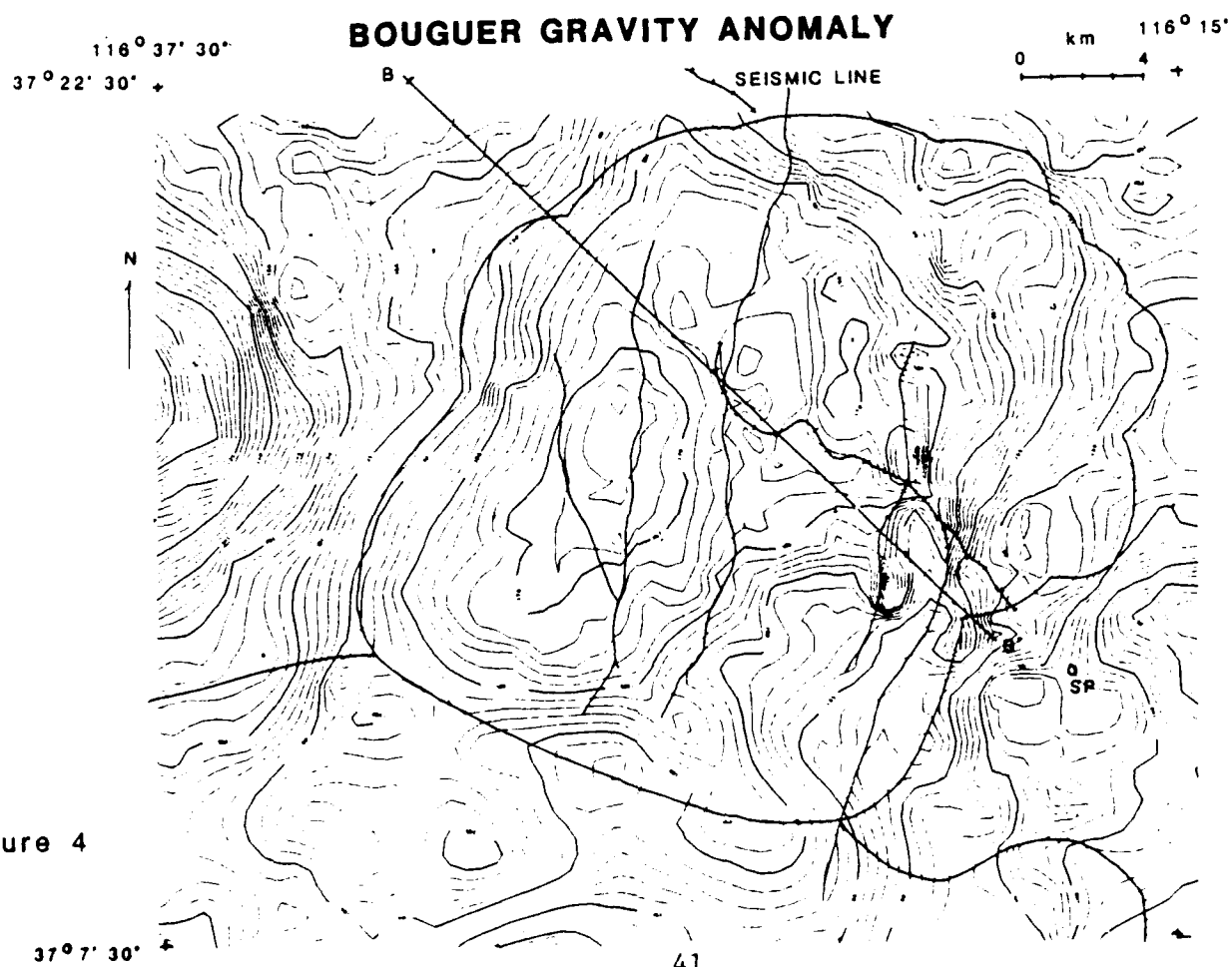


Figure 4

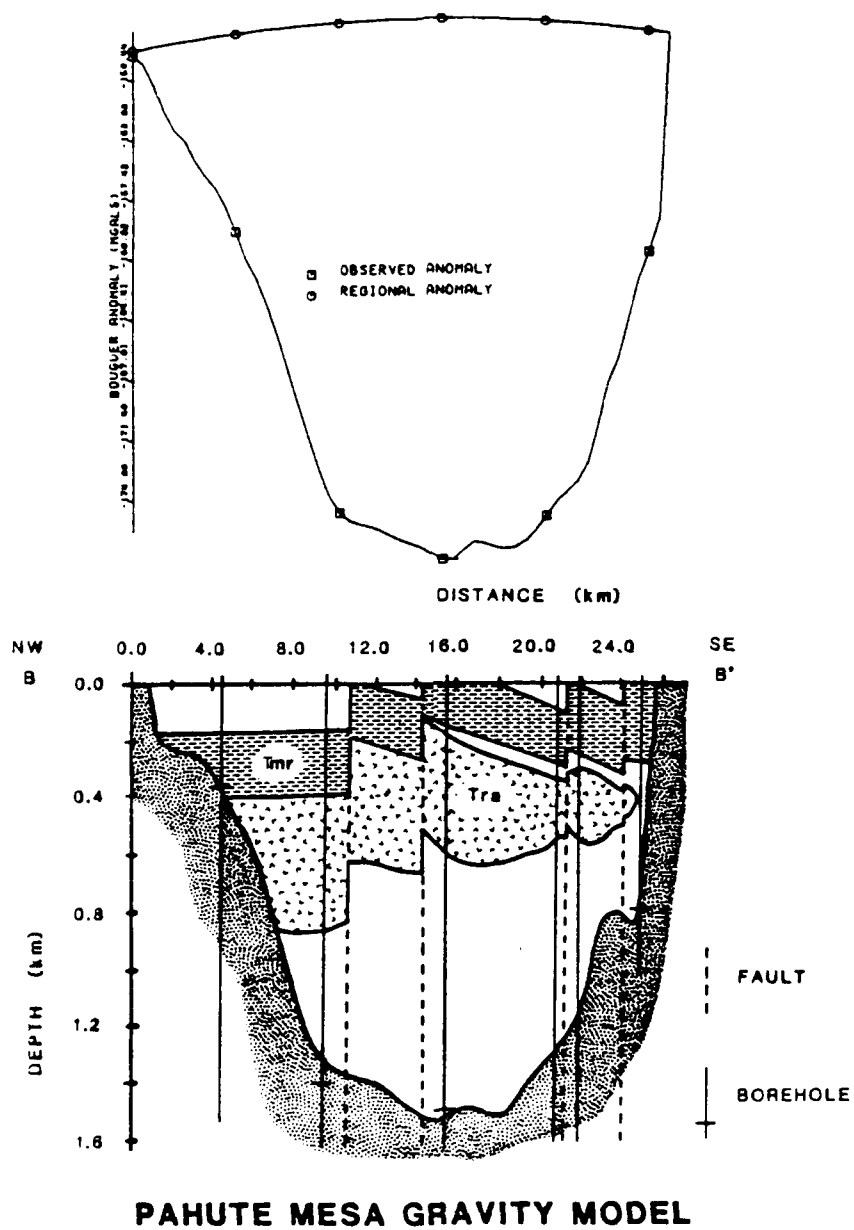


Figure 5

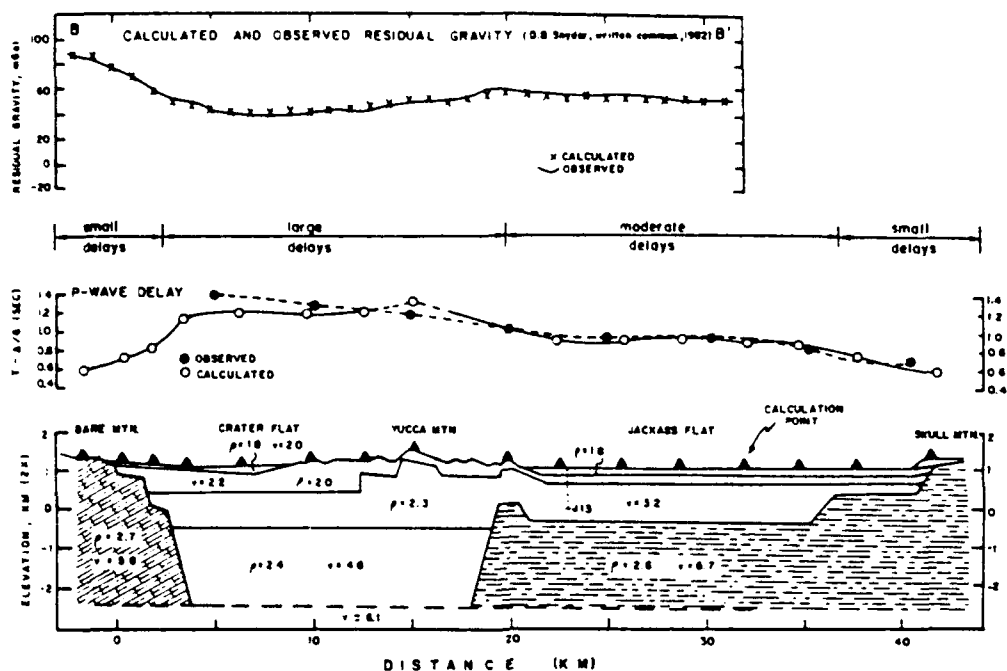
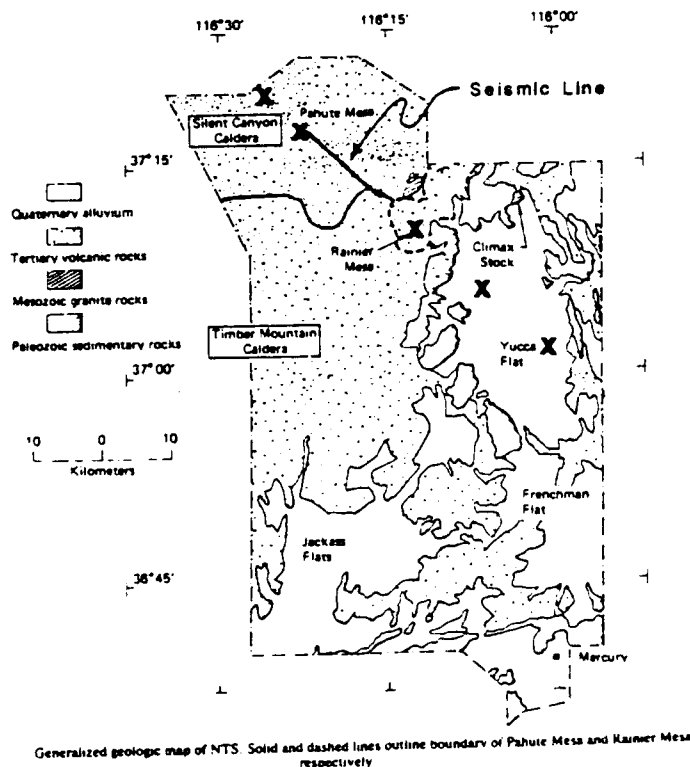


Figure 6

Crustal section modified from Snyder and Carr (1982) with layer densities and velocities (Table 1), observed and calculated traveltimes delays for P-wave arrivals from nuclear sources, and calculated and observed residual gravity. Observed and calculated delay times agree well, except over Crater Flat where the observed delay is 0.2 s larger than that calculated (see text). Drill holes are projected onto the profile.

after Hoffman and Mooney (1984)



X Possible test locations to record

Figure 7

after Taylor (1983)

REGIONAL STUDIES WITH BROADBAND DATA

T. V. McEvilly and L. R. Johnson
University of California, Berkeley

VELOCITY MODEL FOR PAHUTE MESA

Considerable attention has been given to the task of estimating a velocity model for the shallow structure at Pahute Mesa, because such a model is important for other parts of the research effort. Data from all of the events that we have recorded at Pahute Mesa were used in this study (see Figure 1). Since most of these events had depths near 600 meters, it was possible to combine the seismograms recorded from different events and form a composite seismic section for Pahute Mesa. With the use of this composite section, the arrival times of both P and S waves were estimated. These arrival times were converted to velocity models by both a trial-and-error method and by a formal inverse procedure. In both cases the results were similar, and the final model is shown in Figure 2. In order to obtain information on possible reflecting horizons within the caldera, the composite section was subjected to some of the standard processing techniques that are applied to controlled-source reflection data. No definitive reflectors were revealed by this process.

MOMENT TENSOR INVERSIONS

The availability of the refined velocity model for Pahute Mesa allows improved estimates of moment tensors for explosions in that region. The effort has concentrated on two events for which the sets of near-distance recordings are most complete, Harzer and Chancellor. The locations of these events and their recording stations are shown in Figure 1 and the shot parameters are given in Table 1. The station distances, azimuths, and elevations are listed in Tables 2 and 3 along with the maximum accelerations. Ground accelerations were recorded, but for the purposes of the moment tensor inversion these were converted to velocity records, which are shown in Figures 3 and 4.

The data in Figures 3 and 4 were inverted to obtain estimates of the six elements of the symmetric second-rank moment tensor. The velocity model shown in Figure 2 was used to generate the Green functions. The isotropic part of the moment tensor, which is equivalent to the reduced displacement potential of a spherically symmetric explosive source, is shown for the two events in Figure 5. This isotropic part is similar for the two explosions, although it is slightly smaller and has a faster rise time for the Chancellor event. Both show overshoot, but the result for Chancellor has a pronounced minimum at about 2 sec. This may be related to spall closure.

The deviatoric part of the moment tensor has also been examined. It has a lower frequency content than the isotropic part, seems to be more variable, and is less reliably determined.

SOURCE LOCATION IN A LATERALLY HETEROGENEOUS EARTH

A method has been developed for locating seismic sources in a laterally heterogeneous earth that makes use of empirical tectonically regionalized P-wave tau functions and slowness-dependent source and receiver corrections. The method has been tested by applying it to 28 events at the Nevada Test Site which have known locations. Using only readings in the interval 15-95 deg, the method yields a mean mislocation of 3.32 km and a mean sample variance of travel-time residuals of 0.32 sec². This was compared to the standard method of location which assumes a laterally homogeneous model and Jeffreys-Bullen travel times which yielded a mean mislocation of 7.33 km and a mean sample variance of 0.52 sec².

The method was also applied to 49 events in Eastern Kazakh where the mean sample variance was 0.34 sec² as compared to 0.60 sec² for the standard method. For 5 events in Novaya Zemlya the mean sample variance was 0.43 sec² as compared to 0.51 sec² for the standard method. For 12 events in the Tuamotu Archipelago the method gave a mean sample variance of 0.35 sec² as compared to 0.33 sec² for the standard method.

Table 1. Shot Parameters		
	Harzer	Chancellor
Date	6 June 1981	1 Sept 1983
Origin Time	18h 00m 00.1s	14h 00m 00.1s
Latitude	37.303N	37.273N
Longitude	116.326W	116.355W
Surface elevation	2097m	2040m
Depth to shot	637m	625m
Shot Medium	tuff	tuff
Depth to standing water	668m	647m
Magnitude (ML)	5.4	5.3

Table 2. Network Data for Harzer									
Station	Distance (km)	Azimuth (deg E of N)	Elevation (m)	First Peak Acceleration (cm/sec ²)			Maximum Acceleration (cm/sec ²)		
				Z	R	T	Z	R	T
H9	2.37	345	2062	173	115	59	197	278	281
H4	3.47	137	2134	147	19	6	315	139	140
H2	3.52	28	2060	121	115	-11	410	372	296
H1	4.65	5	2112	123	59	-10	148	175	166
H3	4.74	69	2057	71	8	-2	163	257	144
H6	5.61	206	2006	75	62	-39	276	300	306
H8	5.78	310	2060	37	4	-5	75	132	58
H5	6.62	167	2112	53	18	24	105	103	90

Table 3. Network Data for Chancellor									
Station	Distance (km)	Azimuth (deg E of N)	Elevation (m)	First Peak Acceleration (cm/sec ²)			Maximum Acceleration (cm/sec ²)		
				Z	R	T	Z	R	T
C10	1.84	101	2065	363	445	34	1009	794	852
C3	2.11	241	1981	377	189	-126	856	788	788
C2	2.65	323	1981	210	48	83	524	598	417
C0	3.08	19	2071	160	130	9	200	341	463
C5	4.48	185	2048	82	70	12	824	270	298
C4	5.52	133	2135	63	49	13	127	118	135
C9	5.60	286	1998	62	45	20	142	140	199
C6	6.02	19	2062	36	28	-2	94	70	84
C1	9.34	350	2038	27	13	5	90	63	121
C7	9.81	23	2128	6	6	-2	56	81	119
C8	10.82	260	1885	43	8	4	60	44	44

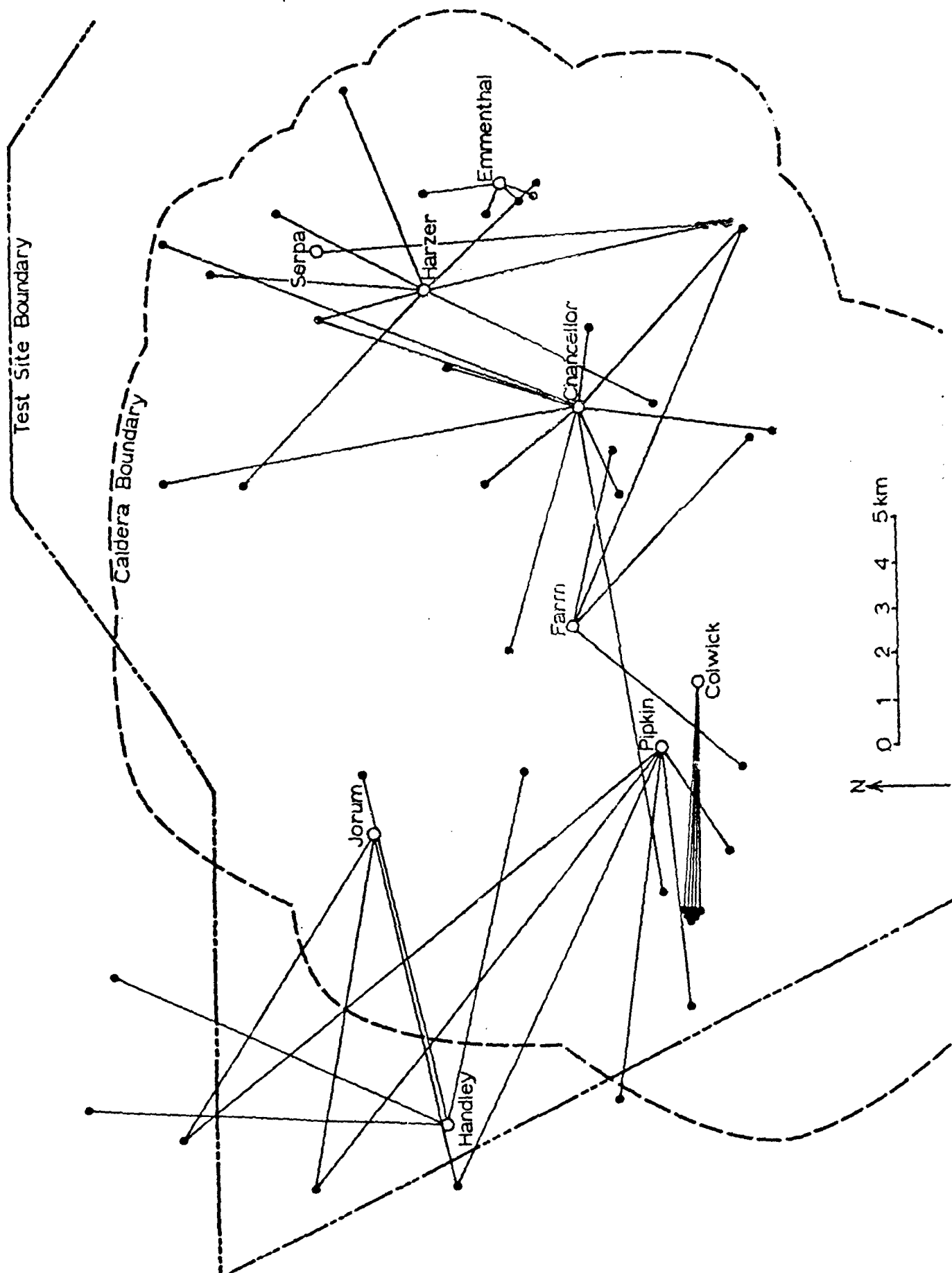


Figure 1. Explosion sites (open circles with names) and respective recording sites (filled circles) for near field data acquisition at Pahute Mesa.

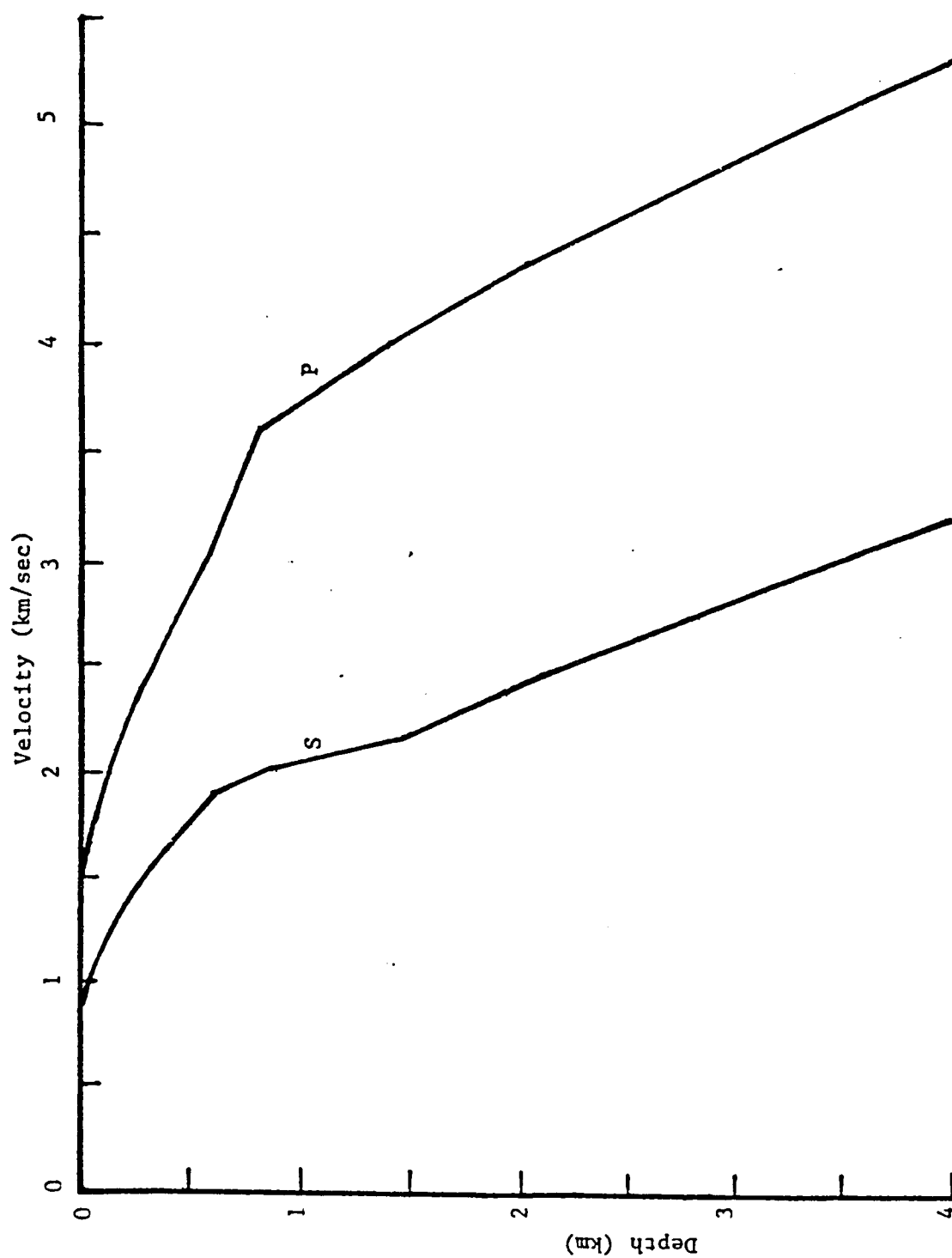


Figure 2. Estimates of P and S velocities in the shallow crust at Pahute Mesa.

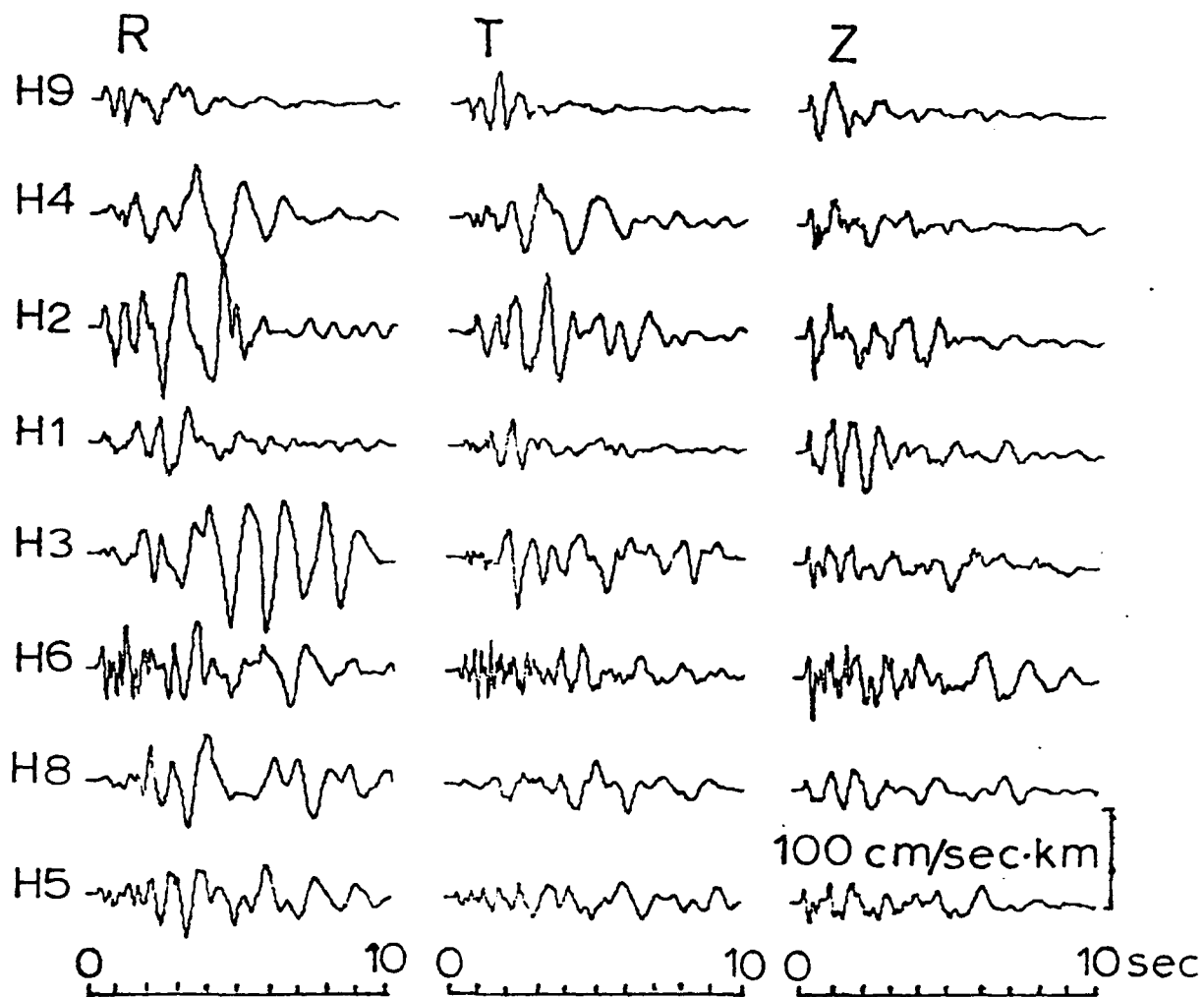


Figure 3. Velocities of ground motion at eight different sites for the event Harzer. The records have been scaled by epicentral distance.

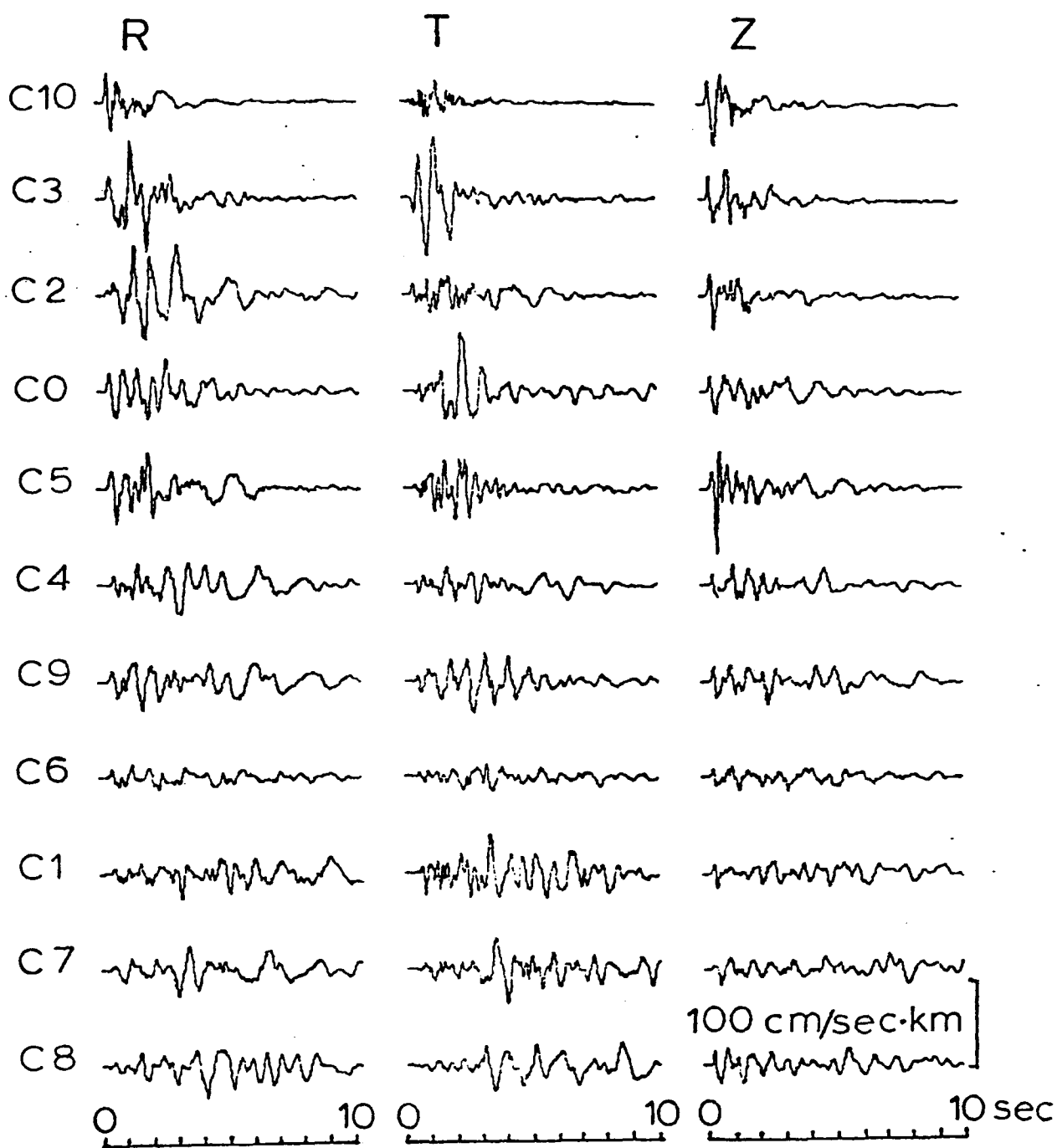


Figure 4. Velocities of ground motion at eleven different sites for the event Chancellor. The records have been scaled by epicentral distance.

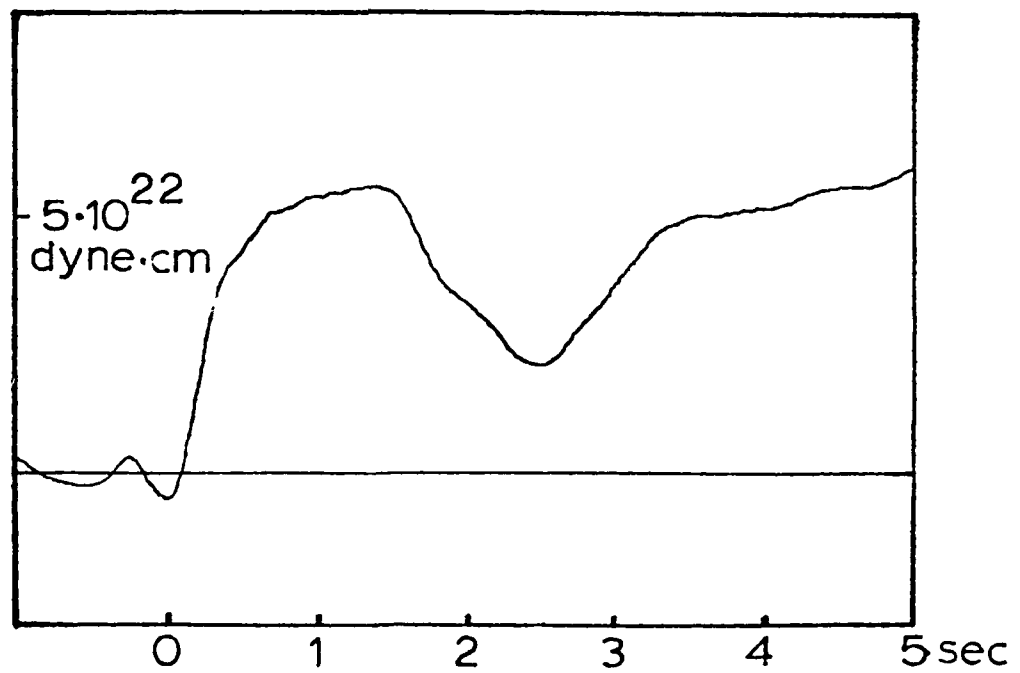
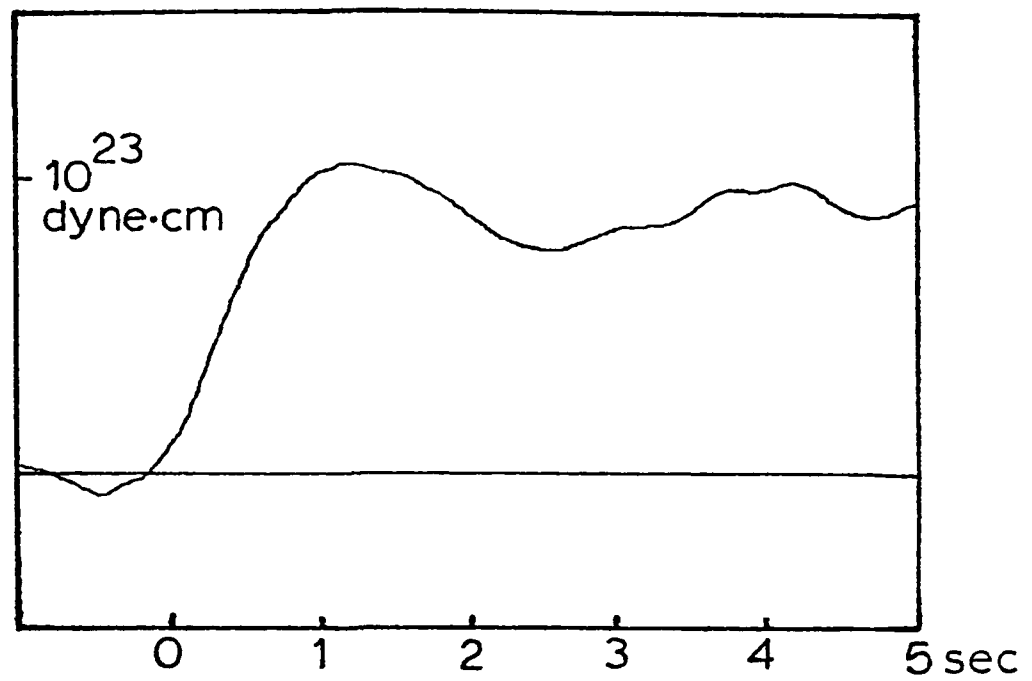


Figure 5. Estimates of the isotropic part of the moment tensor for the events Harzer (top) and Chancellor (bottom).

DETERMINATION OF SOURCE FUNCTION FOR A SEISMIC SWARM

Pierre MECHLER - Florence RIVIERE
RADIOMANA

In despite of the title of this presentation, we will not present a study of source functions, but a way to obtain a signal averaged over the seismic stations of the French Seismic Network, which will enable us to study the source in a future work.

I. Obtention of the averaged signal.

A classical way of averaging signals over a seismic network is to use a "Delay and Sum". In this procedure, a simple stack of the various signals are done, without taking into account the change in the records of each station. To overcome this problem, we decide to define what we will call the best averaged signal in a least square sens.

The technic used is far from beeing new. We suppose each of the records to consist of:

- a common signal but multiplied by a station's factor.
- a noise (mostly wave generated) completely decorrelated from the common signal.

The signals are first supposed to be delayed, so to be in phase, but we will come back later to this point. We compute the correlation matrix of all signals. It can be shown that the station's factors is one of the eigen vectors of this matrix, the one corresponding to the largest of all eigenvalues. This introduce an undetermination: an eigen vector is allways obtained up to a constant, but this is obvious on physical basis, it is possible to multiply the station's factors by an arbitrary number, if in the same time, the common signal is divided by the same value.

The common signal is then, the sum of the records, averaged by the just computed station's factors. The wave generated noise, or residual signal in a given station, is

obtained by a difference between the record in the station and the common signal.

This decomposition of the signals is quite similar to the covariance analysis, well-known in statistical studies. The main difference is that in statistics, the decomposition of the signals is usually done on a larger set of eigen vectors than just the first one. But, in our case, only the first as a meaning, corresponding to a signal beneath France and representing the source function filtered by the propagation. A decomposition on a larger set will have no physical meaning, the coda in each station, are only statistically similar. Of course, such a decomposition has to be done over a seismic network which aperture is small enough compared to the epicentral distance.

This procedure is relatively sensitive to the determination of the arrival time in each station. We were greatly helped in this by the origin of the events we studied. It consist in a "seismic swarm", a serie of very similar events from the same area in Eastern Kazakh, not far from Shagan River. The signals recorded in one station for the various events are more similar than the signals recorded in the stations of the French Seismic Network for the same event. So, in a first step, we computed the common signal in each single stations for a set of 10 events. It was easier to measure the arrival time on this averaged signal, then to obtain a precise arrival time for each record by a correlation technic. We also checked, by iteration, that it was not possible to improve the time determination.

We vary the length of the time window used in the computation. The samplig rate of our records is 50Hz, with an anti-aliasing filter at 16Hz, in fact all of our data were low-pass filtered at 8Hz. The various time windows were between 1024 points (about 20 seconds) and 128 points (2.5 seconds) without real change in the station's factors.

II. Magnitude determination.

The first interpretation is to consider the common signal, in the various stations, as representing the signal arriving beneath France and filtered by an average crust, the station's factors as a measure of the sensitivity of each station, and the residual signal as athe coda (in fact we obtain more than the coda, we also have energy in the beginning of the signal, see later).

We will start by magnitude considerations. We studied two different ways to measure the magnitude. In the first, for each station, we computed for all events a common signal and, in that case, the event's factors. The magnitude being the logarithm of the wave amplitude, plus a distance correction, and as all events are practically at the same distance, the logarithm of the event's factors should be, within a constant correction, the event's magnitude.

Using the magnitude determination of the French Network, we found the best relation between magnitude and log of event's factor to be of the form:

$$mb = a \cdot \log(EF) + b$$

but with a "a" factor not equal to 1. We give in annex the list of all the results, the mean values are:

$$\begin{aligned} a &= 0.837 \quad +/-.086 \\ b &= 5.952 \quad +/-.035 \end{aligned}$$

We also used only nine of the events to recompute a and b, to calculate the magnitude of the last one. Voluntarily, we select the nine smallest events to obtain the magnitude of the largest. The result were:

$$m = 6.17 \quad +/-.03$$

which is exactly the value found by the French Network.

We intent to apply the same technic, on a much larger data set, in order to obtain, not really a magnitude, but a classification of the various events, according to their energy.

This first way to determine a magnitude is rather tedious: each time a new event is added to the data base, all computations have to be redone. An other way, is to use the mean station's factors. We noticed that the station's factors are very similar for a given station and the various events. So, we first computed an average value of the station's factor, in each station for all events, then we computed an approximation of the common signal, using this new set of station's factors and measured it's amplitude. The results are given in annex.

III. Source function.

The common signal, from all stations of the network and a given event, represents an approximation of the incoming signal, beneath France and filtered by the mean french crust. We present here some of the common signal we obtained. In this preliminary part of the work, we have not yet compare our results with a synthetic sismogramm, using a source function and a propagation effect.

In the following figures, we plotted the common signals for all ten events used in this study, and also, for comparison, the actual signals in some stations both for the best event and an average one.

IV. Signal residuals.

The difference between the actual record and the common signal represents more than the coda. As we pointed earlier, we also have energy in the first part of the signal.

In the figures, we show the mean signal computed using all events in the fives stations of Massif Central, in the middle of France. And, for the same stations, the mean residual signal.

On this last plot, some coherency between the signals accross the subarray is clearly seen.

We think that the size of the seismic network is an important parameter for the coherency of the waves accross it. If the aperture is too small, we expect to obtain a high coherency for the signals themselves (up to the amplitude which is known to vary), so the residual signals should represent the coda. If the aperture is larger, then it is possible to observe propagations through the array. We know, from other studies, that the crust, just south of the subarray, presents larg anomalies. We whish to correlate both phenomens.

V. Preliminary conclusions.

This presentation is only a presentation of a current work. Our method for precise magnitude determination has already given us very good preliminary results, and we will improve our statistic by increasing the number of events.

The common signals, obtained for a given quake, over our network will allow a study of the source function. And we really hope to explain the main trends of the residual signals by correlation with the geological structure around the network.

Annex

Magnitude coef. with all events

a	b
0.7527	5.9658
0.8390	5.9690
0.8184	5.9445
0.7185	5.9974
0.8635	5.9124
0.7973	5.9924
0.8387	5.9021
0.8313	5.9924
0.9131	5.9124
0.7698	5.9687
0.8024	5.9529
0.9291	5.9509
0.8525	5.9552
0.8399	5.9574
0.8257	5.9629
0.8985	5.9497
0.8849	5.9441
0.8236	5.9285
0.8575	5.9212
0.8890	5.9227
0.8103	5.9494
0.8578	5.9210
0.8799	5.9135
0.8114	5.9365
0.7131	5.9693
1.1354	5.9337
0.6380	6.0732

Table I

Magnitude computed from common signal

$$m=a*\log(A)+b$$

a=0.886

b=6.406

29/03/81	5.49
13/09/81	6.20
31/08/82	5.34
26/12/82	5.60
20/11/83	5.36
06/10/83	6.03
07/03/84	5.52
10/02/85	5.69
29/03/84	6.00
14/07/84	6.18

Table II

Magnitude computed from station's factors

station	e0	e1	e2	e3	e4	e5	e6	e7	e8	e9
LBF	5.56	6.15	5.43	5.54	5.24	6.03	5.40	5.88	5.97	6.17
LOR	5.50	6.14	/	5.62	5.35	6.03	5.42	5.92	5.97	6.17
AVF	5.66	6.13	5.17	5.57	5.37	5.87	5.61	5.85	6.02	6.18
LSF	/	/	/	/	5.33	/	5.48	5.88	6.01	6.19
SSF	5.60	6.12	5.09	5.63	5.43	5.91	5.65	5.90	5.97	6.12
MFF	/	6.15	5.44	5.50	5.26	6.02	/	5.91	5.98	6.17
GRR	/	/	5.17	5.63	5.39	5.92	5.62	/	5.97	6.15
FLN	/	6.20	5.31	5.58	5.33	5.94	5.47	/	6.02	6.17
LDF	/	/	5.24	5.61	5.37	5.95	5.51	/	6.01	6.17
SMF	5.63	6.19	5.39	5.52	5.28	/	5.42	5.87	5.98	6.17
LRG	5.67	6.16	5.20	5.57	5.33	5.85	5.59	5.85	6.02	6.18
TCF	/	6.17	5.25	5.64	5.29	5.98	5.55	5.93	5.98	6.13
RJF	5.63	6.18	5.26	5.54	5.34	5.92	5.48	5.87	6.02	6.18
FRF	5.63	6.17	5.30	5.53	5.31	5.93	5.47	5.91	5.99	6.19
LPO	5.61	6.17	5.30	5.53	5.34	5.95	5.45	5.87	6.00	6.19
LFF	5.58	6.18	5.26	5.56	5.34	5.96	5.48	5.88	5.99	6.18
EPF	5.59	6.16	5.24	5.57	5.36	6.05	5.49	5.82	5.96	6.17
BSF	5.60	6.11	5.14	5.59	5.38	5.96	5.58	5.93	6.00	6.13
HAU	5.62	6.16	5.20	5.58	5.36	/	5.50	/	5.98	6.16
CDF	5.55	6.17	5.15	5.65	5.37	/	5.60	5.90	5.97	6.10
LMR	5.64	6.13	5.22	5.53	5.31	5.94	5.57	/	6.04	6.15
LPF	/	/	5.23	5.59	5.37	5.92	5.56	5.87	6.02	6.19
CAF	/	/	5.25	5.62	5.34	5.99	5.50	/	5.99	6.16
MZF	/	/	5.30	5.53	5.34	5.93	5.53	5.89	6.03	6.19
CVF	/	/	/	5.57	/	5.96	5.54	5.88	6.01	6.18
BGF	/	/	/	/	5.27	/	5.55	5.91	5.98	6.17
HYF	/	/	/	/	/	/	/	5.90	6.00	6.18
mean	5.60	6.16	5.24	5.58	5.34	5.95	5.52	5.89	5.99	6.17
sig	0.04	0.02	0.09	0.04	0.04	0.05	0.06	0.02	0.02	0.02
LDG	5.5	6.18	5.3	5.6	5.3	5.96	5.5	5.89	6.02	6.17

Table III

Figures Caption

Fig 1 : common signals for the ten events of this study

Fig 2 : Actual signals for event 1 : 13/09/81

Fig 3 : Actual signals for event 4 : 20/11/83

Fig 4 : Averaged records in the 5 stations of Massif Central

Fig 5 : Averaged residual signals in the 5 stations of Massif Central

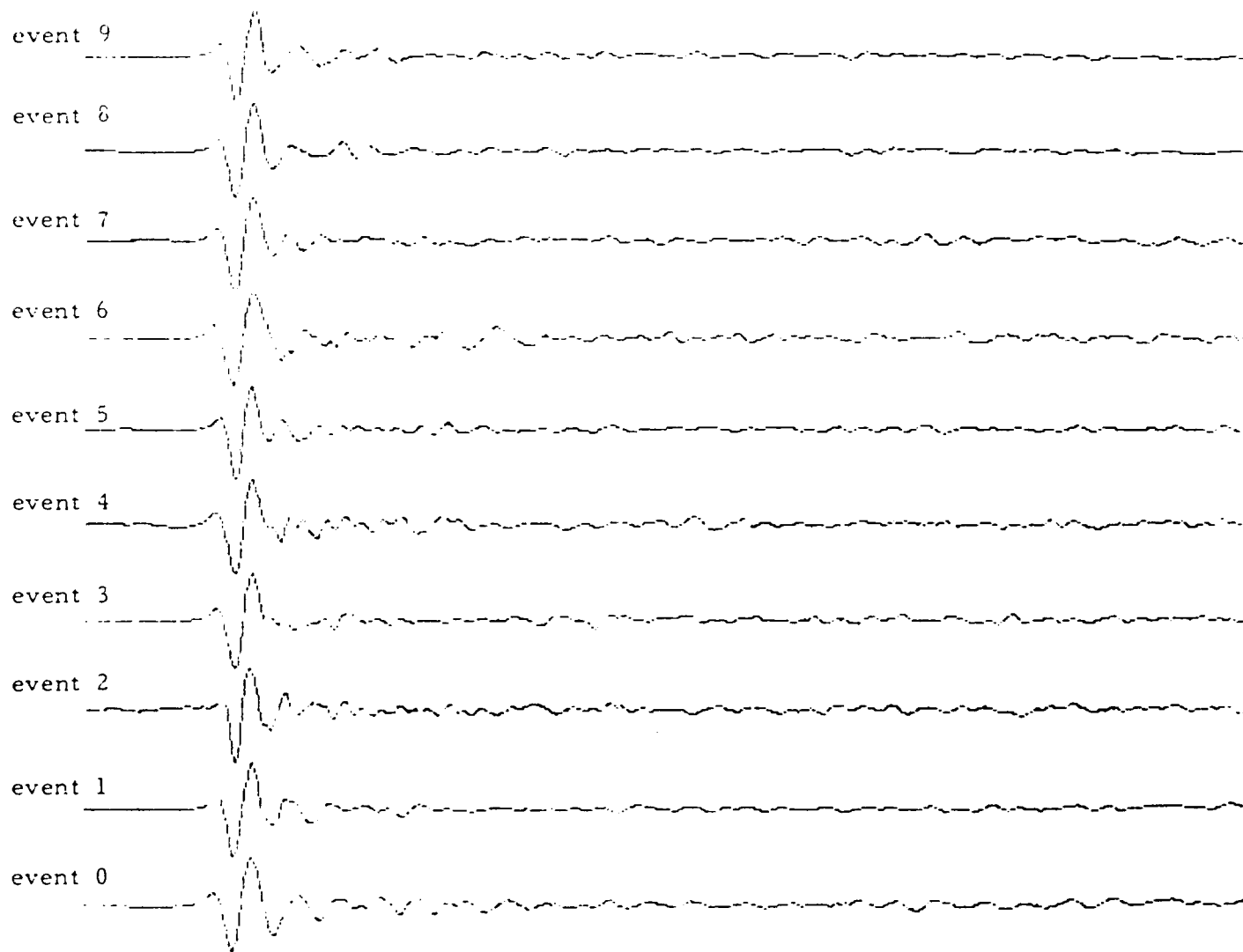


Fig 1

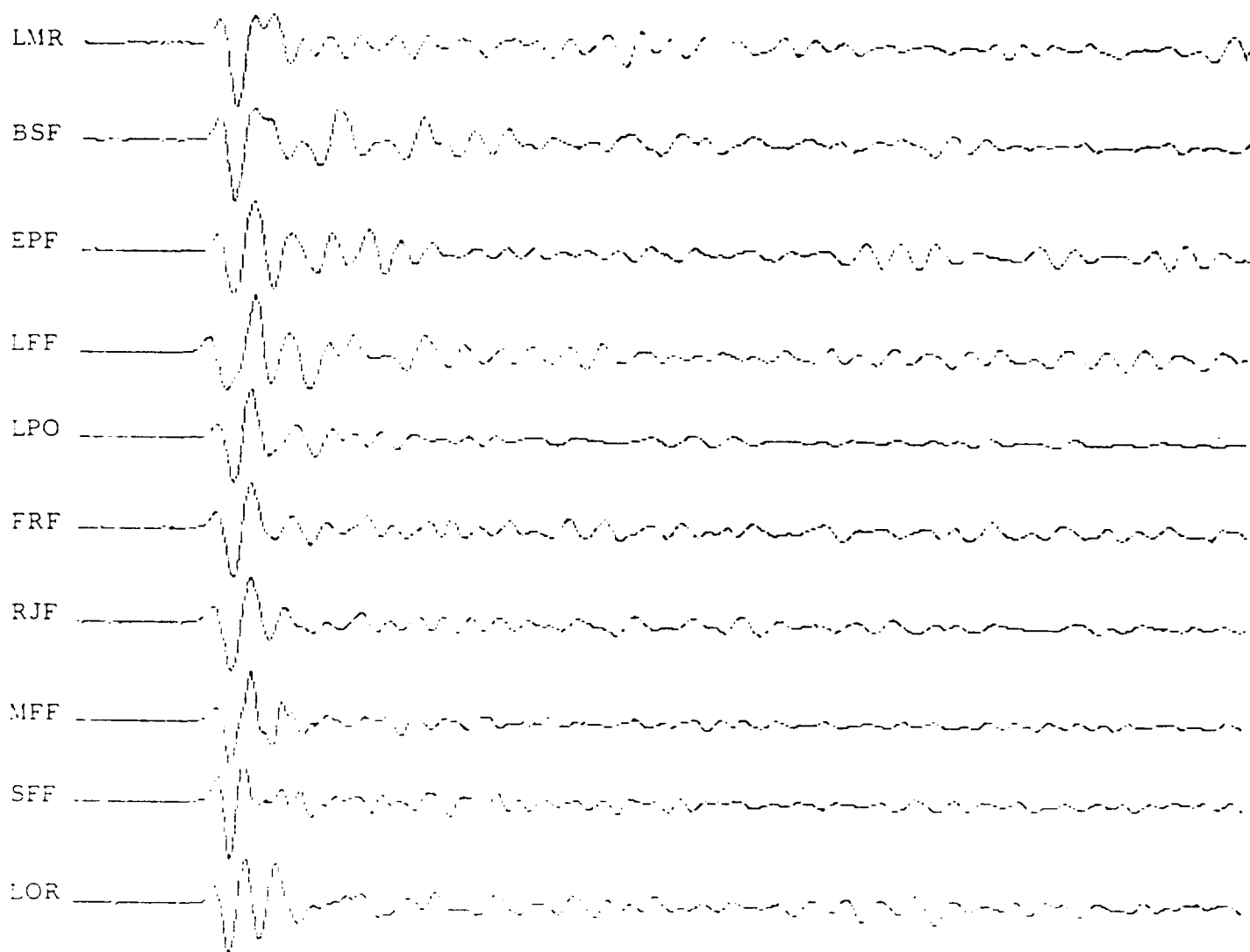


Fig. 1

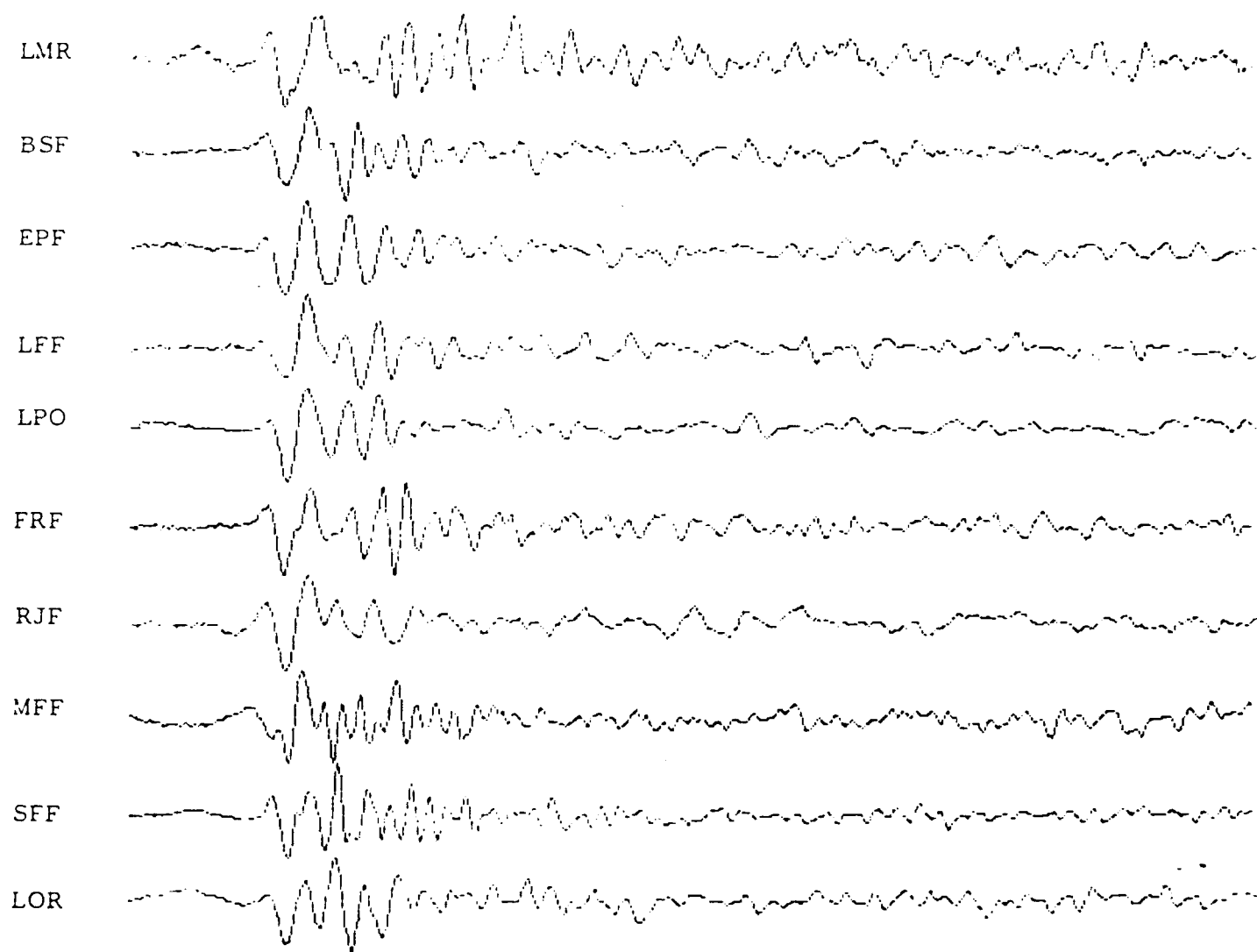


Fig 3

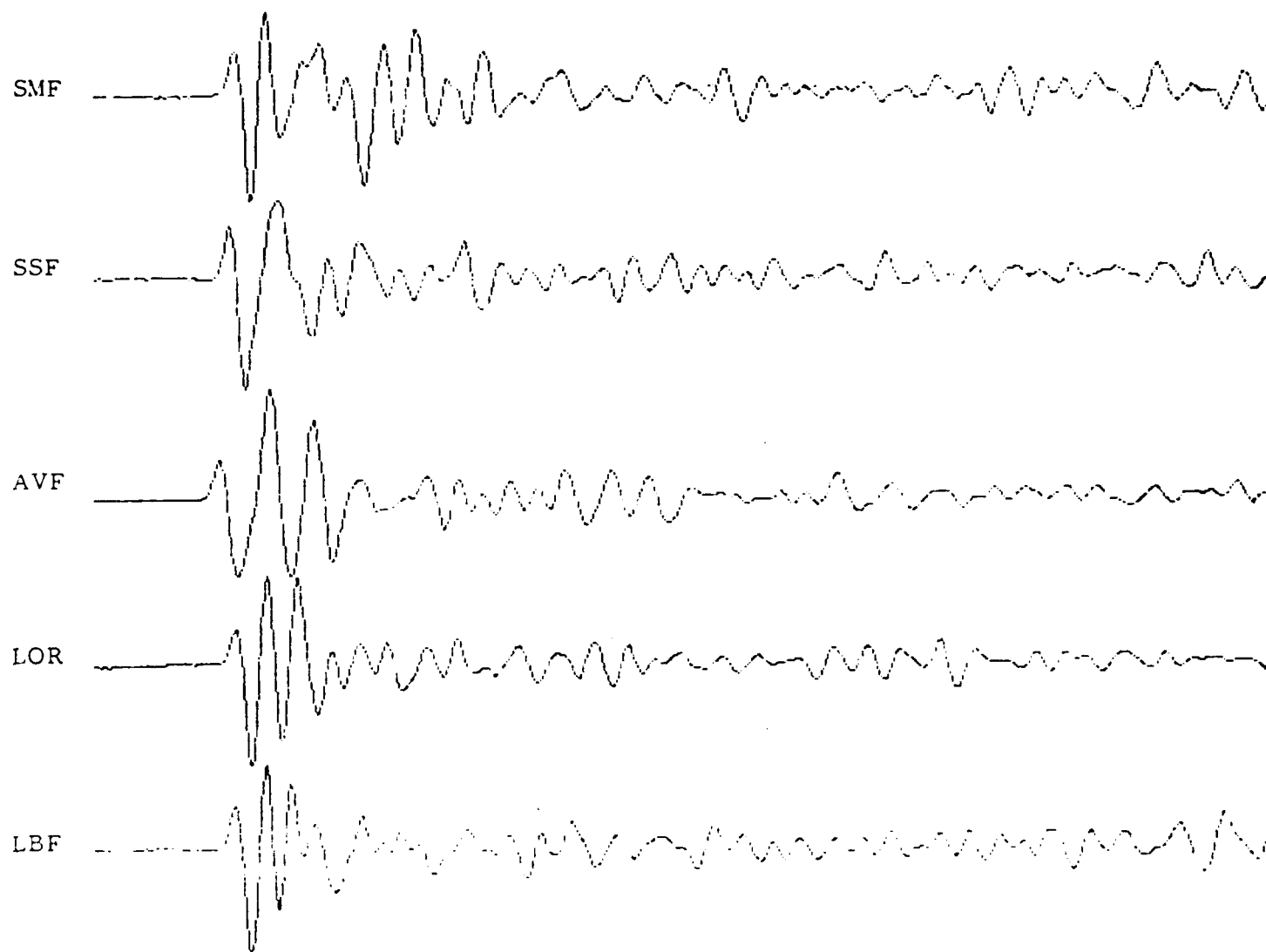


Fig 4

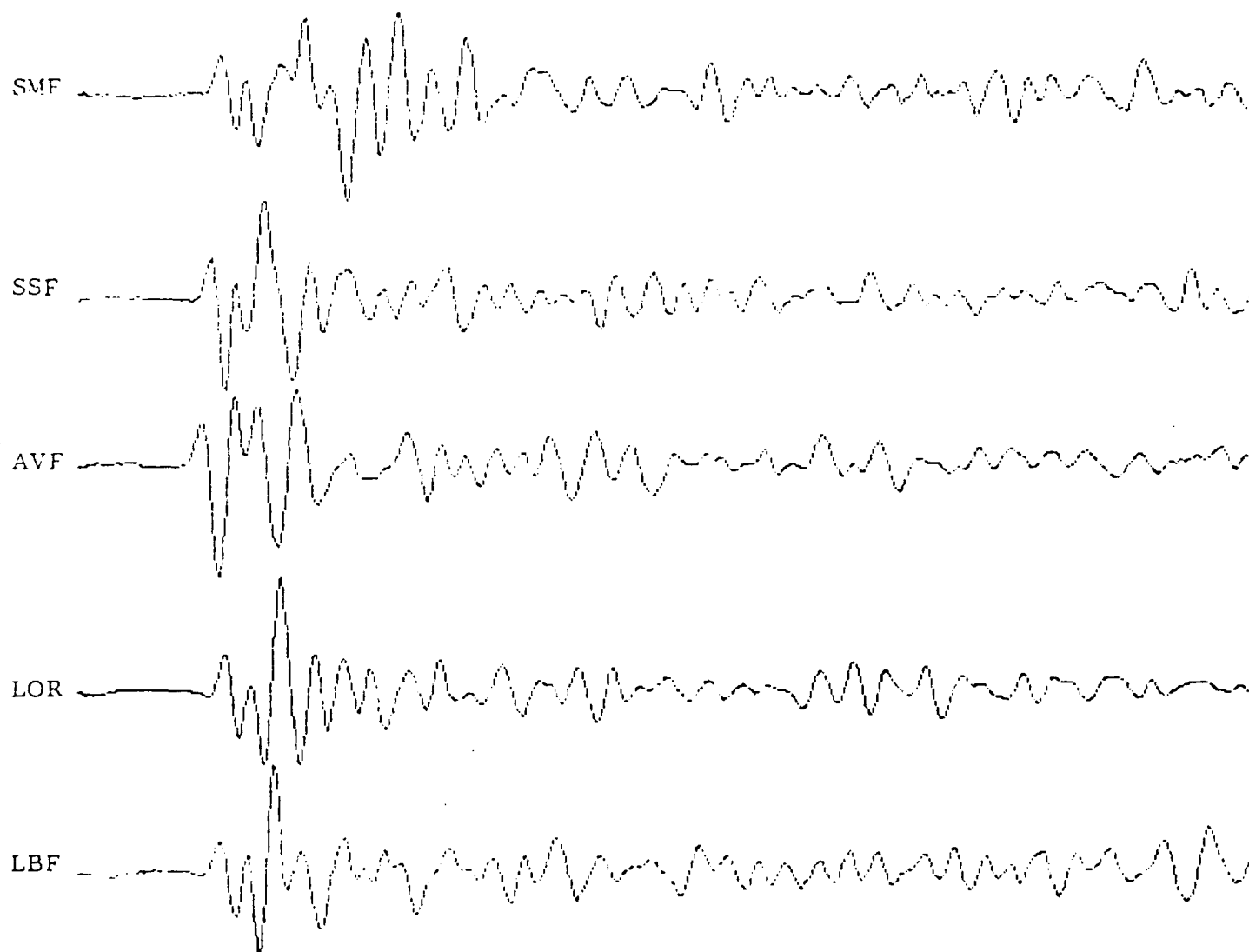


Fig 5

THE DAMAGE MECHANICS OF BRITTLE SOLIDS IN COMPRESSION

C. G. SAMMIS¹ and M. F. ASHBY²

¹Department of Geological Sciences
University of Southern California,
Los Angeles, CA 90089-0741, USA and

²Department of Engineering, University of Cambridge,
Trumpington Street, Cambridge CB2 1PZ, U.K.

INTRODUCTION

When a brittle, inhomogeneous solid is loaded in compression, microcracks nucleate and propagate from the inhomogeneities. The difference between compressive and tensile fracture, which is much better understood, is that a brittle tensile crack is unstable (one crack, once started, accelerates across the sample to give failure); by contrast, brittle cracking in compression is at first stable, so that many small cracks extend, each growing longer as the stress is raised, until they interact in some co-operative way, to give final failure.

Systematic measurements of strength really began about the middle of the last century (see, for example, Jaeger and Cook, 1976) but without much attempt to understand what determined it, or why the compressive strength is ten or more times greater than that in tension. Progress in understanding these problems is more recent. A series of recent papers and reviews (Griggs and Handin, 1960; Paterson, 1978; Hallbauer et al., 1973; Tapponnier and Brace, 1976; Wawersik and Fairhurst, 1970; Wawersik and Brace, 1971; Nemat-Nasser and Hori, 1982; Kobayashi, 1971; Newman, 1978; Ashby and Hallam, 1986; Sammis and Ashby, 1986) have established that, in compression, numerous small cracks nucleate and grow stably (meaning that each increment of crack growth requires an increment in load to drive it). An isolated crack in a very large body continues to grow in this stable way until the length becomes comparable with that of the body itself, but the multitude of cracks which nucleate in most natural rocks behave differently: when the crack length is comparable with their spacing they interact and link, precipitating failure.

The problem is complicated by time-dependent effects (Anderson and Grew, 1976; Martin, 1971; Waza et al., 1980, Sano et al., 1981, Costin and Holcomb, 1981). They have at least two origins. First, cracking in compression is associated with dilation; if the body is saturated with a fluid, then its flow into the dilating region can introduce a time-dependent aspect to fracture. Second, in some brittle solids, notably silicates, crack growth is slow, limited by chemical reaction (often with water) at the tips of the cracks, as well as by the rate of loading. In both cases, a static load which does not immediately cause failure may still do so if left in place for a sufficient length of time.

The understanding of these phenomena is still incomplete. But the physical basis of compressive brittle fracture is much clearer than it was a decade ago. It seems an appropriate time to try to abstract, from the observations and modelling which are currently available, a simplified description of compression-cracking, retaining as far as possible the important physical understanding. The goal is to develop a damage mechanics of brittle solids, from which the stress-strain response and an operational definition of failure can be derived for any given stress state and initial set of material properties. Two attempts to achieve this can be found in the open literature; that of Costin (1983), and that of Sammis and Ashby (1986). Central to the problem is the relationship between stress and crack extension. Costin (1983) postulates an assumed relationship of reasonable form, and develops from it expressions for the failure surface which (with some adjustable parameters) give a good description of a body of experimental data. Sammis and Ashby (1986) and Ashby and Hallam (1986) developed a detailed

physical model for crack extension, which they use to plot stress-strain curves for brittle solids from which failure surfaces can be constructed; but the complexity of the model-based equations makes the process cumbersome. In the present paper we attempt to develop a simpler, model-based, mechanics of brittle compressive fracture, drawing heavily on these two previous pieces of work.

A model-based damage mechanics has the advantage that several important phenomena can be incorporated in a natural way. The failure criterion can be defined in terms of the peak-stress in the stress-strain curve rather than requiring the postulation of a critical damage as in Costin (1983). The initial porosity is included in the modeling, as is the size spectrum of the initial defects. Finally, the effect of pore fluids on the evolution of microcrack damage can also be incorporated.

We have not yet formulated a complete damage mechanics, nor have we tested it against the wealth of compressive failure data in the literature. This paper is thus a progress report; but it contains enough detail to show the strategy and framework of the approach we are using.

THE CRACK INITIATION SURFACE

Almost all brittle solids contain inhomogeneities: holes, little cracks, particles which are poorly bonded or which have different moduli from the matrix. Any of these can act as nuclei for new cracks when the solid is loaded.

The range of possible nuclei is wide, but the spectrum of their characteristics is probably bracketted, at least approximately, by two

extremes: the spherical hole, and the sharp inclined crack (Fig. 1). Both have been studied experimentally and modelled, the first by Sammis and Ashby (1986), the second by Nemat-Nasser and Horii (1982) and Ashby and Hallam (1986), and explicit equations for the initiation of cracking are developed for both. Details of the results are given in Appendix 1; here we note simply that both lead to results which are almost identical, and can be written, for axisymmetric loading, as a linear relationship between the axial stress σ_1 and the radial stress $\sigma_2 = \sigma_3$. For initiation:

$$\sigma_1 = C_1 \sigma_3 + C_2 \quad (1)$$

When cracks nucleate from spherical holes, the constant C_1 (Appendix 1) is predicted to be 3.4. When they nucleate from cracks, C_1 depends on the coefficient of friction between the sliding crack faces; taking $\mu=0.6$ as typical for rocks gives $C_1 = 3.1$.

The constant C_2 depends principally on the fracture toughness K_{IC} of the brittle solid, and on the size scale of the inhomogeneity (the hole or crack). When the nuclei are holes, $C_2 = 1.6 K_{IC}/\sqrt{\pi l}$ where l is the length of the incipient cracks associated with the hole (Fig. 1). When nuclei are inclined cracks, $C_2 = 3.1 K_{IC}/\sqrt{\pi a}$, where $2a$ is the inclined crack length (Fig. 1). Despite the rather different geometry, it is obvious that not only is the form of the nucleation equation identical, but even the constants it contains are almost the same for holes and cracks, encouraging the view that Equation (1) has generality as an equation for damage initiation.

Crack initiation can be detected in several ways: by the start of acoustic emission, by the first non-linearity of the stress-strain curve, or by a sudden increase in internal friction. Figure 2 shows data for crack

initiation obtained by the first two techniques for Westerly granite. Brace, et al., 1966) plotted on axes of σ_1 and σ_3 to allow comparison with Equation (1). The linear relationship is clearly a good description of the data. The slopes C_1 , in both sets of data are close to 4.1 (the models suggest 3.2 - 3.4), and the constants C_2 , in both cases, give $l \approx a \approx 0.6$ mm (taking $K_{IC} = 1$ MPa $m^{1/2}$), which is reasonable.

THE EVOLUTION OF DAMAGE

As the body containing pores, angled microcracks, etc., is loaded, the stress intensity at the tips of the wing-cracks grows. We will assume that the wing-cracks advance so that, at their tips, $K_I = K_{IC}$, though in reality the inhomogeneity of the material may cause them to extend in little jumps. The problem, then, is to estimate K_I at the tip of the wing cracks.

Crack Growth and Interaction

The development of a stress intensity at the wing-crack tip caused by a stress field can be likened to the induced polarisation of an insulator by an electric field. First, there is the polarisation of an isolated atom; but in addition, the polarisation of neighboring atoms adds to the field and causes further polarisation of the first atom. In a rather similar way, the remote stress field ($\sigma_1, \sigma_2, \sigma_3$) induces a contribution to K_I (which we shall call K_I^∞). But the cracks perturb the stress field inside the body, so that a given crack experiences an additional contribution to K_I (which we call K_I^i) from its interaction with the stress fields induced at its neighbors. The problem is like that of induced polarisation because the internal stresses only appear in response to the external loads.

Consider first the stress intensity K_I^∞ which is directly induced at an isolated crack in an infinite medium by the applied stress. Its value depends on the geometry of the defect from which the wing cracks grow. When this is an angled crack, the result for a crack-length $L \gg 1$ is (Ashby and Hallam, 1986, eqn. (6)):

$$\begin{aligned} K_I^\infty &= - \frac{C_3 \sigma_1 \sqrt{\pi a}}{L^{1/2}} + \sigma_3 \sqrt{\pi a} L^{1/2} \\ &= - \frac{C_3 \sigma_1 \sqrt{\pi a}}{L^{1/2}} \left\{ 1 - \frac{\lambda L}{C_3} \right\} \end{aligned} \quad (2)$$

with $C_3 = 0.23$ and $L = l/a$. Figure 20 of Ashby and Hallam (1986) and Figure 20 of Sammis and Ashby (1986) both show that the peak stress occurs at $3 < L < 5$, so the approximation $L \gg 1$ is tolerable. The first of the two terms describes the stress intensity caused by the axial stress σ_1 ; it decreases as the crack extends, giving stable crack growth. The second term describes the closing effect of the lateral stress σ_3 ; it acts on the whole crack length L and thus grows in importance as L increases. The analogous result for a crack growing from a hole (Sammis and Ashby, 1986, eqn. (4) and (5)) is a little more complicated. In the limit of $L \gg 1$, we have:

$$\begin{aligned} K_I^\infty &= - \frac{C_4 \sigma_1 \sqrt{\pi a}}{L^{2.5}} + \sigma_3 \sqrt{\pi a} L^{1/2} \\ &= - \frac{C_4 \sigma_1 \sqrt{\pi a}}{L^{1/2}} \left\{ \frac{1}{L^2} - \frac{\lambda L}{C_4} \right\} \end{aligned} \quad (3)$$

with $C_4 = 1.1$. The interpretation of the two terms is the same as before.

We now consider the interaction between cracks, giving the additional contribution K_I^1 . In our earlier work we modelled interaction by considering the bending displacements between neighboring cracks. This idealization was particularly successful in modelling the interaction of a crack with a free surface, but it is realistic for the interaction between cracks only when they overlap extensively. To avoid this assumption we develop a new model, as follows.

Consider a starter crack or void with vertical wing cracks of length l . When the axial stress σ_1 is applied, sliding (at an angled crack) or bulging (at a void) wedges the wing-cracks open, that is, it induces stress intensity K_I^∞ at the wing crack tips. This crack is now a source of an elastic field in the body. We measure the induced strength of this crack by the mid-point crack opening displacement, δ . The crack is like a dislocation loop of radius l and Burger's vector $b = \delta$, (though note that δ is induced by the external loads and thus increases with stress, whereas the strength of a dislocation loop is fixed). The stresses at a distance $r \gg l$ from a dislocation loop or dipole scale as:

$$\sigma = C \frac{Gb l}{r^2} \quad (4)$$

Our model is that the locally induced stresses of a crack of radius l and strength δ , at a distance $r \gg l$ from the crack center scale as:

$$\sigma_c = C_5 \frac{E \delta l}{(r-l)^2} \quad (5)$$

where we might expect $C_5 \approx 0.5$.

The stress obviously varies with angle around the crack; in some places it will have components which will tend to open other cracks, in some places

it will tend to close them. We focus on the region in which the crack field has an opening component. A second crack lying in this region now experiences a K_I^∞ from the applied stress and a K_I^i from the induced field of the first crack. Its magnitude is:

$$K_I^i = \sigma_c \sqrt{\pi \ell} \quad (6)$$

It remains to evaluate σ_c , insert the result into this equation, and add the two contributions to K_I .

The crack opening displacement δ is known. Both when the wing cracks grow from voids and when they grow from angled cracks (or from anything else), δ is related to K_I^{TOT} by:

$$\delta = c_6 \frac{K_I^{TOT} \sqrt{\ell}}{E} \quad (7)$$

when $c_6 = 4$ (Tada, Paris and Irwin, 1973). (This expression is completely general, and does not depend on details of crack origins or loading). Thus, combining Equations (4), (5) and (6)

$$K_I^{TOT} = K_I^\infty + K_I^i = K_I^\infty / \left(1 - C_7 \frac{\ell^2}{(r-\ell)^2} \right) \quad (8)$$

The second term in the brackets describes the interaction, and C_7 combines the constants C_5 , C_6 , $\sqrt{\pi}$ etc. It's value is roughly $C_7 \approx 3.5$.

The total stress intensity at a "typical" crack can now be written in dimensionless variables $L = \ell/a$ and $R = r/a$ as follows. For wing crack growth

from an angled crack:

$$\frac{K_1^{TOT}}{\sigma_1 \sqrt{\pi a}} = \frac{C_3}{L^{1/2}} \left\{ 1 - \frac{\lambda L}{C_1} \right\} \left/ \left\{ 1 - C_7 \frac{L^2}{(R-L)^2} \right\} \right. \quad (9)$$

and for holes:

$$\frac{K_1^{TOT}}{\sigma_1 \sqrt{\pi a}} = \frac{C_4}{L^{1/2}} \left\{ \frac{1}{L^2} - \frac{\lambda L}{C_4} \right\} \left/ \left\{ 1 - C_7 \frac{L^2}{(R-L)^2} \right\} \right. \quad (10)$$

Inverting these equations gives, for angle cracks:

$$\tilde{\sigma}_1 = \tilde{\sigma}_3 \frac{L}{C_3} + \frac{L^{1/2}}{C_3} \left(1 - C_7 \frac{L^2}{(R-L)^2} \right) \quad (11)$$

and, for holes:

$$\tilde{\sigma}_1 = \tilde{\sigma}_3 \frac{L^3}{C_4} + \frac{L^{5/2}}{C_4} \left(1 - C_7 \frac{L^2}{(R-L)^2} \right) \quad (12)$$

where $\tilde{\sigma} = \sigma \sqrt{\pi a} / K_{IC}$ is the dimensionless stress. For holes, $\pi a^2 / r^2$ is the area of holes per unit area of sample, or the porosity. Denoting the porosity by f_a , we thus have $R = (\pi / f_a)^{1/2}$. When fractures are initiated at angle cracks, f_a is interpreted as that fraction of the total area which contains starter cracks, where an area πa^2 is associated with each starter crack of length $2a$. Again $R = (\pi / f_a)^{1/2}$.

It is convenient to define damage $0 < D < 1$ as

$$D = \lambda^2 N_a = L^2 f_a / \pi$$

Where N_a is the number of starter flaws per unit area.

Equations (11) and (12) are plotted in Figure 3 for two different confining stresses at fixed for initial porosity (or crack density). The stress passes through a maximum and then falls as the damage increases.

The peak stress corresponds to one definition of failure. The failure envelope for Westerly granite in Figure 2 was generated by plotting peak σ_1 , as a function of σ_3 .

Damage also lowers the modulus of the cracked body. If the modulus of the solid is E_0 , then introducing the holes or initial, inclined cracks, lower the modulus to $E = E_0/(1+2f_a)$, where $f_a = N_a \pi a^2$ is the area fraction of holes or cracks. The cracking which occurs on loading further lowers the modulus. Sammis and Ashby (1985) show that the modulus may be approximated

$$E = \frac{E_0}{1+2f_a+2D(1-3\lambda)^2} \quad (13)$$

The strain is simply $\epsilon = \sigma/E$, or

$$\epsilon = \frac{\sigma_1}{E_0} (1+2f_a+2D(1-3\lambda)^2) \quad (14)$$

These results can be used to calculate the stress-strain curve, and the failure strain.

PLASTIC YIELDING

As the confining pressure is increased, brittle fracture is made increasingly difficult. A critical pressure may be reached at which true plasticity replaces crack extension. This transition can be illustrated by plotting a yield (or a creep) surface, defined by:

$$\frac{1}{2} ((\sigma_1 - \sigma_2)^2 + (\sigma_2 - \sigma_3)^2 + (\sigma_3 - \sigma_1)^2) = \sigma_y^2 \quad (15)$$

This is shown as broken lines on Figure 2. The yield strength, σ_y , can be derived from hardness data, since $\sigma_y \approx H/3$.

DISCUSSION

As pointed out in the introduction, our damage mechanics formulation is not yet complete or tested. We conclude this progress report by discussing some areas which require additional work.

Crack Growth from a Distribution of Nuclei of Different Sizes

In most solids, the starter flaws are not all the same size. This is evident from the observed change in failure mode associated with increasing confining pressure. For unconfined samples, a few of the largest flaws are activated and grow until they intersect the sample ends. The sample fails by "vertical slabbing". The application of even a small confining stress suppresses the growth from these larger flaws, and allows the nucleation of cracks from smaller or less favorably oriented starter flaws. Before any single crack can grow sufficiently long to intersect the sample ends, the density of activated flaws has increased enough to produce a shear instability and the sample fails by faulting. At very large confining pressures the extreme suppression of crack growth allows the activation of so many flaws that many shear instabilities are produced, resulting in pseudo-ductile deformation.

Another indication of the importance of including a range of flaw-sizes in our model is the negative curvature of the failure surface in Figure 2. Note that our model surface is approximately linear when all flaws are the same size. Activation of additional, smaller flaw with increasing stress will produce the observed negative curvature.

In order to introduce this behavior into our model, we will assume that the size distribution of starter flaws may be approximated by the Weibull distribution.

$$f_a(a) = f_a^{\text{tot}} \exp - (a/\bar{a})^n \quad (16)$$

where f_a^{tot} is the total area fraction of starter defects of all sizes and \bar{a} is a measure of the average size of the initial flaws. The parameter n sets the width of the distribution: small n corresponds to a broad distribution while for large n all flaws have $a \approx \bar{a}$.

The number of flaws which have been activated depends on the stress state (σ_1 and σ_3). Writing the initiation condition as

$$\sigma_1 = C_1 \sigma_3 + C_2 K_{IC} / \sqrt{\pi a^*} \quad (17)$$

we can find the smallest flaw, a^* , which will be activated for given values of σ_1 and σ_3 :

$$a^* = \frac{1}{\pi} \left[\frac{C_2 K_{IC}}{\sigma_1 - C_1 \sigma_3} \right]^2 \quad (18)$$

Hence any stress state, the "activated area fraction" of flaws will be

$$f_a(a^*) = f_a^{\text{tot}} \exp - \left[\frac{C_2}{\tilde{\sigma}_1 - C_1 \tilde{\sigma}_3} \right]^{2n} = f_a(\tilde{\sigma}_1, \tilde{\sigma}_3) \quad (19)$$

where $\tilde{\sigma} = \frac{\sigma \sqrt{\pi \bar{a}}}{K_{IC}}$. Increasing $\tilde{\sigma}_1$ at constant $\tilde{\sigma}_3$ causes smaller flaws to be activated.

Note that the definition of damage given above for the case where all flaws are the same size is still valid

$$D = \int_{\infty} a^*(\sigma_1, \sigma_3) \int_{\infty} \pi \ell^2 dN_a = L^2 \int_{\infty} \pi a^2 dN_a = L^2 f_a(\sigma_1, \sigma_3) \quad (20)$$

since L is a constant for given (σ_1, σ_3) . The damage mechanics will be as developed above except that f_a is now a function of the stress state.

Crack Initiation And Growth In A Saturated Porous Medium

When pores are saturated, the stress state, and thus the stress intensity factor is different than that given in Equation (3). Fluids in the initial inclined cracks might be expected to lower the effective coefficient of friction. We are now developing these models for comparison with "effective stress laws" in current use.

Crack Interaction

Central to the entire damage mechanics approach to brittle failure in compression is the crack interaction. Sammis and Ashby (1986) and Ashby and Hallam (1986) point out that physically, this interaction takes the form of mutual growth enhancement of parallel neighboring cracks. How well this phenomena is represented by Equations (5)-(7) remains to be tested. We are currently testing this hypothesis in two ways: (1) by generating crack initiation and failure envelopes (like Figure 2) for the wide range of materials for which triaxial data currently exist, and (2), by performing model experiments on two- and three-dimensional arrays of holes and cracks. The fact that Costin (1983) got promising results postulating a critical damage failure criterion and ignoring interactions suggests that the final results may not be too sensitive to the exact functional form assumed for the interaction.

APPENDIX 1: INITIATION OF CRACKING

(a) Crack nucleation at a hole

Sammis and Ashby (1986) give the criterion for the initiation of cracking from a spherical hole as:

$$\frac{\sigma_1 \sqrt{\pi a}}{K_{IC}} = \frac{-(1+L)^{4.1}}{\sqrt{L} \{0.62 (1 - 1.8\lambda) - \lambda(1+L)^{4.1}\}} \quad (A1)$$

Where σ_1 is the axial stress, $\lambda = \sigma_3/\sigma_1$ is the ratio of radial (σ_3) to axial (σ_1) stress, a is the hole radius, $L = l/a$ is the normalized crack length and l is the absolute value of the crack length. K_{IC} is the fracture toughness of the material. For initiation L is small so that $1+L \approx 1$.

Replacing λ by σ_3/σ_1 and rearranging gives:

$$\sigma_1 = 3.4 \sigma_3 + \frac{1.6 K_{IC}}{\sqrt{L} \sqrt{\pi a}} \quad (A2)$$

Note that the second term on the right is a constant for a given most-dangerous flaw characterized by a hole of radius a with a starter crack of length $L = l/a$. The equation predicts a linear relationship between σ_1 and σ_3 with a slope of 3.4 (or thereabouts) independent of the flaw distribution. The intercept allows \sqrt{l} to be calculated.

(b) Crack Nucleation At An Inclined Crack

Nemat-Nasser and Hori (1982) and Ashby and Hallam (1986) analyse the nucleation of wing cracks from an initial inclined crack. The condition can

be written as:

$$\frac{\sigma_1 \sqrt{\pi a}}{K_{IC}} = \frac{-\sqrt{3}}{\{(1-\lambda)(1+\mu^2)^{1/2} - (1+\lambda)\mu\}} \quad (A3)$$

where $2a$ is the length of the initial inclined crack, μ is the coefficient of friction, and the other symbols are defined above. Replacing λ by σ_3/σ_1 and rearranging gives:

$$\sigma_1 = \left\{ \frac{(1+\mu^2)^{1/2} + \mu}{(1+\mu^2)^{1/2} - \mu} \right\} \sigma_3 + \frac{\sqrt{3} K_{IC}}{\sqrt{\pi a}} \quad (A4)$$

As before, the second term on the right is constant for a given most-dangerous flaw, characterized by a length $2a$. The coefficient of σ_3 has a value between 3 and 5, depending on the value of μ (between 0.5 and 1).

smc357

REFERENCES

- Anderson, O.L., and Grew, P., (1976), Rev. Geophys. Space Phys., 15, 77-104.
- Ashby, M.F., and Hallam, S.D., (1986), Acta Metall., 34, 497-510.
- Brace, W.F., Paulding, B.W., and Scholz, C., (1966), J. Geophys. Res., 71, 3939-3953.
- Costin, L.S., (1983), J. Geophys. Res., 88, 9485-9492.
- Costin, L.S., and Holcomb, D.J., (1981), Tectonophysics, 79, 279-296.
- Griggs, D. and Handin, H., (1960), Ch 13 in Rock Deformation, Eds. Griggs, D. and Handin, H., J. Geol. Soc. Am. Memoir 79, 347.
- Hallbauer, D.K., Wagner, H. and Cook, N.G.W., (1973), Int. J. Rock Mech. Min. Sci. Geomech. Abstr., 10, 713-725.
- Jaeger, J.C. and Cook, N.G.N., (1969), Fundamentals of Rock Mechanics, Methuen & Co., London.
- Kobayashi, S., (1971), J. Soc. Mater. Sci. Japan, 20, 164.
- Martin, R.J., (1972), J. Geophys. Res., 77, 1406-1419.
- Mogi, K., (1966), Rock Mech. Eng. Geol., 4, 41-55.
- Nemat-Nasser, S. and Horii, H., (1982), J. Geophys. Res., 87, 6805.
- Newman, J.B., (1978), in Developments in Concrete Technology - 1, Ed. Lydon, F.D., Applied Science, 5, 151.
- Paterson, M.S., (1978), Experimental Rock Deformation - The Brittle Field, Springer-Verlag, Berlin.
- Sammis, C.G., and Ashby, M.F., (1986), Acta Metall., 34, 511-526.
- Sano, O., Ito, I. and Terada, M., (1981), J. Geophys. Res., 86, 9299-9311.
- Schock, R.N., and Heard, H.C., (1974), J. Geophys. Res., 79, 1662-1666.
- Tada, H., Paris, P.C., and Irwin, G.R., (1973), The Stress Analysis of Cracks Handbook, Del. Res. Corp., St. Louis, Mo.
- Tapponnier, P., and Brace, W.F., (1976), Int. J. Rock Mech. Min. Sci. Geomech. Abstr., 13, 103-112.
- Wawersik, W.R., and Brace, W.F., (1971), Rock Mech., 3, 61-85.
- Wawersik, W.R., and Fairhurst, A., (1970), Int. J. Rock Mech. Min. Sci. Geomech. Abstr., 7, 561-575.
- Waza, T., Kurita, K., and Mizutani, H., (1980), Tectonophysics, 67, 25-34.

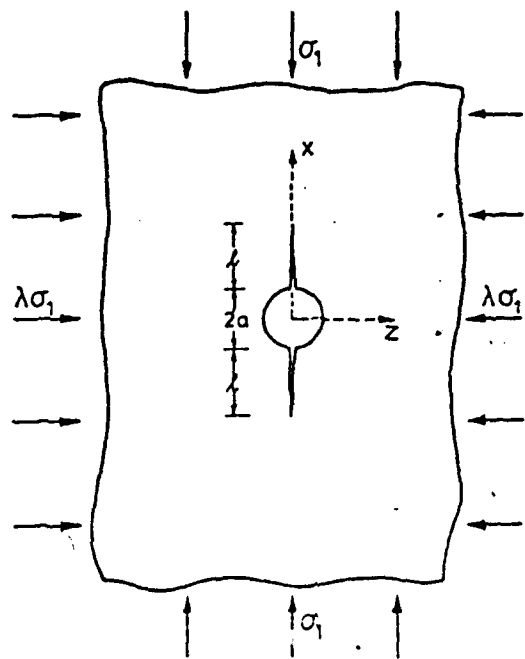
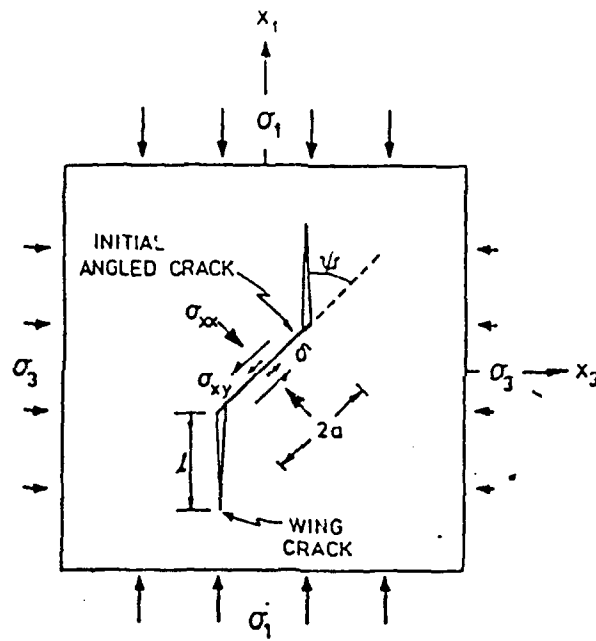


FIGURE 1 Starter-flaws for which crack nucleation and growth has been analysed. The sharp angle crack and spherical pore are considered end-members of the spectrum of flaw geometries in rock.

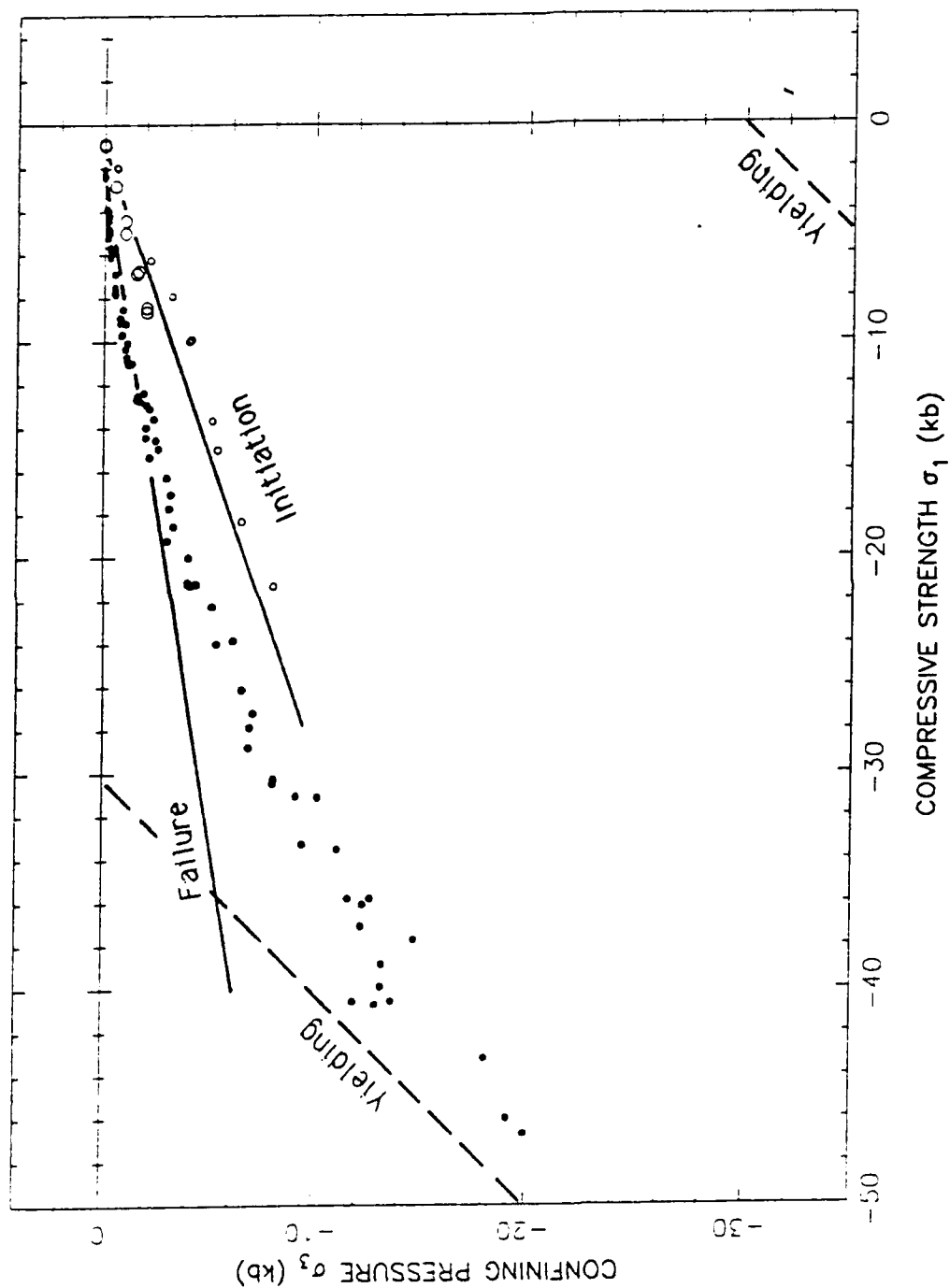


FIGURE 2. Compressive strength as a function of confining pressure for Westerly Granite. Open circles represent crack Initiation data; solid circles are failure data. The crack initiation line is from Equation (1). The failure surface is the peak stress calculated using Equations (11) and (12) as discussed in the text. Data are from Mogi (1966), Brace *et. al.* (1966), and Schock and Heard (1974).

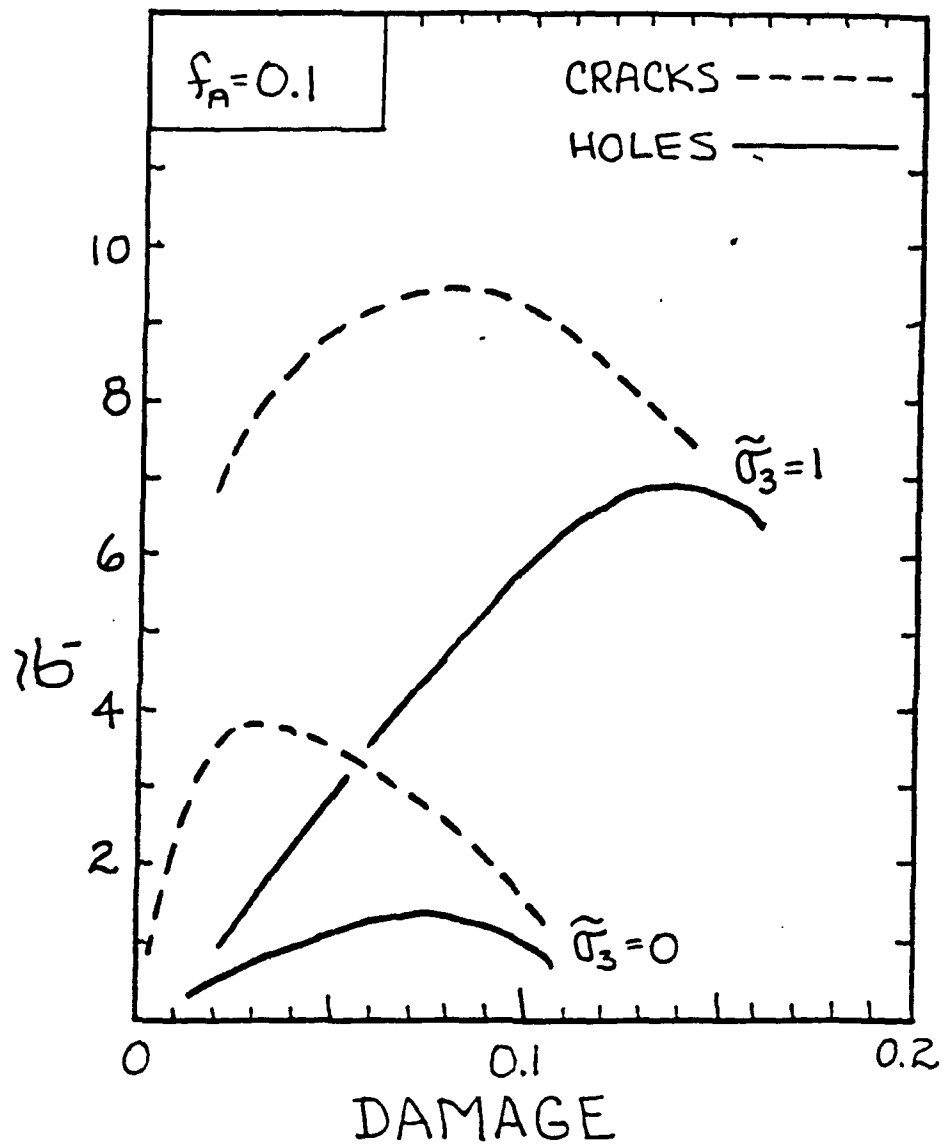


FIGURE 3 Axial stress as a function of damage for two values of the confining stress. The peak value of $\tilde{\sigma}_3$ is taken as the failure stress. The broken curves were calculated using Equation (11) for angle cracks while the solid curves were calculated using Equation (12) for holes.

AFGL / DARPA Seismic Research Symposium

U. S. Air Force Academy

Colorado Springs - 6-8 May 1986

Paper Title : Sources spectra determination for a recent seismic
crisis in East of France (December 84-January 85)

Paper authors : B. Massinon - J.L. Plantet - Radiomana

Grant n° 85 0033

In the last annual report we have described a method (Campillo and al 1984)
to extract from the Lg waves train the Q factor associated to the propagation
region and the source spectrum.

We have applied these results for some quakes occuring in Remiremont
(Vosges) in December 84/ January 85 and recorded on the seismic stations
of the LDG network. The aim of this study was to evaluate the source
amplitude spectrum for the main shock and some precursors and after
shocks, and check if these results extracted from Lg waves in the far
field were coherent with those obtained at short distance from the epicenter.

Seismic data :

Among the 28 SP seismic stations of the LDG network only 8 having recorded
this crisis with a reasonable signal upon noise ratio have been selected.
In the Figure 8 are represented the data recorded for the main shock
(12/29/84 ; $M_L = 4.8$) and the stations versus epicenter repartition.
All quakes are superficial, between 5 and 10 km depth. Seismic data are
numerically recorded on magnetic tape with a sampling rate of the
50 samples / sec which allows to process signals spectra up to 15 Hz.

Results :

- After shock 01.02.85

$$M_L = 4.0 :$$

This after shock is recorded at HAU station ($\Delta = 21 \text{ km}$)
without saturation.

After deconvolution of the seismograph response, the amplitude spectrum of the Sg signal is computed.

It represents an amplitude spectrum of the source.

A source displacement model of the form :

$$\Omega(f) = \frac{\Omega(o)}{\sqrt{1 + \left(\frac{f}{f_c}\right)^{2\alpha}}} \quad (\text{Boatwright 1978})$$

is computed by least squares to fit this amplitude spectrum (Fig. 9 a)

We find : corner frequency $f_c = 3.6 \text{ Hz}$

slope $\neq 1$

The seismic moment M_o is also available by the following relation ship
(Street and al 1975 ; Hermann and Kijko 1983)

$$M_o = \frac{4\pi \rho \beta^3 r_o \Omega(o)}{R_{\theta\phi}}$$

$r_o = 1 \text{ km}$

$\Omega(o)$: displacement source spectrum at very low frequency

β : shear wave velocity = 3.5 km/s

ρ : density 2.2 g/cm^3

$R_{\theta\phi}$: coefficient taking into account both radiation pattern $\neq 1$

We find $M_o = 2.8 \times 10^{20} \text{ dyne . cm}$

We also compute from Lg_1 , Lg_2 , Lg_3 waves trains recorded
in the 8 stations situated at more than 200 km from the epicentral area,
a mean amplitude source spectrum. For this computation we correct
the Lg_1 , Lg_2 , Lg_3 , spectra from :

- elastic and anelastic attenuation
- station response
- seismograph response

Figures 9 b , 9 c , 9 d represent an evaluation of the $\pm \sigma$ limits for the 8 source spectra and the mean amplitude source spectrum. (continue line).

We also figure the source spectrum computed from HAU Sg waves (dotted line) as a reference.

As a result , source spectra obtained with Lg waves in the far field are similar to the one obtained in the near field (HAU) namely. Lg₁ waves lead to a source spectrum which $\Omega(o)$, f_c and slope are very comparable to those of HAU.

Seismic moments computed on the source spectra from Lg waves and the one extracted from Sg waves at HAU are of the same order.

- Main shock 12.29.84 $M_L = 4.8$

Source amplitude spectra on Lg₁ , Lg₂ , Lg₃ waves are computed by the same method described in the first case (After shock 01 02 85 $M_L = 4.0$).

For this main shock case no records are available at HAU.

Figure 10 represents the source spectra we obtain :

- $\pm \sigma$ amplitude spectra corresponding to all the 8 stations
- the source spectrum which fits the mean amplitude spectrum values.
- corner frequency f_c , slope of the spectrum and seismic moments which are very similar .
- fault dimensions and stress drops computed for each of the three cases with, for the circular fault radius, two different formula proposed by Brune and Madariaga.

$$L = 0.37 \frac{\beta}{f_c}$$

(Brune)

$$L = 0.21 \frac{\beta}{f_c}$$

(Madariaga)

and

$$\Delta\sigma = \frac{7}{16} \cdot \frac{M_o}{L^3}$$

- Small foreshock 12.24.84 $M_L = 3.0$

This last example of source evaluation is given to figure out the limits of our far field method. This small foreshock is recorded by 8 stations among those which recorded the previous cases.

Figure 11 presents the source amplitude spectra obtained at HAU on Sg waves and on Lg₁ , Lg₂ , Lg₃ waves recorded on the 8 stations at 200 km and more from the epicenter. Computations and representations are identical as the ones of Figure 9 on the aftershock.

For this small foreshock the corner frequency is of the order of 7 to 9 Hz, to be compared to 3.6 Hz for the after shock ($M_L = 4.0$) and around 2 Hz for the main shock ($M_L = 4.8$).

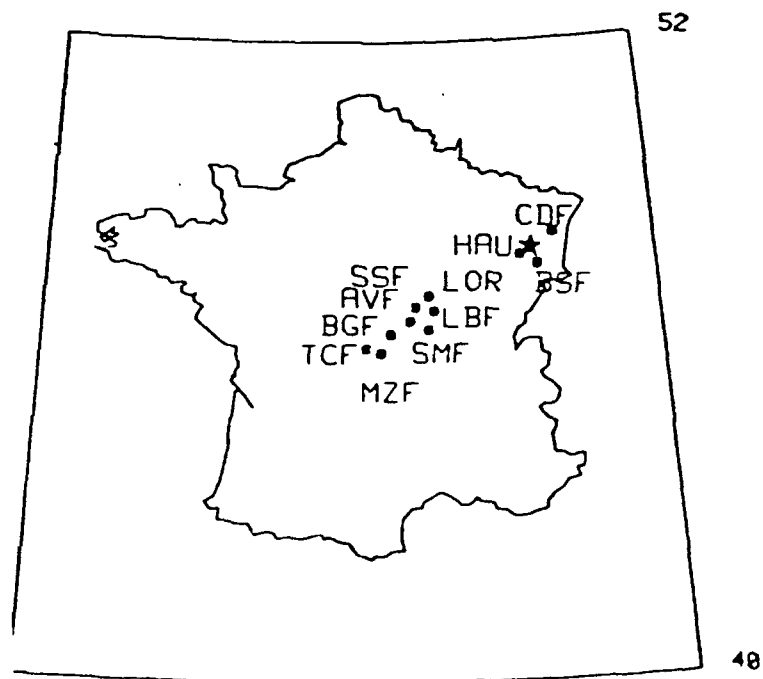
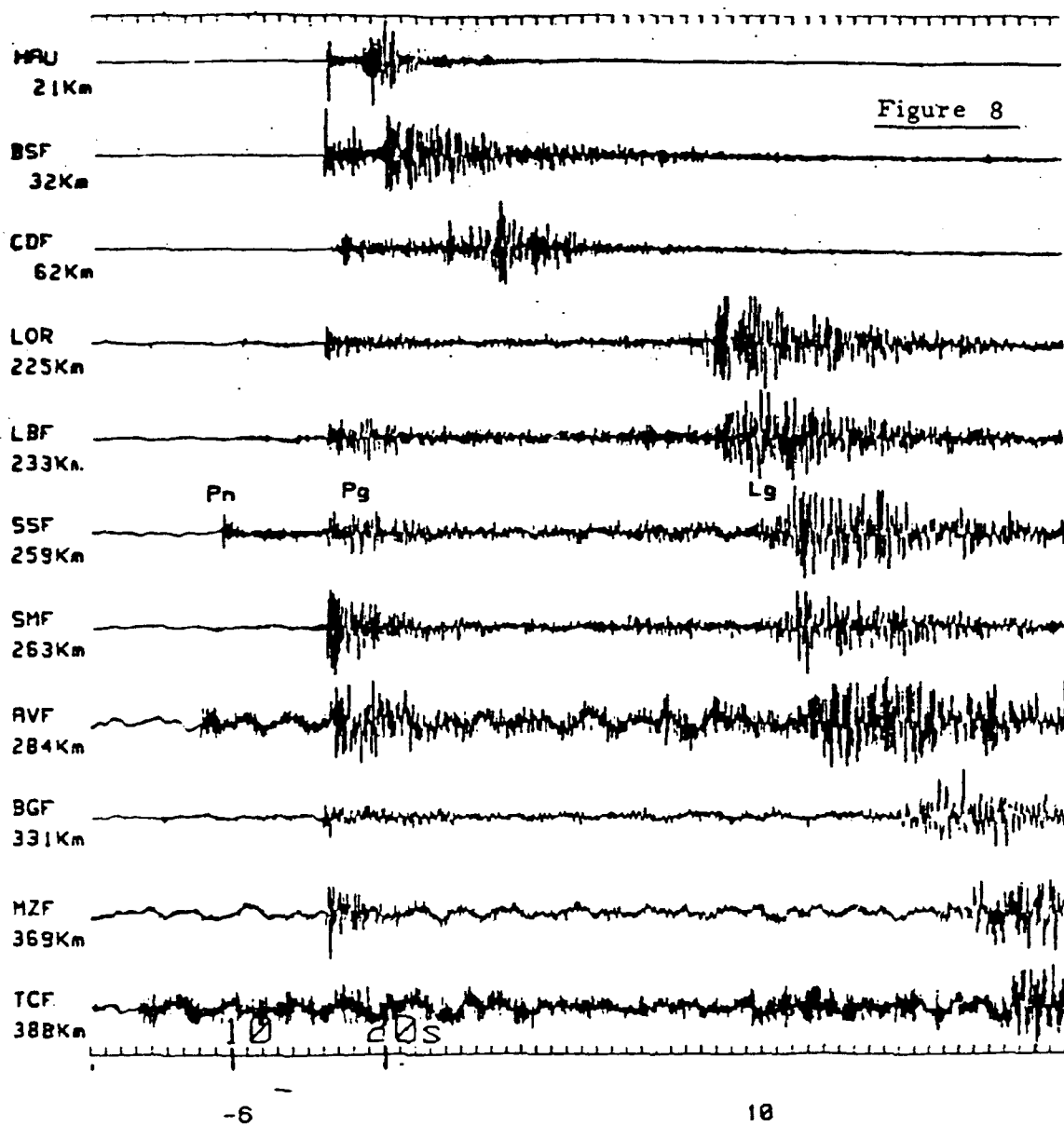
The seismic moment is of the order of some 10^{19} dyne .cm.

But essentially , the spectra definition particularly for Lg₃ waves and even Lg₂ is here rather poor and do not guarantee a reasonable fiability on the results.

Conclusion :

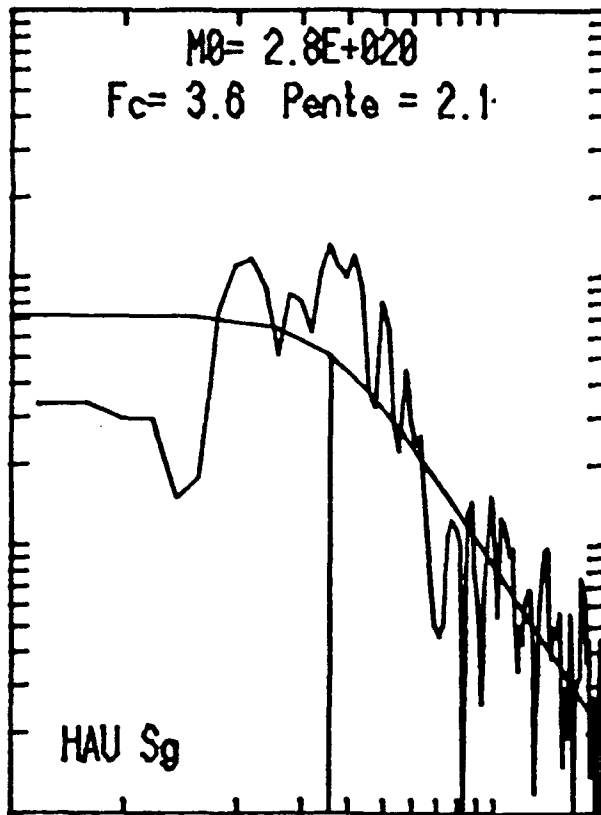
This attempt to evaluate the source amplitude spectrum of the earthquake by processing the Lg waves train recorded at large distances seems to be reliable as shown on the Remiremont seismic crisis.

It is necessary to apply this method on more different cases but we notice already that as long as the Lg waves are well defined, they bring information from the source which lead to approach its main parameters.

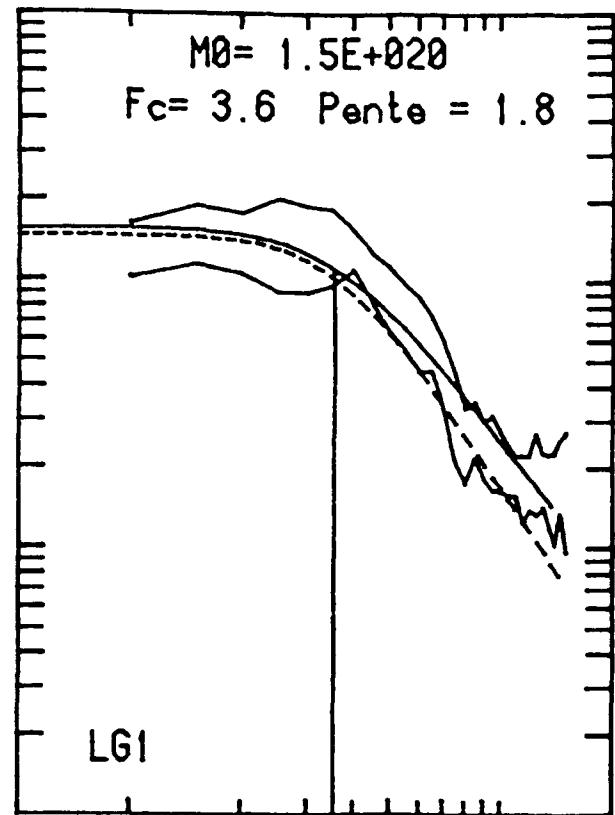


Seismic data and stations- epicenter configuration for the main shock
($M_L = 4.8$) Remiremont crisis

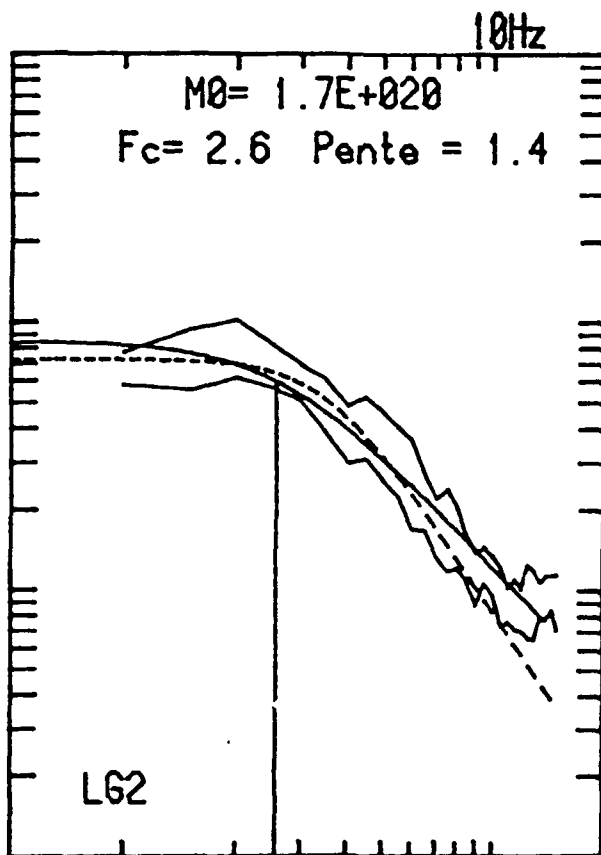
Figure 9



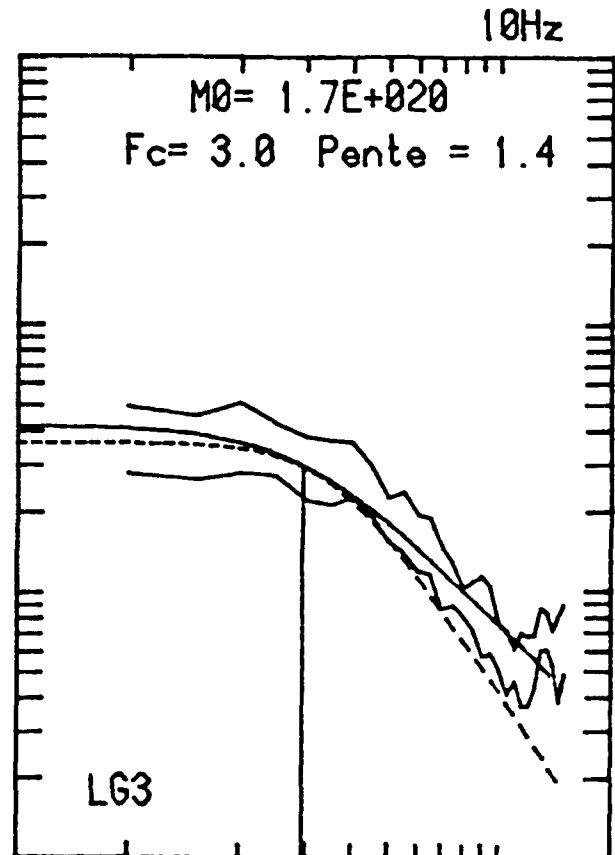
a)



b)



c)



d)

Remiremont crisis - Aftershock 010285 - $M_L = 4.0$

Figure 10

	RAYON DE LA FAILLE	
	BRUNE	MADARIAGA
LG1	770m	430m
LG2	690m	390m
LG3	600m	330m

	CHUTE DE CONTRAINTE	
	BRUNE	MADARIAGA
LG1	20b	115b
LG2	40b	220b
LG3	85b	500b

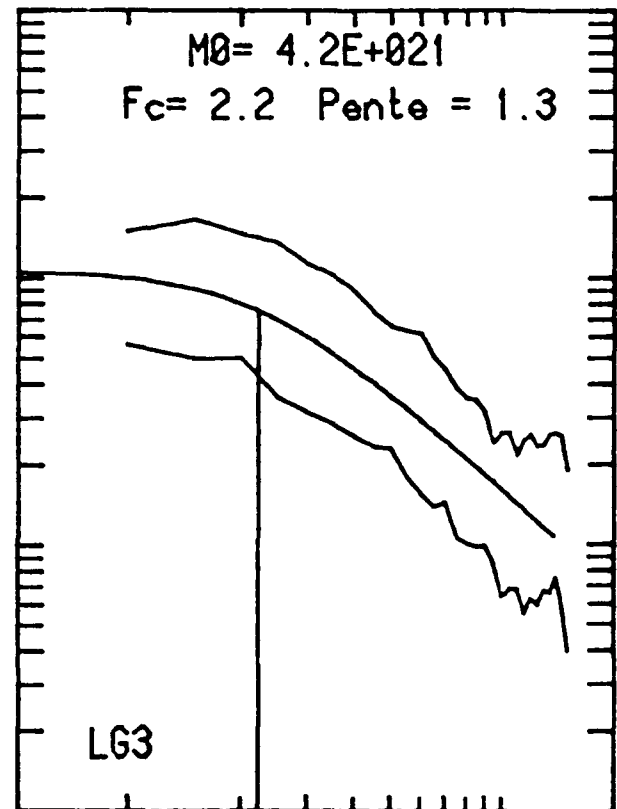
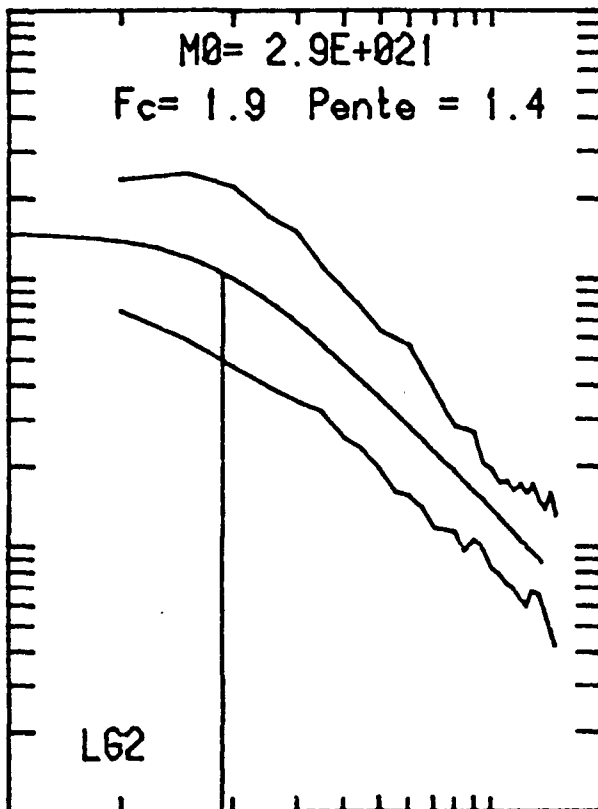
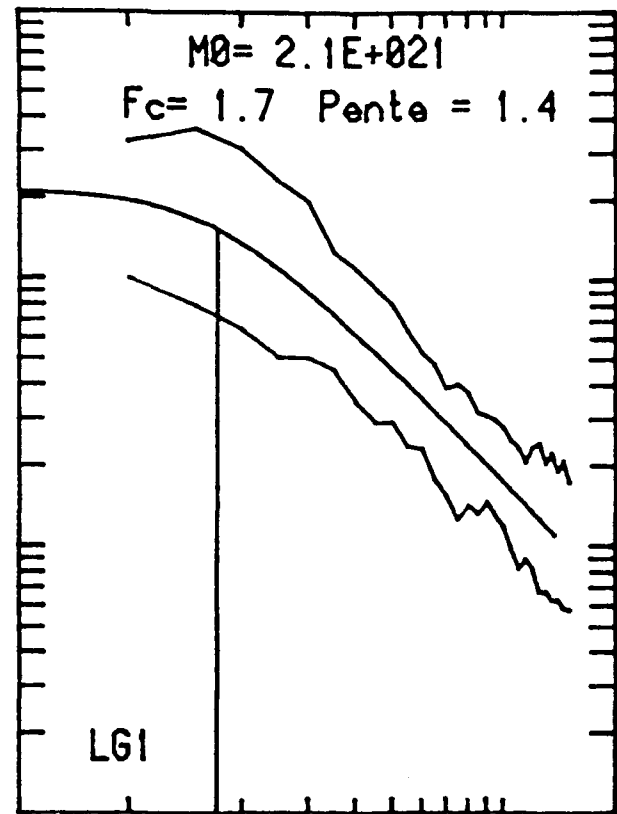
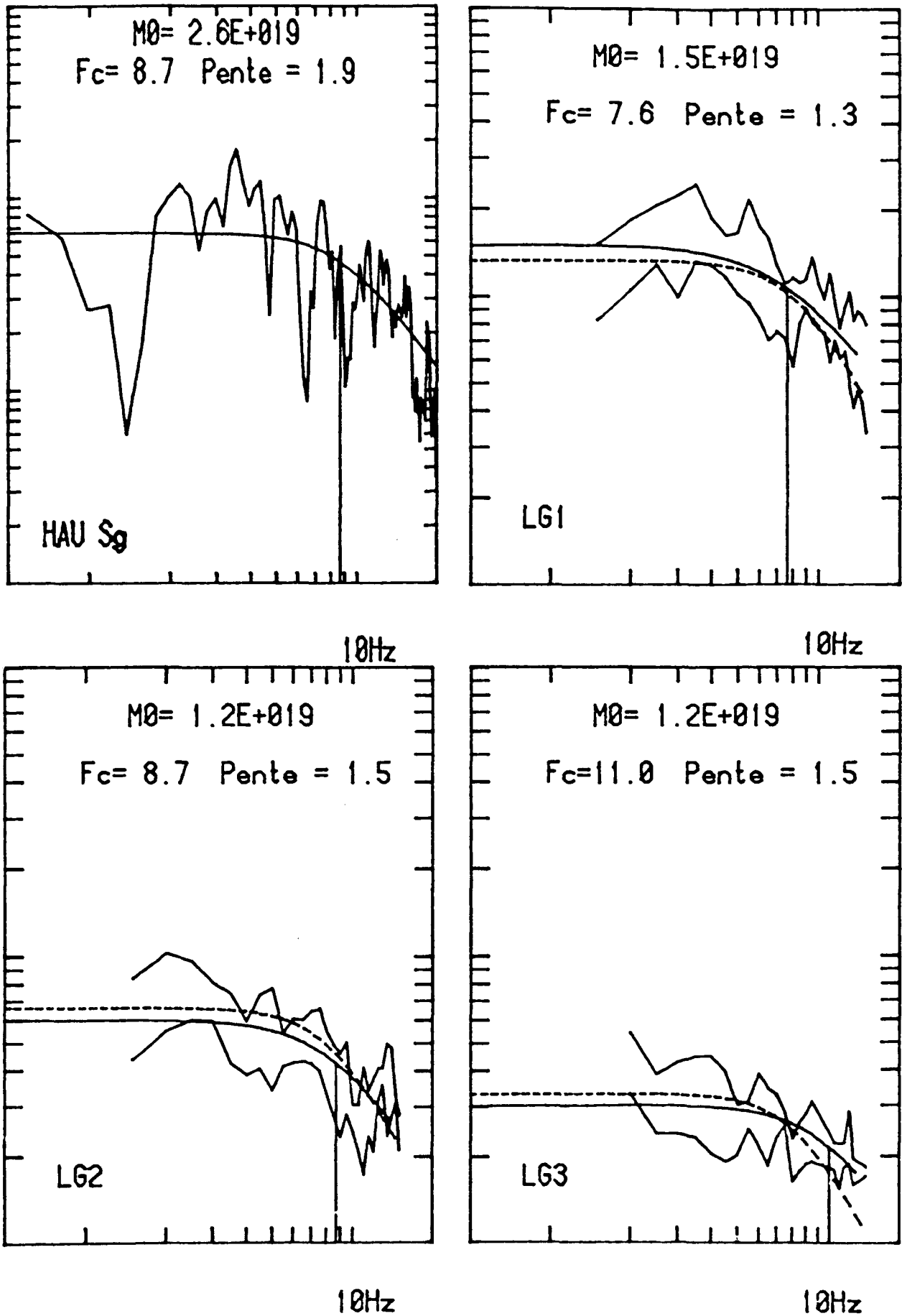


Figure 11



Remiremont crisis - Foreshock 12 24 84 - $M_L = 3.0$

Focussing and Defocussing of Body Waves by Three-Dimensional Structure in Source and Receiver Regions

AUTHOR:

Vernon F. Cormier, Earth Resources Laboratory, Dept. of Earth, Atmos., and Planet. Sci., Massachusetts Institute of Technology, 42 Carleton St., Cambridge, MA 02142

RESULTS

Forward calculations have been completed in several models on the effects of three-dimensional structure in the source and receiver site on the focussing and defocussing of teleseismic body waves. The choice of models and experiments was designed to separately examine the effects of structure beneath source and receiver sites. Although the models that were examined differed between source and receiver sites, their scale lengths and intensity of velocity fluctuation were similar. This allowed at least a qualitative test of reciprocity of the asymptotic methods used in the forward calculations. The technique used in the forward calculations consisted of body wave synthesis by dynamic ray tracing and Gaussian beams. In experiments that investigated the effects of receiver structure, a plane wave incident on a three-dimensional structure was expanded into Gaussian beams. In experiments that investigated the effects of source structure, the propagator matrix of dynamic ray tracing was employed to connect a 3-D source region to a 1-D whole earth model (Cormier, 1986).

Calculations were performed (Nowack and Cormier, 1985) in three-dimensional models of the upper 75 - 100 km. of the crust and mantle beneath the NORSAR array (Thomson and Gubbins, 1982), a model for a region in northern California (Zandt, 1981), and a model generated by random

perturbations to a 1-D velocity structure (McLaughlin and Anderson, 1985). In both the NORSAR and Zandt models, azimuthal variations in teleseismic amplitude were found to be on the order of a factor of 2 and variations in travel time were found to be on the order of several 0.1's of a second. These models had a maximum of 4 to 8% velocity fluctuation over scale lengths of 10 to 100 km.

A significant result obtained with the NORSAR and California models was that the scale-lengths and intensities of perturbations were such that the amplitude variations were nearly independent of frequency (Figures 1 and 2), and hence adequately predicted by simple ray theory. This result has important consequences for the yield estimation of underground nuclear explosions by measurements of classical body wave magnitudes, m_b , versus broader band measurements of radiated energy in the time and frequency domain. If deep seated, broad scale length (50km. and greater), velocity anomalies of 2% or more are a common occurrence in the upper mantle of the earth, they will act to focus and defocus body waves over a broad frequency band. The focussing and defocussing caused by these broad anomalies will be independent of frequency and will thus introduce a scatter in broader band measures of radiated energy which will be equivalent to that seen in the narrow band m_b measurement. Focussing and defocussing by structure in either the source or receiver region will also affect the coda of P waves if a portion of this coda is generated in either region. These effects may help explain why broader band and integrated coda measures of body wave energy often do not exhibit significantly less scatter than classical m_b measurements.

The results obtained with a random model (Figures 3-4) show that a model having a maximum velocity fluctuation as small as 0.8 per cent is capable of producing caustics and multipaths at teleseismic range. The production of multipaths strongly depends on the anisotropy of the distribution of scale

lengths, i.e., the ratio of characteristic vertical to horizontal scale length. The multipaths of the random model, however, occurred over too small an area and were too closely spaced in arrival time to be resolved with standard seismograph systems operating in the 0.01 to 4 Hz. band.

CONCLUSIONS

Broad scale length (50 to 100 km), deep seated structure can affect short period as well as broad band and coda measures of radiated seismic energy. Its effects, however, may be easily correctable if a 3-D model of the source region is known from block inversion of travel time residuals. A resolvable block size of about 20 km. may be all that is necessary to formulate corrections based on azimuth of teleseismic station and source location within a test site.

Calculations with a random velocity model demonstrated that a smaller intensity of velocity fluctuation (0.8%) can produce even larger amplitude variations if the smallest scale length of fluctuation is on the order of 10 km. The random model was constructed such that the smallest scale length of velocity fluctuation was shorter in the horizontal direction than in the vertical direction. At teleseismic range, this model generated isolated caustics, which were elongated along the azimuth of approach. The waveform distortion associated with these caustics was small. The fact that the caustics were generated at all by such mild 3-D perturbations is significant. It suggests that this type of synthetic modeling may be useful in limiting some of the attributes of the heterospectrum of the earth's lithosphere.

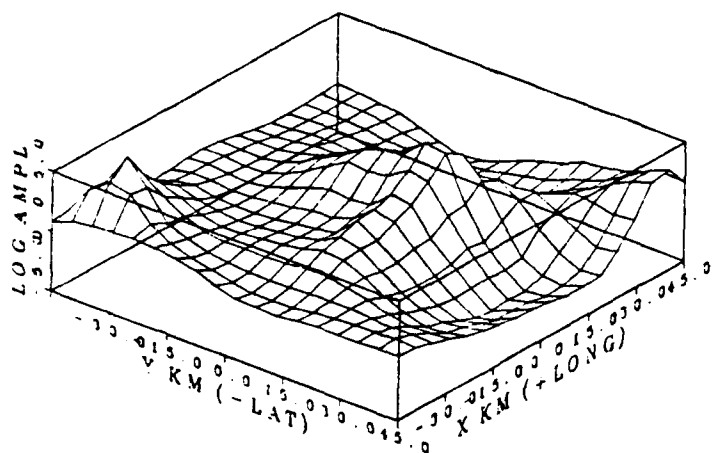
In future work, the model of Taylor (1983) for the Nevada test site will be investigated. This model has a deep high velocity anomaly situated to the northeast of Pahute Mesa, which may account for the deep minimum seen in body wave amplitudes of Pahute tests recorded at teleseismic stations to the

northeast (Lay et al., 1983). The patching technique developed for connecting 3-D models to 1-D radially, symmetric models of the whole earth should aid in investigating any fine structure of teleseismic amplitudes predicted by 3-D models of the source region.

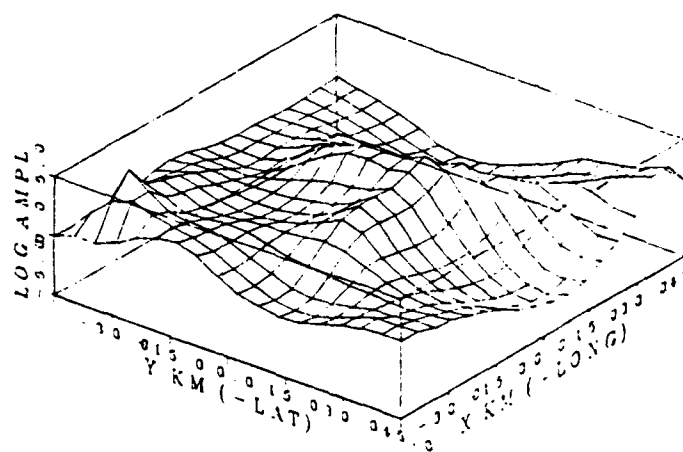
REFERENCES

- Cormier, V.F., 1986. An application of the propagator matrix of dynamic ray tracing: the focussing and defocussing of body waves by three-dimensional velocity structure in the source region, *Geophys. J. R. Astr. Soc.*, submitted.
- Lay, T., Wallace, T.C., and Helmberger, D.V., The effects of tectonic release on short-period P waves from NTS explosions, *Bull. Seism. Soc. Am.*, 74, 819-842, 1983.
- McLaughlin, K.L., and L.M. Anderson, 1985. Stochastic dispersion of P waves due to scattering and multipathing, Teledyne-Geotech, Final Report No. TGAL-85-8, ARPA Order No. 4511.
- Nowack, R.L., and Cormier, V.F., 1985. Computed amplitudes using ray and beam methods for known 3-D structures (abstract), *EOS, Trans. Am. Geophys. Un.*, 66, 980.
- Taylor, S.R., Three-dimensional crust and upper mantle structure at the Nevada Test Site, *J. Geophys. Res.*, 88, 2220-2232, 1983.
- Thomson, C.J. and D. Gubbins, 1982, Three-dimensional lithospheric modeling at NORSAR: Linearity of the method and amplitude variations from the anomalies, *Geophys. J.R. astr. Soc.*, 71, 1-36.
- Zandt, G., 1981. Seismic images of the deep structure of the San Andreas Fault system, central coast ranges, California, *J. Geophys. Res.*, 86, 5039-5052.

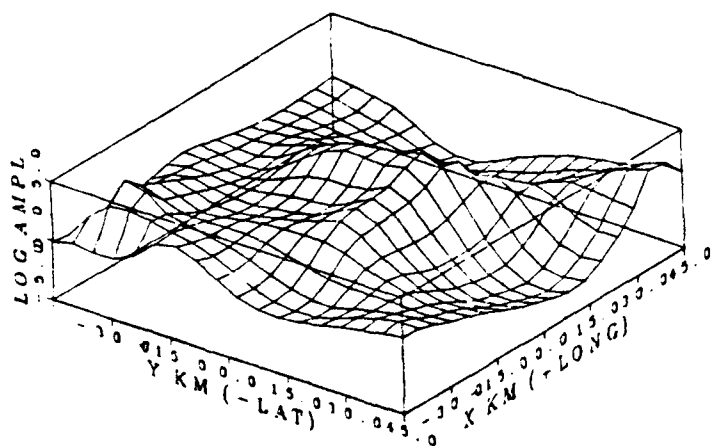
LOG AMPLITUDE VARIATIONS
PARAXIAL RAY THEORY



LOG AMPLITUDE VARIATIONS
GAUSSIAN BEAM - 8 HZ



LOG AMPLITUDE VARIATIONS
GAUSSIAN BEAM - 4 HZ



LOG AMPLITUDE VARIATIONS
GAUSSIAN BEAM - 1 HZ

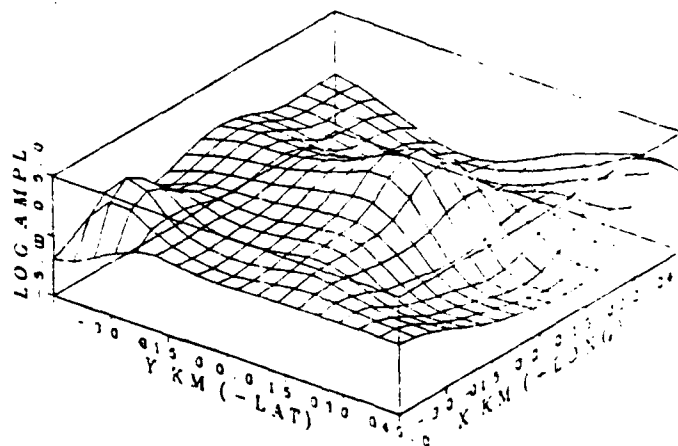


Figure 1 Variations in amplitude for a vertically incident plane wave on the NORSAR model. Results for several frequencies are shown.

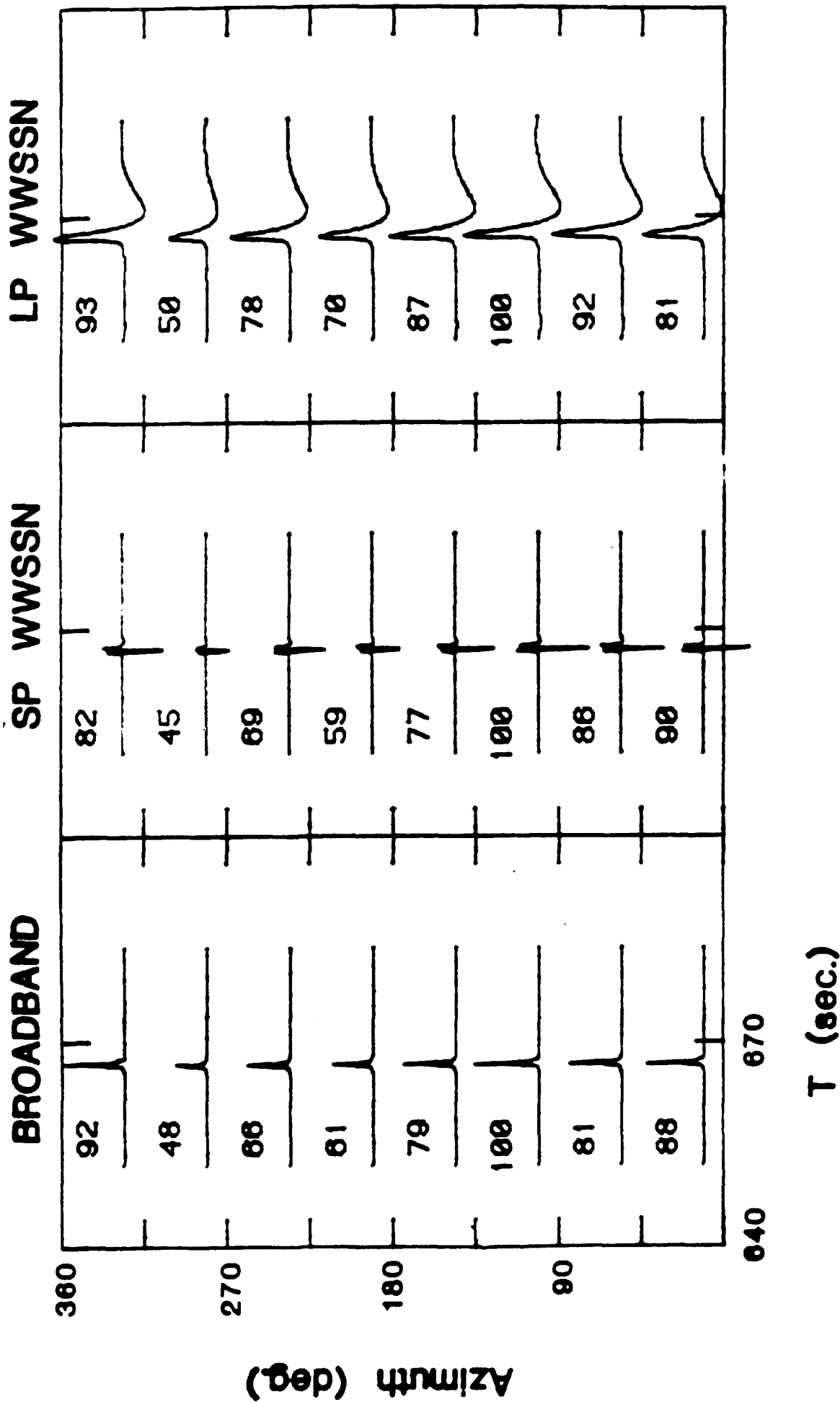


Figure 2 Synthetic seismograms constructed by superposition of Gaussian beams for stations at 70° and variable azimuths from an explosive point source at a constant location S0 at 9.6 km. depth in the Zandt model. Seismograms are shown for a broad band, WWSSN short period and long period instrument response.

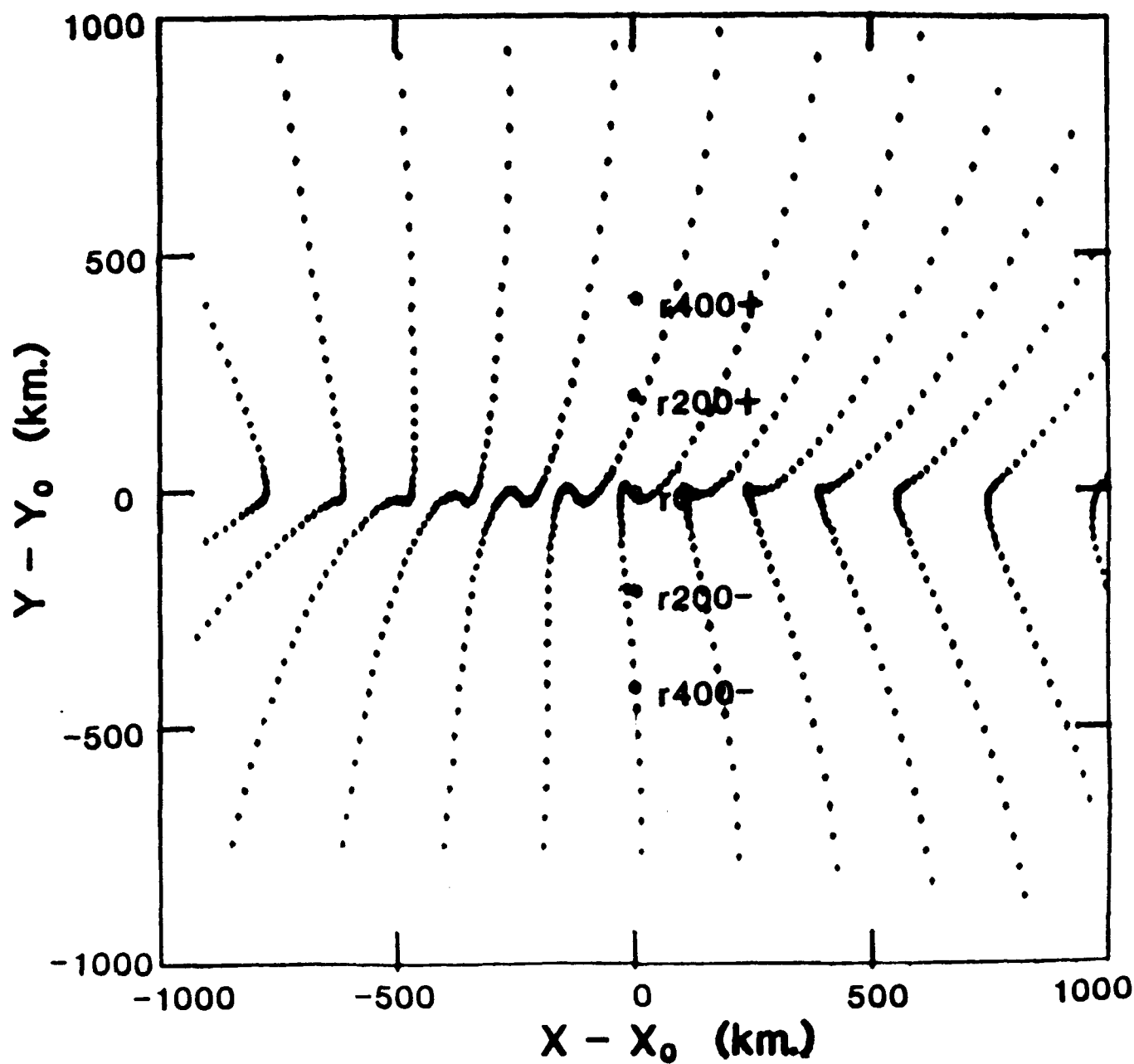


Figure 3 Ray end points near a station at 70° distance from source s10- in the random model. The locations of a profile of stations in the vicinity of a caustic intersection is given by the labeled points r400- to r400+.

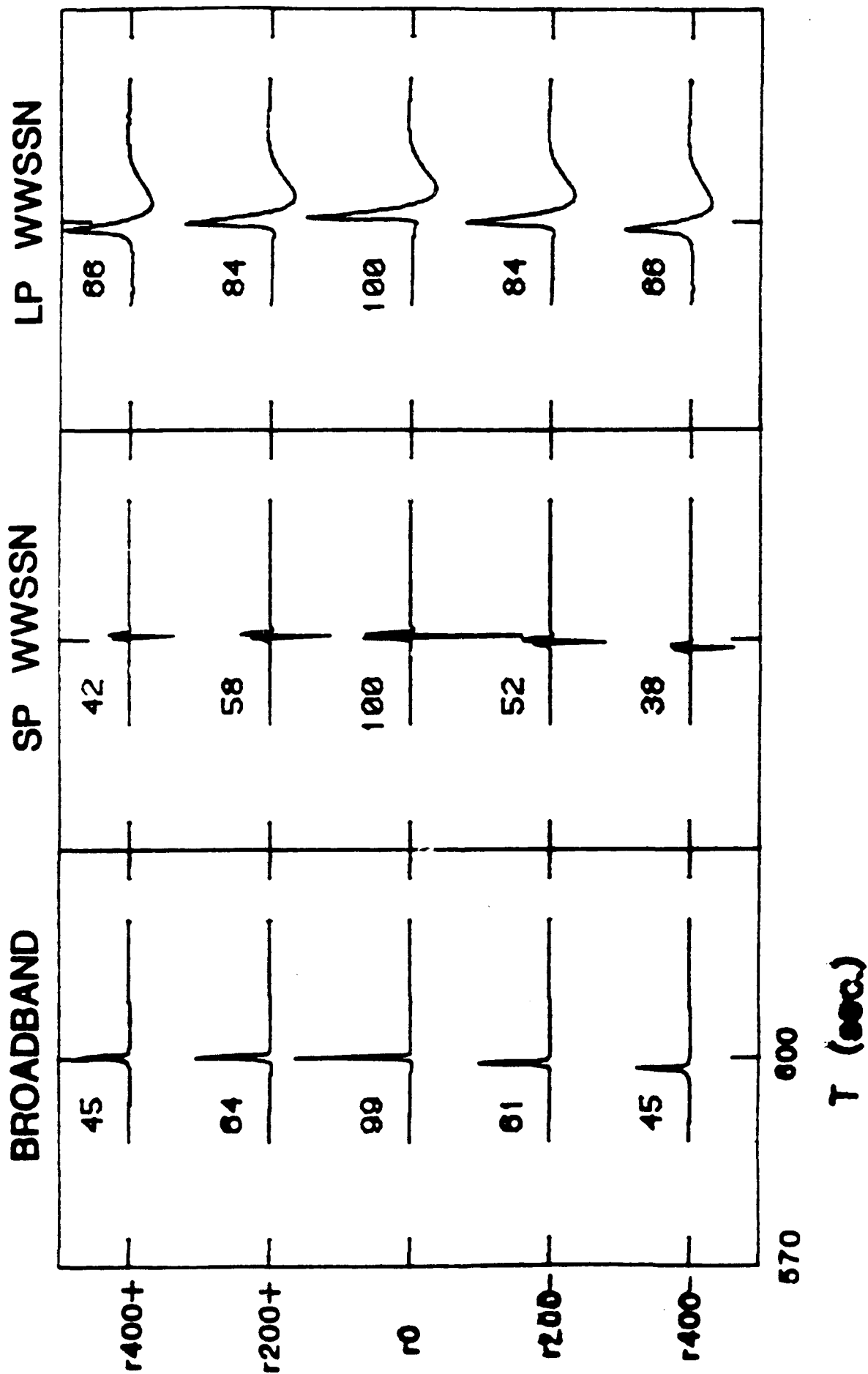


Figure 4 Synthetic P waves for the profile of stations in the vicinity of the caustic shown in the plot of ray end points in Figure 3

REGIONAL EVENT DETECTION USING THE NORESS ARRAY

F. RINGDAL

NTNF/NORSAR, Post Box 51, N-2007 Kjeller, Norway

INTRODUCTION

Since January 1985 data from the small-aperture array NORESS in Norway have been processed in real time at the NORSAR data center at Kjeller. The data used in the detection processing comprise 25 SPZ channels, deployed over an area 3 km in aperture and sampled at a 40 Hz rate. The detection algorithm has been described by Mykkeltveit and Bungum (1984), and briefly consists of

- Digital narrow-band filtering (six filter)
- Beamforming (conventional and incoherent)
- STA/LTA detector applied to each beam
- Frequency-wavenumber analysis of detected signals
- Association of regional phases to aid in locating events.

Preliminary results from the NORESS processing have earlier been presented in NORSAR Semiannual Technical Summaries (SATS). In this paper, we discuss in particular the automatic detection performance for events at regional distances, and the spectral characteristics of signal and noise at very high frequencies.

REGIONAL DETECTABILITY

An assessment of the NORESS detection capability at regional distances has been obtained by comparing the automatic NORESS detector output to the bulletins produced on the basis of local seismic networks in Fennoscandia. In particular, we have used as a data base the catalogue of seismic events in Northern Europe regularly compiled at the University of Helsinki.

The time period covered by this study is the 6-month interval April-September 1985, during which the RONAPP processor was operated with a fixed beam deployment (re. NORSAR SATS 84-85). A total of 477 events reported in the Helsinki catalogue, with local magnitudes in the range 1.7-3.3, were cross-checked with the NORESS detection list. The epicentral distances from NORESS ranged from 500-1500 km. For each event, the expected arrival times at NORESS for P, Sn and Lg were computed, using standard travel time tables, and matched to NORESS detection entries.

Fig. 1 shows the magnitude-distance distribution of the events in the data base. Events detected at NORESS are shown as crosses, non-detections are indicated as triangles. In this figure, "detection" means that at least one phase (P, Sn or Lg) was reported by NORESS.

A summary of the statistics on automatic detection of primary vs. secondary phases is given in Table 1. We note that, at low magnitudes, many events are detected only on secondary phases. It is also noteworthy that several events, even in the higher magnitude range, are detected as P-phases only. However, visual inspection of the signal traces shows that in virtually all of these cases an Lg phase may be identified by the analyst. Thus, the lack of secondary phase detections is a problem within the automatic processor that requires improvements in the algorithms in order to extract emergent phases in the coda of a preceding P-phase.

Table 1

Summary of automatic NORESS detection statistics for the regional data base.

<u>M_L</u>	<u>1.5-2.0</u>	<u>2.1-2.5</u>	<u>2.6-3.0</u>	<u>3.1-3.5</u>
P detection only	13	39	16	0
P + secondary phase*	16	105	30	3
Secondary phase only*	28	88	2	0
No detection	48	87	2	0
Total	105	319	50	3

* "Secondary phase" meaning Sn or Lg (or both) detected.

Fig. 1 shows that there is only a slight degradation in detection capability with increasing distance for the range considered. As an initial estimate of detection thresholds, we have therefore combined the data in the distance range 700-1400 km and estimated detection thresholds as shown in Fig. 2 (detection on either P, Sn or Lg) and Fig. 3 (P-detection only). The method described by Ringdal (1975) has been applied.

From Fig. 2 we observe that the 50 and 90 per cent regional detection thresholds are close to $M_L = 1.9$ and 2.5 , respectively. When only P phase detections are counted (Fig. 3), the respective thresholds are $M_L = 2.3$ and 2.7 .

It would clearly be desirable to tie these thresholds to the global m_b scale. It has, however, not been possible to do this for the present data set, since all of the 477 reference events are much too small to have any teleseismic detection. Nevertheless, the local magnitude scale in question has been developed so as to be consistent with world-wide m_b , and the differences are not thought to be significant. This topic will be subject to further study.

As a final note, we remark that the large majority of reference events are mining explosions, mostly from mines in Western Russia. We have not yet attempted systematically to compare the detectability of these explosions to that of the (very few) earthquakes in the data base, but initial studies do not indicate major differences for the two source types.

HIGH-FREQUENCY STUDIES

The recently installed high-frequency recording system (HFSE) at NORESS has provided a unique opportunity to study noise and signal characteristics at frequencies up to at least 50 Hz. These studies have only begun, but it is already apparent that much important information can be extracted from the high frequency part of the spectrum. Based on about 50 regional events analyzed so far, it appears that the signal-to-noise ratio of P and Sn phases

does not show any appreciable decay with increasing frequency up to at least 50 Hz for events within about 500 km epicentral distance. At greater distances, the signal spectra drop more rapidly than the noise spectra, but even at 1000 km distance, the P-wave of $M_L = 3.0$ events have significant signal-to-noise ratio up to about 25-30 Hz.

An example of a high-frequency recording is shown in Fig. 4, corresponding to an $M_L = 5.0$ earthquake off the west coast of Norway on February 6, 1986 (distance = 417 km). The unfiltered record shows the expected amplitude pattern, i.e., Lg as the dominant phase, Pg much larger than Pn. The picture changes dramatically when considering the high-frequency part of the record. In the filter band 30-50 Hz, the Pn and Sn phases dominate the seismogram, and the Pg and Lg phases are not even visible.

Fig. 5 shows HFSE spectra from the vertical component for the same event. We see that Lg exceeds the preceding noise (which in fact is the Sn coda) only up to about 10 Hz, whereas Pn has large SNR over the entire frequency band.

In conclusion, the NORESS regional detection capability appears to be $M_L = 2.5$ or better out to at least 1500 km. Many small events are detected only on secondary phases, and the further improvement of automatic detection of such phases is important. At distances up to 500 km, considerable improvements in detection capability are possible by taking advantage of the high frequencies which propagate very efficiently in this distance range. The high frequency band is also potentially valuable for improved phase identification, especially to separate Pn from Pg and Sn from Lg.

REFERENCES

- Loughran, L.B. (ed.) (1985): NORSAR Semiannual Technical Summary, 1 Oct 84-31 Mar 85.
- Loughran, L.B. (ed.) (1985): NORSAR Semiannual Technical Summary, 1 Apr - 30 Sep 1985.
- Mykkeltveit, S. & H. Bungum (1984): Processing of regional seismic events using data from small-aperture arrays, BSSA, 74, 2313-2333.
- Ringdal, F. (1975): On the estimation of seismic detection thresholds, BSSA,

NORESS REGIONAL DETECTION
AZIMUTH RANGE 15-175 DEGREES

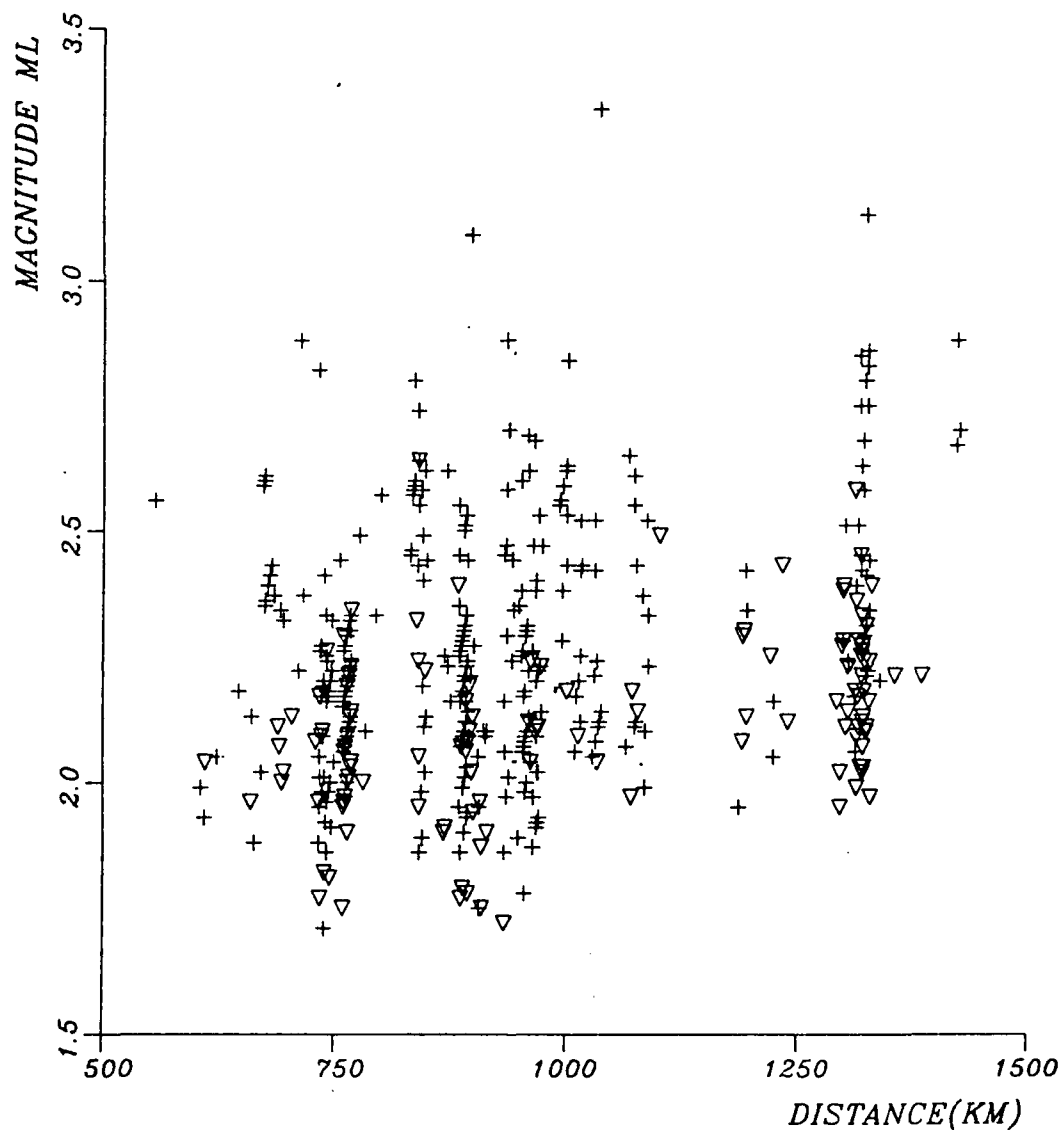


Fig. 1 Distribution of 489 regional events in the data base as a function of epicentral distance from NORESS and local magnitude M_L . Crosses denote events detected automatically at NORESS (either P, Sn or Lg phase), whereas non-detected events are marked as triangles.

NORESS REGIONAL DETECTION
DISTANCE 700-1400 KM, AZIMUTH 15-175 DEG

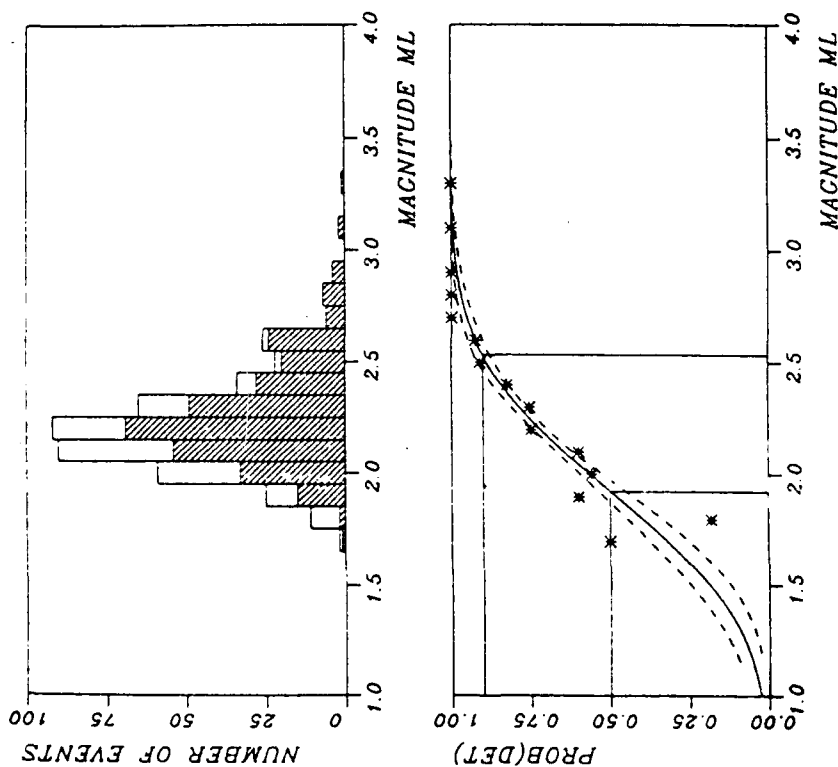


Fig. 2 Distribution of events by magnitude (upper part), with events detected for at least one phase (P, Sn or Lg) corresponding to the hatched columns. The bottom part of the figure shows the estimated detection probability curve as a function of magnitude, with the observed detection percentages marked as asterisks.

NORESS P-PHASE DETECTION
DISTANCE 700-1400 KM, AZIMUTH 15-175 DEG

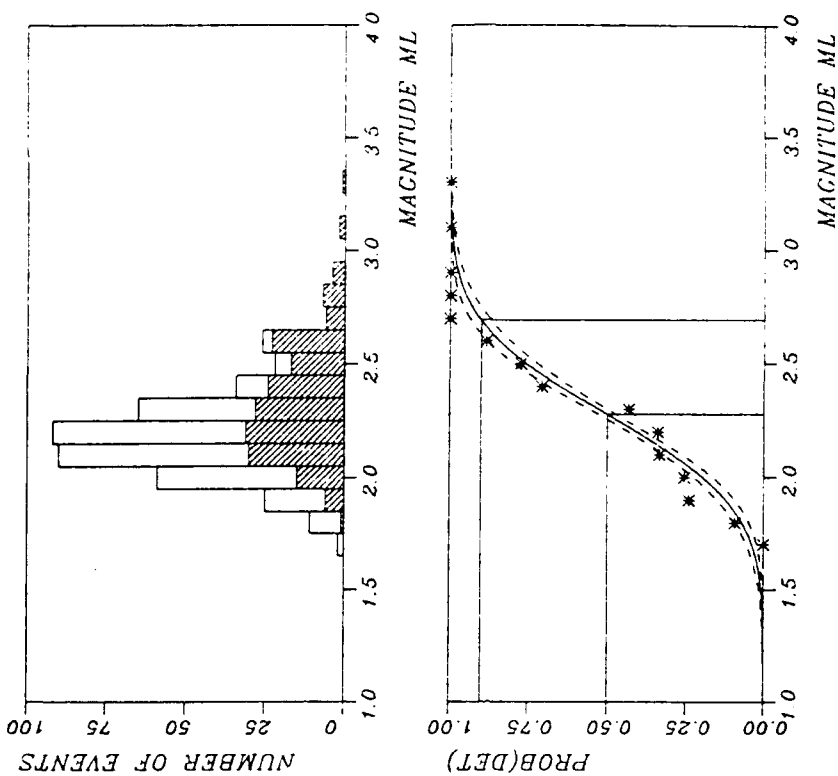


Fig. 3 Same as Fig. 2, except that only events with a detected P-phase are counted as detections.

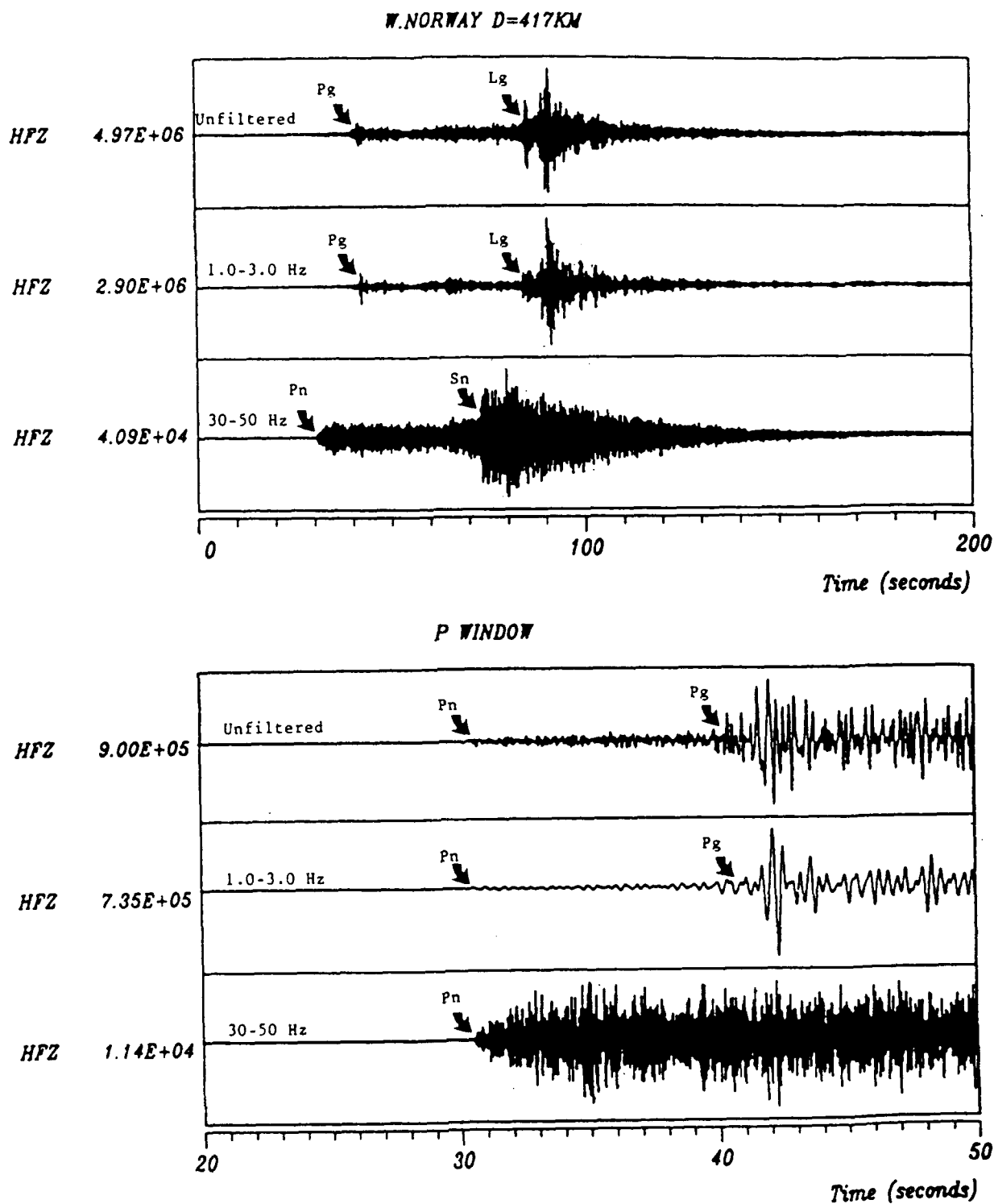


Fig. 4 Time domain plots of the HFSE recordings on the SPZ channel at NORESS for an $M_L = 5.0$ earthquake off the west coast of Norway (distance = 417 km). The upper part covers the entire wavetrain (unfiltered and in two filter bands as indicated). The bottom part is an expanded view of the P window. Note the prominence of Pn and Sn in the high-frequency band.

HFZ 86036 17.54.30

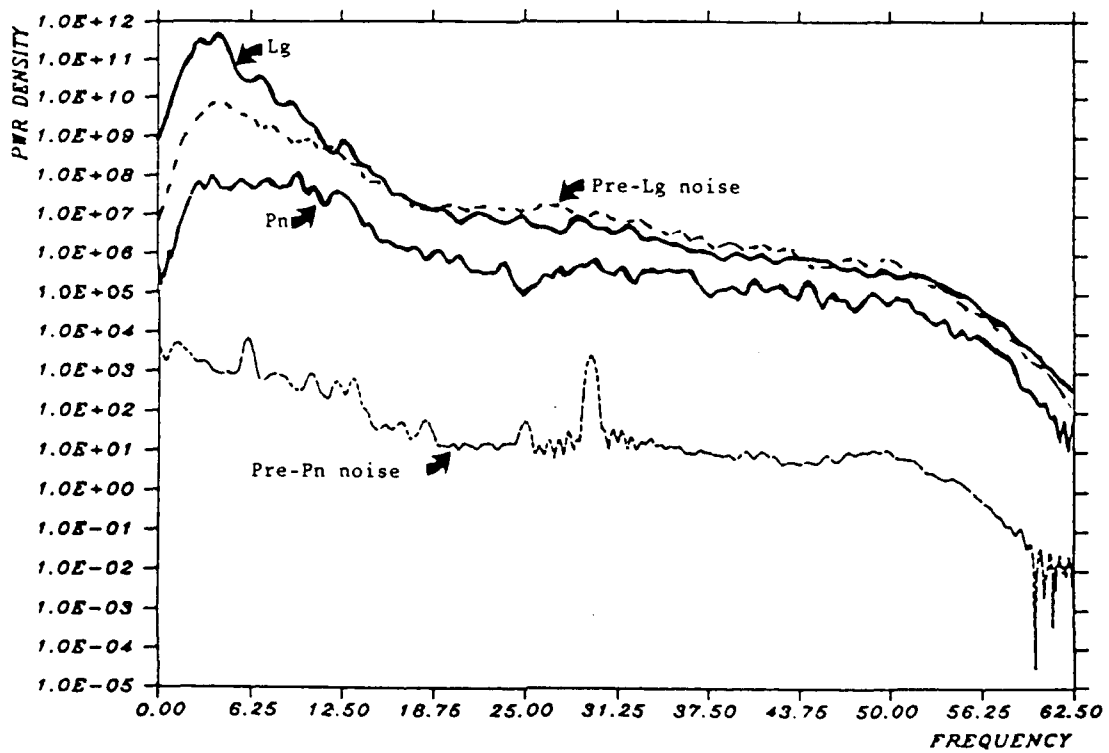


Fig. 5 Spectral plot of the Pn and Lg phases for the event shown in Fig. 4. Note that the Pn SNR remains approximately constant across the entire high-frequency part of the spectrum.

THE NATURE OF TELESEISMIC P CODA AT NORESS

ANTON M. DAINTY
M. NAFI TOKSOZ
EARTH RESOURCES LABORATORY
DEPARTMENT OF EARTH, ATMOSPHERIC, AND PLANETARY SCIENCES
MASSACHUSETTS INSTITUTE OF TECHNOLOGY

SUMMARY

Six events showing teleseismic P coda recorded at the NORESS array in the distance range 35° - 85° have been analysed. The events were two Semipalatinsk presumed explosions, two deep focus (≈ 400 km) earthquakes in the Japan-Bonin trench, and two crustal earthquakes with focal depth < 15 km in Alaska and Yunnan, China. The analysis methods were measurement of coda power relative to the energy in first P, determination of the decay rate in time of the coda power spectrum, frequency-wavenumber analysis, and measurement of the wavenumber spectrum. The model tested states that the coda consists of two components produced by scattering of Lg to P in the crust near the source and P to Lg near the receiver. The near source component will not be present for deep focus events. The model predicts: (1) crustal earthquakes have highest power in the coda relative to first P and deep focus events lowest; (2) coda decays exponentially; (3) the near source component has the same phase velocity and azimuth as first P, the near receiver component has the phase velocity of Lg in the receiver region and random azimuth; (4) the differences predicted in (1) are due to differences in the strength of the near source component. The tests (1) and (2) are considered weak tests of the model, but (3) and (4) seem to be quite demanding. The model passes all four tests on the events examined.

INTRODUCTION

Measurements on teleseismic and regional coda have been proposed for the estimation of magnitude (e.g. Bullitt and Cormier, 1984) and as a discriminant (Dainty and Harris, 1985). The nature of the coda is not well understood, however; it apparently consists of scattered waves (Aki and Chouet, 1975) but the wave types involved and whether single or multiple scattering is important are subjects of controversy (Dainty, 1985). This study is an attempt to determine the wave types present in coda and the location of the scatterers for events recorded at the NORESS regional array. To date, the work has encompassed six teleseismic events (Table 1); coda from 20 to 120 seconds after first P has been examined. The distance to these events ranges from 35° to 85° . The events consist of two presumed nuclear explosions from the Semipalatinsk test site, two deep focus earthquakes from the Japan-Bonin trench and two shallow focus (crustal) earthquakes.

Table 1

Date	OT (UTC)	Latitude	Longitude	Depth (km)	m_b	Agency	Location
1984 Nov 17	18:27:13.1	28.286°N	139.849°E	465	5.3	PDE	Bonin
1985 Feb 10	3:27:7.6	49.877°N	78.816°E	0	5.9	EDR	Semipalatinsk
1985 Mar 9	14:8:4.1	66.215°N	150.063°W	12	5.9	PDE	Alaska
1985 Apr 10	16:26:18.6	29.979°N	138.790°E	398	5.8	PDE	Honshu
1985 Apr 18	5:52:52.7	25.898°N	102.870°E	5	5.7	PDE	Yunnan
1985 Apr 25	0:57:6.5	49.907°N	78.932°E	0	5.9	PDE	Semipalatinsk

ANALYSIS AND MODEL

The principal methods of analysis are determination of coda and first P power as a function of frequency and time, standard frequency-wavenumber analysis and wavenumber spectra. A brief description of these methods is given in Dainty and Harris (1985); this discussion will

emphasise additions to their description. Power as a function of time and frequency is found by taking the power spectrum in overlapping five second windows and averaging over a one octave frequency band. Frequency-wavenumber spectra for linear wavenumber North and East are found for five second windows by standard techniques at a specified frequency, with averaging in the coda. The averaging is accomplished by determining frequency-wavenumber spectra in contiguous windows over a specified time interval, correcting for the coda decay found from analysis of coda power as a function of frequency and time, and averaging the corrected spectra. The wavenumber spectrum estimates the power in the wavefield as a function of linear wavenumber without regard to azimuth at a specified frequency f : it is equivalent to integrating a frequency-wavenumber spectrum around a circle centered on the wavenumber origin (Dainty and Harris, 1985). Averaging in the coda is accomplished by the same technique used for frequency-wavenumber spectra. Since the linear wavenumber $k = f/c$, where c is the phase velocity, the wavenumber spectrum has the potential of identifying components of the wavefield by their phase velocity.

The results of these analyses have been compared with a model of teleseismic P coda. In this model the coda consists of two dominant components due respectively to scattering of Lg to teleseismic P near the source and scattering of teleseismic P to Lg near the receiver. If single scattering is assumed, the coda decays exponentially (Dainty and Harris, 1985). The decay may be characterised by a Q , and the ratio of the coda power to the energy in first P is proportional to the side scattering turbidity (side scattering cross-section per unit volume) in the source and receiver regions. This implies that the power ratio will depend on the source type and depth: deep focus earthquakes will have a small ratio (weak coda) due to lack of scattering near the source, whereas crustal earthquakes will have strong coda due to the high level of Lg available for scattering near the source. Explosions will have a contribution from the source region, but not as strong as crustal earthquakes.

Frequency-wavenumber analysis and wavenumber spectra should allow a quantitative identification of the two components of the coda. For explosions and crustal earthquakes frequency-wavenumber spectra of the coda should show a peak at the same phase velocity

and azimuth as first P, representing energy scattered near the source and travelling to the receiver as P. Energy scattered near the receiver should have random azimuth and hence might not be evident on frequency-wavenumber analysis, but wavenumber spectra should show a peak at high wavenumber (low phase velocity, $c \approx 3.5$ km/s) corresponding to energy travelling as Lg. Explosion and crustal earthquake wavenumber spectra should also show a peak at low wavenumber corresponding to the high phase velocity component from the source region; the relative size of the peaks will indicate the relative contribution of scattering near the source and near the receiver.

RESULTS AND DISCUSSION

The analyses discussed above were carried out on the events of Table 1 for the frequency range 0.9 - 7.2 Hz. Measurements of coda decay and coda power to first P ratio were carried out for frequencies of 0.9, 1.8, 3.6 and 7.2 Hz, provided signal to noise ratio was adequate, for the Bonin, Semipalatinsk (Feb 10), Alaska and Yunnan events. Q increased with frequency, ranging from 160 at 0.9 Hz for Yunnan to 2200 at 7.2 Hz for Bonin. If the decay results are cast in terms of the apparent total turbidity (Dainty, 1985), this quantity is approximately independent of frequency and has an average value of 0.005 km^{-1} (mean free path of ≈ 200 km). The Yunnan event has an apparent total turbidity of 0.01 km^{-1} , presumably reflecting greater attenuation in the source region. The ratio of coda power to first P energy shows a stronger coda relative to first P for the two crustal earthquakes, as expected, but is rather variable, probably because of focussing-defocussing effects on first P. These results are consistent with the model, but could likely be consistent with other models too.

Results from frequency-wavenumber analysis and wavenumber spectra were more definitive. In both methods the analyses were carried out at the peak power frequency, which ranged between 1 and 2 Hz. Frequency-wavenumber analysis for the explosions and crustal earthquakes shows a strong component of the coda with phase velocity and azimuth similar to first P; the deep focus earthquakes had a component with a similar azimuth to first P, but much

slower (5 - 6 km/s) phase velocity. These results are in accord with the model. The wavenumber spectra provide even stronger evidence for the model. Figures 1-3 show such spectra for the Bonin (deep focus), Semipalatinsk (Feb 10; explosion) and Yunnan (crustal) events, for both first P and coda. There is a biasing effect towards high wavenumber (low phase velocity) due to the finite aperture (3 km) of the NORESS array, which may be assessed by examining the first P peak: true phase velocities for first P are between 12 and 16 km/s. The effect should be less for lower phase velocities. The deep focus event (Figure 1) shows a pronounced shift from high velocity (low wavenumber) energy in first P to low phase velocities typical of Lg in the coda, indicating that the coda consists of energy scattered near the receiver. The explosion (Figure 2) however retains a component of similar phase velocity to first P in the coda, of about equal amplitude to the low velocity Lg component. The crustal event (Figure 3) has a coda dominated by high phase velocity energy that must have been scattered near the source. Lg to P scattering near the source is attractive because it would explain the difference between the explosion (generates low Lg) and the crustal earthquake (generates high Lg).

REFERENCES

- Aki, K. and B. Chouet (1975). Origin of coda waves: source, attenuation, and scattering effects. *J. Geophys. Res.* 80, 3322-3342.
- Bullitt, J.T. and V.F. Cormier (1984). The relative performance of m_b and alternative measures of elastic energy and explosion yield. *Bull. Seis. Soc. Am.* 74, 1863.
- Dainty, A.M. (1985). Investigation of Q and backscattering in codas. in *The VELA Program a Twenty-Five Year Review of Basic Research*, A.U. Kerr, ed., pp 273-277, Defense Advanced Research Projects Agency, Washington, D.C.
- Dainty, A.M. and D.B. Harris (1985). Analysis of coda at NORSAR and NORESS. *7th Ann. DARPA/AFGL Seismic Res. Symp.*, 131-152.

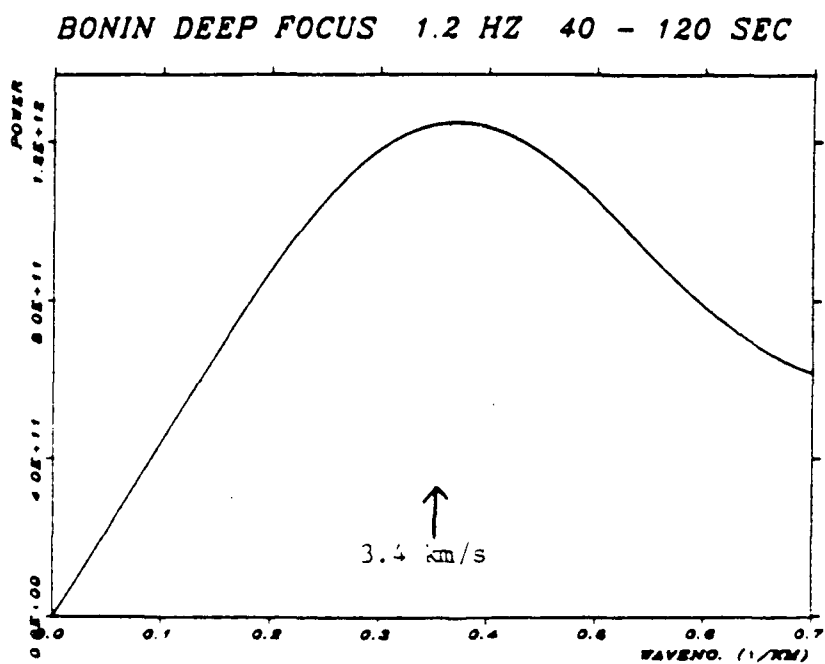
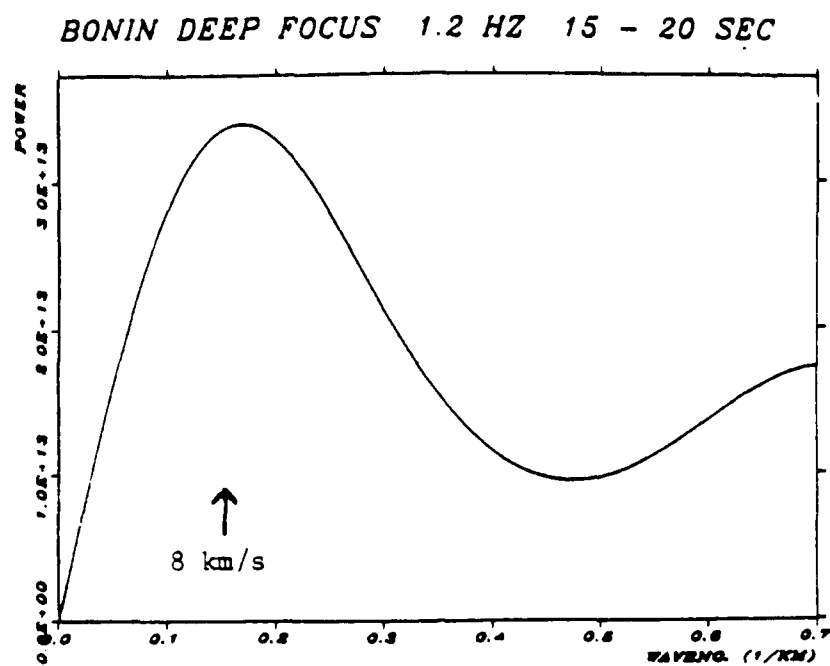


Figure 1. Wavenumber spectra for the Bonin event. First P is shown at the top with coda from 25 to 105 sec after first P at the bottom. Frequency is shown on the Figure; selected phase velocities are indicated.

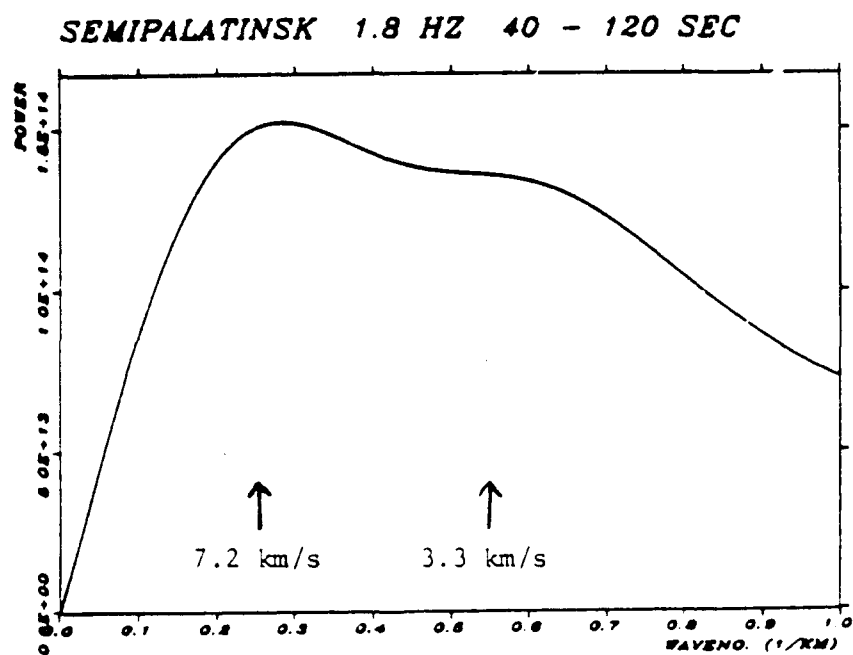
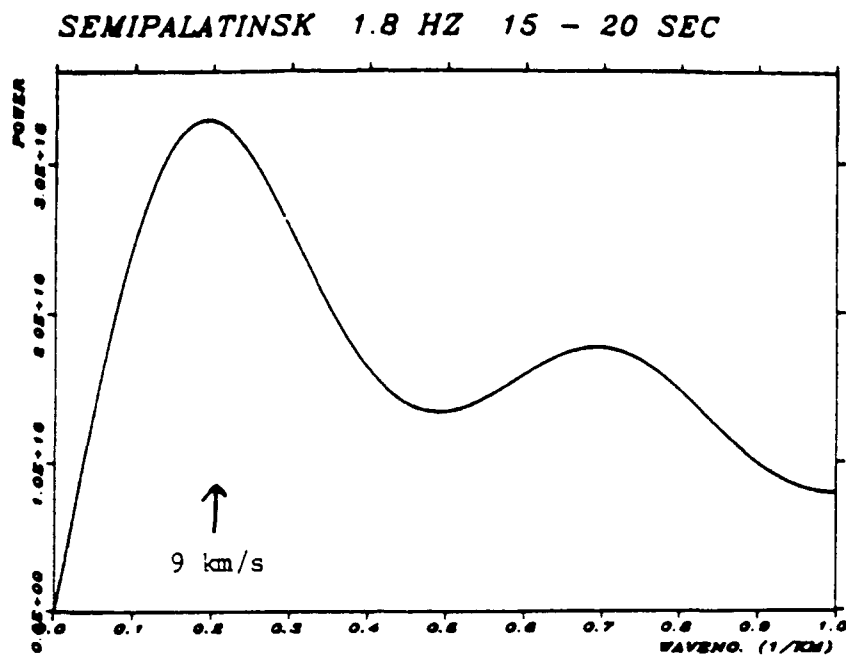


Figure 2. As for Figure 1, but for Semipalatinsk event of Feb 10.

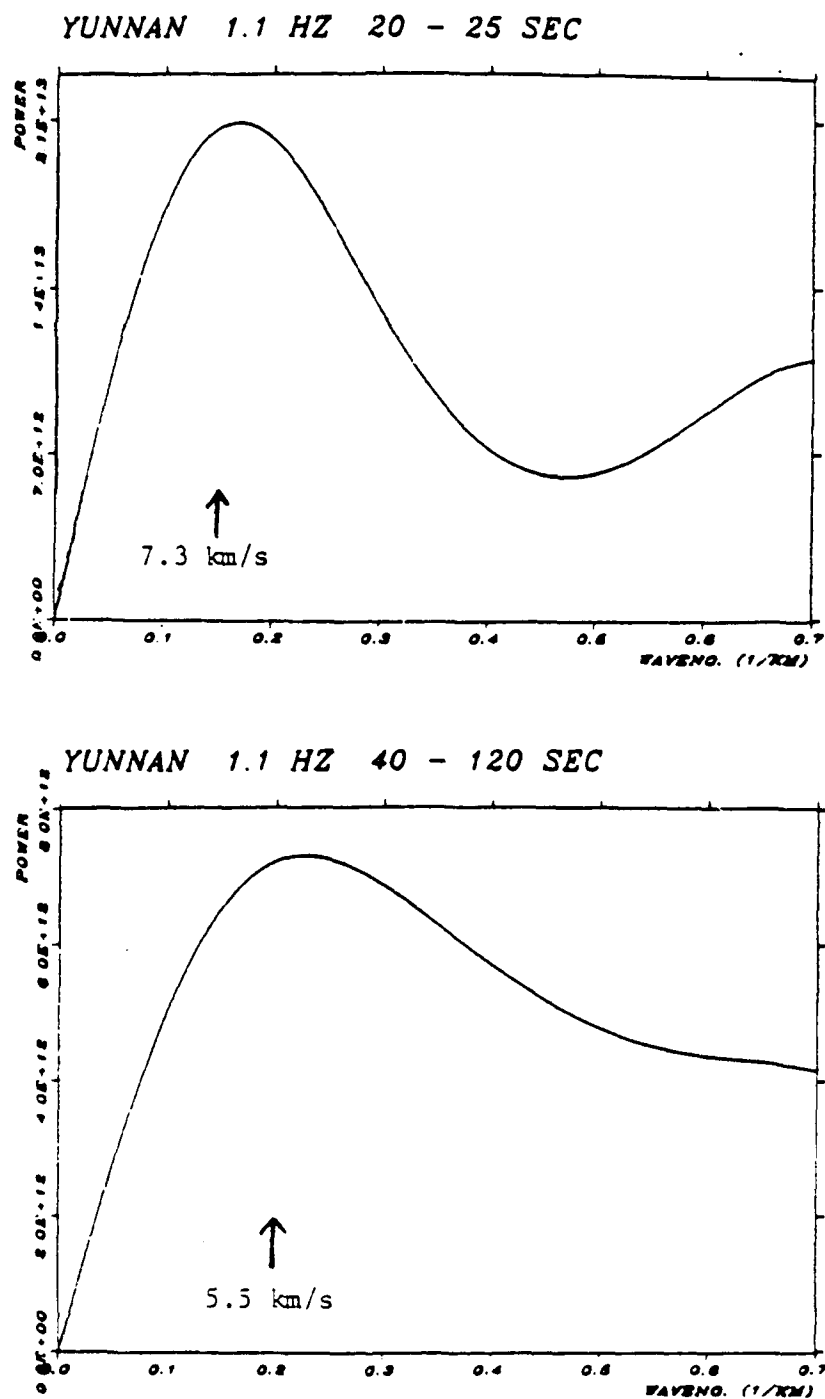


Figure 3. As for Figure 1, but for Yunnan event. Coda wavenumber spectrum is for 20 to 100 sec after first P.

PROPAGATION CHARACTERISTICS OF REGIONAL PHASES
AND NORESS REAL TIME PROCESSING PERFORMANCE

S. Mykkeltveit and T. Kværna
NTNF/NORSAR, Post box 51, N-2007 Kjeller, Norway

The performance of the RONAPP real time processing package (Mykkeltveit and Bungum, 1984) for regional events recorded on the NORESS array is currently being evaluated. Detailed knowledge of propagation path effects must be obtained for the purpose of calibrating the real time processor. This contribution gives i) the results from a general mapping study aimed at obtaining such calibration data and ii) the results from an investigation of RONAPP performance for events in Western Norway and the North Sea.

PROPAGATION CHARACTERISTICS OF REGIONAL PHASES RECORDED AT NORSAR

Previous investigations (Kennett and Mykkeltveit, 1984; Kennett et al, 1985) limited to specific regions have shown that prominent geological features exist within regional distance from NORESS that strongly influence the characteristics of secondary phases. We have recently completed a study utilizing data from the NORSAR data archive, corresponding to regional events at all azimuths. For the 170 events in this data base, the seismograms were band-pass filtered in three different frequency bands, centered on 1.0, 2.0 and 4.0 Hz. For each of these bands, arrivals corresponding to distinct phase onsets were picked by an STA/LTA detector. In this manner, our off-line analysis ties in with the on-line processing of NORESS data with respect to detection of the regional phases.

The primary aim of the analysis was to characterize the relative strength of the Sn and Lg phases. The case of dominant Lg (over Sn) was subdivided into three different codes as follows:

- (1) Only Lg can be seen in the S wavetrain.
- (2) Lg is the dominating phase, but Sn can be discerned.
- (3) Lg is still the dominating phase, but Sn is not very much smaller.

An equivalent subdivision, also on a three-point scale, was adopted for the case of dominant Sn. Finally, a code was assigned to the case of comparable Lg and Sn amplitudes.

Fig. 1 shows the results derived from analysis of the data in our data base. In this figure, we assign the character of the S wavetrain as observed in the NORSAR seismometer record to the source area. We have confined ourselves to the use of three codes only in this figure, but color-coded maps including all 7 codes defined above have also been prepared. These maps offer more details and often show gradual transitions from dominating Lg to dominating Sn in certain directions. Inspection of Fig. 1 and a tectonic map of the same area leads to the following conclusions:

- Lg wave propagation is very efficient for propagation paths that are confined to continental shield type structures (dominant to the east of NORSAR) not intersected by major tectonic units. In these directions, 1 Hz Lg waves propagate to 20° from the source, while at 4 Hz Lg is seen out to about 10° from NORSAR.
- No Lg is observed, or Sn dominates over Lg for propagation paths that cross significant tectonic features like graben structures (in the North Sea) and continental margins.
- Particularly at 4 Hz there is a close connection between some of the finer tectonic details and the propagation characteristics. Since Lg is a phase mostly composed of waves trapped in the crust, this phase is likely to be highly susceptible to changes in the crustal structure.

RONAPP PERFORMANCE FOR EVENTS IN WESTERN NORWAY AND THE NORTH SEA

For an evaluation of RONAPP we would like to find a region with events that have been reliably located by another agency, based on a local network. One such region within regional range from NORESS is Western Norway with the adjacent North Sea. During the period April-September 1985 a total of 230

events in this region were reported by the University of Bergen. These events are typically earthquakes offshore and explosions onshore. The magnitudes are in the range M_L 1.5-3.5, and the epicentral distances relative to NORESS range from 200 to nearly 700 km.

The seismograms from these events are rich in regional phases, and quite frequently Pn, Pg, Sn and Lg are clearly seen in the records. An example is shown in Fig. 2. As can be seen from Fig. 1, Lg is dominant for onshore locations in Western Norway, whereas the importance of Sn increases with increasing frequency for offshore locations. For higher frequencies than those in Fig. 1, the importance of Sn increases further. Data from a high-frequency system (125 Hz sampling rate) recently installed within NORESS shows considerable Sn energy in the band 30-50 Hz from an earthquake (PDE mb 5.0) in this region at a distance of 417 km from NORESS (see Ringdal, this volume).

The real time location by RONAPP of a regional event results from consecutive detections of P- and S-type arrivals with a common azimuth. The range is estimated from the travel-time difference between the first P phase (assumed to be Pn) and the strongest phase in the S wavetrain, which is assumed to be Lg, propagating at a constant group velocity of 3.5 km/s. Fig. 3 shows the differences between P and Lg azimuths for the class of events that was also automatically located by RONAPP, based on the detection of both a P- and S-type arrival. The median of the absolute values of these differences is 5 degrees. This is an estimate then of the consistency that should be expected among the azimuths automatically determined for the various phases. Fig. 4 shows the differences between the ranges estimated by the NORESS online processing and the ones corresponding to the network solutions. As can be seen from this figure, there is a tendency by the NORESS event location procedure to underestimate the range for events in this region. The general tendency of underestimation of range can be explained by i) the fact that the travel-time model used in RONAPP is based on a 40 km thick crust, whereas the crust is typically 30 km thick in Western Norway and ii) that for approximately 30 events we found reason to believe that the Pn phase had gone undetected, and the P phase detected is

most likely to be Pg. Fig. 4 shows that there are approximately 20 events for which the range difference exceeds 40 km. By inspecting the relevant plots, it was found that the cases with large underestimation of the range are related to mistaking Sn for Lg. With proper phase assignments, the ranges for these 9 events are correctly determined. The main reason for overestimating the range is that the strongest detection in the S wavetrain is in the Lg coda.

Fig. 5 shows deviations from expected arrival times (based on the network locations) for all detections by RONAPP that can be associated with the 230 events (the criterion is that the azimuth estimated for the detected phase must be within 30° of the azimuth from the network location). These detections are classified as P detections if the estimated phase velocity exceeds 6 km/s, and as either Sn or Lg (depending on arrival time relative to expected arrival times for Sn and Lg) if the phase velocity is below this value. As is indicated by this figure, the class of P detections is made up of slightly early Pn detections (can be corrected by travel time model modifications) and Pg arrivals typically 4 or 5 seconds after Pn. The Lg onset detections are typically early by about 3 seconds, and there is a fair amount of Lg coda detections. These results suggest that the group velocity of 3.50 km/s used by RONAPP for the Lg onset in the range estimation should be changed to approximately 3.60 km/s for this region.

REFERENCES

- Kennett, B.L.N. and S. Mykkeltveit (1984): Guided wave propagation in laterally varying media: II - Lg waves in northwestern Europe, *Geophys. J.R. astr. Soc.*, 79, 257-267.
- Kennett, B.L.N., S. Gregersen, S. Mykkeltveit and R. Newmark (1985): Mapping of crustal heterogeneity in the North Sea Basin via the propagation of Lg waves, *Geophys. J.R. astr. Soc.*, 83, 299-306.
- Mykkeltveit, S. and H. Bungum (1984): Processing of regional seismic events using data from small-aperture arrays. *Bull. Sesim. Soc. Am.*, 74, 2313-2333.

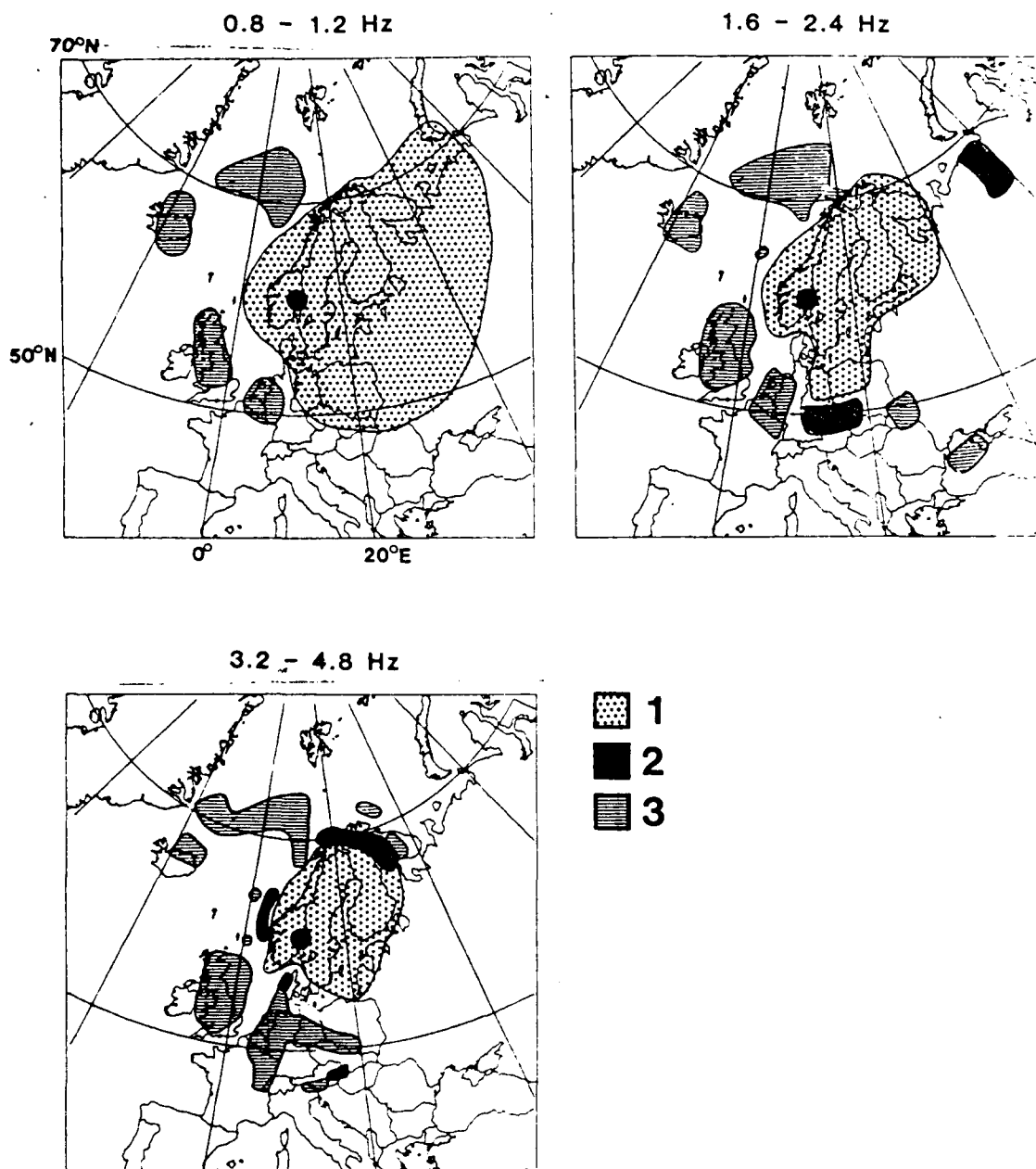


Fig. 1 Characterization of Lg versus Sn propagation efficiency for the three different filter bands. The shading codes are as follows: (1) Lg dominant phase in the S wavetrain; (2) Lg and Sn comparable and (3) Sn dominant. Note that the codes are assigned to the source area, and all characterizations are related to seismograms as they appear on NORSEAR (filled circle) seismometers.

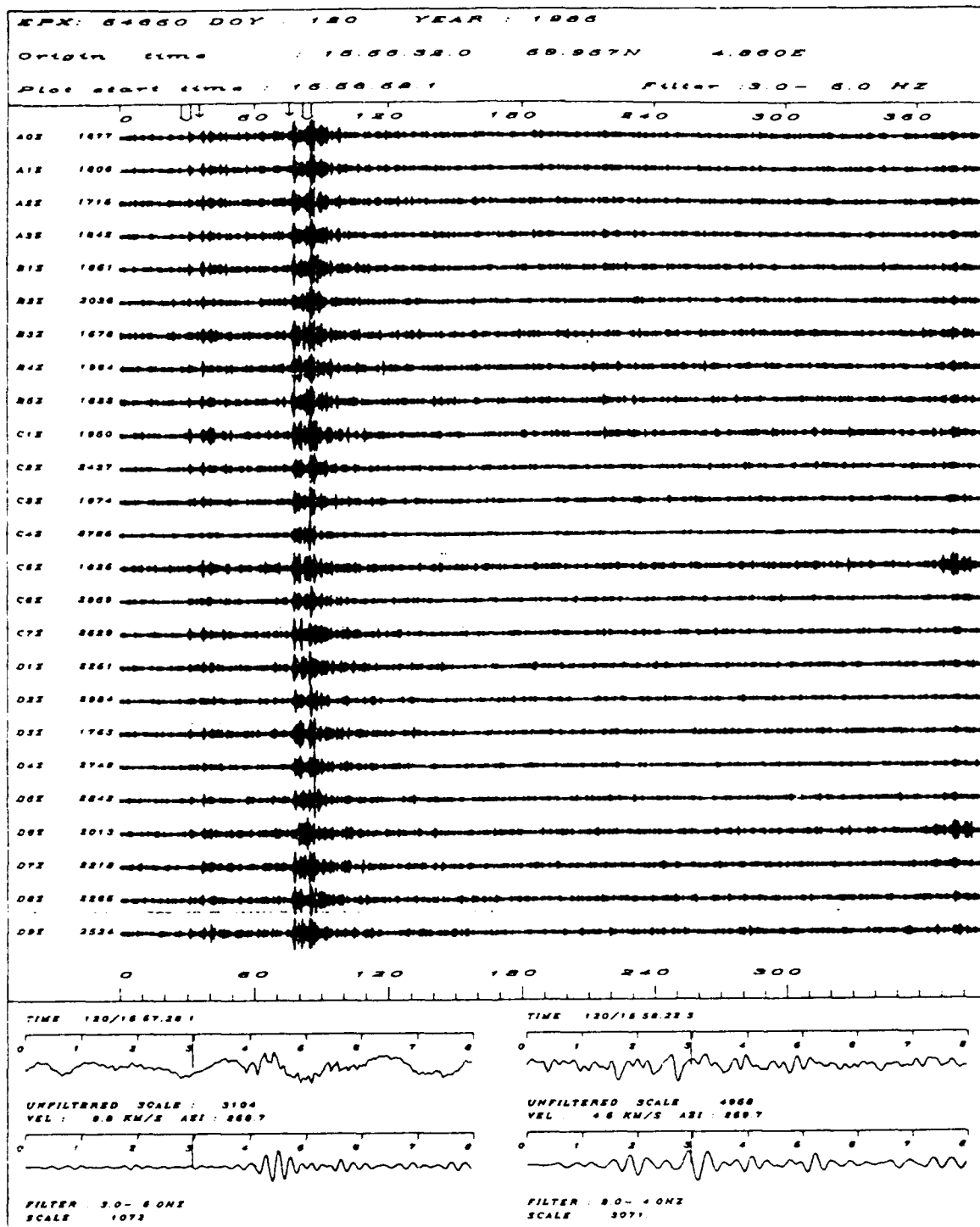


Fig. 2 Individual NORESS traces for one of the events (M_L 2.1, distance 350 km) reported by the University of Bergen. The panel covers 6½ minutes of bandpass filtered records (3-5 Hz). The four arrows on top of the records indicate detections by the RONAPP real time processing package. The broad arrows correspond to Pn and Lg arrivals, which have been combined to locate the event at the geographical position given on top of the figure. The two additional detections correspond to Pg and Sn arrivals. P and Lg beams are shown in the bottom part of the figure.

NORESS EVALUATION
NORESS P-LG AZIMUTH DIFFERENCES
DATA BASE 230 WESTERN NORWAY EVENTS

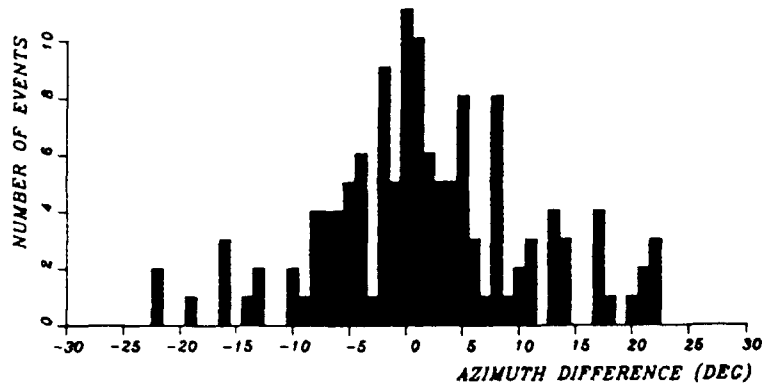


Fig. 3 The histogram shows the differences between the azimuths automatically estimated for the P and Lg phases by the routine, real time processing of NORESS data, for the events reported by the University of Bergen.

NORESS EVALUATION
RANGE DIFFERENCES (NORESS MINUS NETWORK)
DATA BASE 230 WESTERN NORWAY EVENTS

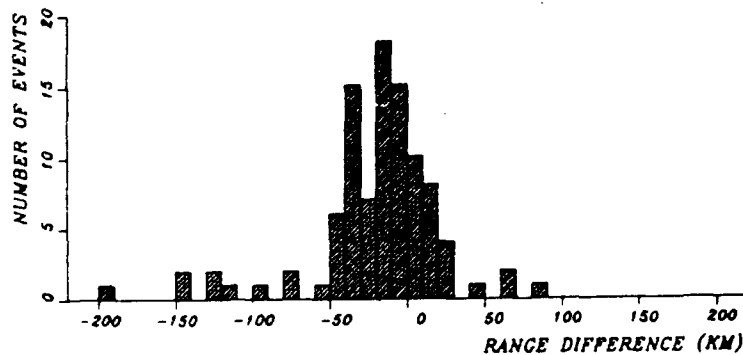
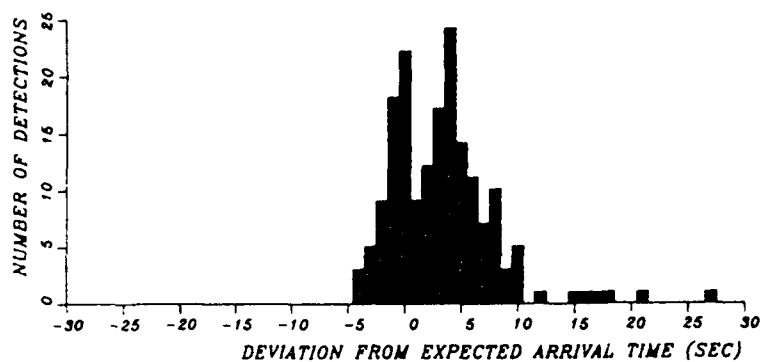
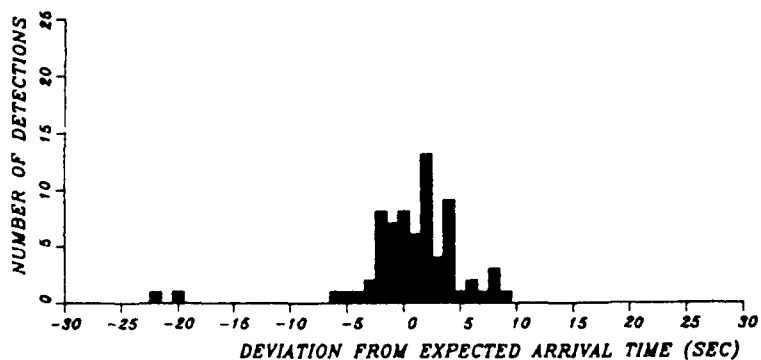


Fig. 4 The histogram shows the differences between the ranges estimated by the NORESS online processing and the ones corresponding to the network solutions. 35 events with known location at an explosion site at range 290 km, for which this difference was between -10 and -20 km, are not included in the figure.

NORESS P DETECTIONS
DATA BASE 230 WESTERN NORWAY EVENTS



NORESS SN DETECTIONS
DATA BASE 230 WESTERN NORWAY EVENTS



NORESS LG DETECTIONS
DATA BASE 230 WESTERN NORWAY EVENTS

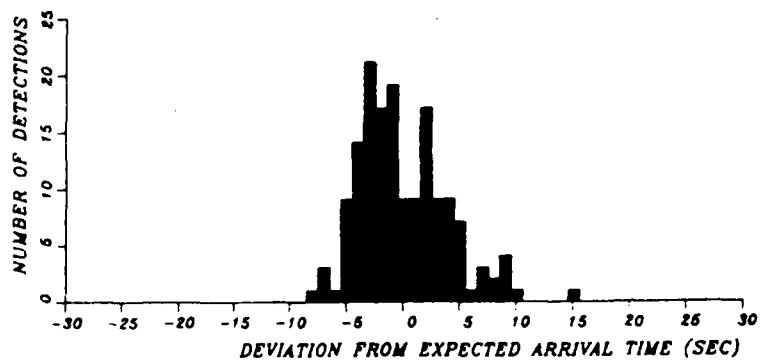


Fig. 5 Deviations from expected arrival times for P (top), Sn (middle) and Lg (bottom) for NORESS detections corresponding to the 230 Western Norway events.

WAVEFIELD DECOMPOSITION USING ML-PROBABILITIES
IN MODELLING SINGLE-SITE 3-COMPONENT RECORDS: PRACTICAL APPLICATIONS
ON LOCATIONS OF EVENTS AND SCATTERING

E.S. Husebye¹⁾, A. Christoffersson²⁾, S.F. Ingate³⁾ and B.O. Ruud¹⁾

1) NTN/NORSAR, Kjeller, Norway; 2) Univ. of Uppsala, Sweden;

3) MIT, ERL, Cambridge, USA

Abstract. In this paper a novel approach to 3-component seismogram analysis is presented. The P, S, Love and Rayleigh model representations are similar to those used previously, but we use a Maximum Likelihood (ML) estimator and rather than, e.g., Principal Component (PC) estimator. The reason is that the ML-approach permits a model test in terms of χ^2 -probabilities on whether a specific phase or wavelet type is present in the records as a function of time and azimuth. In addition, apparent angle of incidence or apparent velocity is estimated jointly with probability. For a single 3-component time-domain seismogram, the covariance matrix provides only 6 independent observations, thus restricting analysis to rather simple wave models. Exploiting wavefield structure in this manner appears very beneficial for seismogram analysis; practical applications hereof will be given in terms of epicenter determinations at any distance, locations of scattering sources and noise directionality.

1. INTRODUCTION

Polarization properties of scalar and vector fields have been topics of extensive research in areas ranging from electromagnetics (optics and radio transmission) to physical oceanography, seismology and not at least seismic prospecting including VSP-profiling. Seismologists have for many years attempted to exploit the information potential of three-component records for wave propagation modelling, retrieval of structural information and source parameters. Such efforts appear to have been frustrated, primarily due to the technique of analysis employed - in other words, a certain failure to produce results in a useful manner, at least for frequencies above 0.2 Hz. Therefore, 3-component seismogram analysis techniques have

not become a viable alternative to those often used for arrays of vertical-component seismometers such as frequency-wavenumber (f-k) analysis. A disadvantage of arrays is that only amplitude and timing information is utilized, excluding wavefield polarization properties. Our novel technique for extracting wavefield structure is given in section 2, and then associated practical analysis results follow.

2. THEORY

The method for analysis of 3-component data is based on the following model:

$$y(t) = \Lambda z(t) + \epsilon(t) \quad (1)$$

where $y(t) = [y_1(t), y_2(t), y_3(t)]^*$ is a vector containing the observed 3-component recordings at time t , and $*$ denotes vector transpose. Similarly, $z(t)$ is a k -dimensional representation of the signal at time t ; $k = 1$ in cases of P, SV and SH motion and the Λ is a matrix of unknown constants:

$$\Lambda = \begin{Bmatrix} \lambda_{11} & \dots & \lambda_{1k} \\ \lambda_{21} & \dots & \lambda_{2k} \\ \lambda_{31} & \dots & \lambda_{3k} \end{Bmatrix}$$

relating the signal to the observed data. $\epsilon(t)$ is the residual noise vector. Four basic assumptions are made: (i) $z(t)$ and $\epsilon(t)$ are uncorrelated; (ii) $\epsilon(t)$ has zero expectation, i.e., $E(\epsilon(t)) = 0$; (iii) the components of $z(t)$ are linearly independent, i.e., the signal is k -dimensional, with no interference between P, SV and SH; and (iv) All moments up to at least second order exist. These basic assumptions imply that the zero-lag second order moments of $y(t)$ can be written as

$$\Sigma(t) = \Lambda \Phi(t) \Lambda^* + \psi(t) \quad (2)$$

where $\Sigma(t) = E(y(t)y(t)^*)$; $\Phi(t) = E(z(t)z(t)^*)$; and $\psi(t) = E(\epsilon(t)\epsilon(t)^*)$.

Averaging eq. (2) over a time widow $T_1 < t < T_2$ yields the following structure:

$$\Sigma = \Lambda \Phi \Lambda^* + \psi \quad (3)$$

$$\text{where } \Sigma = \int_{T_1}^{T_2} \Sigma(t) dt ; \quad \Phi = \int_{T_1}^{T_2} \Phi(t) dt ; \quad \psi = \int_{T_1}^{T_2} \psi(t) dt$$

is the expected 3x3 symmetric covariance matrix of the recordings, the signal and noise covariance matrices, respectively. The structure of the Λ and Φ matrices depends on the particle motion of the incoming wave being P, SV, SH, L (Love) or R (Rayleigh). Further details on the modelling are given by Christoffersson et al, 1986 (submitted JGRAS).

2.1 Estimation

The unknown parameters in equation (3) can be estimated on the basis of the observed second-order zero-lag moments over a time window

$$S = \frac{1}{T_2 - T_1 + 1} \cdot \sum_{t=T_1}^{T_2} y(t) y(t)^* \quad (4)$$

There are several possible estimators that could be used. Most are based on some fitting-function, i.e., minimizing some weighted function F of the difference between observed S and the theoretical Σ . Our preference so far is for the Maximum Likelihood (ML) estimator, which is based on Gaussian assumptions and minimizes

$$F = \log |\Sigma| - \text{tr}(\Sigma^{-1} S) - \log |S| - q \quad (5)$$

where q is the dimension in the data ($q = 3$ for 3-component data), and $\text{tr} =$ trace of the matrix. The ML-estimator is preferred mainly because it is possible to test the validity of the models under the Gaussian assumptions

and white noise. Let F denote the minimum in equation (5). From the general properties of ML-estimators it follows that $(N-1)F$ is asymptotically distributed as chi-square (χ^2) with degrees of freedom equal to 6 minus the unknown parameters and $N = (T_2 - T_1 + 1)$.

2.2 Signal information extracted

The essential information extracted for a given time window is the χ^2 -probabilities of P, SV, SH, L or R-wave presence in the 3-component records as a function of time and azimuth as illustrated for P in Fig. 1. In plots like this, the probability measure may be replaced by the apparent velocity (only P and SV) because the Λ matrices contain powers for the dimensions spanned by the signal. The χ^2 -tests are mutually exclusive; e.g., P and SV cannot be triggered simultaneously. Finally, the estimated probabilities, that is, the max. value for each time step, can be used as a simple weight function.

2.3 Discussion

Our approach to wavefield decomposition or 3-component record analysis is in several respects similar to those of other investigators. e.g., see Christoffersson et al (1986) for references. A real problem here is whether further refinements of 3-component record analysis are feasible. This would entail use of more complex particle motion models requiring more observational degrees of freedom, which is equivalent to processing of 3-component array data. Our remark here is that for the time being we favor extensive analysis of observational data rather than attempting further methodological refinements.

3. PART 2 - PRACTICAL APPLICATIONS

In the subsequent sections we demonstrate practical applications of our 3-component analyzing technique, that is, wavefield decomposition results for event and scattering source locations, and noise directionality studies.

3.1 Event locations using broad-band records

The conventional approach to event location is that of using P arrival times from networks of stations. For arrays and single-site 3-component stations bearing (azimuth) and epicentral distances estimates are needed for event locations. This entails that relatively more information is extracted from the records as schematically illustrated in Fig. 1. The outcome of an experiment of event locations using the NORESS broad-band recordings of 6 large earthquakes in the distance range 40-155° are illustrated in Table 1 (e.g., for details see Husebye et al, 1986 - submitted BSSA).

3.2 Event locations at local and regional distances

In such cases, data analysis is tied to short period recordings, say 2-12 Hz, determining epicenter locations is with azimuth from estimated probabilities in the time/azimuth plane and distance derived from differential travel times of phases like Pg, Pn, Sg, Sn, Lg, etc. An instructive example of 3-component analysis of local events is given in Fig. 2. For comparison, semblance analysis of the corresponding NORESS array recordings per se is also given. With extensive practical experience we consider it feasible to locate events using single-site 3-component records within at least 50 km of "true" epicenter locations (e.g., for details see Ruud et al, 1986, manuscript in preparation).

3.3 Event locations at teleseismic distances - short period records

In such cases the distance estimate has to be derived from apparent velocities alone, and thus large errors of 10-15 deg may ensue. However, practical experience say in terms of probability/velocity distributions of past events in the same general area combined with seismicity knowledge may ensure reasonable event locations in such cases as well - say within 5-10 deg.

3.4 Location of scattering sources

It is well established that significant parts of P- and S-wave codas represent scattering contributions from secondary sources in the lithosphere both at the source and receiver ends. Although theoretical treatments consider such contributions to be randomized, more prominent ones would "behave as deterministic", that is, being repeatable. Since the 3-component analysis "identifies" secondary wavelets, those with Pg-velocities (receiver end) have been located for a suite of 15 teleseismic events. The essence of these results was that dominant scatterers were found in NE quadrant and at distances of 100-300 km. An intriguing observation is that transverse (SH) motions are occasionally found in the middle of the P-wave train, entailing a depth to an anomalous body beneath NORESS at 15-20 km, but never seen on all the four 3-component stations at A0, C2, C4 and C7 for one event.

3.5 Noise directionality

Practical 3-component analysis often resulted in "triggering" prior to P-wave onset. This phenomenon can be associated with hydroelectric power station operation at Hunderfossen ($\Delta \sim 73$ km, $az \sim 310$ deg), and Braskereidfoss to the east ($\Delta \sim 14$ km, $az \sim 105$ deg). The former is characterized by Pg and Sg phases while the latter with Rg phases ($vel \sim 2.7$ km s⁻¹) as illustrated in Fig. 3. Noise directionality is occasionally observed for strong surf on the coast, being of the Sg/Lg type and most prominent in the 1-3 Hz frequency band (e.g., see Ingate et al, BSSA, 1985).

4. FINAL REMARKS - CONCLUSION

The high-quality records from NORESS testify towards the source and propagation complexities of high-frequency seismic waves. The key to a proper understanding and analysis of such phenomena is that of parameterizing to the largest possible extent the information in the event records. In this respect, extracting polarization characteristics of the wavefield is highly significant as demonstrated here.

Event	Origin Time h m s	Lat. (deg)	Long. (deg)	H (km)	m_b /err. (deg)	Dist. (deg)	Azi (deg)	Vel. (km/s)	Region
6/6-85 (1)	02.40.12.8 (02.40.05)	0.95N (0.20N)	28.43W (28.70W)	10 (33)	6.3 (0.80)	67.10 (67.90)	224.21 (224.20)	17.4 (16.8)	Central Mid-Atlantic Ridge
29/7-85 (2)	07.54.44.3 (07.54.42)	36.19N (37.54N)	70.89E (71.54E)	101 (33)	6.7 (1.45)	42.10 (43.50)	93.30 (94.0)	13.60 (11.60)	Hindu Kush Region
23/8-85 (3)	12.41.59.7 (12.42.02)	39.42N (39.31N)	75.27E (75.39E)	33 (33)	6.4 (0.14)	43.9 (44.0)	89.0 (89.0)	13.80 (11.50)	Southern Xinjiang, China
21/9-85 (4)	01.37.13.8 (01.37.15)	17.82N (16.94N)	101.67W (102.61W)	33 (33)	6.3 (1.26)	85.21 (86.40)	298.59 (299.0)	22.4 (19.30)	Near coast of Guerrero, Mexico
5/10-85 (5)	15.24.02.2 (15.23.57)	62.26N (61.29N)	124.31W (124.94W)	10 (33)	6.5 (1.01)	52.49 (53.50)	335.88 (335.10)	15.0 (13.5)	Northwest Territories, Canada
7/11-85 (6)	19.12.29.8 (19.12.08)	35.20S (35.18S)	179.36W (178.16W)	33 (33)	6.2 (0.98)	153.5 (153.7)	20.3 (18.1)	32.0 (55.1)	East of North Island, New Zealand

TABLE 1. Focal parameters, taken from the PDE listings of USGS, for the events used in analysis. Parameters in parentheses are those estimated from the single-site 3-comp. broadband recordings (NORESS). The distance differences between the two sets of event location estimates are listed in the m_b column.

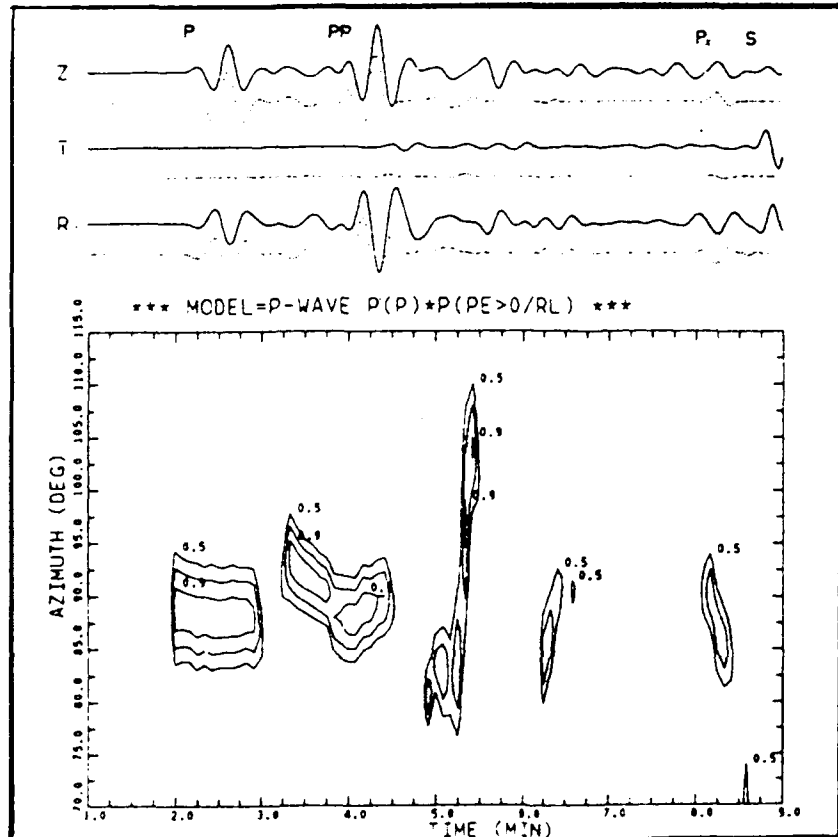


FIG. 1. 3-component analysis of a Hindu Kush earthquake (Event 2 in Table 1). Probabilities are plotted as a function of time (min) and azimuth (deg). Window length is 20 sec, time and azimuth increments are 5 sec and 1 deg, respectively. Original but rotated broadband traces are displayed at top; the stippled ones are probability filtered. From the figure and results in the table, we have that azimuth and distance (differential P, PP, S times) resolutions are very good for low-frequency body waves.

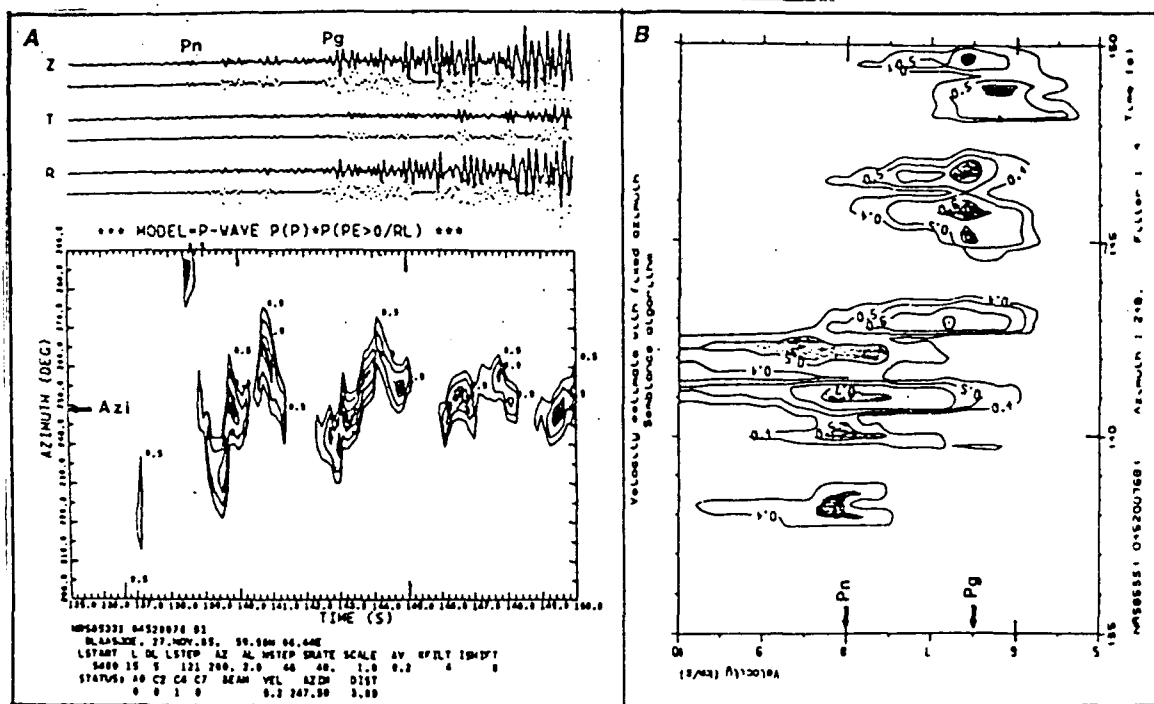


FIG. 2. (a) 3-component probability plot for local explosion ($\Delta \sim 3$ deg) for site C4; (b) semblance analysis using whole NORESS with azimuth fixed at 248 deg, same time interval. Note similarity in results, i.e., identification of major Pn and Pg wavelets.

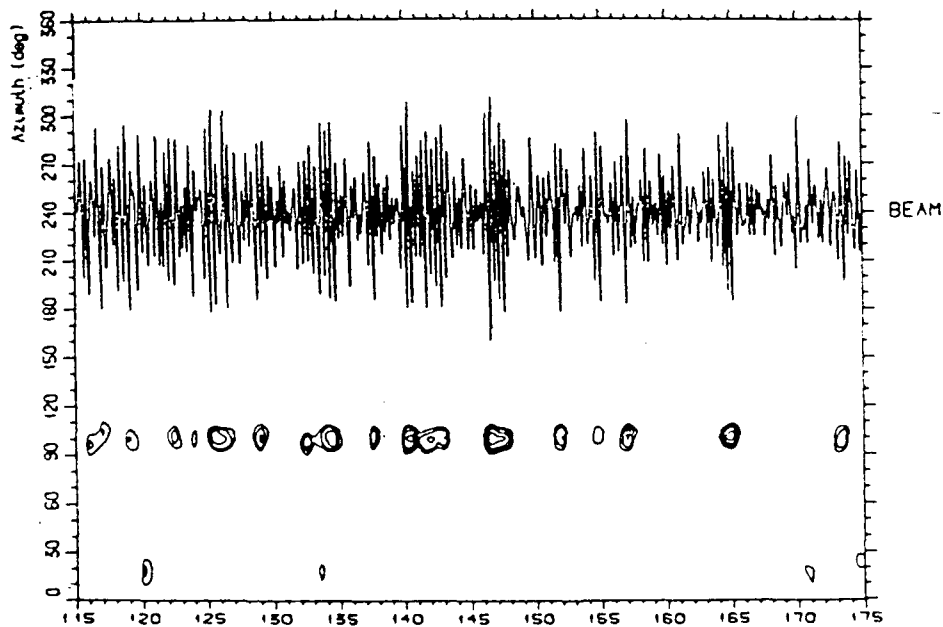


FIG. 3. Noise directionality as illustrated for presumed vibrations at Braskereidfoss power station at 06.47, 27 May 1985 (spring flooding in river Glomma?). Semblance analyzed used with $vel = 2.7 \text{ kms}^{-1}$; triggering occurred only at $az \sim 100$ deg. The associated beam wavelets are also displayed. Such effects are also manifested in the NORESS detection log, and naturally generate Pg-triggering in 3-component analysis.

OBSERVATIONAL AND THEORETICAL STUDIES OF REGIONAL WAVE PROPAGATION

C.A. Langston, A. Lakhtakia, V.K. Varadan, and V.V. Varadan
Department of Geosciences
Department of Engineering Mechanics
The Pennsylvania State University
University Park, Pennsylvania 16802

Introduction

The research program discussed here is concerned with several short-period wave propagation topics which have direct bearing on explosion discrimination and location. To repeat an obvious but important point, determination of source parameters is controlled by the knowledge one has of the wave propagation. There is a complete trade-off between source and structure effects so one has to be known to estimate the other. In our current research program, we have been developing and using methods to treat wave propagation at regional distances in a variety of elastic earth models.

Analysis of Small Events

Source depth is a very important parameter for the discrimination problem since it is unlikely, for practical reasons, that explosion sources will ever be buried at depths greater than a kilometer or so. Clear evidence of greater source depth in a seismic signal nearly guarantees that the source is an earthquake. We have undertaken an analysis of data from a series of aftershocks from the 1968 Meckering earthquake of Western Australia to try to determine obvious diagnostic depth phases in the short-period data. These events are being used for several reasons. Although the main event is interesting in its own right, crustal structure between the source area and the WWSSN station MUN where the aftershocks were recorded is well known and relatively homogeneous. The area lies at the edge of the Yilgarn block which is part of the Australian Shield. Topography is gentle and the crustal section is characterized by high velocity crystalline rocks with virtually no sedimentary section. The area has been traversed by several refraction and reflection surveys so that crustal wave velocities are well known (Mathur, 1974). Thus, this knowledge of the crustal structure can be used in an attempt to understand the nature of the short-period seismogram at near-regional distances through the computation of synthetic seismograms.

Figure 1 displays synthetic seismograms of the vertical component of motion at distances of 60 to 100 km for a shallow dipping thrust fault. Mundaring station was about 80 to 90 km from the aftershock zone. The choice of mechanism is based on the focal mechanism of the main M6.8 earthquake but is not important for the purposes of this discussion. The Meckering earthquake was caused by rupture along a shallow dipping thrust fault (Vogfjord and Langston, 1986) which ruptured the surface but

was less than 6 km deep at its deepest extent. Thus, it is likely that aftershocks were within 10 km of the surface.

The synthetic seismograms were computed using a wavenumber integration technique (Barker, 1984) which yields the entire seismogram. The earth model, derived from reflection and refraction profiles, is displayed in Table 1. The synthetic seismograms show that the character of the short-period waveform changes dramatically with source depth (Figure 1). At 2 km depth, the waveforms are simple showing what would be interpreted as "P" and "S" wave arrivals. The "P" arrival actually consists of a number of crustal reflections, the direct wave, and the Sp wave which travels horizontally under the free surface. The "S" wave is composed primarily of the fundamental mode Rayleigh wave which is efficiently excited for this shallow depth source. This phase should more correctly be called the Rg phase. Synthetic seismograms for a source at 10 km depth show that the fundamental mode Rayleigh is not well excited but is included as a minor arrival in the S wavetrain. More importantly, notice the appearance of a relatively large secondary arrival after the direct P. This is the Sp wave which travels along the free surface. The increase in source depth over the 2 km case has caused this phase to move back in time relative the direct wave. Thus, this phase can be used to directly estimate source depth by measuring its arrival time relative to the first arrival.

Data from Meckering aftershocks are available from the Mundaring WWSSN station. Two such events are shown in Figure 2. Notice that event A shows a very simple waveform with a distinctive Rg phase arriving after the S wave. This implies a very shallow source depth according the synthetic seismogram calculation. The P wave of event B shows two distinct phases early in the seismogram which suggests the P and Sp phases. This event is interpreted to be deeper than event A.

The study mentioned here is in an early stage of development. Other questions which must be addressed are the influence of source mechanism on the relative amplitudes of phases in the short-period record, the effects of perturbations in the velocity model, and effect of anelastic attenuation. It is probably not possible to retrieve standard source parameters such as the focal mechanism from such a limited data set without extremely good control on crustal structure. However, the mere existence of an easily observable secondary phase may be as good a depth estimator as pP is in teleseismic short-period data. If phases of this type can be extracted from the data, then this technique would offer an attractive and simple discriminator of explosions from earthquakes.

In related work we are computing synthetic seismograms for regional phases at larger distances. In particular, we are interested in the structure effect on relative phase amplitudes which will affect yield estimates. Figure 3 shows vertical component seismograms recorded at Urumqi, PRC for 5 large Semipalatinsk explosions. Epicentral distance is 950 km and the seismograms show relatively large P phases compared to Pg. These data were obtained from the PRC and were recorded by the broad-band Soviet Kirnos instrument. Hence the spectacular sweep in frequency seen in the data from 1 hz P waves to 30 second

Rayleigh waves. The large P wave suggests that structure in the upper-most mantle along this path is similar to structure in the Eastern United States where velocity increases with depth producing high amplitude turning rays (Langston, 1982). The relative excitation of these regional phases are being explored for Asian structures.

Theoretical Scattering Problems

A part of our work is concerned with obtaining accurate solutions to difficult wave scattering problems. Using the "T-matrix" or extended boundary condition method of Waterman(1975) and Varadan and Varadan(1980) we have solved the problem of SH and P-SV line sources located in a waveguide with a corrugated free surface. The particular problem attacked in this initial effort was posed to examine Lg and Pg scattering due to topography on and in the crustal waveguide. Model parameters were chosen to represent typical average crustal velocities and topography seen in the Basin and Range province of Western U.S. We are currently examining these newly obtained solutions to look at the effect of topographic scattering on wavetrain durations and effective attenuation. Although 2D solutions, these results are useful in examining the physics of scattering and will be incorporated in analysis of Pg and Lg data from explosions and earthquakes in the Western U.S.

The T-matrix method is an exact method insofar as there are no theoretical approximations made in the solutions. Its extension to simple 3 dimensional structure is straightforward since it makes use of orthogonality conditions in relating the coefficients of the plane wave expansion of the incident wave field to the coefficients of the expansion of the geometry of the scatterer. In this sense the method is simpler than many common methods of computing plane layer responses. Even so, there is probably a practical limitation to the method when many deterministic scatterers, such as many crustal layers, are considered.

Figure 5 shows the geomtry of the line source problem. An elastic layer over halfspace model is assumed with a corrugated free surface. The line source is buried within the layer at $y=0$ and $x=0$. Figure 5 shows some sample results of the scattering calculation. The amplitude curves are for P and SV waves radiated into the halfspace. Note that the presence of the corrugated free surface significantly increases the amount of shear wave radiated into the halfspace for high angles of incidence. Surface displacements have also been computed using these solutions to examine the scattered field for waves in the crustal waveguide.

References

- Barker, J.S. A seismological study of earthquakes at Mammoth Lakes, California. Ph.D. Thesis, Pennsylvania State University, University Park, PA 16802 (1984).
- Langston, C.A. Aspects of Pn and Pg propagation at regional distances. Bull. Seism. Soc. Am., 72:457-471 (1982).
- Mathur, S.P. Crustal structure in southwestern Australia from seismic and gravity data. Tectonophysics, 24:151-182 (1974).
- Varadan, V.K. and V.V. Varadan. Acoustic, Electromagnetic, and Elastic wave scattering - focus on the T-matrix approach, Pergamon Press, New York (1980).
- Vogfjord, K. and C.A. Langston. The October 14, 1968 Meckering, Australia earthquake: A chip of the old block. preprint (1986).
- Waterman, P.C. Scattering by periodic surfaces. J. Acoust. Soc. Am., 57:791 (1975).

Table 1

Southwestern Australia crustal model used in the synthetic seismogram calculations(Mathur, 1974)

V_p (km/sec)	V_s (km/sec)	Rho(gm/cc)	Q_p	Q_s	Thickness(km)
6.13	3.54	2.78	1000	500	10
6.70	3.87	2.94	1000	500	7
7.49	4.32	3.10	1000	500	25
8.39	4.84	3.45	1000	500	--

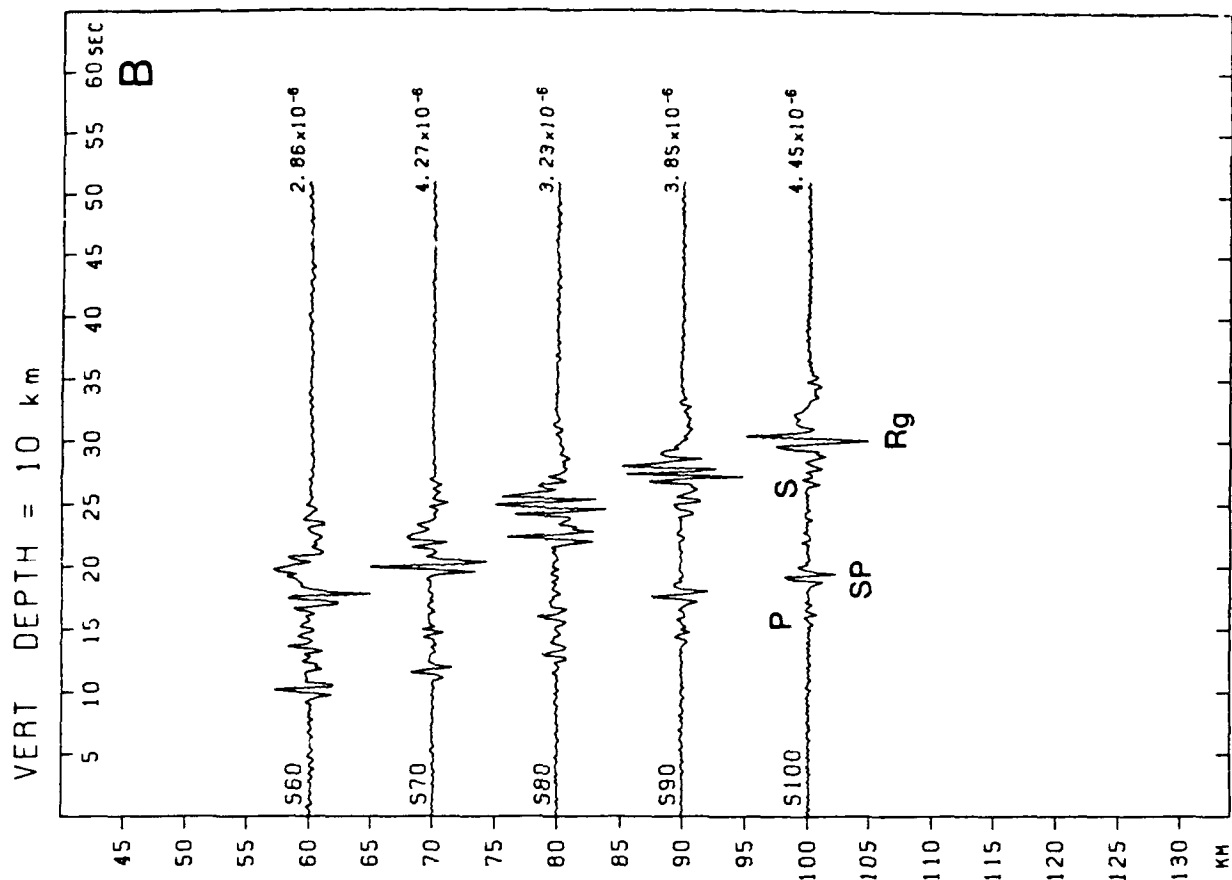
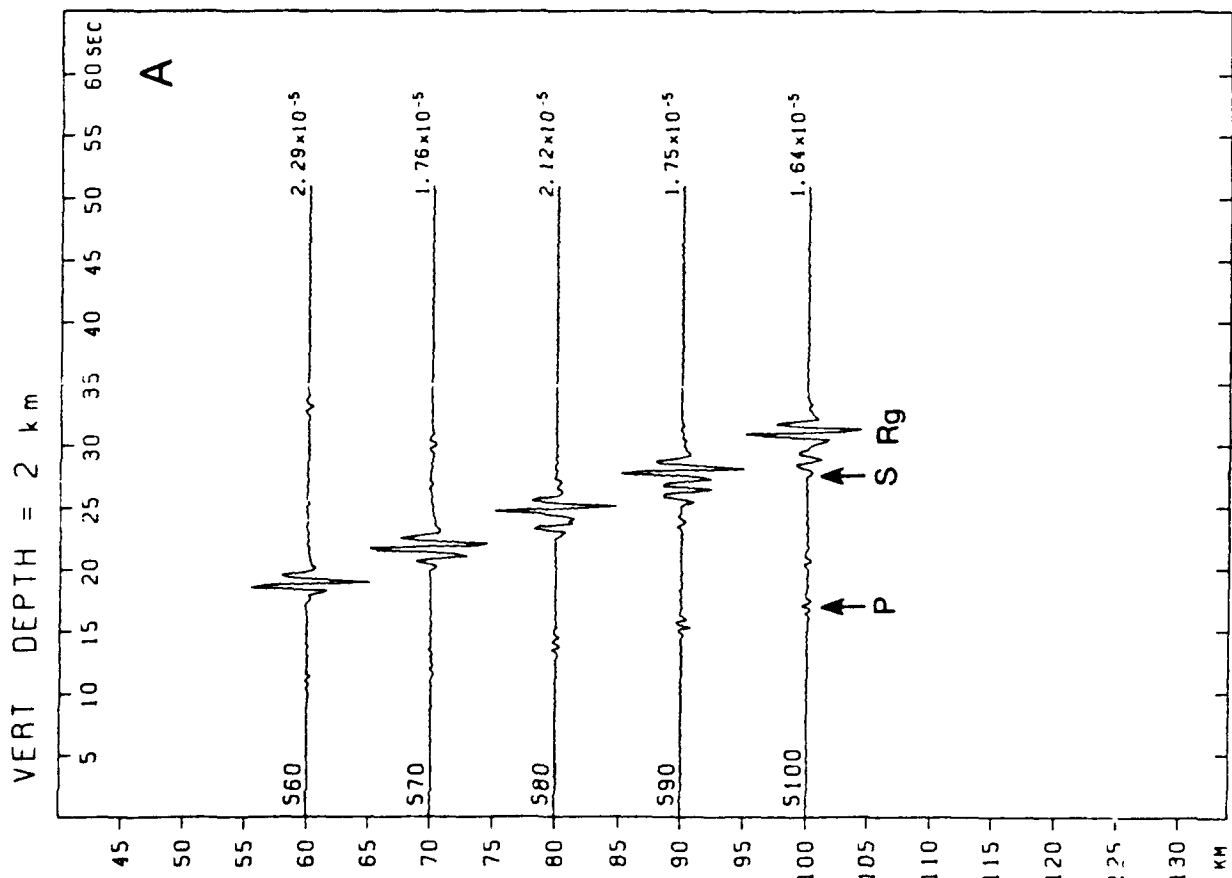


Figure 1: Wavenumber integration synthetic seismograms for a thrust fault point source at 2 km (A) and 10 km (B) depth. The vertical component of motion is shown as a function of range. Major phases are denoted on the bottom seismograms.

MECKERING AFTERSHOCKS MUN - SPZ

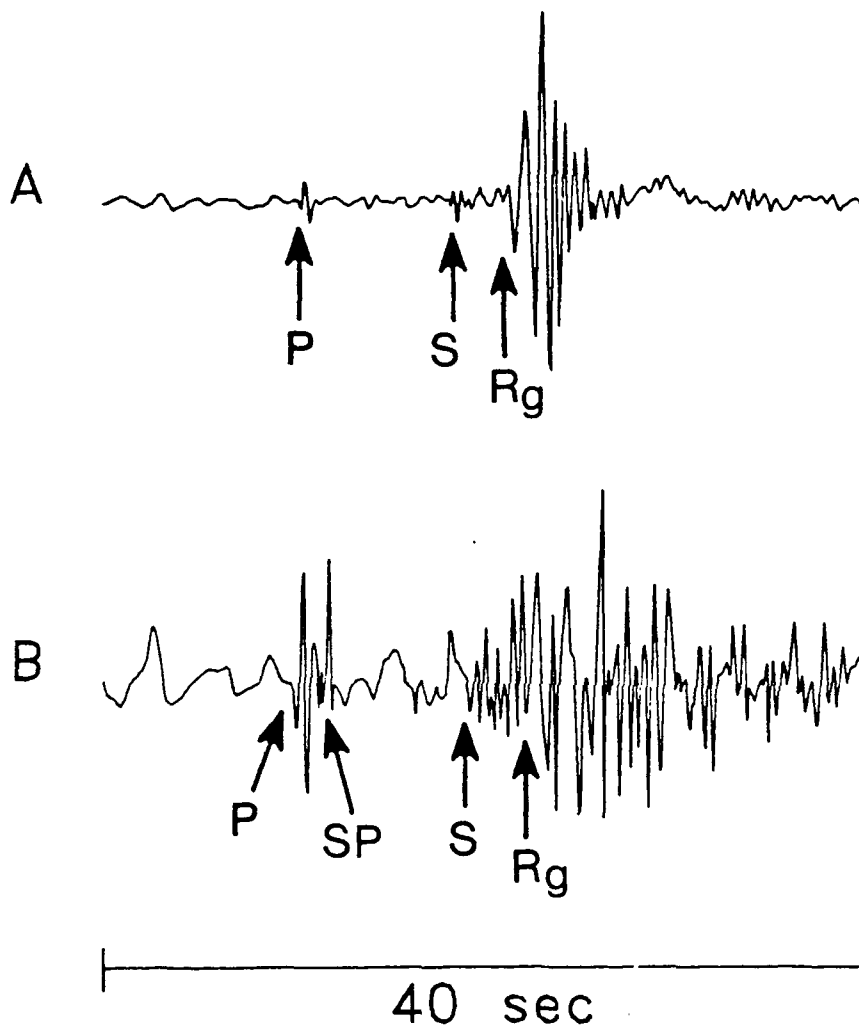


Figure 2: Two Meckering aftershocks recorded at the WWSSN station MUN (Mundaring, Australia) at a distance of 80 to 90 km. Aftershock A shows a characteristic simple waveform with simple P and S arrivals and a very large Rg phase. Synthetic seismogram calculations suggest that, irregardless of source mechanism, sources at 2 km depth and less will display this kind of waveform. Event B, however, shows a double P arrival suggesting P and the SP surface phase. The Rg phase is relatively small, compared to the body wave phases, suggesting a larger source depth. The SP - P time suggests a source depth of 5 km.

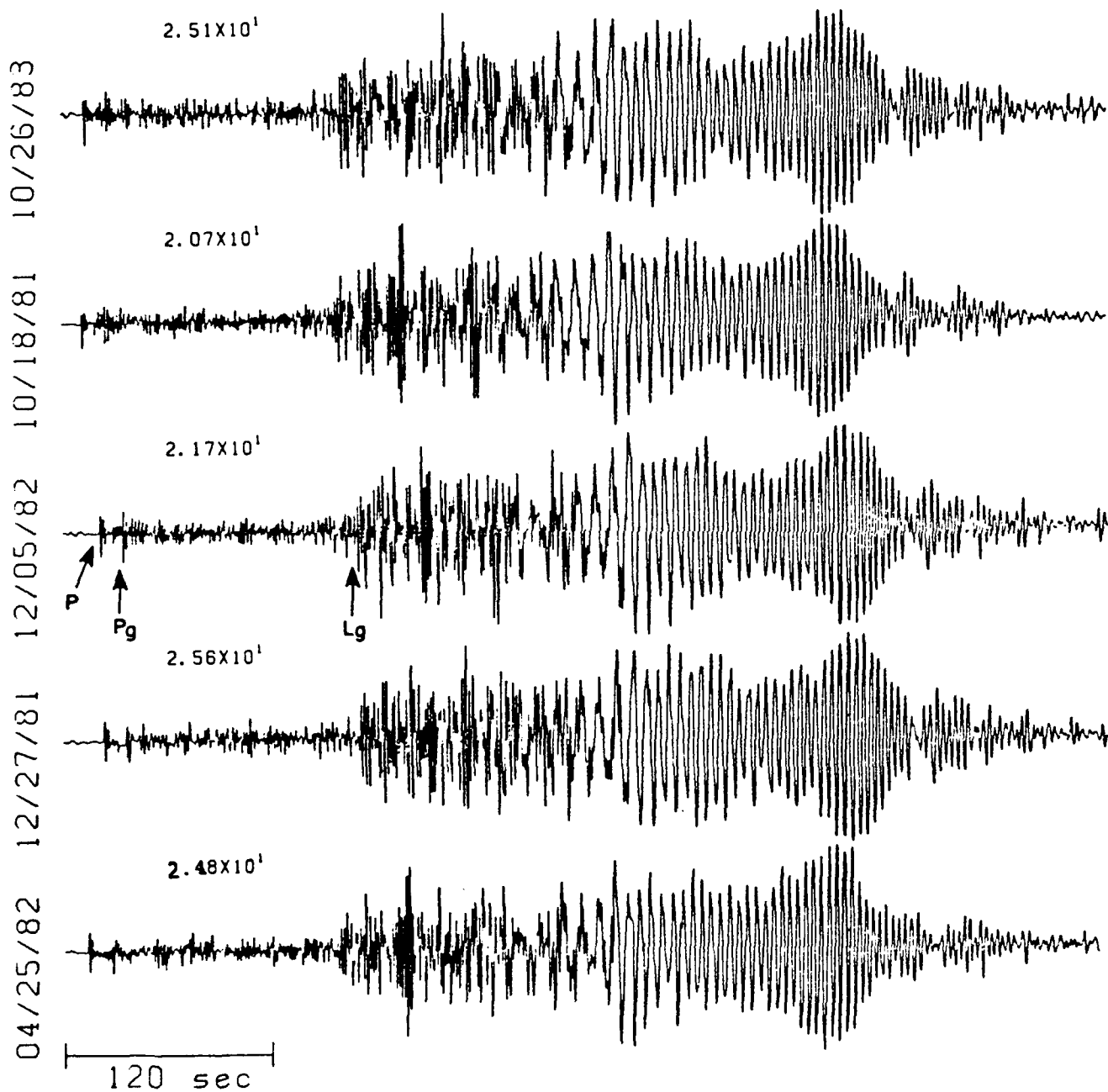


Figure 3: Vertical component of motion for 5 Semipalatinsk explosions recorded at Urumqi, PRC. Distance is 950 km.

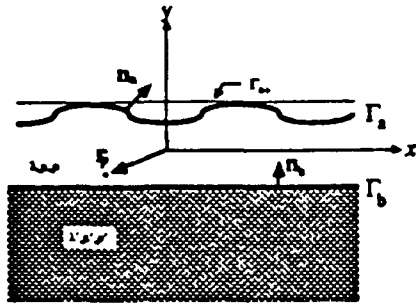


Figure 4: Schematic of the geometry for the line source problem..

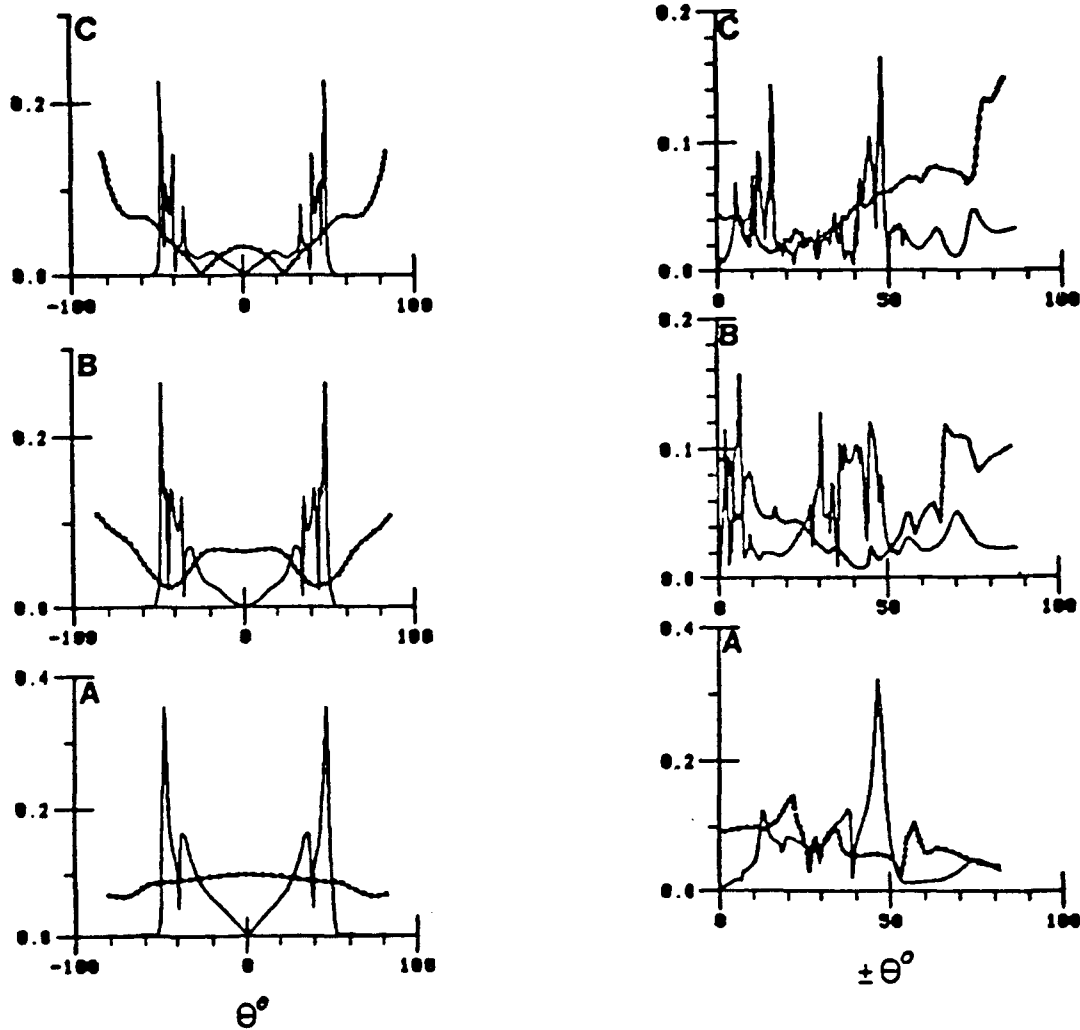


Figure 5: Far-zone P wave and SV wave radiated amplitudes, in the lower half-space, due to the P-wave line source located at $r_p = (0,0)$. These amplitudes are drawn as functions of θ , the angle with respect to the $-y$ axis. The surface Γ_a is specified by $y = a - b \cos(2\pi x/L)$ while Γ_b is the plane $y = -d$. The relevant parameters are $v_p = 6$, $v_s = 3.5$ km/sec, $\rho = 2.7$ gm/cm³ for the layer, and $v_p = 8$, $v_s = 4.5$, $\rho = 3.2$ for the halfspace. Also $a/L = d/L = 1.0$ and $b/L = 0.05$. The normalized frequency is (A) $k_p L = 5.0$, (B) $k_p L = 7.5$, (C) $k_p L = 10.0$. The left hand side shows amplitude for a planar free surface, the right-hand side for free-surface corrugation.

AFGL/DARPA REVIEW OF NUCLEAR TEST
MONITORING BASIC RESEARCH
U.S. AIR FORCE ACADEMY, 6 - 8 MAY 1986

TITLE: SOURCE CHARACTERIZATION AND YIELD ESTIMATION FROM Lg AND P-CODA MEASUREMENTS

AUTHOR: Douglas R. Baumgardt, ENSCO, Inc.

Contract No.: F19628-85-C-0057

INTRODUCTION

A number of recent studies have revealed that Lg measurements can provide remarkably stable and precise estimates of relative yield of underground nuclear explosions (Alexander, 1984; Nuttli, 1986). The two key issues in yield estimation with Lg amplitudes are absolute yield determination accuracy and precision in relative yield determination. In order to use Lg amplitudes for absolute yield estimation, i.e., to use Lg-magnitude versus yield relations for NTS explosions to estimate yields of explosions in another part of the world, it is necessary to correct Lg magnitudes for propagation effects. Most propagation-path correction methods, such as that of Nuttli (1986), assume that only anelastic attenuation and geometric spreading cause Lg amplitudes to decay with distance. However, geologic blockages are also known to profoundly affect Lg propagation (Ruzaikin et al, 1977), and such effects are not currently accounted for in Lg propagation path corrections. The relative precision of estimating yields with Lg amplitudes has been improved by making measurements on digital seismic traces. Digital prefiltering, spectral-magnitude measurements, and time-domain measurements of window-averages or rms-Lg amplitudes has permitted more stable magnitude estimates than peak-to-trough type measurements on analog traces.

The purpose of this study has been to investigate yield-determination with Lg amplitudes utilizing digital single-channel and array data. The three primary objectives include: (1) to investigate the spectral-slope method for determining Lg attenuation, (2) to determine if Lg-Q measurements, determined by this method, are predictive of Lg amplitude variations for different paths in Eurasia, and (3) to develop and study analysis techniques for using digitally recorded Lg waves for yield estimation.

Lg AMPLITUDE VARIATIONS IN EURASIA

NORSAR data for 17 presumed Soviet PNEs and presumed weapons tests at Semipalatinsk were used in this study. Their locations are shown in the top map in Figure 1. The bottom map shows some of the major geologic features in western Eurasia. Although western Eurasia is generally viewed geologically as a stable, laterally homogeneous craton, there are a number of major tectonic features, in particular large sedimentary basins, which may have an important effect on Lg propagation.

Figure 2 shows a set of incoherent beam plots for SW-NE trending line of events in northwestern Russia. The plots were made by stacking log-rms amplitudes made on each NORSAR channel aligned to P. Each channel was prefiltered from 0.6 to 3.0 Hz prior to stacking. Figure 2 shows that the S_n -Lg wave train is well recorded for the first two events. However, beginning with event 6 (August 11, 1984), the Lg amplitudes are sharply reduced. As can be seen from Figure 1, the Lg waves from events 6, 2A, 14A, and 13A must cross the Timan ridge, the Pechora sedimentary basin, and, in the case of event 13A, the northern Urals. We argue that these structures partially block Lg and reduce its amplitude more than what would be expected from anelastic attenuation and geometric spreading.

From studies of incoherent beams of other events, we have observed blockages associated with the Pri-Caspian sedimentary basin and the Ural Mountains. The top map in Figure 4 summarizes our observations. We conclude that lateral variations in the thickness of the sedimentary column above the basement is the dominant geological effect on Lg propagation efficiency across western Eurasia.

Lg SPECTRA AND Q-ESTIMATION

We have used the spectral-slope method described by Tang and Alexander (1985) to estimate frequency-independent Q for Lg. All Lg spectra were computed for a 51.2 second window starting at about the 3.5 km/sec group-velocity time. Spectra for each channel were smoothed and averaged over the array. The array-average spectra were then corrected for noise and an ω^2

explosion source model. The high-frequency decay of the corrected spectra were then fit by eye to the linear, frequency-independent Q model of the form

$$\log A(f) = \log A_0 - \left(\frac{2.3\pi\Delta}{Q U} \right) f$$

where Δ is distance in km, U is the group velocity, assumed to be 3.5 km/sec, and f is frequency in Hz.

The array average spectra for the 07/09/72 (event 5A) and 10/04/71 (event 3A) PNEs are shown in Figure 3. The bottom plot shows the two spectra on the same scale as the average of the noise spectra between the two events, plotted as a dashed line. In the top plot in Figure 3, the spectrum of event 5A has been increased at all frequencies by one log amplitude unit in order to separate it from event 3A. Both these events occurred in the western Russian platform, their Lg waves look very similar (see Figure 2) and have not undergone any blockages. Yet event 3A seems to have an anomalously low Q of 585 with γ of 0.17 deg^{-1} , compared to that of event 5A. As shown in top of Figure 3, this low Q for event 3A seems to have resulted from a spectral null at 2 Hz which resulted in the slope being underestimated. We have observed similar nulls in spectra of other PNEs and these nulls appear to have been produced by source effects, such as multiple events. Thus, we conclude that event 3A has the same Lg Q as event 5A.

The map in Figure 4 summarizes our Q estimation results. We have found that Q ranges from 775 to 1045 with corresponding γ s ranging from 0.1 to 0.15. Local fluctuations in Q do not appear to correlate strongly with Lg amplitude fluctuations or geology. Some of these variations may be caused by Q estimation uncertainties caused by spectral nulls. However, our preliminary conclusion is that geologic blockage effects on Lg amplitudes are not corrected by Lg Q estimates.

Lg AMPLITUDE MEASUREMENTS FOR NTS EXPLOSIONS

We have also been studying Lg spectral magnitudes for NTS events recorded at the RSTN stations. Our approach has been to apply a suite of narrow Gaussian band pass filters across the 0 to 5 Hz band for time windows on P

noise, P, P coda, Lg-precursor P coda, Lg, and Lg coda. We then compute rms averages in the windows in each band and average the log-rms values over a selected frequency band.

Figure 5 compares 0.75 to 3.0 Hz spectral magnitudes for P and Lg, measured on the vertical component at RSSD, with the scaled depth ($h/Y^{1/3}$) of the explosion relative to the scaled depth of the water table. The 15 events were tested at one of two yields below 150 kt. The X symbols represent the high-yield events and the O symbols represent the low-yield events. Points to the right of the vertical dashed line represent events detonated below the water table.

The results show the expected result that events above the water table have lower P and Lg amplitudes, due to reduced coupling, than events of comparable yield below the water table. Also, Figure 5 shows that P and Lg amplitudes correlate with increasing depth below the water table, although the depth dependence is stronger for P than for Lg. In general, we have found that Lg magnitudes have significantly less magnitude yield scatter than P wave magnitudes for events located near or below the water table.

The explosions we have studied with RSTN data have yields in a limited range below 150 kt. In order to extend the yield range, we are collecting and calibrating additional digital data from LRSM recordings of the older, high-yield U.S. explosions. This data, which we are putting into an explosion Lg database at the CSS, will be combined with the RSTN data assess the overall yield estimation precision of digitally-measured Lg amplitudes.

References

Alexander, S.S. (1986). Relationship Among Near-Field, Regional, and Teleseismic Observations of Seismic Source Parameters, in The Vela Program, Executive Graphic Services, 817-829.

Nuttli, O.W. (1985). Yield Estimates of Nevada Test Site Explosions Obtained from Seismic Lg Waves, *J. Geophys. Res.*, 91, 2137-2152.

Ruzaikin, A.I., I.L. Nersesov, V.I. Khalturin, and P. Molnar (1977). Propagation of Lg and Lateral Variations in Crustal Structure in Asia, *J. Geophys. Res.*, 82, 307-316.

Tang, L. and S.S. Alexander (1985). Estimates of Average Q for Lg Propagation in Eurasia, Abstract in EOS, Trans. Am. Geophys. Union, 66, 305.

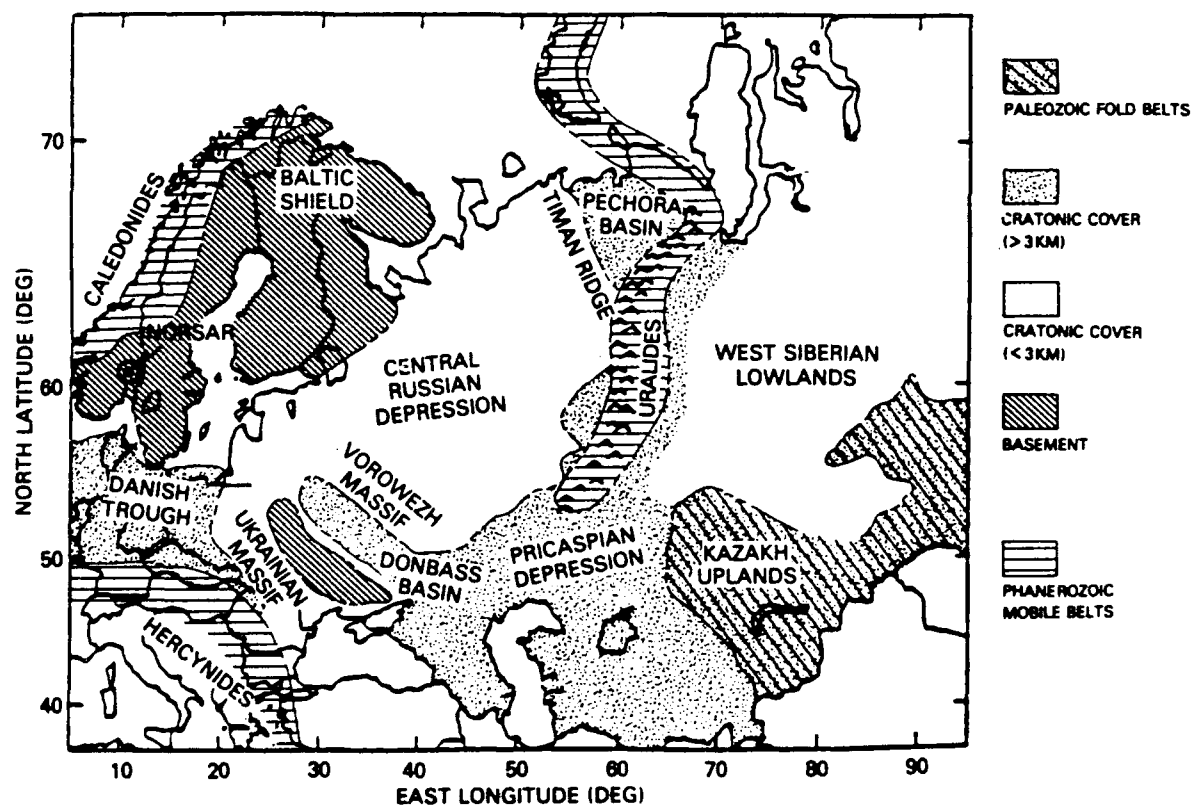
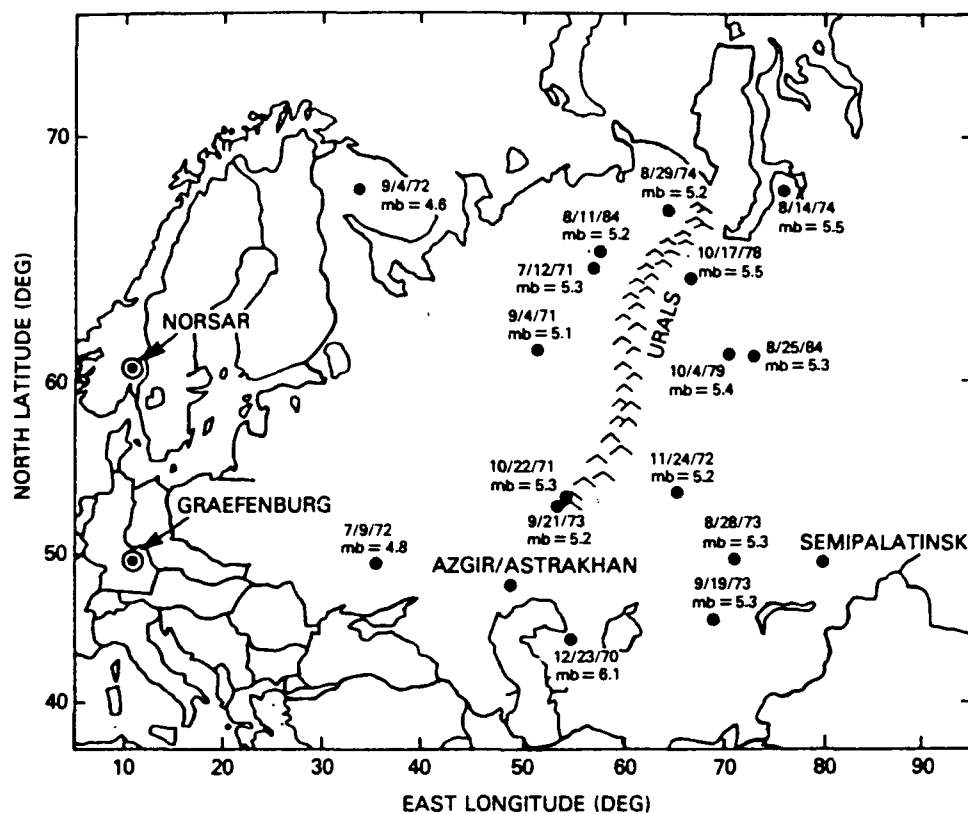


FIGURE 1 **Top:** ISC or NEIS locations of the presumed underground nuclear explosions used in this study. **Bottom:** Map showing the major geologic features in western Eurasia.

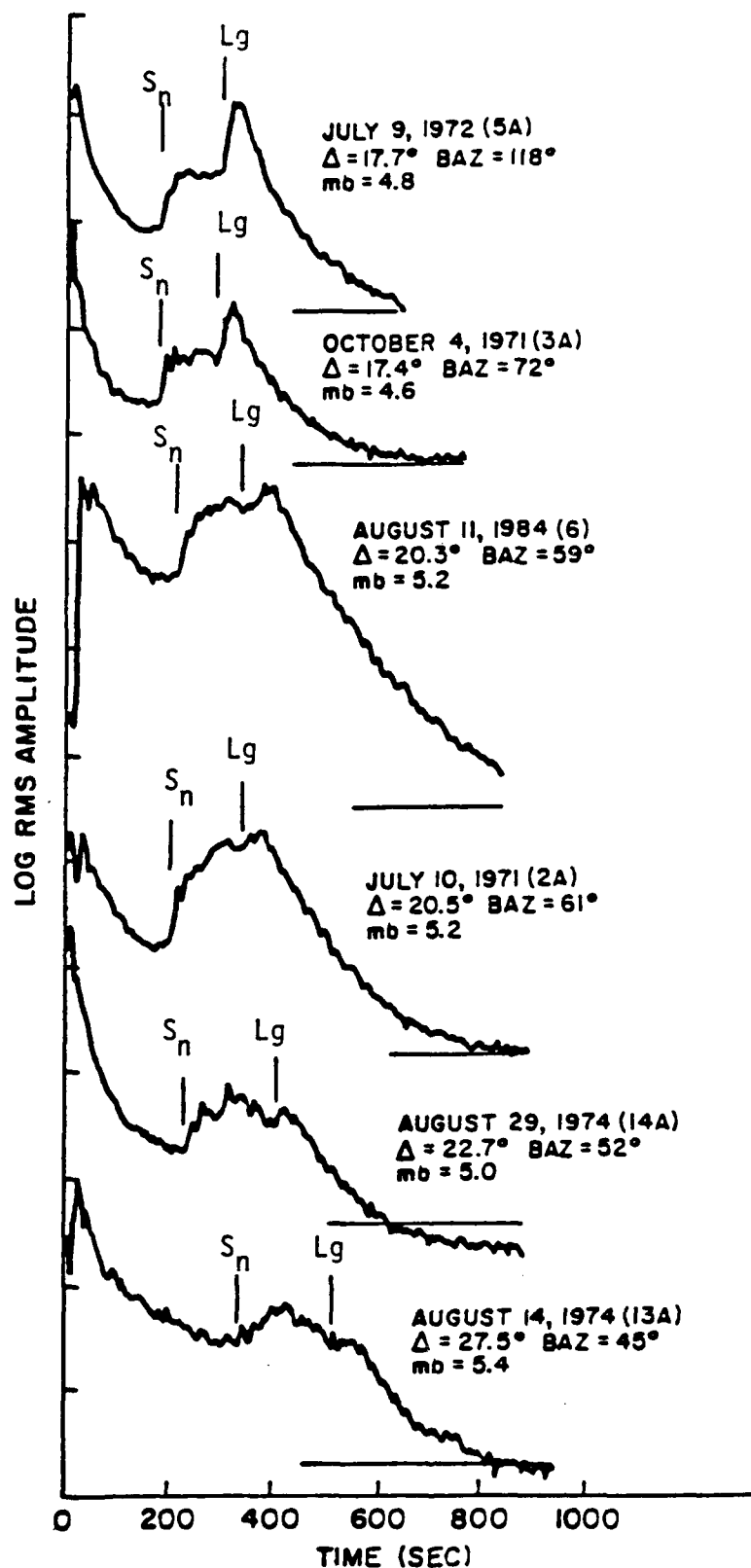


FIGURE 2

Array-stacked log-rms amplitude coda plots of PNEs located in northwestern Russia. Tick marks on amplitude scale indicate 0.5 log-rms units. Horizontal lines indicate average P background noise levels. Each trace was pre-filtered in the 0.6 to 3 Hz band.

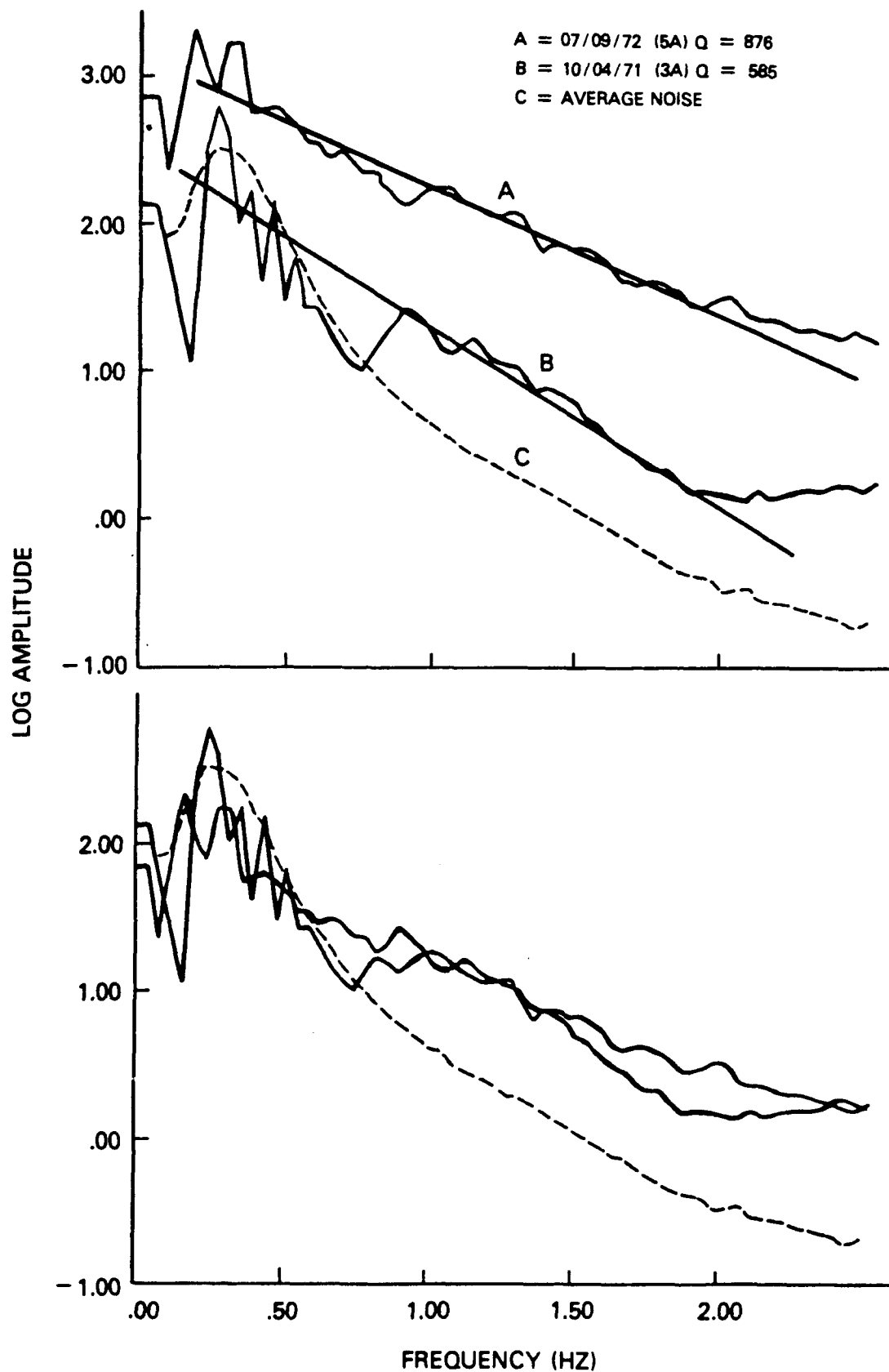


FIGURE 3

Spectra of events 5A and 3A. Top plot shows the spectra separated by one log unit. Lines on the top plot indicate the high-frequency slopes used to estimate Q. The dashed line in both plots indicates the average noise spectrum between the two events.

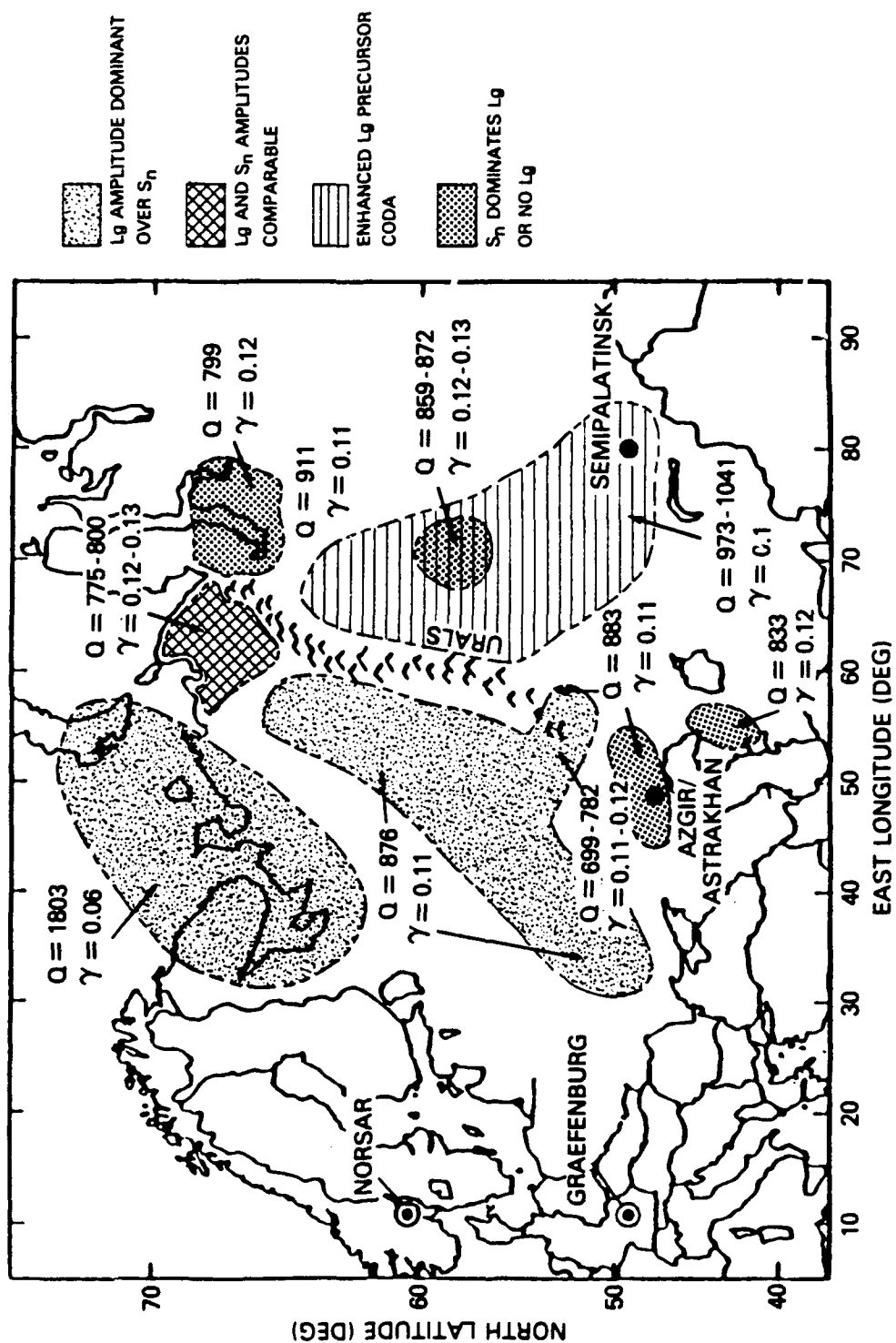


FIGURE 4 Map summarizing the relative S_n and Lg excitation and spectral Q measurements for NORSAR recordings from presumed Soviet PNEs.

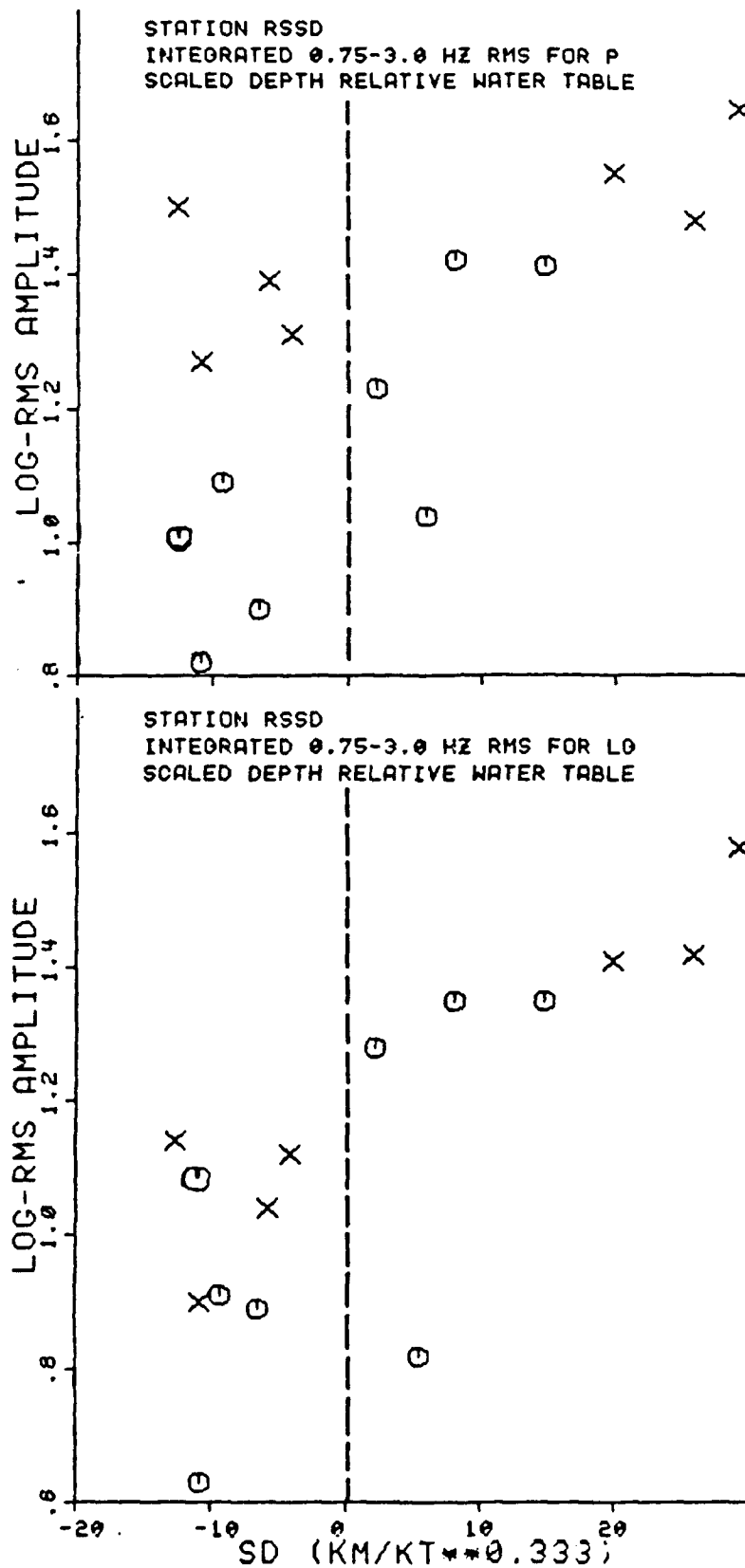


FIGURE 5 Plots of spectral magnitude for P (top) and Lg (bottom) versus scaled depth with respect to the water table for 15 events at WTS. Points to the right of the dashed line denote explosions below the water table. Open circles indicate the lower yield events and the X's indicate higher yield events.

THE TECTONIC RELEASE SIGNATURE AT REGIONAL DISTANCES

Terry C. Wallace
Department of Geosciences
University of Arizona

INTRODUCTION

One of the main consequences of decreasing the yield limit in a threshold test ban is the increased reliance on regional distance seismograms for monitoring purposes. Most schemes for determining the yield at regional distances are based on the amplitude of phases such as Pg or Lg. Here we investigate the effect of tectonic release on the character of Pn-Pg wavetrain, and whether it introduces any bias in the yield determination.

There is an apparent frequency dependence of the tectonic release signature at regional distances. At periods of 5-15 seconds, Wallace et al. (1983) show that the P_{n1} waveforms from Pahute Mesa explosions are sometimes strongly distorted by tectonic release, which amounts to superimposing the wavefield from a strike-slip shear dislocation on the explosion signature. On the other hand, Alexander (1980), Pomeroy et al. (1982) and Gupta and Blanford (1983) present results which indicate that tectonic release has little effect on 3 Hz Lg amplitudes. A similar problem is rectifying the far-field representation of the tectonic release with the observations of the tangential component of strong-ground motion. The observed near-field SH waves are much more complicated and significantly smaller than expected.

We attempt to explain both the frequency dependence of the tectonic release and the near-field/teleseismic incompatibility with a distributed shear dislocation model. In the near-field, the modeled waveforms are highly complicated due to interference of the various sources. At regional distances the Pg arrivals due to the deviatoric component of the source are smaller than expected from a single point source due to the depth dependence of the Pg excitation.

FREQUENCY DEPENDENCE OF TECTONIC RELEASE

It is a fairly straight forward process to invert for the moment tensor (MT) of a seismic source provided adequate Green's functions can be constructed, although for shallow explosions high frequency data is required to constrain the M_{zi} components. The explosion moment is the average of the trace of the moment tensor, and the deviatoric component is the remainder. We inverted the regional body waves recorded on the broadband Lawrence Livermore National Laboratory network for three Pahute Mesa explosions (CHESHIRE, FARM and POOL) in different frequency bands in an attempt to isolate any frequency dependence of the deviatoric component of the MT.

At long periods (>2 seconds) a two layered crust over a halfspace mantle was a sufficient travel path structure to recover the moment tensor. Table 1 shows the isotropic and major double couple components of the MT. Also shown is the size of the minor double couple, an indication of the likelihood that the major double couple actually represents tectonic release. The inversion was performed in a linear fashion, which requires that all the elements of the MT have the same time history. It was assumed that the explosion had a Helmberger-Hadley time history with $k=15$, $B=0$. Although this is a poor representation for the tectonic release time history, it probably is sufficient considering the uncertainty of the travel path structure.

TABLE 1: MOMENT TENSOR INVERSION RESULTS

<u>Event</u>	<u>date</u>	<u>Mex (dyne-cm)</u>	<u>Mdc</u>	<u>Mmdc</u>
FARM		$.01 \times 10^{24}$.003	.002
CHESHIRE	2-14-76	.67	.36	.07
POOL	3-17-76	.42	.19	.12

Figure 1 shows the frequency dependence of the deviatoric part of the moment tensor. The LLNL records were low pass filtered at different frequencies, as shown on the abscissa. The resulting moment tensor had the long-period isotropic component subtracted from it, and the largest remaining eigenvalue was assumed to represent the tectonic release (the direction of the eigenvectors was not considered). As can be seen, the apparent size of the tectonic release decreases with increasing frequency.

It is difficult to determine the cause of the frequency dependence of tectonic release. One possible explanation is a strong depth dependence of P_g excitation by a strike-slip source (the orientation of the tectonic release). At high frequencies it is possible that the distributed nature of tectonic release results in destructive interference.

NEAR-FIELD TECTONIC RELEASE

Figure 2 shows the three components of ground motion from BOXCAR recorded at a distance of 7.4 km. Below the observations are synthetics calculated using an explosion source function and velocity structure determined by Barker et al. (1985). Wallace et al. (1986) determined a seismic moment of 0.86×10^{24} dyne-cm for the tectonic release from this event on the basis of teleseismic modeling. The SH waves that would be expected for this size tectonic release are shown below the observed tangential component. The gross mismatch indicates two things: (1) significant off azimuth energy, and (2) the inadequacy of a point source representation for the tectonic release.

On the basis of our teleseismic modeling of the SH energy from nuclear explosions, we would argue strongly that there is appreciable release of tectonic strain, and that the tangential energy is not a product of asymmetry of the explosion source (see Wallace et al. 1985; 1986). If the tectonic release is purely a triggered fault motion as suggested by Aki and Tsai

(1972), then it would be expected that the strong-motion SH waves would be similar to those produced by a similar sized earthquake. Figure 3 compares the SH waves from an aftershock of the 1979 Imperial Valley earthquake ($M_L = 5.0$, $M_0 = 0.7 \times 10^{24}$ dyne-cm, recorded at 10.4 km distance) to the BOXCAR record and a synthetic for a simple dislocation model. Apparently the point source representation is sufficient for the earthquake, implying that at least some component of the tectonic release is due to a mechanism other than a triggered fault motion. Archambeau (1972) proposed a mechanism for tectonic release which is due to the loss of strength of material in a volume about the explosion.

In an attempt to simulate the Archambeau model we constructed a spherically symmetric, distributed source. Figure 4 illustrates the distributed model as 16 point sources (of equal moment) about the working point. The elastic radius, or extent of shear stress drop, expected for Archambeau's model is given by:

$$R_e = \frac{F \rho \alpha^2 \Psi\{\infty\}}{\Delta \sigma}$$

where F is the ratio of the tectonic release moment to the explosion moment, $\Delta \sigma$ is the stress drop, ρ and α are the source region density and P wave velocity respectively, and $\Psi\{\infty\}$ is the static level of the explosion displacement potential. For BOXCAR (1000kt), and the F factor calculated on the basis of the tectonic release moment of 0.87×10^{24} dyne-cm, the elastic radius should be on the order of 1.1 km if the stress drop is 100 bars. This radius seems extraordinarily large, and indeed would have a significant effect on a recording only 7 km away. The value of 100 bars for stress drop is taken from the "average" intraplate earthquake (Liu and Kanamori, 1983). In earlier work (Wallace et al., 1983) it was shown that the sP waveform from BOXCAR required a much higher stress drop: 300-500 bars. This is consistent with the work of McKeown and Dickey (1969) who showed that the aftershock

distribution of explosions with large F factors is confined to a region much smaller than expected for an earthquake of comparable moment. Using a stress drop of 500 bars the elastic radius for BOXCAR is 0.3 km. We used this radius to define the sphere of the distributed sources.

Figure 5 shows a comparison of the observed tangential and distributed source synthetic waveforms for BOXCAR. Although the match is not perfect, it does preserve the character of the interference pattern. Also shown in figure 5 is the long-period teleseismic SH pulse from the distributed source compared with that from a point source. It is apparent that the distributed source model will satisfy both the local data and far-field observations. The moment that is required in the near-field is $.38 \times 10^{24}$ dyne-cm, or 2 times smaller than the moment derived on the basis of teleseismic data.

CONCLUSIONS AND SUGGESTIONS

It is apparent that underground explosions which have a substantial component of non-isotropic radiation are releasing the tectonic stress in a volume about the source. At the high frequencies which are recorded at 5-50 km from the source the tectonic release can not be modeled as a point source. There is little effect on the estimation of explosion source functions from near-field data, (see Stump and Johnson, 1984) but it makes the recovery of the deviatoric component of the moment tensor difficult. One possible scheme for a stable yield estimation from near-field data would be to first use a polarization filter and reject tangential motion.

It is much more difficult to explain the frequency dependence of tectonic release. At long-periods (>2 seconds) the regional distance body waves can be inverted for the deviatoric component of the moment tensor, and the results are consistent with the teleseismic analysis of SH. At short periods, the deviatoric component of Pg is smaller than expected. At least some of this

reduction may be due to unmodeled propagation effects, but it is still not possible to rectify the explosion excitation of Pg with the lack of double couple excitation. There are at least two possibilities which warrant further study: (1) a frequency dependent time function for the tectonic release, and (2) asymmetry in the explosion or tectonic release.

REFERENCES

- Aki K. and Y.B. Tsai (1972). Mechanism of Love wave excitation by explosive sources, J. Geophys. Res., 77, 1452-1475.
- Alexander, S.S. (1980). Comparison of source and propagation characteristics in Eurasia, North Africa and the U.S. using regional seismic and remote sensing observations, DARPA Symposium, Grand Island, New York.
- Archambeau, C.B. (1972). The theory of stress wave radiation from explosives in prestressed media, Geophys. J., 29, 329-366.
- Gupta, I.N. and R.R. Blandford (1983). A mechanism for generation of short-period transverse motion from explosions, Bull. Seism. Soc. Am., 73.
- Hartzell, S.H., L.J. Burdick and T. Lay (1983). Effective source functions for Pahute Mesa nuclear tests, WCCP-R-83-3.
- Liu and Kanamori (1980). Determination of source parameters of mid plate earthquakes from the waveforms of body waves, Bull. Seism. Soc. Am., 70, 593-613.
- McKeown, F.A. and D.D. Dickey (1969). Fault displacement and motion related to nuclear explosions, Bull. Seism. Soc. Am., 59, 2259-2269.
- Wallace, T.C., D.V. Helmberger and G.R. Engen (1983). Evidence of tectonic release from underground nuclear explosions in long-period P-waves, Bull. Seism. Soc. Am., 73, 593-613.
- Wallace, T.C., D.V. Helmberger and G.R. Engen (1985). Evidence of tectonic release from underground nuclear explosions in long-period S-waves, Bull. Seism. Soc. Am., 75, 157-174.
- Wallace, T.C., D.V. Helmberger and T. Lay (1986). A note on the revised moments for Pahute Mesa tectonic release, Bull. Seism. Soc. Am., 76, 313-318.

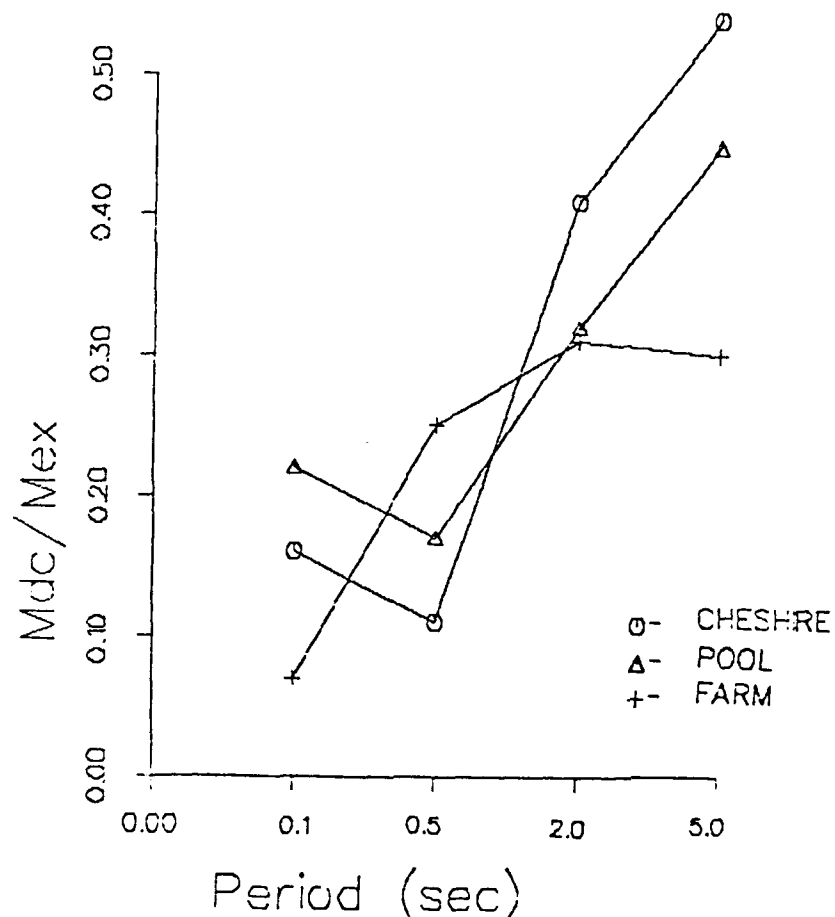


Figure 1: The ratio of the deviatoric to explosion moment for Pahute Mesa explosions CHESHIRE, POOL and FARM. Mex is only determined at long-periods.

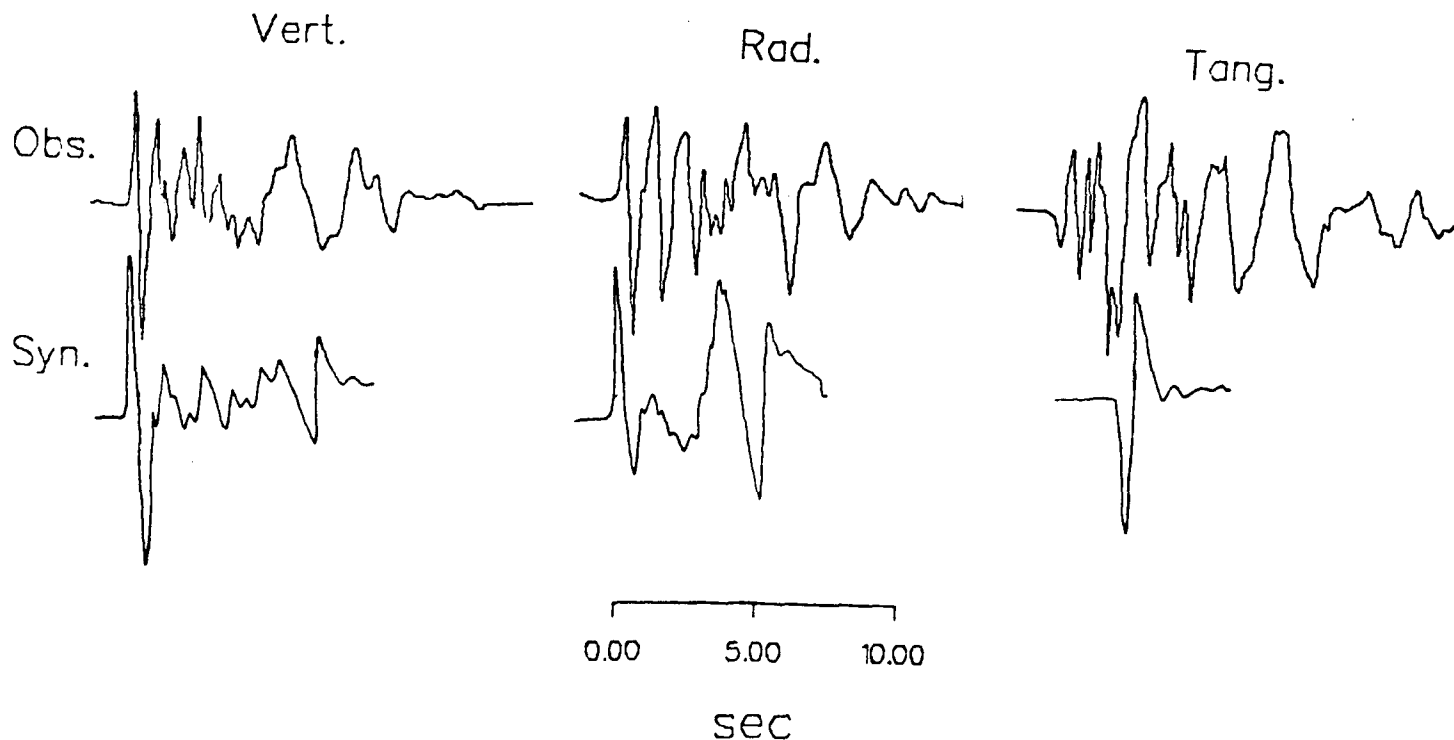


Figure 2: Comparison of strong-ground motion from BOXCAR observed at a recording site 7.4 km away from the source with synthetic seismograms calculated using the explosion model of Hartzell et al. (1983). The tangential model is from the best fitting point source double couple.

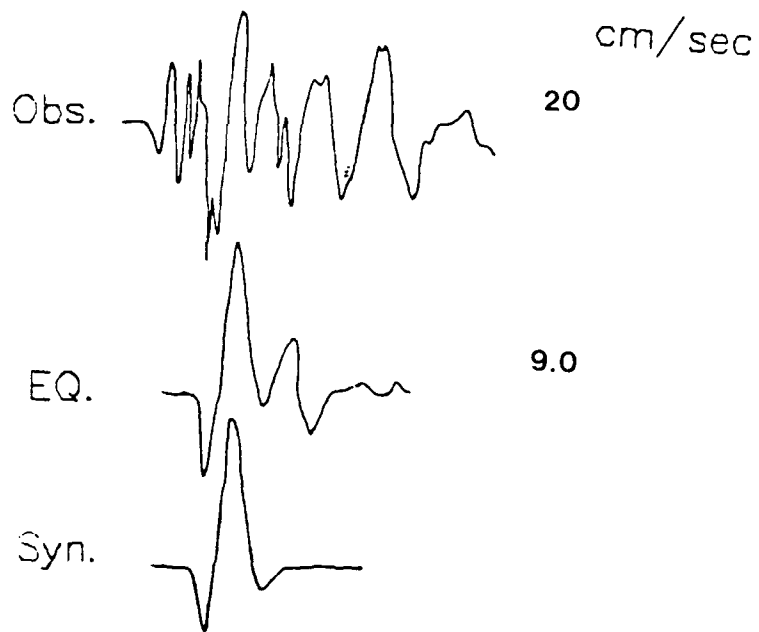


Figure 3: Comparison of BOXCAR and Imperial Valley aftershock with synthetic SH wavetrain. The explosion and earthquake have approximately the same far-field moment.

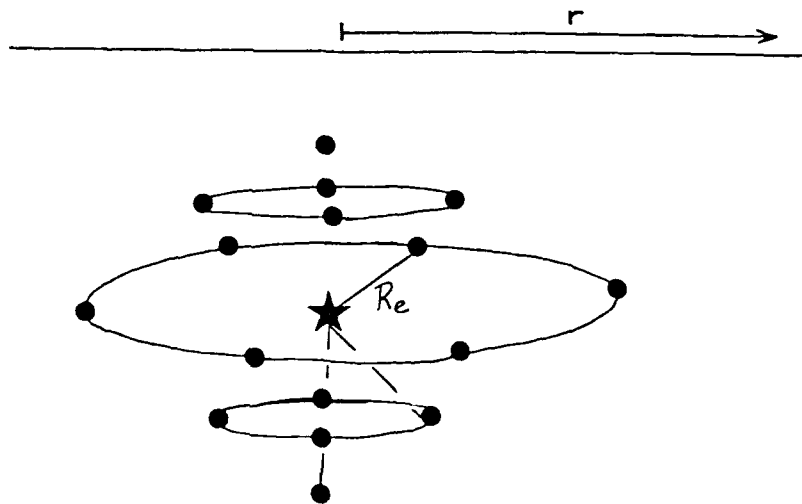


Figure 4: Schematic of the distributed source tectonic release model (sources are shown in solid dots). All sources are at a distance of one elastic radius.

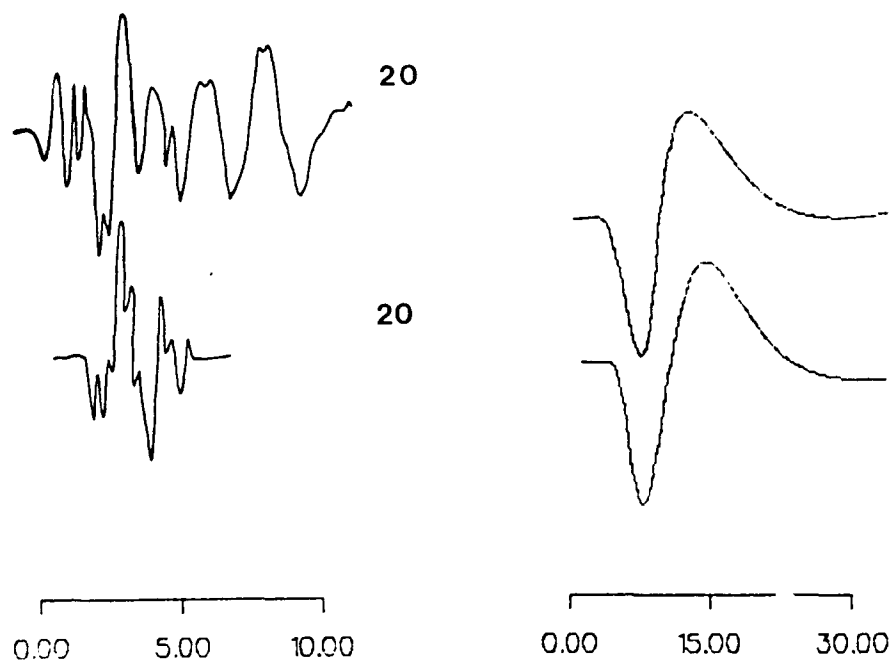


Figure 5: Distributed source SH waves in the near- and far-field. The strong motion fit requires a total moment of 0.38×10^{24} dyne-cm. The far-field comparison is for a single point source of moment 0.38×10^{24} and 16 sources of 0.22×10^{23} dyne-cm. There is no difference in waveform or amplitude.

Lg MAGNITUDES OF SELECTED SHAGAN RIVER, EAST KAZAKHSTAN EXPLOSIONS

Otto W. Nuttli

Saint Louis University

INTRODUCTION

Amplitudes of Lg waves of approximately 1-sec period provide a stable estimate of magnitude, $m_b(Lg)$, and explosion yield, Y, for Nevada Test Site explosions. When these relations are applied to seven non-NTS explosions of announced yield in Colorado, New Mexico, Mississippi, Algeria and East Kazakhstan, the estimated yields differ from the announced values by between 3 and 35% (Nuttli, 1986).

In the present study $m_b(Lg)$ values are determined for a selected number of Shagan River, East Kazakhstan explosions. Figure 1 shows the location of the test site and of WWSSN stations whose data are used. The closest station is NIL (Nilore, Pakistan) at approximately 1875 km and the most distant is KON (Konberg, Norway) at about 4375 km.

DATA AND RESULTS

Maximum Lg amplitudes, as measured in the group velocity window of 3.2 to 3.6 km/sec, are extrapolated to an epicentral distance of 10 km by the formula (Nuttli, 1986)

$$A(10 \text{ km}) = A(\Delta) (\Delta/10)^{1/3} \sin(\Delta/111.1) / \sin(10/111.1)^{\frac{1}{2}} \exp[\gamma(\Delta - 10)]$$

where $A(10 \text{ km})$ is the hypothetical Lg amplitude at 10 km epicentral distance and $A(\Delta)$ is the observed amplitude at distance Δ , in kilometers. The reference level of the $m_b(Lg)$ scale was set so that $m_b(Lg)$ and $m_b(P)$ values are numerically the same for eastern North America earthquakes (Nuttli, 1973).

This leads to the relation

$$m_b(Lg) = 5.0 + \log_{10} [A (10 \text{ km})/110]$$

where $A (10 \text{ km})$ is the ground motion, in micrometers, extrapolated from a distance Δ .

The coda-Q method of Aki and Chouet (1975) as adapted by Herrmann (1980) was used to obtain approximate values of Q_0 (Q at 1-Hz frequency) for each source-to-station path. Station corrections then were determined for a selected number of explosions by determining departures of individual station $m_b(Lg)$ values from the average $m_b(Lg)$ values. These station corrections are in the form of correction to the Q_0 values. Adjustments to the coda-Q determined values of Q_0 varied between 0 and 6.8% for ten stations.

$m_b(Lg)$ values were determined for 62 Shagan River explosions between 1965 and 1985. Their $m_b(P)$ values, as determined by the ISC or the USGS, varied between 5.4 and 6.2. A linear least-squares fit of the $m_b(Lg)$ and $m_b(P)$ data gave

$$m_b(Lg) = 0.597 \pm 0.392 + (0.892 \pm 0.067) m_b(P)$$

where the values following the \pm signs are standard deviations. The data do not cover a large range of $m_b(P)$ values. If a unit slope is assumed, as would be expected from the definition of the $m_b(Lg)$ scale, the data satisfy the relation

$$m_b(Lg) = (-0.036 \pm 0.122) + m_b(P)$$

For water-saturated NTS explosions, the corresponding relation is (Nuttli, 1986)

$$m_b(Lg) = (0.31 \pm 0.02) + m_b(P)$$

Combining the last two equations results in an estimated $m_b(P)$ bias of 0.35 magnitude units between NTS and Shagan River, assuming that the same yield explosion in water-saturated rock at NTS and Shagan River will produce the same $m_b(Lg)$ values.

Figure 2 shows $m_b(Lg)$ plotted versus time, from 1976 through 1985, for Shagan River explosions. There appears to be an upper limit, of $m_b(Lg)$ about 6.1 to 6.2, for explosions after autumn 1979. Between 1976 and autumn 1979 there is a suggestion of a somewhat smaller upper limit, between about 5.9 to 6.0.

Table 1 gives estimates of the yields of the Shagan River explosions studied, assuming that the NTS-derived relations between $m_b(Lg)$ and explosion yield for water-saturated rocks are applicable. Two estimates based on $m_b(Lg)$ values are given. The first was obtained by fitting the NTS data by a quadratic equation, and the second by a linear equation (Nuttli, 1986). Also included in Table 1 are yield estimates by Dahlman and Israelson (1977) and upper-bound yield estimates by Sykes and Cifuentes (1984).

For seven of the fifteen explosions for which Dahlman and Israelson (1977) gave estimated yields, the $m_b(Lg)$ estimates are almost the same as theirs. For the remaining eight their estimated yield values are larger, in two cases by as much as a factor of three. In twenty of twenty-one cases the Sykes and Cifuentes (1984) upper-bound yield estimates are smaller than those obtained by $m_b(Lg)$. For the seven explosions of largest estimated yield by Sykes and Cifuentes (1984), the $m_b(Lg)$ values are within 40% of their values. The percentage differences in estimated yields get larger for the smaller explosions.

Nineteen explosions since April 1976 have $m_b(Lg)$ values exceeding 6.00,

corresponding to an estimated yield of 150 kt. None have $m_b(Lg)$ values exceeding 6.21, corresponding to an estimated yield of 300 kt. The January 15, 1965 cratered explosion had an $m_b(Lg)$ -estimated yield of 103 to 109 kt, compared to an announced value of 125 kt (Marshall et al, 1979).

CONCLUSIONS

Lg-wave amplitudes recorded at WWSSN stations in southern Asia and Scandinavia can be used to determine $m_b(Lg)$ values for Shagan River explosions of $m_b(P) \geq 5.5$. The Scandinavian stations, at larger epicentral distances, have Lg amplitudes five to ten times larger than the southern Asian stations, which indicate large differences in Q for the two paths.

For well-determined $m_b(Lg)$ values, taken to be those based on the data of five or more stations, the largest occurred for the December 27, 1981 event, which had an $m_b(Lg)$ of 6.15. The corresponding yield estimate is about 250 kt.

The $m_b(P)$ magnitude bias between Shagan River and Nevada Test Sites, as determined by $m_b(Lg)$ values, is 0.35 units. This assumes that explosions of the same yield at the two sites detonated in similar material would produce identical $m_b(Lg)$ values. This assumption, when made for explosions of announced yields at five widely disparate test sites, gives estimated yields within 3 to 35% of the announced values.

REFERENCES

- Aki, K. and B. Chouet (1975). Origin of coda waves: source, attenuation, and scattering, J. Geophys. Res., 80, 3322-3342.
- Dahlman, O. and H. Israelson (1977). Monitoring Underground Nuclear Explosions, Elsevier Scientific Publishing Co., Amsterdam, Holland.
- Herrmann, R. B. (1980). Q estimates using the coda of local earthquakes, Bull. Seism. Soc. Am., 70, 447-468.
- Marshall, P.D., D.L. Springer and H.C. Rodean (1979). Magnitude corrections for attenuation in the upper mantle, Geophys. J. R. Astron. Soc., 57, 609-638.
- Nuttli, O. W. (1973). Seismic wave attenuation and magnitude relations for eastern North America, J. Geophys. Res., 78, 876-885.
- Nuttli, O. W. (1986). Yield estimates of Nevada Test Site explosions obtained from seismic Lg waves., J. Geophys. Res., 91, 2137-2151.
- Sykes, L. R. and I. L. Cifuentes (1984). Yields of Soviet underground nuclear explosions from seismic surface waves: compliance with the Threshold Test Ban Treaty, Proc. Natl. Acad. Sci. USA, 81, 1922-1925.

TABLE 1

YIELD ESTIMATES OF EAST KAZAKHSTAN EXPLOSIONS

— Estimated explosion yield, in kilotons —

Date	$m_b(Lg)$	quadratic eq. this study	linear eq. this study	Dahlman and Israelson (1977)	Sykes and Ci- fuentes (1984)*
01/15/65**	5.87	103	109	110	---
02/10/72	5.55	42	42	43	---
11/02/72	6.04	171	183	350	---
12/10/72	6.09	200	212	620	---
07/23/73	6.13	225	239	420	---
12/14/73	5.87	103	109	150	---
05/31/74	5.68	60	62	140	---
10/16/74	5.26	20	17	43	---
12/27/74	5.69	62	64	51	---
04/27/75	5.47	34	33	60	---
10/29/75	5.45	33	31	90	---
12/25/75	5.83	92	97	90	---
04/21/76	5.19	17	14	20	---
06/09/76	5.27	20	18	25	---
07/04/76	5.90	113	120	90	---
08/28/76	5.60	48	49	---	---
11/23/76	5.86	100	106	---	---
12/07/76	5.71	65	68	---	---
05/29/77	5.58	45	46	---	---
06/29/77	5.15	15	13	---	---
09/05/77	5.51	38	37	---	---
11/30/77	5.71	65	68	---	---
06/11/78	5.75	74	76	---	---
07/05/78	5.67	59	60	---	---
08/29/78	5.80	85	89	---	61
09/15/78	5.87	104	109	---	59
11/04/78	5.57	45	44	---	10
11/29/78	6.01	156	167	---	69
06/23/79	5.92	120	127	---	186
07/07/79	5.87	103	109		
08/04/79	6.01	156	167	---	146
08/18/79	6.03	166	177	---	152
10/28/79	6.06	182	194	---	67

TABLE 1 (Concluded)

Date	$m_b(Lg)$	— Estimated explosion yield, in kilotons —			
		quadratic eq. this study	linear eq. this study	Dahlman and Israelson (1977)	Sykes and Ci- fuentes (1984)*
12/02/79	6.05	176	188	---	70
12/23/79	6.12	219	232	---	152
06/12/80	5.74	71	74	---	---
06/29/80	5.71	65	68	---	19
09/14/80	6.09	200	212	---	184
10/12/80	5.92	120	127	---	48
12/14/80	5.92	120	127	---	57
12/27/80	6.00	152	162	---	39
03/29/81	5.45	32	31	---	---
04/22/81	5.97	139	148	---	57
09/13/81	6.10	206	219	---	94
10/18/81	6.09	200	212	---	82
12/27/81	6.15	241	254	---	210
04/25/82	6.13	226	239	---	105
07/04/82	6.14	234	247	---	192
12/05/82	6.21	293	305	---	---
10/06/83	5.93	126	131	---	---
10/26/83	6.10	206	219	---	---
02/19/84	5.74	71	74	---	---
03/07/84	5.68	60	62	---	---
03/29/84	5.97	139	148	---	---
04/25/84	5.86	100	106	---	---
05/26/84	6.07	188	200	---	---
07/14/84	6.17	257	270	---	---
10/27/84	6.10	206	219	---	---
12/02/84	5.97	139	148	---	---
12/16/84	6.08	194	206	---	---
12/28/84	6.13	226	239	---	---
02/10/85	5.98	144	152	---	---

* Sykes and Cifuentes (1984) considered these upper-bound estimates.

** Marshall et al (1979) state that the announced yield was 125 kt, in a cratered, water-saturated sandstone.

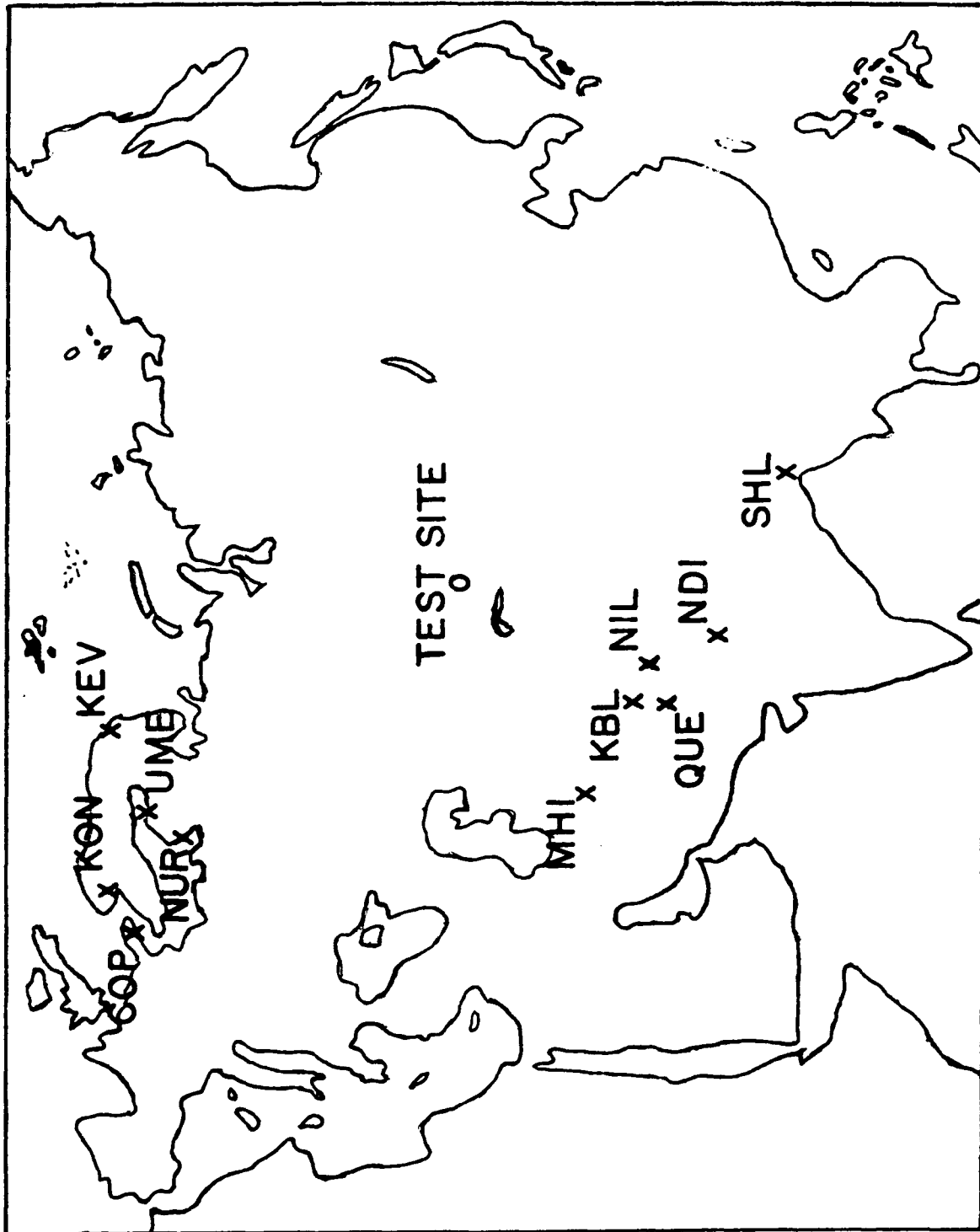


Figure 1. Location of the Shagan River Test Site and of the WWSSN stations whose data were used.

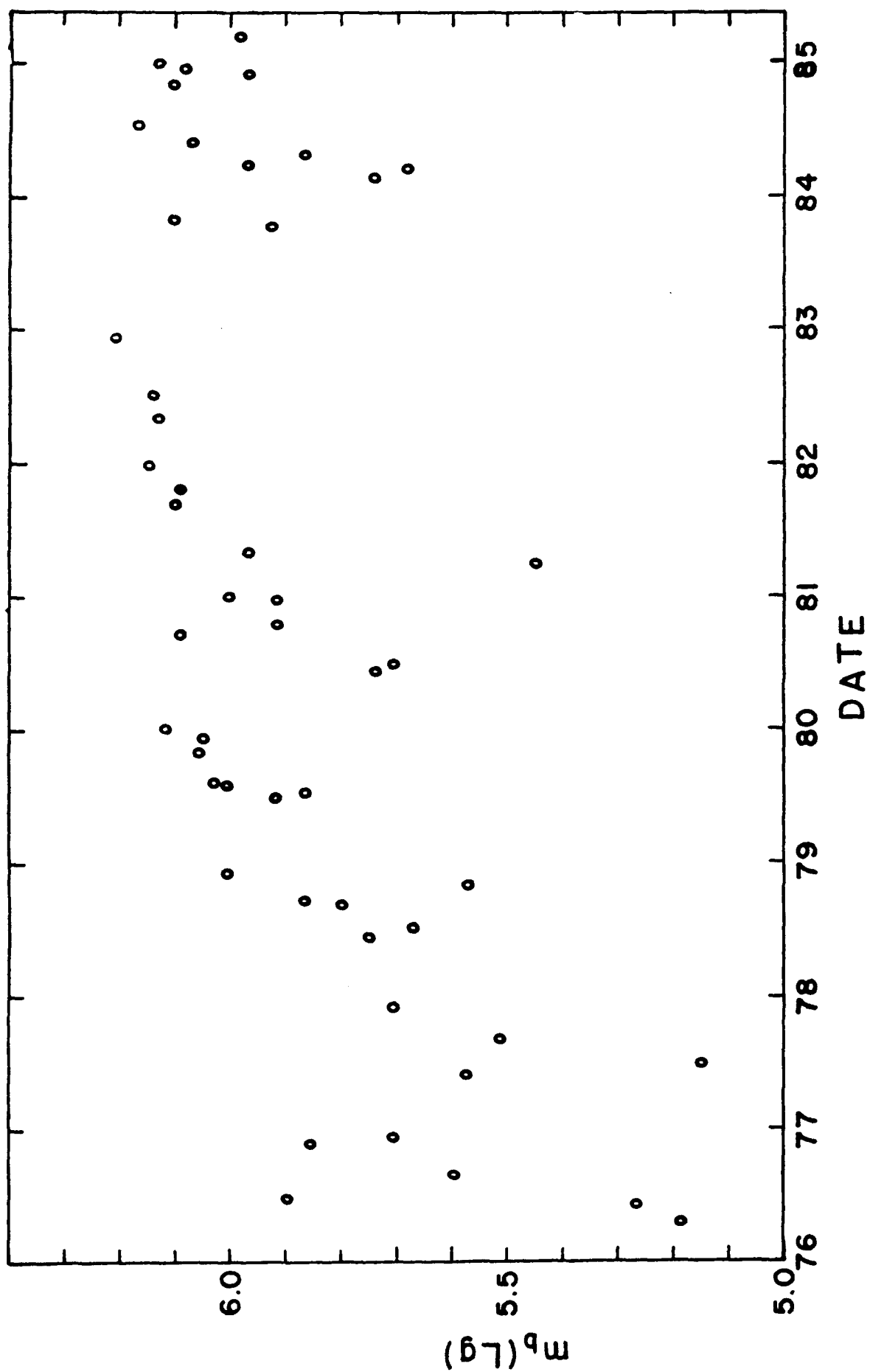


Figure 2. $m_b(Lg)$ values of Shagan River Test Site explosions from 1976 to 1985.

ANALYSIS OF TELESEISMIC P WAVE AMPLITUDE AND CODA
VARIATIONS FOR UNDERGROUND EXPLOSIONS

THORNE LAY, CHRISTOPHER LYNNEs, JOAN WELC
DEPARTMENT OF GEOLOGICAL SCIENCES
UNIVERSITY OF MICHIGAN

A large data set of more than 2200 teleseismic P wave recordings from 59 NTS events is being analyzed with the intent of establishing the near-source contribution to observed amplitude, travel time and coda variations. The data have been processed uniformly, enabling one-to-one correlations between magnitude and travel time anomalies, as in Figure 1. Pahute Mesa observations have a stronger correlation coefficient (0.302 for individual observations, 0.364 for station averages) than for Yucca Flat events (0.191 for individual observations, 0.207 for station averages), supporting a focussing/defocussing interpretation of the Pahute Mesa amplitude pattern. However, much of the travel time pattern originates far from the source region, given a strong correlation ($ccc=0.946$) found between station-averaged residuals for the two subsites. The station-averaged amplitude and travel time patterns for the two sites are shown in stereographic projections in Figure 2. The differenced patterns (Pahute Mesa - Yucca Flat) are shown on the right, indicating the near-source component. Note that the differenced patterns retain slowly varying components, which we are attempting to explain deterministically using backprojection and thin lens modeling procedures. Figure 3 shows an example of backprojecting the anomalies to surfaces at different depths beneath NTS. This procedure is used to constrain the spatial dimensions of the upper mantle heterogeneity.

The complete waveform information in the first 15 sec of the P arrivals for the entire data set is being analyzed as well, using statistical and deterministic procedures. The statistical procedure involves computing the energy temporal centroid of the P wave envelope for each station, applying corrections to the centroid accounting for station and source effects, and averaging the resulting

measurements for each event. These average complexity (energy flux) anomalies are then correlated with known event parameters as in Figure 4, in order to empirically establish the mechanisms affecting the waveforms. Correlations with position in the test site for Pahute Mesa events, and with magnitude (and hence pP delay and burial depth) for Novaya Zemlya events have been detected. Inspection of the azimuthal patterns of the individual complexity measurements shows slowly varying patterns for Pahute Mesa that will further constrain the causes of the waveform variations. Analysis of the frequency dependence of the coda variations has shown that some events in Pahute Mesa have azimuthal patterns of late high frequency arrivals, possibly produced by early aftershocks. Figure 5 shows observations for GREELEY, for which stations in the loop directions of the tectonic release radiation pattern have late high frequency energy. Figure 6 shows examples of the azimuthal patterns of the differences between the envelope centroid times for high and low frequency passbands for several NTS events. The slowly varying patterns, together with the differences in pattern from event to event demonstrate that near source effects are responsible. We are attempting to establish whether these variations are due to tectonic release or whether they are related to the upper mantle heterogeneity that produces the first arrival amplitude patterns.

An attempt to provide a deterministic interpretation of some of the P wave coda in the first 15 sec of the teleseismic waveforms is being made using slant stacking procedures. The basic idea is to seek scatterer locations in the near-source vicinity. Energy ratio coherency measures and semblance are being used to appraise the slant stacking output. Station and event weighting filters have been developed to reduce the influence of correlated noise in the data, and the full 1300 waveform data set for Pahute Mesa events is being utilized.

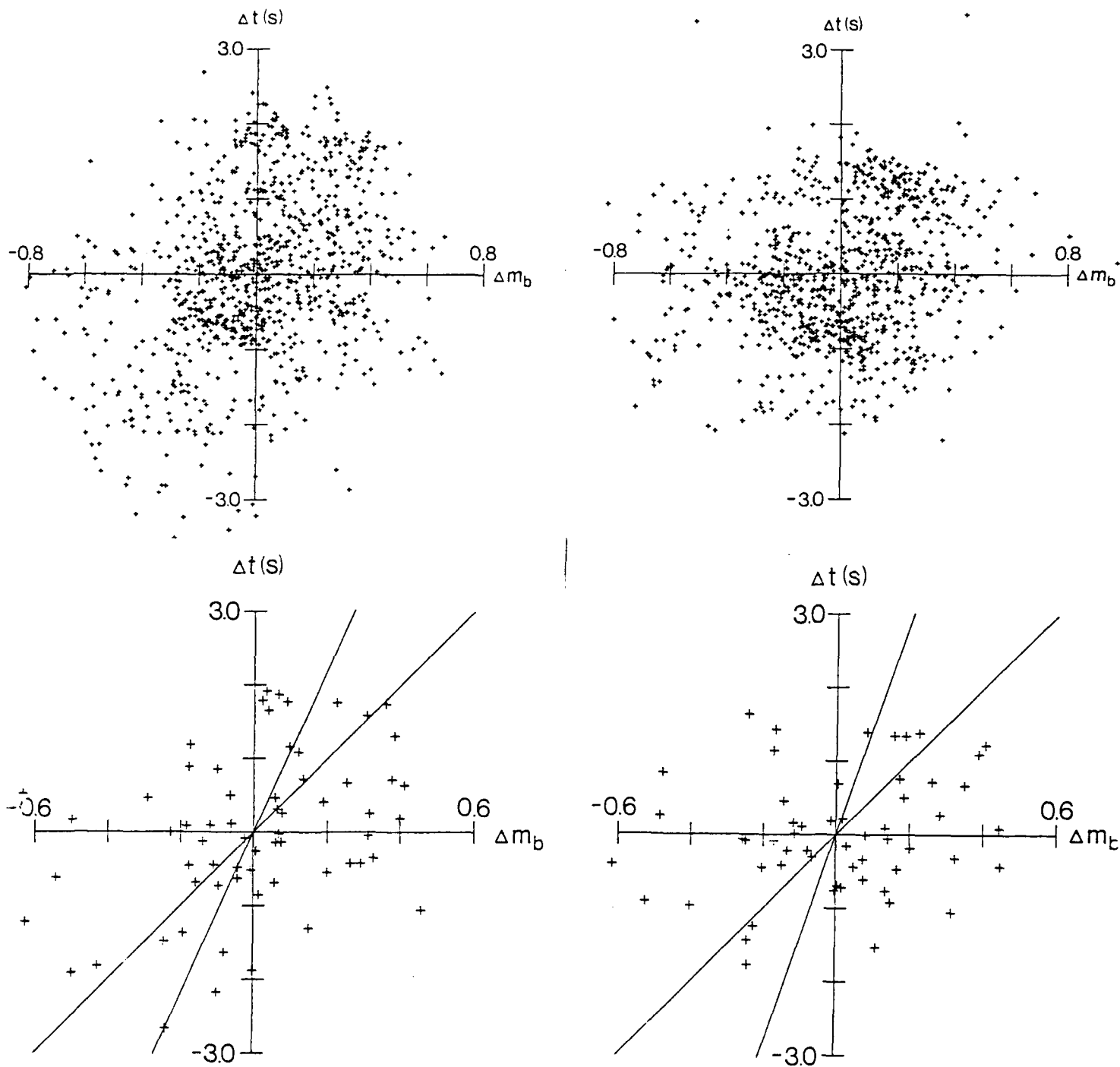


Figure 1. Top: One-to-one correlation of magnitude and travel time anomalies for Pahute Mesa events (left) and Yucca Flat events (right). Bottom: A similar correlation, except using the average station anomalies rather than individual observations.

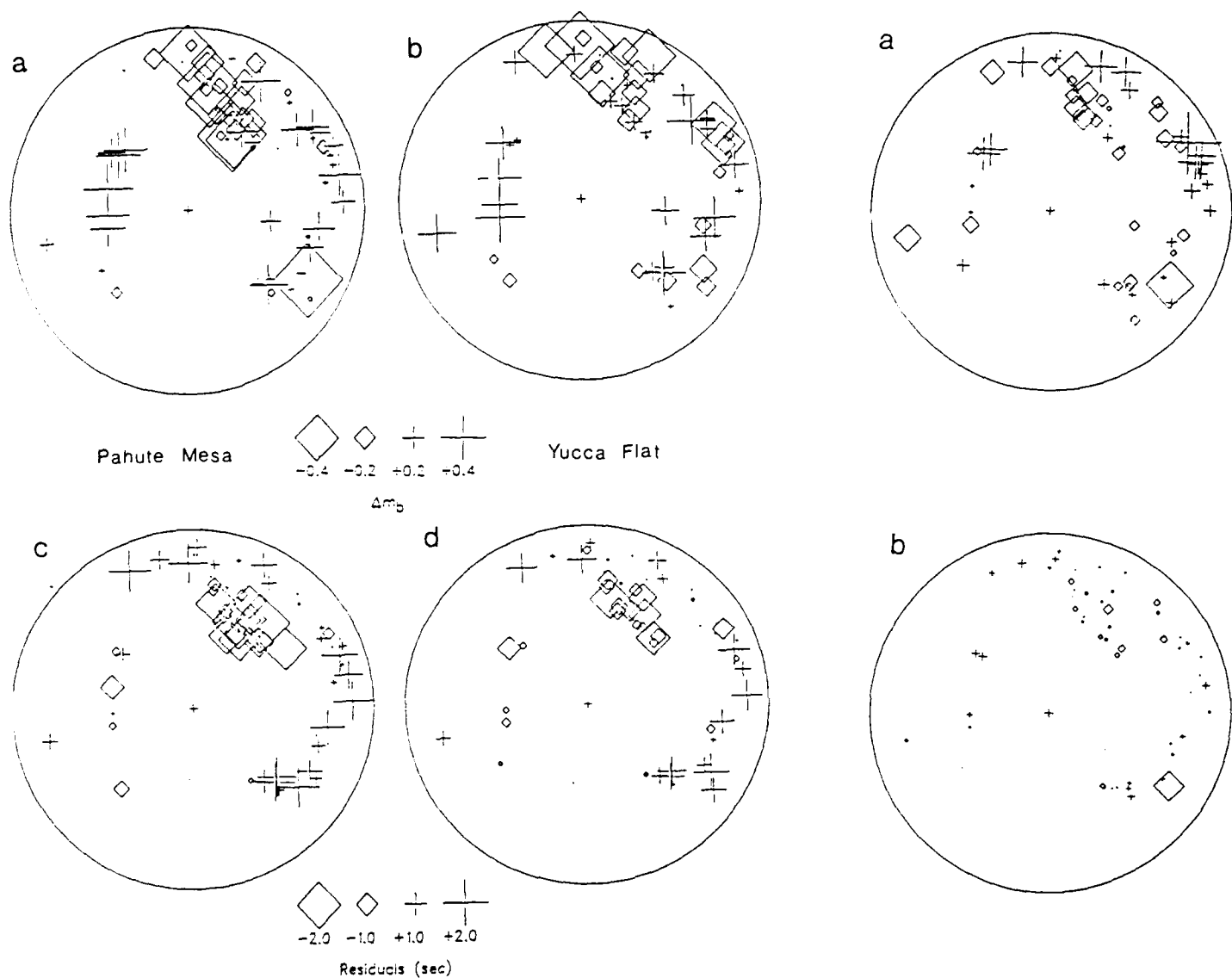


Figure 2a.

Figure 2b.

Figure 2. a) Lower hemisphere, equal area projections showing the average station magnitude and travel time anomalies for Pahute Mesa events (left) and Yucca Flat events (right). Note the shift of the amplitude patterns between the two sites and the mutual shift relative to the travel time patterns. The outer perimeter is for a 45° take-off angle for a reference velocity of 7.8 km/sec. b) Similar projections of the difference in station anomalies obtained by subtracting the Yucca Flat values from those for Pahute Mesa.

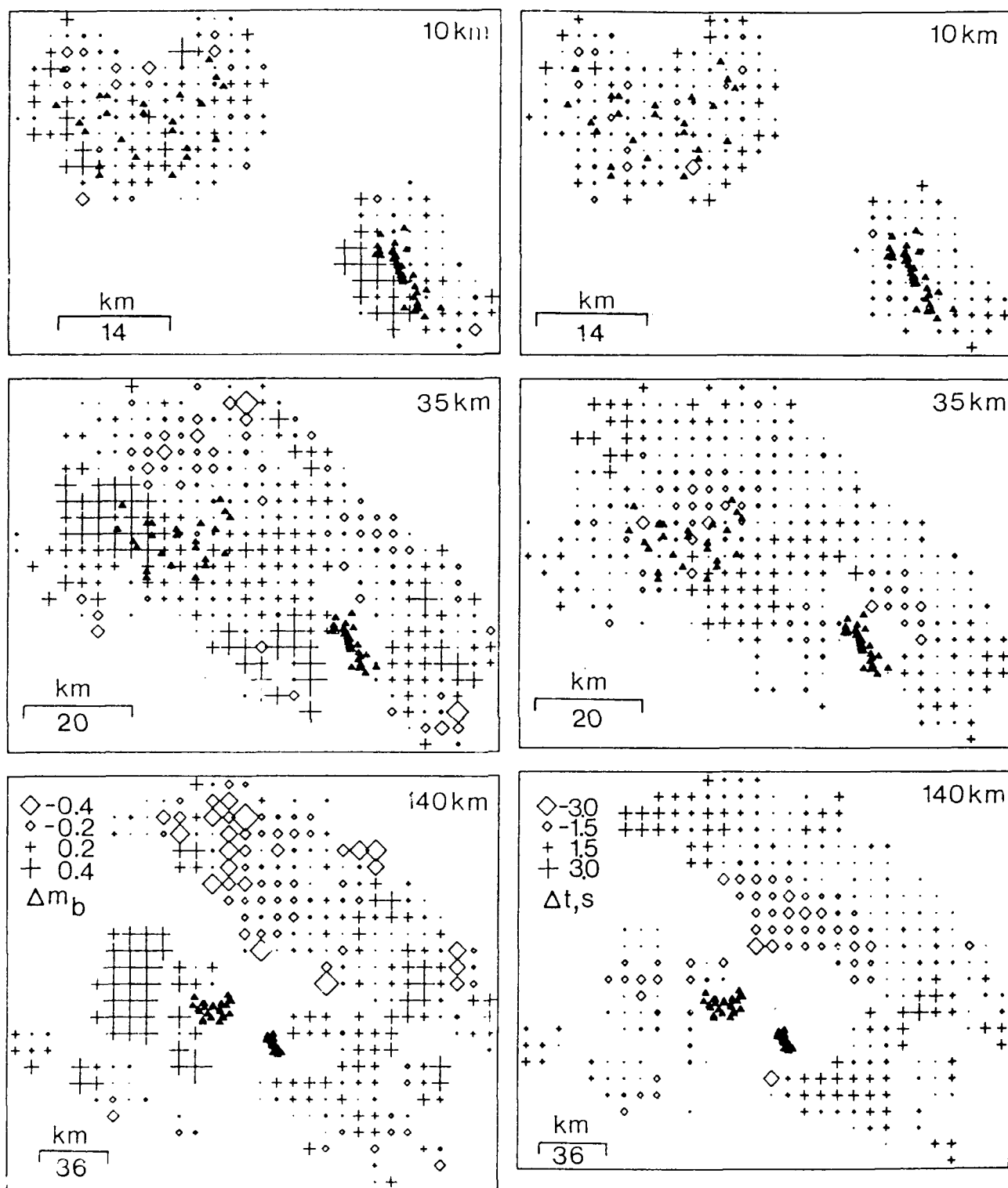


Figure 3. Backprojections onto surfaces below NTS for amplitude (left) and travel time (right) anomalies for both Pahute Mesa and Yucca Flat events. The surfaces have been bin-averaged to smooth the pattern for the 2000 observations. Note that a depth of greater than 35 km is suggested for the origin of the common amplitude and travel time features for the two test sites.

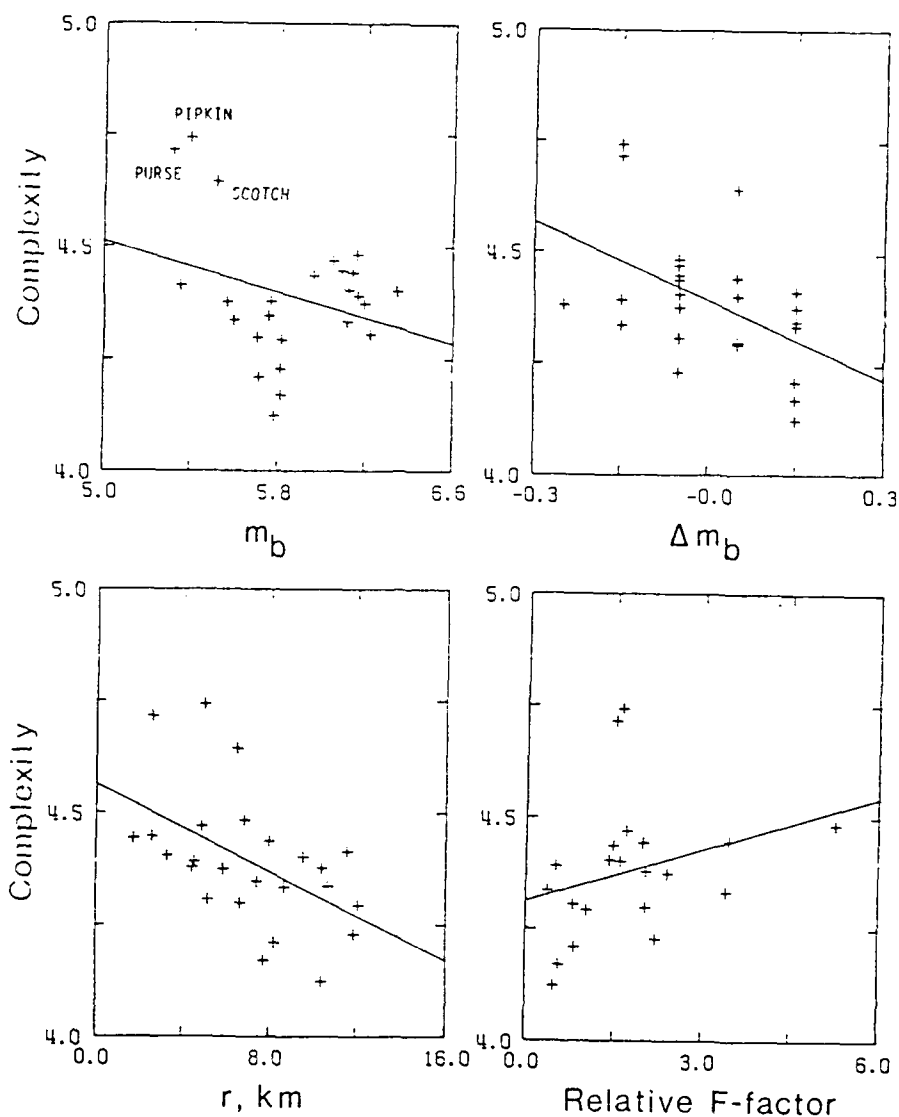


Figure 4a.

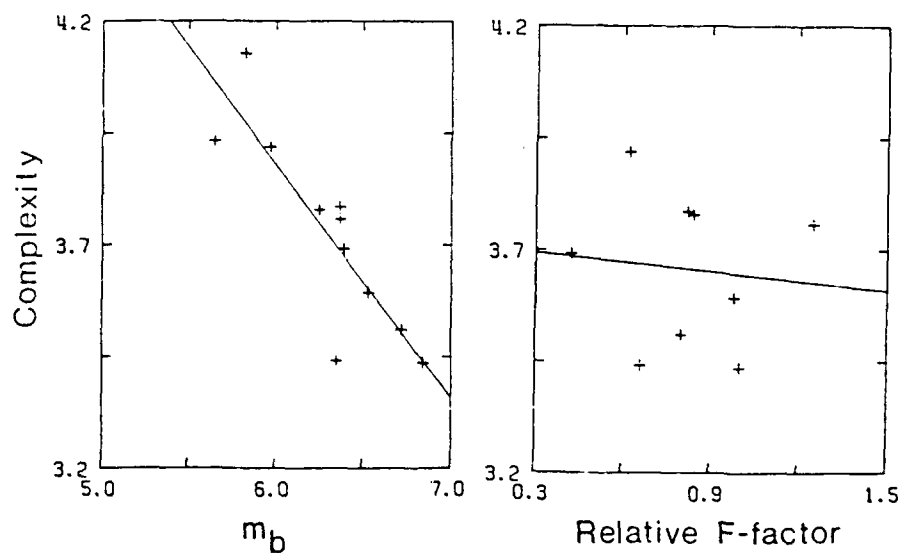


Figure 4b.

Figure 4. a) Regression of average event complexity factors for Pahute Mesa events on m_b , event magnitude anomaly, distance from the center of the mesa, and relative tectonic release F-factor. b) Regression of average event complexity factors for Northern Novaya Zemlya events on m_b and F-factor.

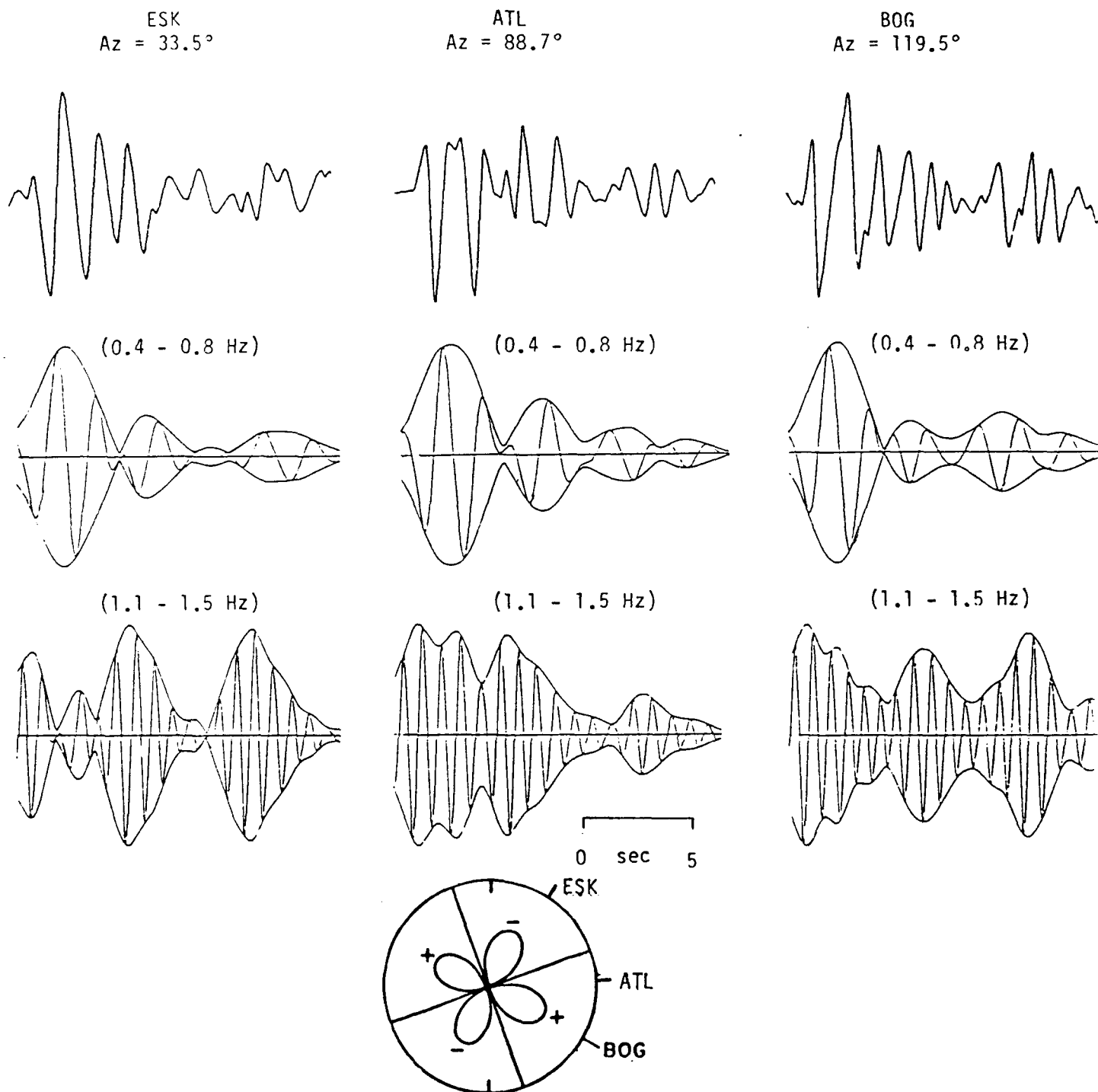


Figure 5. Example of frequency dependence of the coda envelopes for observations for GREELEY. The top row is the original trace for three WWSSN stations. The middle row is the narrowband filtered trace with passband 0.4 - 0.8Hz, and the bottom row is a higher passband of 1.1 - 1.5Hz. The instrument response has been deconvolved in all the filtered traces. Note the late, high frequency pulse for ESK and BOG, which are in loop directions of the tectonic release P radiation pattern. ATL is along the tectonic release P radiation node. 173

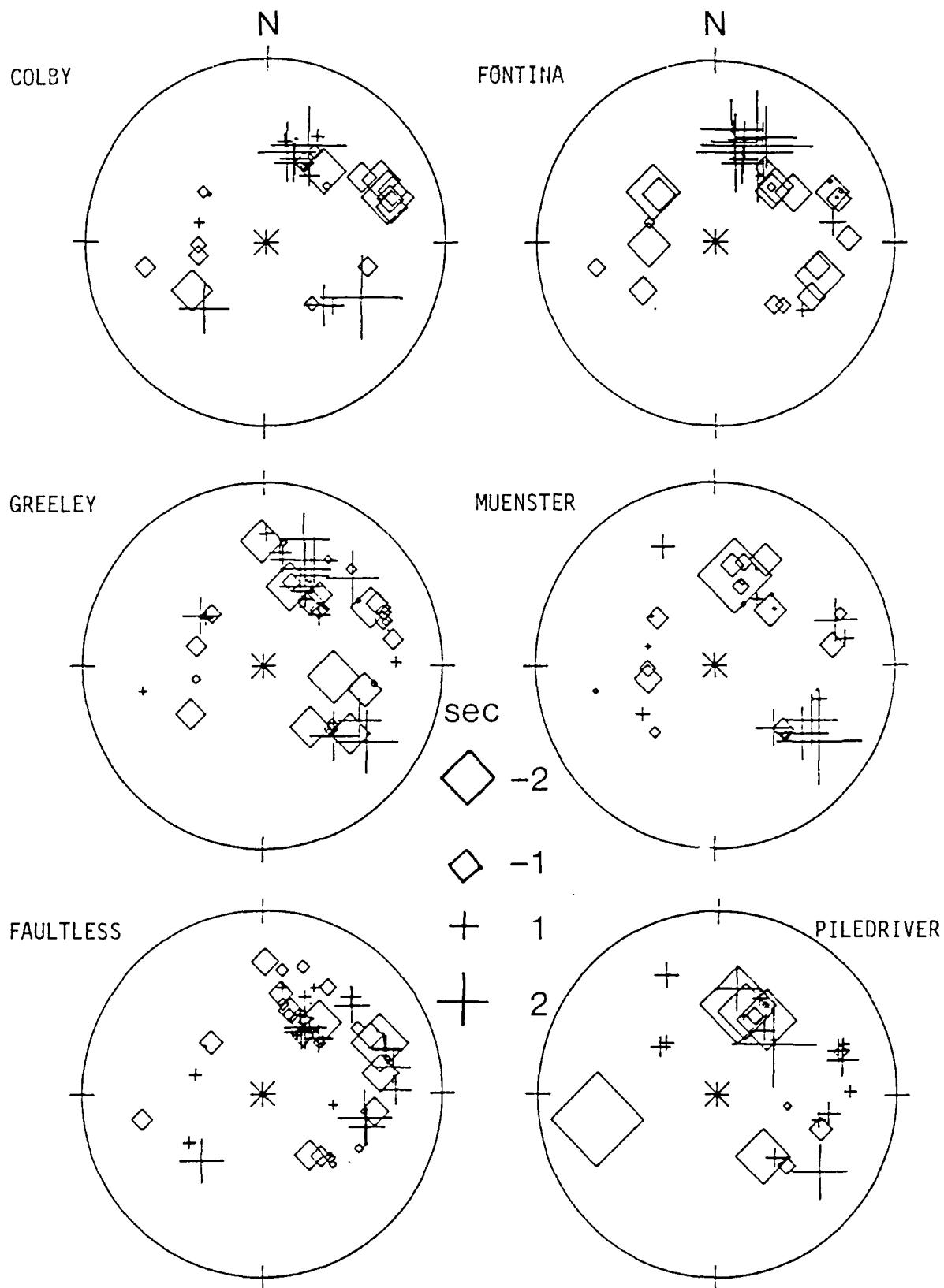


Figure 6. Lower hemisphere stereographic projections of the difference in energy temporal centroid for the 0.8 - 1.2 Hz and 0.4 - 0.8 Hz bands. Plus symbols indicate late relative high frequency arrivals.

COMPARISON OF MATCHED-FILTERS TO TIME-VARIABLE FILTERS FOR AMPLITUDE
DETERMINATION OF NORMAL MODES IN SURFACE WAVE ANALYSIS

DAVID R. RUSSELL
HORNG-JYE HWANG

ST. LOUIS UNIVERSITY

A currently accepted method for amplitude determination of normal modes is phase-matched filtering (Stevens, 1986). The phase-matched filter (PMF) involves centering a zero-lag symmetric window in the time domain on the "pseudo-autocorrelation" function, found by removing the phase of a particular mode of interest (Herrin and Goforth, 1977). It can be shown (Jenkins and Watts, 1968), that the bias in the amplitude spectrum caused from time-windowing an autocorrelation function is proportional to the second derivative of the amplitude spectrum:

$$B(\omega) = \frac{\pi^2}{M^2} A''(\omega) \quad (1)$$

where

B = bias
 M = one-sided width of symmetric time-domain window
 A'' = second derivative of amplitude spectrum
 ω = angular frequency

In this case it is assumed that a cosine window is used; other windows will change the coefficient multiplying the second derivative. This bias can be significant in the vicinity of band-edges of the spectrum or in any region of high curvature. It can be reduced by extending the window width M , but this may introduce extraneous noise (or signals) into the spectrum.

To reduce the problem of bias and noise, the following time-variable filter is constructed:

$$\bar{f}(t) = \frac{1}{2\pi} \int_{-\infty}^{\infty} F(\omega) \left[S\left(t + \frac{2\pi\alpha}{|\omega|}\right) - S\left(t - \frac{2\pi\alpha}{|\omega|}\right) \right] \cos\left(\frac{\omega t}{4\alpha}\right) e^{j\omega t} d\omega \quad (2)$$

where

$F(\omega)$ = pseudo-autocorrelation function
 $S(\)$ = unit step function
 α = M/T
 M = one-sided width of cosine window at period T

Taking the Fourier transform of $\bar{f}(t)$ gives the amplitude spectrum of the mode of interest. The above integral consists of a sum of symmetrically windowed Fourier harmonics about zero-lag in the time domain. In the traditional sense of a TVF, the windows are symmetric about the group velocity peaks found from multiple filter analysis (Dziewonski and Hales, 1972, p. 74). Equation (2) is similar to the traditional TVF after residual dispersion is applied (Dziewonski and Hales, 1972, p. 76), except that the basis for this method is phase-matched filtering instead of multiple filter analysis.

To test the method, a normal mode synthetic seismogram was constructed at a distance of 6000 km from the source. The signal was lagged behind itself by 300 seconds (to simulate multiple events) and superimposed on the original signal. Gaussian noise was then added to the superimposed signal to give the effect of random noise (figure 1). The noisy seismogram was then phase-matched filtered about the original signal and both PMF and TVF analysis was performed. Figure 2 shows the effect of using a $M=300$ second window for the PMF and an $M=3T$ family of windows for the TVF. Due to the wide window width, neither of the spectra show significant bias, but the TVF has a superior signal to noise level. Figure 3 demonstrates the effect of narrowing the window. For the PMF, $M=75$ seconds. The TVF still has $M=3T$, but the maximum window width is not allowed to exceed 75 seconds. At long periods (> 60 seconds), both methods exhibit bias in the amplitude spectra. However, the TVF is still superior in reducing short period noise.

Another test was made with an earthquake source mechanism at a distance of 1000 km. The fundamental mode and a single higher mode was constructed

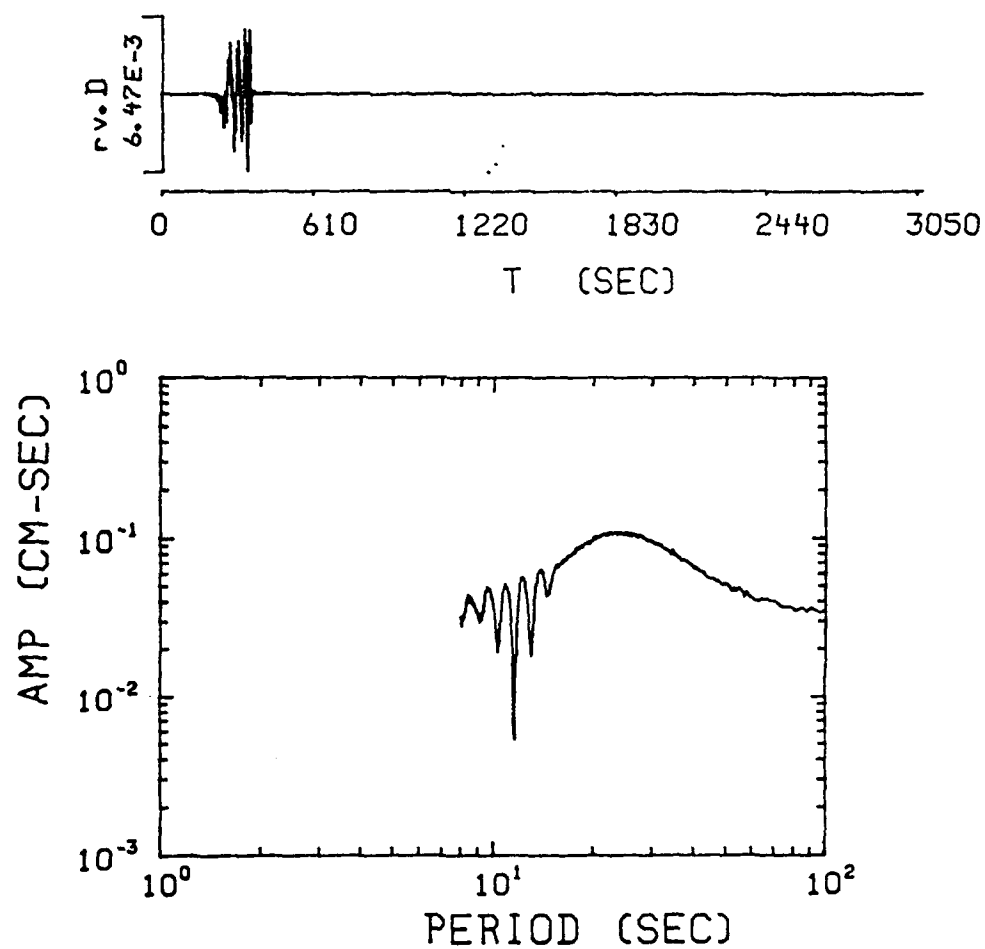


Figure 4. Synthetic normal mode seismogram of an earthquake recorded at 1000 km; fundamental and 1 higher mode present.

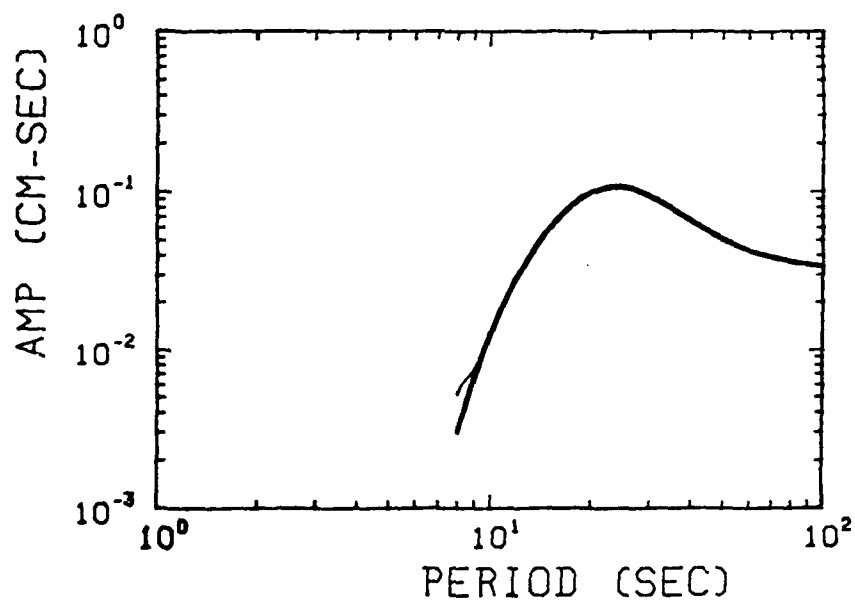
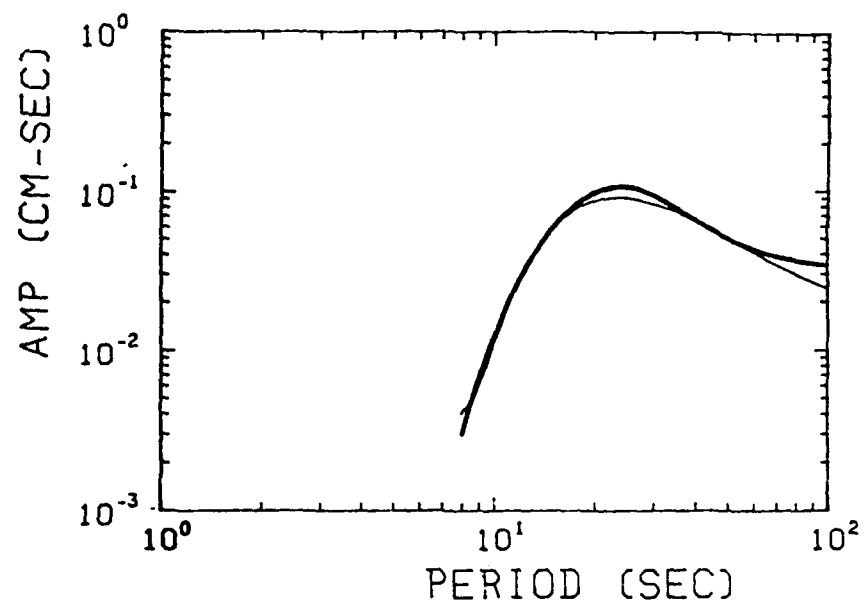


Figure 5. Heavy lines: theoretical fundamental mode of the earthquake.

Top: PMF with $M=75$ seconds.

Bottom: TVF with $M=3T$.

to see the effect of the two techniques on isolating the fundamental mode (figure 4). In figure 5, the PMF had to have a maximum window width of $M=75$ seconds to isolate the fundamental mode. Observe the bias at periods greater than 60 seconds and at 20 seconds, illustrating the effect of curvature on the windowed amplitude spectrum (equation 1). The TVF was constructed with $M=3T$ and no long period constraints. This was possible since the higher mode was limited to the shorter periods. The TVF amplitude spectrum shows little difference from the theoretical fundamental mode.

Other tests on synthetics show that it is possible to reduce the width of the TVF window to $M=2T$ without significant distortion. However, these tests were made on given seismograms, and more analysis is needed to generalize the window width as a function of curvature of amplitude spectra.

REFERENCES

- Dziewonski, A., and A. L. Hales (1972). Numerical analysis of dispersed seismic waves, *Methods of computational physics*, vol. 11, Academic Press, New York, 39-85.
- Herrin, E., and T. Goforth (1977). Phase-matched filters: application to the study of Rayleigh waves, *Bull. Seis. Soc. Am.* 67, 1259-1275
- Jenkins, Gwilym M., and D. G. Watts (1968). *Spectral Analysis and Its Applications*, Holden Day, San Francisco.
- Stevens, Jeffry L. (1986). Estimation of Scalar Moments from Explosion-Generated Surface Waves, *Bull. Seis. Soc. Am.* 76, 123-152.

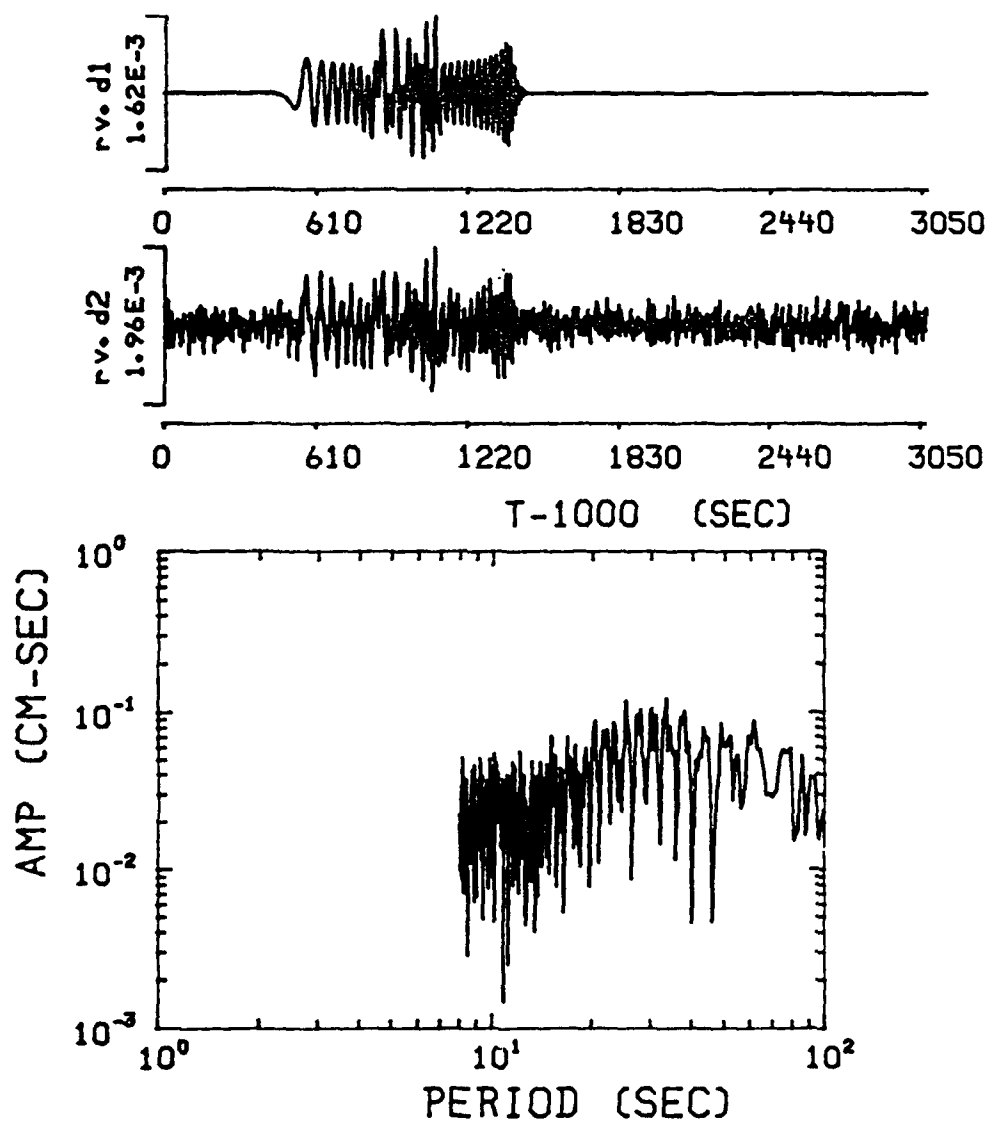


Figure 1. Synthetic normal mode explosion recorded at 6000 km.

Top: signal lagged and superimposed at 300 seconds.

Center: Gaussian noise added to signal.

Bottom: Amplitude spectrum of noisy seismogram.

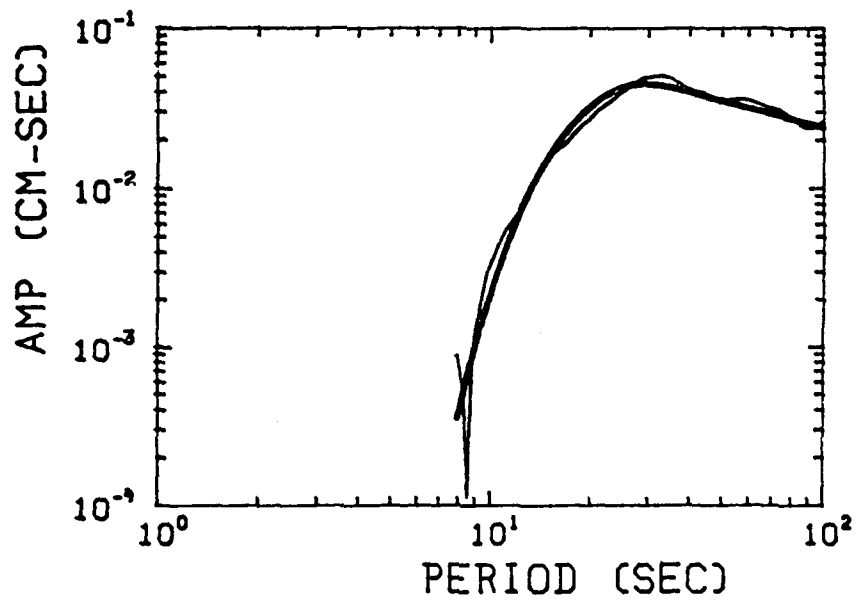
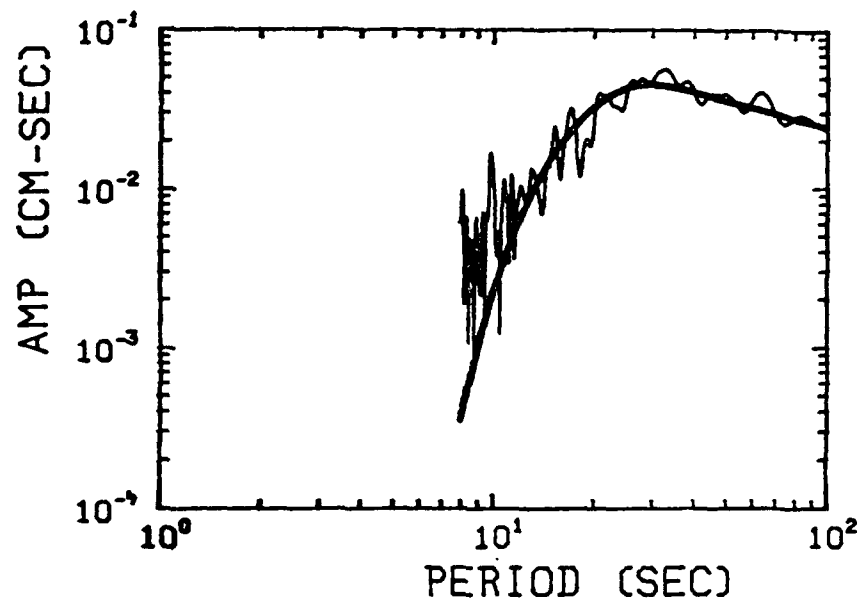


Figure 2. Heavy lines: theoretical fundamental mode of the explosion.

Top: PMF with $M=300$ seconds.

Bottom: TVF with $M=3T$.

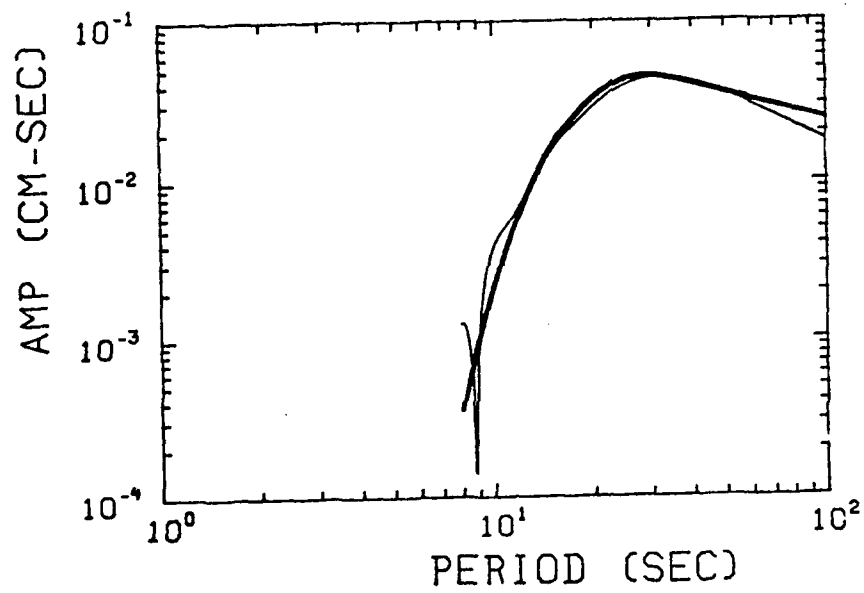
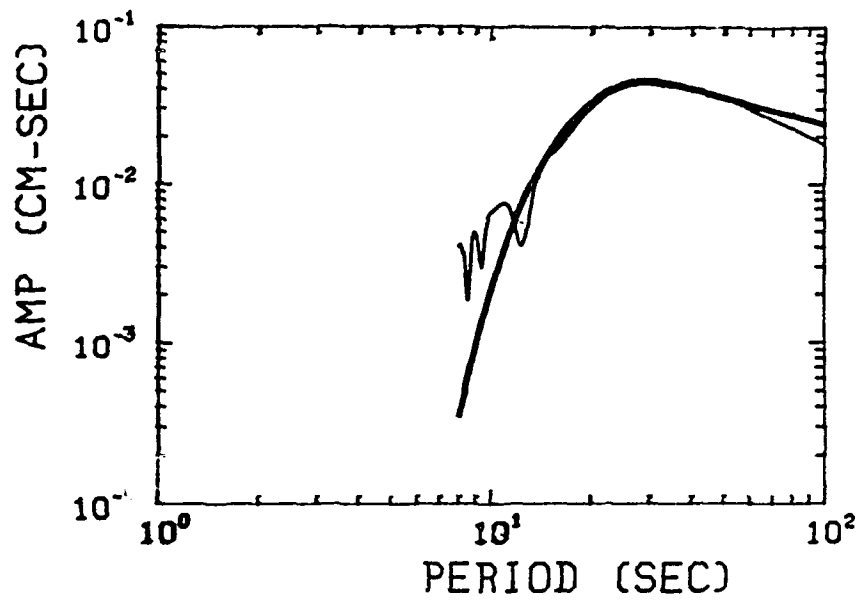


Figure 3. Heavy lines: theoretical fundamental mode of the explosion

Top: PMF with $M=75$ seconds.

Bottom: TVF with $M=3T$; window limited to 75 seconds and less.

ANELASTIC PROPERTIES OF THE CRUST AND UPPER MANTLE
IN STABLE AND TECTONICALLY ACTIVE REGIONS

H.J. Hwang and B.J. Mitchell
Department of Earth and Atmospheric Sciences
Saint Louis University

INTRODUCTION

An understanding of the attenuation rate of seismic waves with distance is fundamental to our capability to determine magnitudes of earthquakes and yields of nuclear events. It is also pertinent to detection studies, because seismic wave attenuation rates will govern the maximum distance to which seismic waves may be reliably recorded. We have determined the attenuation rate of seismic surface waves in several different regions of the Earth, some of which are relatively stable, and some of which are tectonically active, in order to determine the manner in which Q values and the frequency-dependence of those values, in the crust and upper mantle vary regionally. At shorter periods, our results pertain to properties of the crust, and are therefore important to an understanding of L_g propagation. At longer periods, they provide information on the upper mantle; they therefore should contribute to our ability to determine yields using teleseismic body waves.

DATA ANALYSIS

Most determinations of seismic wave attenuation are characterized by large uncertainties which limit our ability to study details of the distribution of the anelastic properties, or Q , of the Earth. Hwang and Mitchell (1986) recently showed that in two-station methods, measured attenuation coefficients, at long periods, are extremely sensitive to

noise contamination, and they developed a method which combines modal isolation and frequency-domain Wiener filtering, which appears to provide more stable and reliable determinations than methods previously developed.

New attenuation data, as well as phase and group velocity information, have been obtained for eastern South America, western South America, the Indian shield, and the Himalayas (Figure 1). These include both two-station data, as well as single-station data, which have been combined to yield dispersion and attenuation coefficient curves which span the range between a few seconds and 50-100 seconds, depending upon region. An example of the attenuation coefficient data for fundamental- and first higher-mode Rayleigh waves in the stable portion of eastern South America appears in Figure 2.

Our previous determinations of attenuation coefficients in stable regions were restricted to shorter periods, 30-50s at the long-period end, and were accompanied by larger standard deviations. As a consequence, our models were very poorly constrained at larger depths corresponding to the lower crust and upper mantle.

VELOCITY INVERSIONS

The phase and group velocity data were inverted using a differential inversion program, written by D.R. Russell, which minimizes the magnitude of the error vector of the solution plus the differences between adjacent solution elements (Twomey, 1977). In addition to the new data described above, older dispersion data for eastern and western North America were also reinverted using the new inversion scheme. Par-

tial derivatives of phase velocity with respect to layer parameters for these models were used in the Q inversion discussed in the following section. The dispersion data for all of the stable regions could be explained by models which do not include an upper mantle low-velocity zone. Because of the limited resolving power of the data at upper mantle depths, however, a minor low-velocity zone cannot be excluded on the basis of the surface wave data. Low-velocity zones are present, with varying degrees of severity and resolvability in all of the tectonically active regions. In regions where both Rayleigh wave and Love wave data are available, there is no need to invoke anisotropy of elastic properties to explain the data, at least to depths of about 150 km.

Q INVERSIONS

The attenuation coefficient data were inverted using methods which have been discussed in several previous studies (e.g. Mitchell, 1980), using the formulation of Anderson et al. (1965). A model resulting from the inversion of data in eastern South America is shown in Figure 2. In this stable region, as well as others, we find shear wave Q values in the lower crust and upper mantle which are lower than those previously found in stable regions. We attribute this difference to improved data quality at longer periods, compared to that of our earlier studies.

As a rule, shear wave Q values in tectonically active regions are significantly lower than those in stable regions, throughout the crust and upper mantle. There is, however, a large variability in the Q models, even among those for stable regions. In particular, shear wave Q values at crustal depths beneath the Indian shield are significantly

lower than those of other shields. These lower values may be related to higher than normal reduced heat flow values which have been determined in the Indian shield (Rao *et al.*, 1976). A comparison of shear wave Q models for several regions appears in Figure 3.

FREQUENCY DEPENDENCE OF Q

It is possible to study the frequency dependence of shear wave Q in the crust, over a limited period range, by comparing the theoretical Q values of 1-Hz Lg waves produced by the velocity and Q models described above, with observed Q values of Lg. Theoretical values of Lg Q can be obtained by computing short-period synthetic seismograms at several distances, measuring amplitudes of Lg at each distance, and computing the Q values needed to explain the amplitude fall-off with distance. In this way we obtain a Q value for Lg in much the same way that observers obtain it from real seismograms.

This process results in theoretical Q values which are very similar to observed values in tectonically active regions. Our Q models for those regions can therefore be independent of frequency and satisfactorily explain observed surface wave attenuation over a broad period range (1 s to several 10's of seconds). In stable regions, however, the models we obtain predict Lg Q values which are lower than those observed. This result indicates that shear wave Q is frequency-dependent in those regions, being higher at a period of 1 s than at longer periods.

REFERENCES

Anderson, D.L., A. Ben-Menahem, and C.B. Archambeau, Attenuation of

- seismic energy in the upper mantle, J. Geophys. Res., 70, 1441-1448, 1965.
- Hwang, H.J., and B.J. Mitchell, Inter-station surface wave analysis by frequency-domain Wiener deconvolution and modal isolation, Bull. Seism. Soc. Am., in press, 1986.
- Mitchell, B.J., Frequency dependence of shear wave internal friction in the continental crust of eastern North America, J. Geophys. Res., 85, 5212-5218, 1980.
- Rao, R.V.M., G.V. Rao, and H. Narrain, Radioactive heat generation and heat flow in the Indian shield, Earth Planet. Sci. Lett., 30, 57-64, 1976.
- Twomey. S., Introduction to the Mathematics of Inversion in Remote Sensing and Indirect Measurements, Elsevier Scientific Publishing Co., Amsterdam, 237 pp.

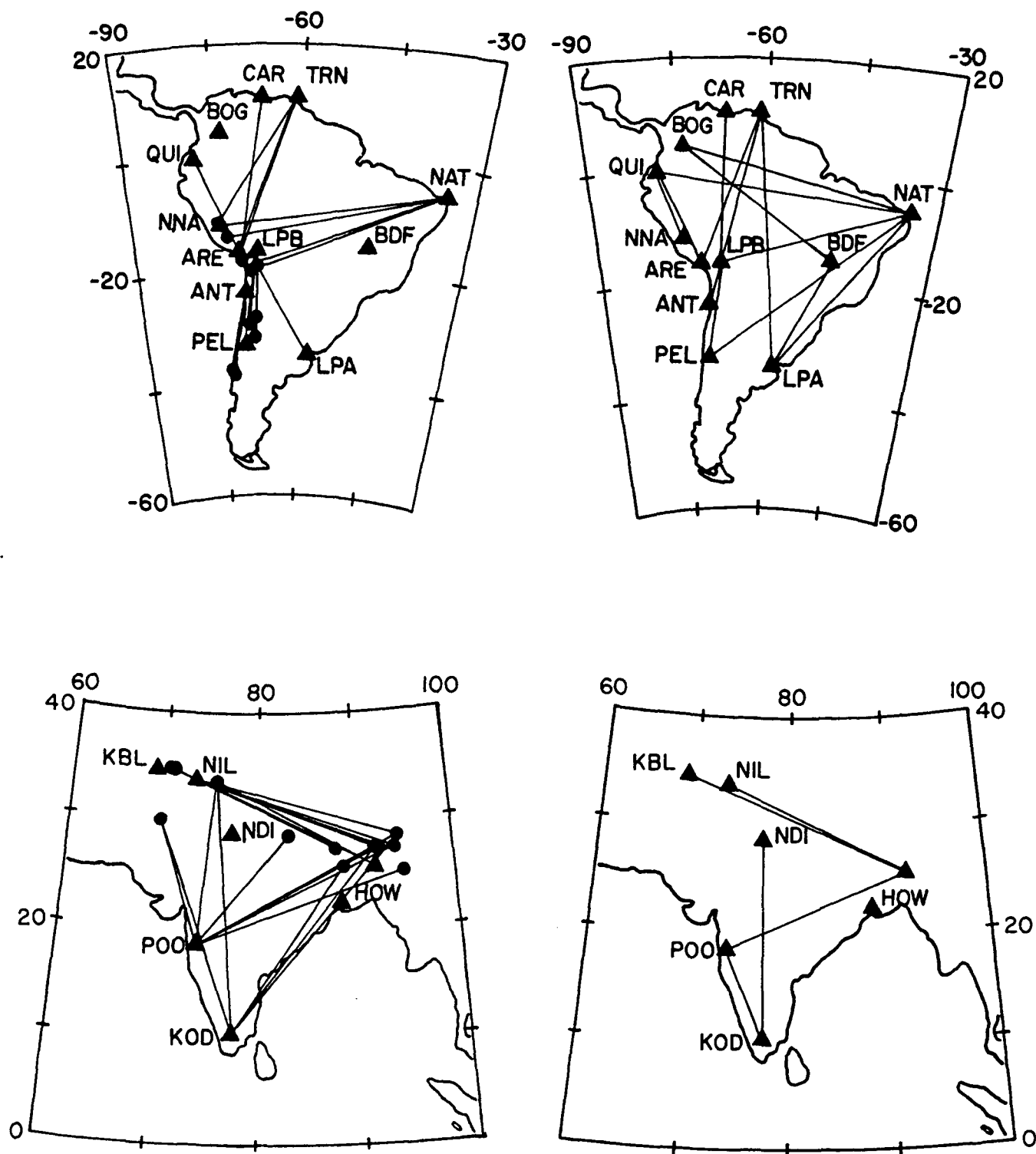


Figure 1. Surface wave paths across South America (top) and India (bottom) used for determining dispersion and attenuation. Single-station paths are shown on the left and two-station paths on the right.

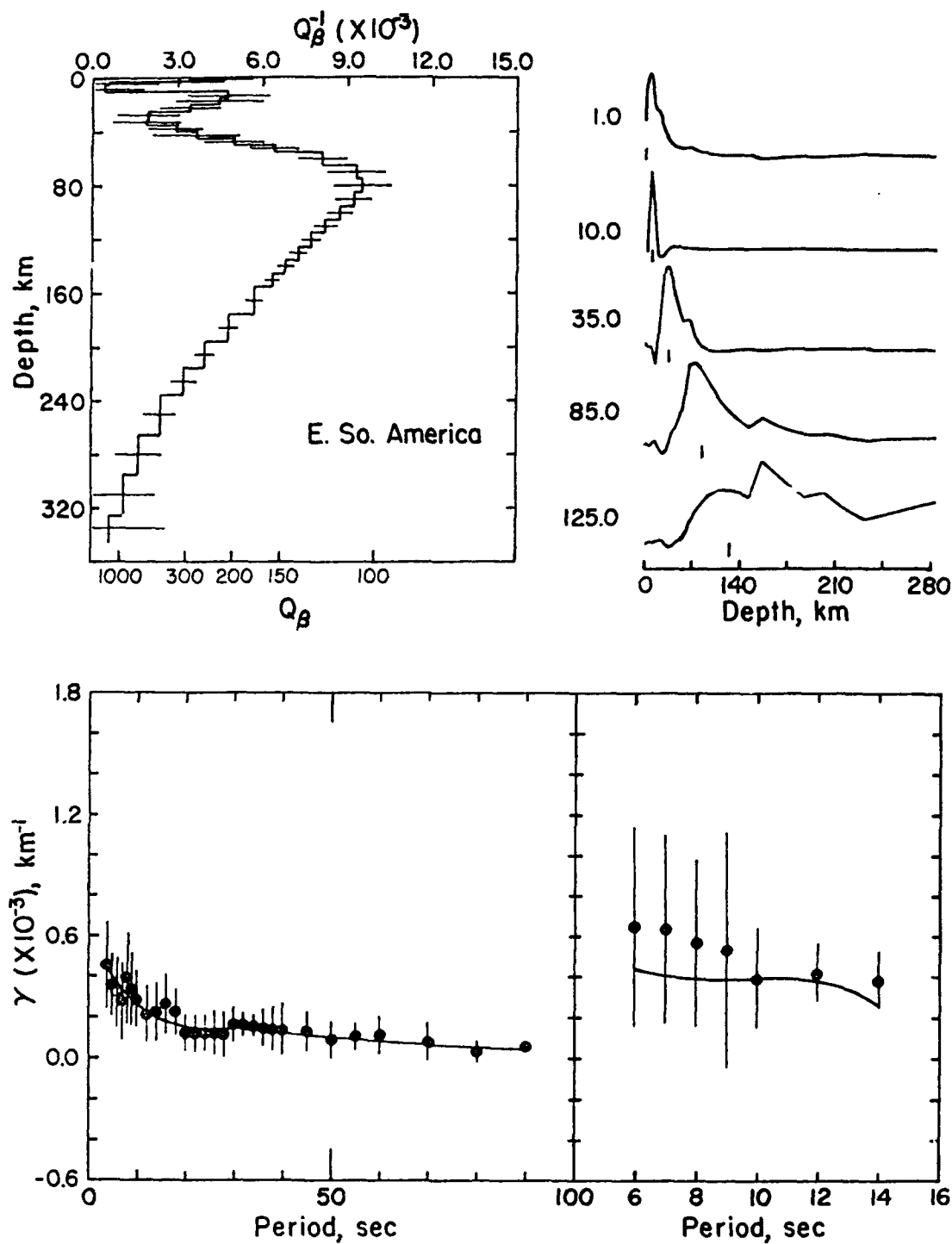


Figure 2. Shear wave Q model for eastern South America (upper left), along with resolving kernels (upper right). Comparison of observed and theoretical attenuation coefficient values for fundamental-mode Rayleigh waves (bottom left) and first higher-mode Rayleigh waves (bottom right) are shown for the model above.

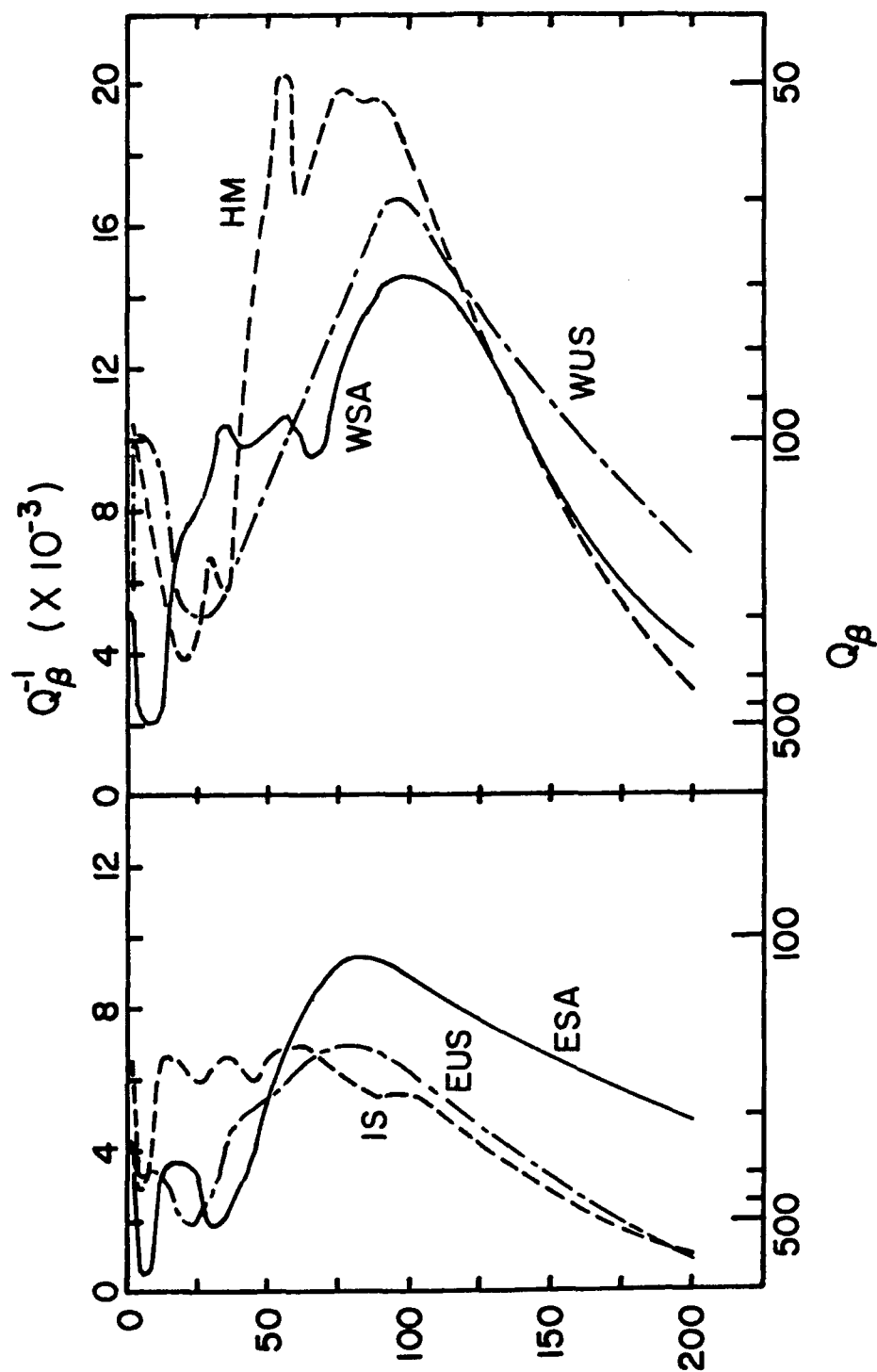
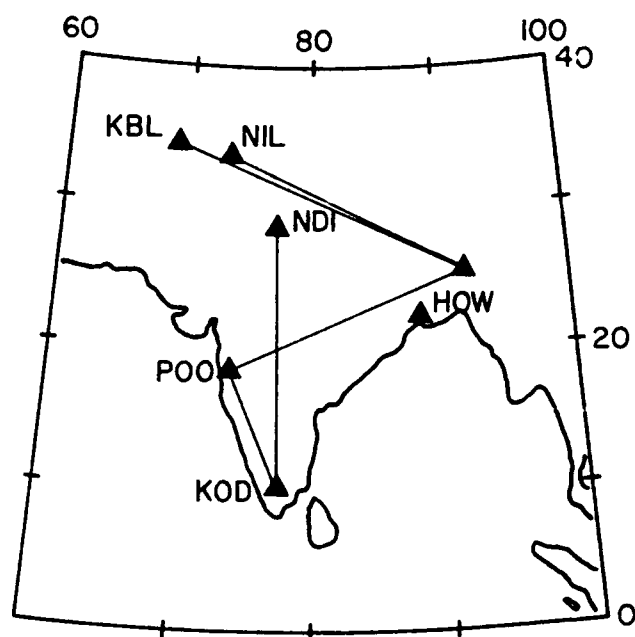
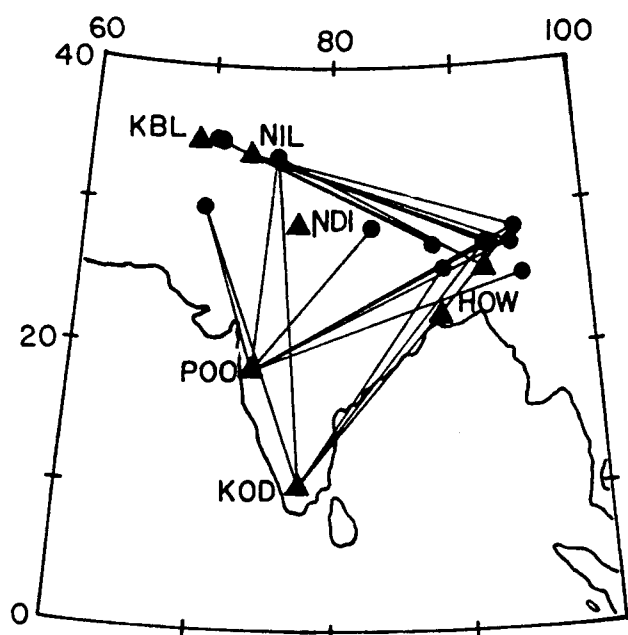
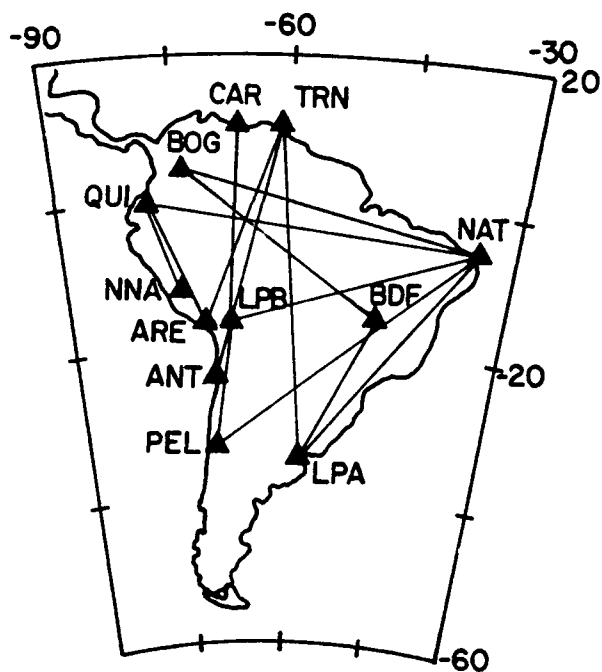
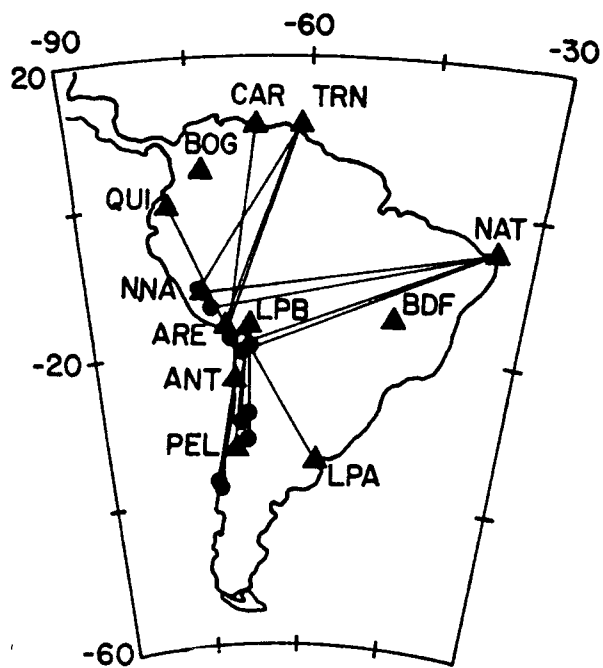
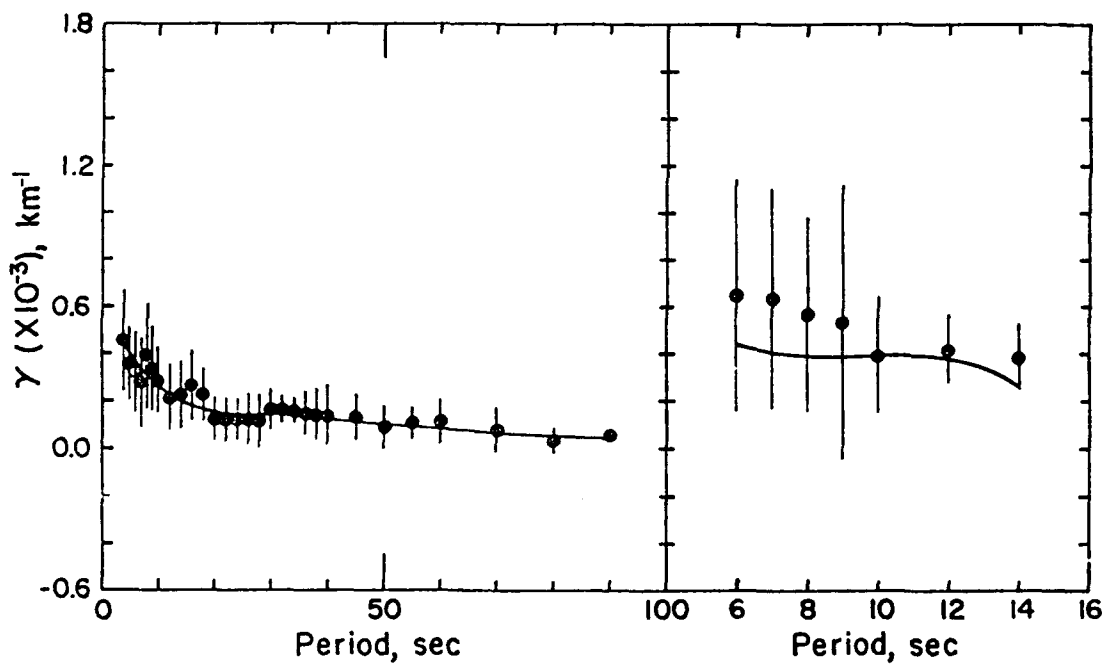
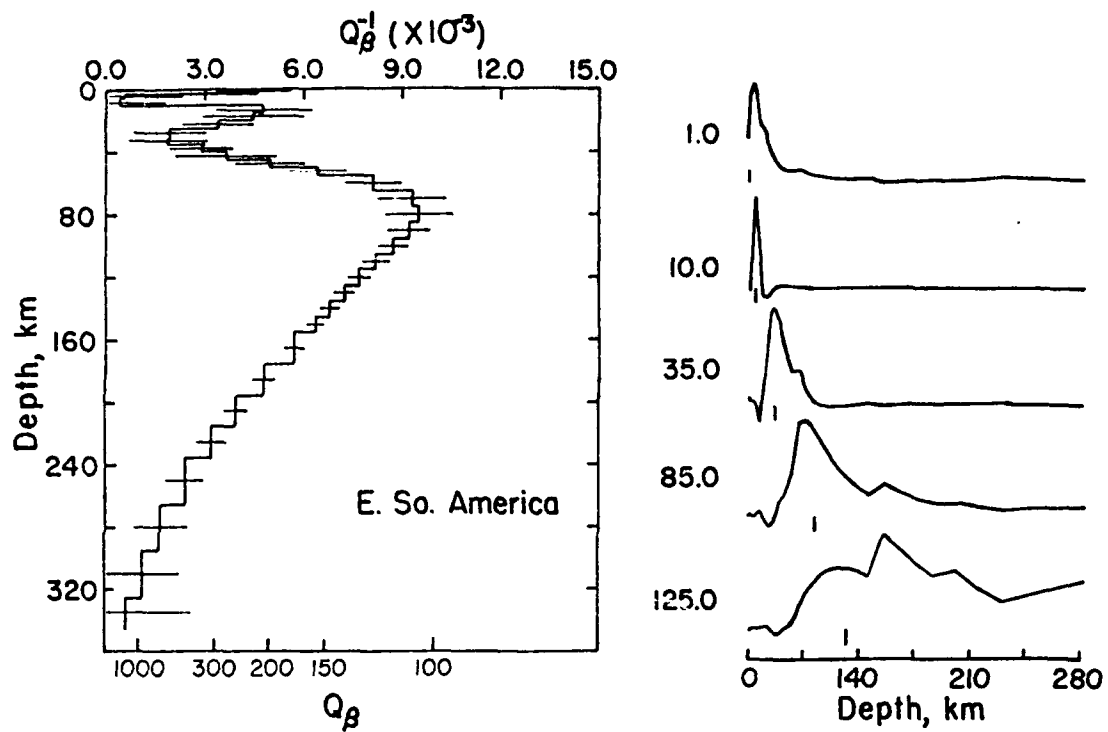
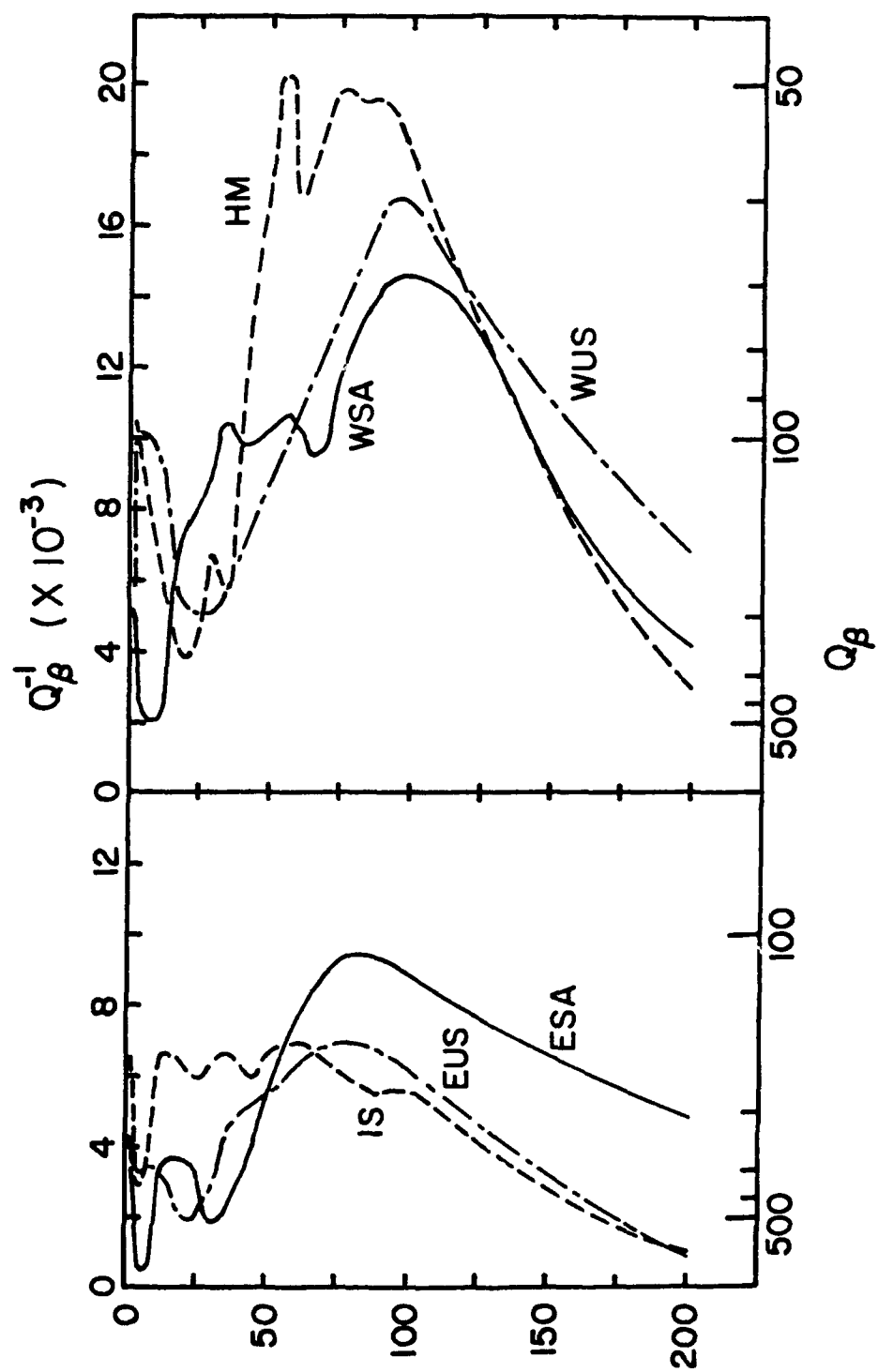


Figure 3. Summary of shear wave Q distributions with depth for stable regions (left) and tectonically active regions (right). IS - Indian Shield, EUS - Eastern United States, ESA - Eastern South America, HM - Himalaya Mountains, WSA - Western South America, WUS - Western United States.







P WAVE ATTENUATION, m_b BIAS and
the THRESHOLD TEST BAN TREATY

Thomas C. Bache, Steven R. Bratt and Lolitia B. Bache

Science Applications International Corporation
10210 Campus Point Drive, San Diego, California 92121

INTRODUCTION

Concern about Soviet compliance with the 150Kt TTBT limit is motivated by the large m_b of Shagan River tests and by the pattern of testing at that site (Figure 1). Before 1976 a broad range of yields were tested at Shagan River, including four with $m_b > 6.0$. The yields of Novaya Zemlya tests were sharply reduced after 31 March 1976. For the first two years of the threshold the Shagan River test yields were a factor of 1.5 - 2.0 less than for previous tests at that site. During 1978 the yield increased, and many tests since then have yields that are about a factor of two larger than the yield limit apparently observed in 1976-1978. There are two main competing hypotheses to explain this pattern:

1. The m_b bias between NTS tuff/rhyolite and Shagan River is large (0.4-0.5) and all Shagan River yields are 150Kt or less. For some reason the Soviets chose to restrict their testing to 75-100Kt during the first two years after the limit went into effect.
2. The m_b bias between NTS tuff/rhyolite and Shagan River is moderate (about 0.2 or so). The events in 1976-1978 (maximum $m_b = 5.92$) have yields up to 150Kt. Events after 1979 have yields up to twice that level.

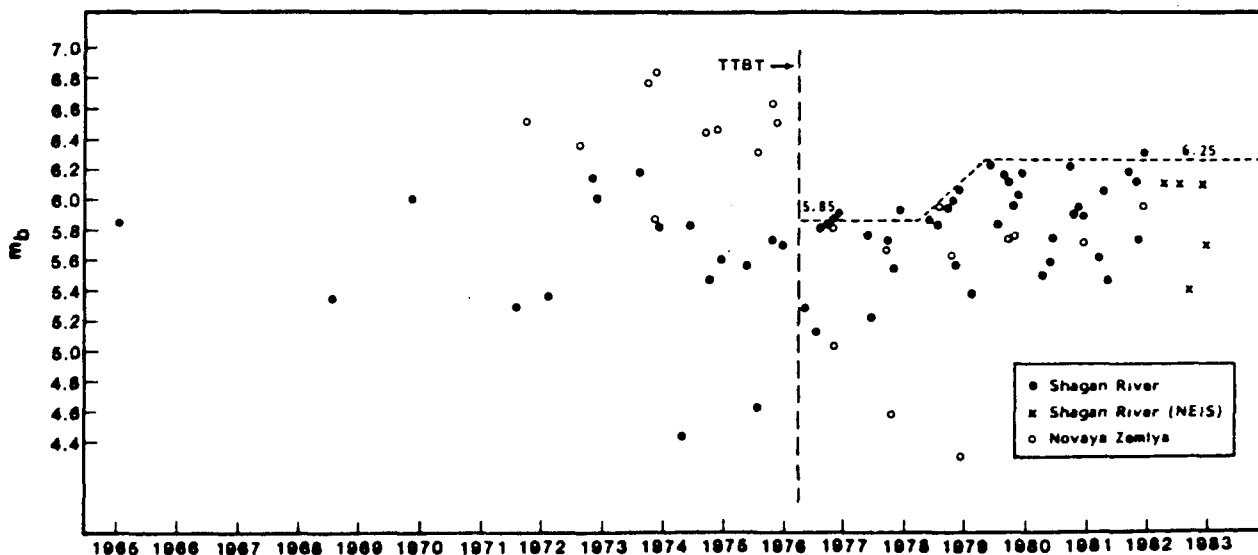


Figure 1 The m_b are plotted versus time for all large Novaya Zemlya and Shagan River explosions. Except for the NEIS m_b , the Shagan River m_b are from Marshall et. al. (1985) and the Novaya Zemlya m_b were computed by Marshall (personal communication) with the same method. The date on which the TTBT limit began to be observed is marked. The horizontal lines are drawn at the indicated m_b .

The major causes for m_b bias are differences in source coupling and average path attenuation. Large source coupling differences exist (e.g., between saturated and unsaturated tuffs), but given the paucity of data from the Shagan River site, we can only make some informed guesses about the contribution of source coupling differences to m_b bias. The average path attenuation differences between NTS and E. Kazakh seem easier to estimate. NTS is in a tectonic region known to have high attenuation. A cursory examination of waveforms from NTS and E. Kazakh explosions shows that the latter are much richer in high frequency energy. Some attenuation bias is almost certainly present, but precisely how large is it?

APPROACH

Our approach involves the following steps:

- A. We analyze recordings of U.S. and Soviet explosions using data from the arrays EKA, YKA, WRA, GBA and NORSAR. Our technique is to average over array elements and over many similar events at a test site. The result is smooth and consistent spectra that display the combined effect of the source and attenuation ($t^*(f)$).
- B. Using these spectra we develop $t^*(f)$ models that explain the spectral character from below 0.5 Hz to as high as 8 Hz (for E. Kazakh).
- C. We explore tradeoffs between source and attenuation models.
- D. The m_b bias is estimated with synthetic seismograms that provide a good match to the data in both the time and frequency domain.
- E. Our results are compared to results from other studies and the conclusions summarized within a broad context.

This approach differs from that of previous studies by using spectra that are more consistent and simpler to interpret. Also, our interpretation is based on synthetic seismograms that force a specific statement of all assumptions. Thus, there is no way to avoid confrontation with the uncertainties. Finally, we have tried to be reasonably complete, synthesizing much of the relevant evidence in one study.

RESULTS

The array spectrum for each event is obtained by averaging spectra from the individual array elements. For each element we compute the energy density spectra for short time windows isolating the P wave, then subtract the power spectrum for a noise sample taken before P. These "noise-corrected" energy density spectra are then averaged over all elements of the array and converted to Fourier spectra.

The array spectra variations are consistent with yield-dependent corner frequency variations. Correcting for the source, we can deduce the attenuation. We assume that the NTS explosions can be represented by the Mueller and Murphy (1971) tuff/rhyolite source model while E. Kazakh explosions are represented by the Mueller/Murphy granite model. We make "source corrections" to each event spectrum with these assumptions and average the "source-corrected" spectra for groups of similar events. The results are shown in Figure 2 for E. Kazakh and in Figure 3 for NTS. The m_b bias depends on attenuation below about 2 Hz, but this

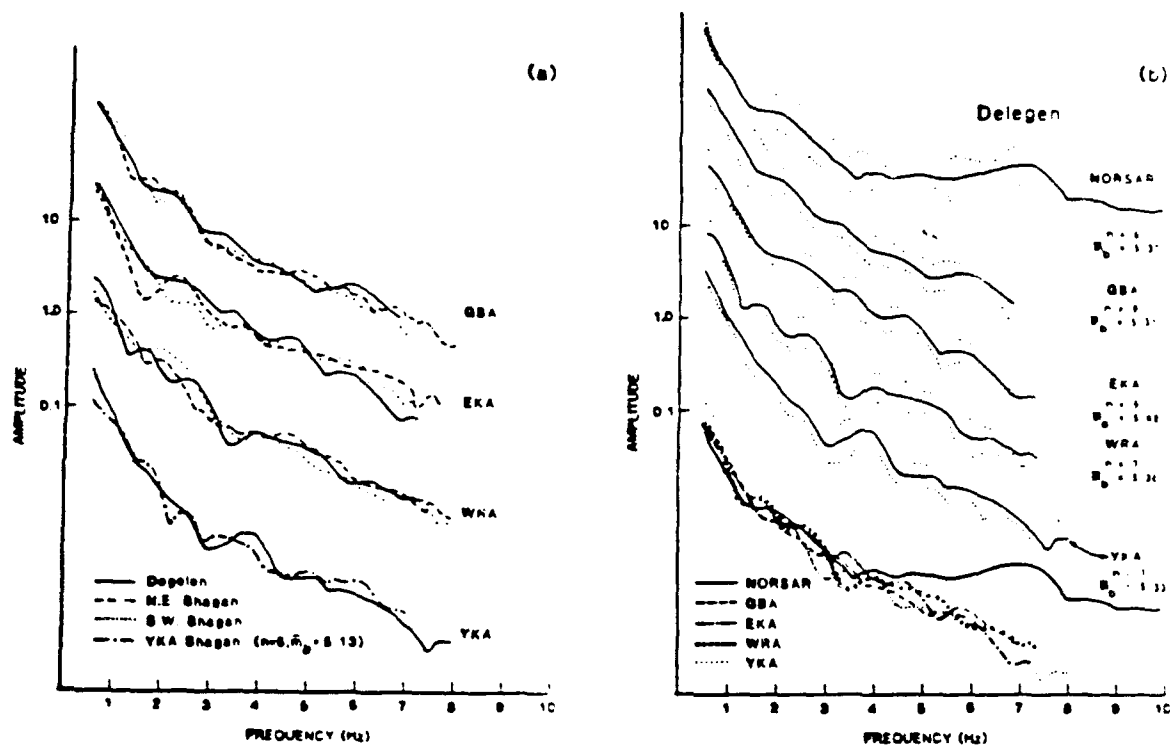


Figure 2 Source corrected path spectra are plotted for each data set considered. In (a) we compare the path spectra from different portions of the test site at each UKAEA station (at YKA there are too few data to bisect the Shagan River site). In (b) the mean spectrum for the Degelen paths is shown with dotted lines indicating the sample standard deviation. At the bottom of (b) is shown a comparison of the mean spectra for the paths from that particular source area to each station. (Reproduced from Bache et al., 1986).

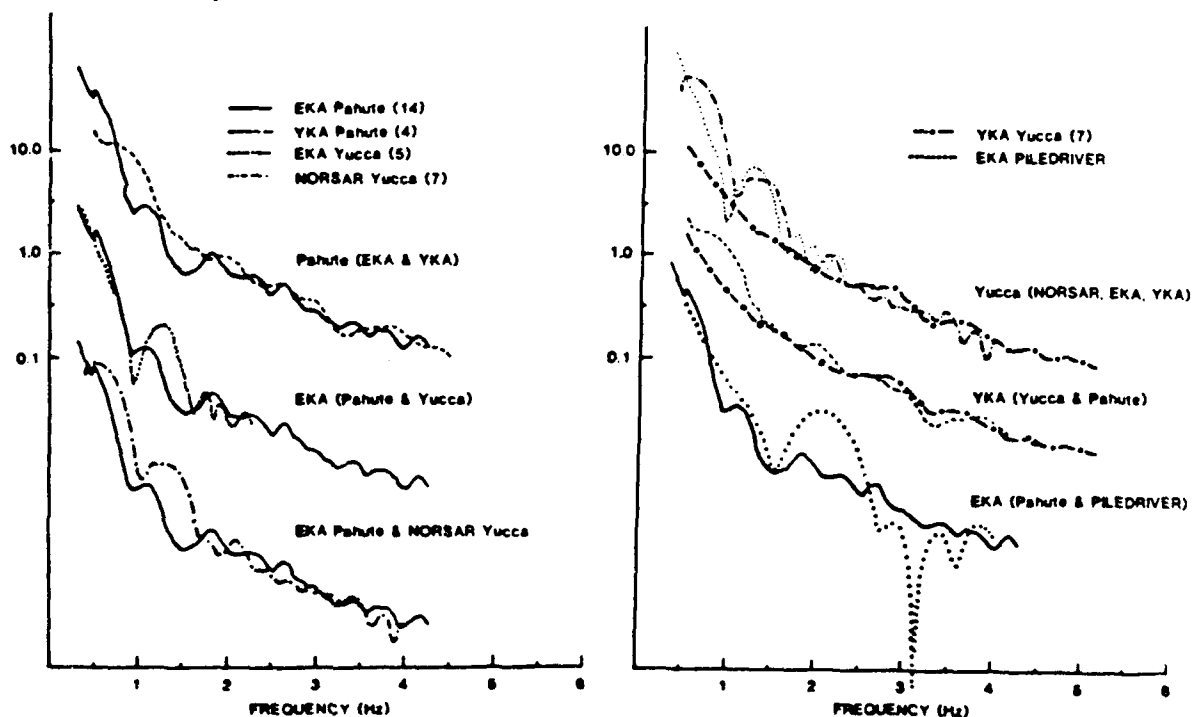


Figure 3 The path-average spectra for Piledriver and five event populations are compared. The number in parentheses indicates the number of events in each population. In each of these comparisons the spectra have been aligned so they coincide at high frequencies.

depends on our assumptions about the source. This is indicated in Figure 4, where the source-corrected path spectra are shown for several choices for the source model.

For any reasonable source assumptions, it is clear that frequency-dependent attenuation is required to match the data. We use a two-parameter absorption band model. The parameters are t_0^* (the long period t^*) and r_m , which controls the frequency-dependence. A variety of models that fit the data are shown in Figure 5. All give time domain waveforms that match the data equally well. The m_b for various synthetic seismograms are plotted in Figure 6 with the " m_b bias" due to attenuation effects only. There can be additional bias due to source-coupling differences. For example, the differences between Mueller-Murphy tuff and granite sources introduces an additional bias of 0.2 m_b . However, there is little or no evidence that source-coupling differences this large occur at NTS, much less at E. Kazakh.

The "medium bias" results are most consistent with conventional ideas for source spectra and the attenuation differences at long period between NTS and shield-like regions. The "small bias" can occur if the E. Kazakh explosions have substantially more high frequency energy than the Mueller-Murphy granite source, or if the apparent attenuation differences near 1 Hz reflect r_m differences with Δt_0^* rather small.

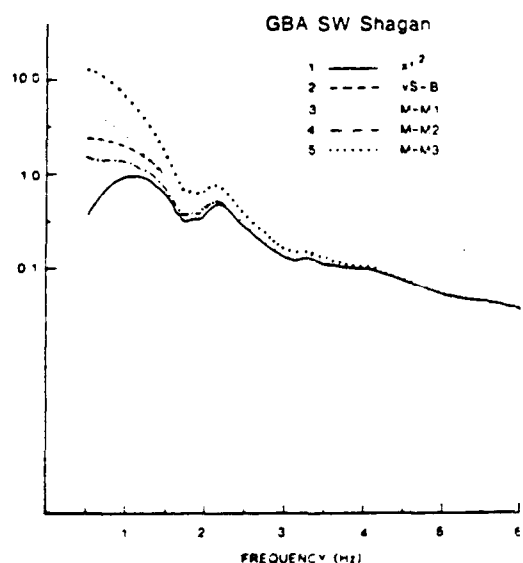


Figure 4

The effect of several alternative source corrections are shown for the GBA S.W. Shagan spectra. The amplitudes are normalized to be identical at high frequency. The M-M1 is the standard Mueller-Murphy granite source. The VS-B is the von Seggern and Blandford (1972) granite source with the same assumptions (m_b 6.0 corresponds to 150Kt and $m_b = 0.9$ for W). The M-M2 and M-M3 sources are nearly the same as M-M1, except that the frequencies have been shifted down (M-M2) or up (M-M3) by a factor of 1.6.

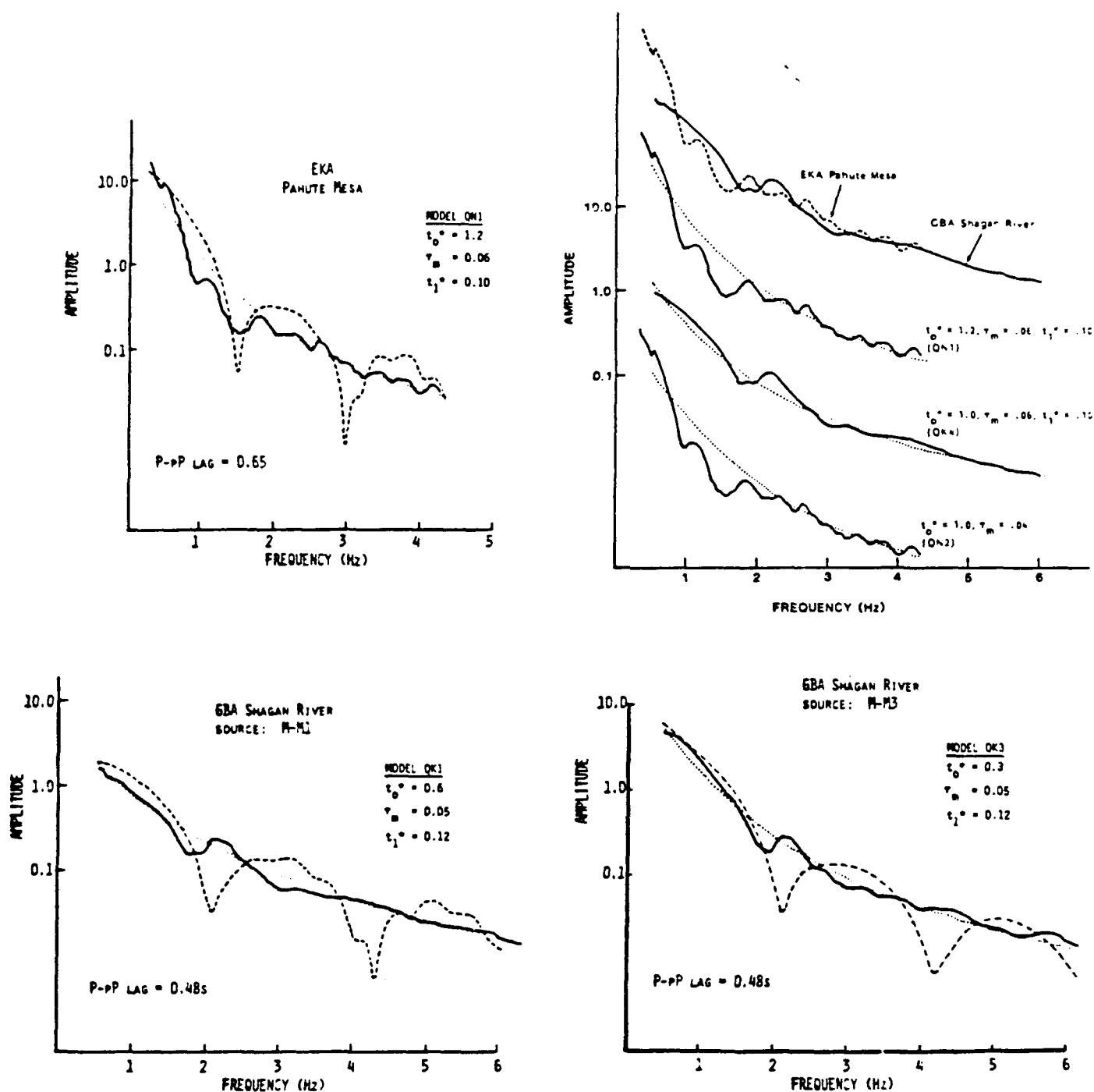


Figure 5 Source-corrected EKA Pahute Mesa and GBA Shagan River spectra are compared with the spectral effect of the indicated attenuation model. For the GBA Shagan data attenuation models are shown for two choices for the source model. Also shown in three of the plots is the spectrum of a synthetic seismogram (processed the same way as the data) with the indicated P-pP lag time.

Estimates of m_b Bias Due to Attenuation Differences

Synthetics	E. Kazakh Source	NTS Attenuation	E. Kazakh Attenuation	Δt^*	$\Delta t^*(1\text{Hz})$	m_b
Large Bias						
N1-K1	M-M1	QN1	QK1	0.6	0.39	0.55
Medium Bias						
N2-K1	M-M1	QN2	QK1	0.4	0.24	0.33
N1-K3	M-M3	QN1	QK3	0.3	0.16	0.32
N1-K4	M-M1	QN1	QK4	0.2	0.14	0.20
Small Bias						
N2-K3	M-M3	QN2	QK3	0.1	0.01	0.00
N2-K4	M-M1	QN2	QK4	0.0	-0.01	-0.02

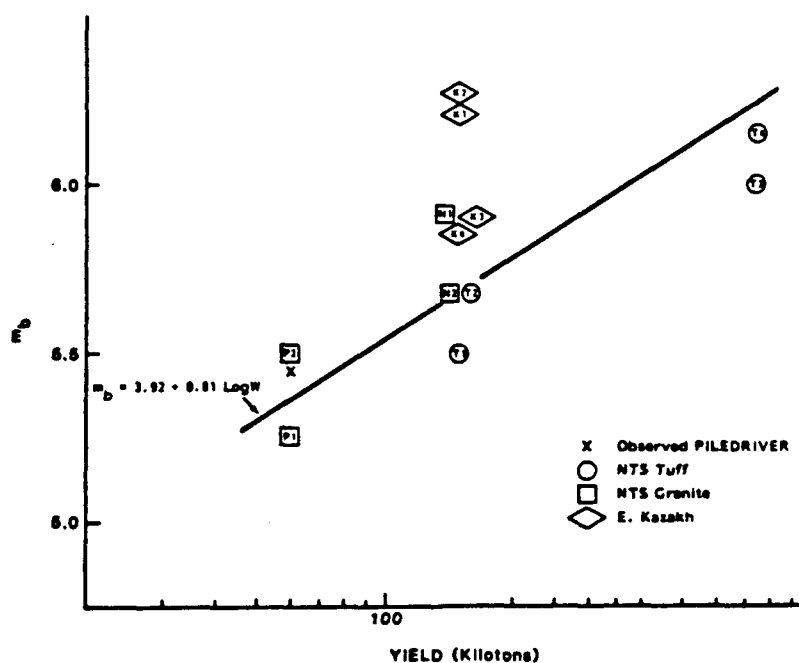


Figure 6 Synthetic m_b are plotted versus yield. The line is a fit to m_b -yield data for NTS explosions below the water table (Murphy, 1981). The differences are tabulated at the top.

There are many other lines of evidence that can be pursued to help decide which m_b bias estimate should be preferred. Key elements include the following:

- o Our results are entirely consistent with those obtained by Murphy (1985) with network-average spectra. However, our spectra are broader-band, forcing us to include frequency-dependence in the attenuation, and we consider more variations in the possible source spectrum.
- o There are large uncertainties in the source spectrum for explosions in hard rock. The data from U.S. and French Sahara explosions are not adequate to exclude the Mueller-Murphy granite source. However, they are easier to explain if the French Sahara source is smaller than the U.S. granite source, and if the U.S. granite source has larger overshoot (smaller Ψ_∞) than conventional models.
- o The best available analysis of the surface wave data (Stevens, 1986) concludes that a source spectrum with large overshoot is more consistent with the E. Kazakh data.
- o Direct measurement of m_b bias between NTS and sites on the Canadian Shield should give an upper bound for the NTS - E. Kazakh bias. The SDCS experiment (Der et al., 1981) provides a reciprocal estimate for this. These results can only be used to support m_b bias greater than 0.2 by constructing ad hoc arguments for discarding the measured m_b bias in favor of "inferred" or "corrected" values.
- o Taken at face value, the Shagan River cratering explosion indicates that 150Kt corresponds to m_b 5.92 (total bias of about 0.25). There is no compelling evidence to suggest that this should be corrected upward by more than 0.1 for the difference between cratering and contained explosions (Day et al., 1986). We cannot use any one event to estimate bias with much confidence, but note that this event cannot be used as evidence to support large m_b bias estimates.

We also computed spectra for explosions at the French Sahara and Mururoa test sites. The source spectrum assumptions again control conclusions about attenuation. The simplest interpretation is that attenuation at the Sahara site is intermediate between that for NTS and Shagan River. The attenuation for Mururoa appears to be greater (higher t^*) than for NTS.

CONCLUSIONS

We conclude that there is no way of conclusively proving either hypothesis listed in the Introduction without more information about the source coupling of the Shagan River explosions. The second hypothesis (yields over 150Kt at Shagan River) easily explains the data if the Shagan River source spectra are different (more overshoot, higher corner frequency) from conventional source models for explosions in hard rock. But these conventional models have not been shown to

match the hard rock data, and these data may be easier to explain with lower amplitude, higher overshoot source spectra of the kind that lead to the lower m_b bias estimates.

It is possible to start with either one of the two hypotheses (or many others) and work backward to fit all the data within a framework consistent with that hypothesis. When data do not fit, plausible ad hoc corrections can be introduced to explain the discrepancy. The data are often ambiguous, and there are many things (e.g., source coupling and frequency-dependent attenuation) we do not understand very well. Taking all factors into consideration, the low m_b bias hypothesis seems more consistent with all the data in the sense that fewer ad hoc arguments are required to explain away data inconsistent with this hypothesis.

REFERENCES

- Bache, T.C., S.R. Bratt, and H. Bungum (1986) "High Frequency P Wave Attenuation Along Five Teleseismic Paths from Central Asia," Geophys. J., R. Astr. Soc., (in press).
- Day, S.M., N. Rimer and T.G. Barker (1986) "Numerical Study of Depth of Burial Effects on the Seismic Signature of Underground Explosions," S-Cubed Report No. SSS-R-86-7398, La Jolla, CA.
- Der, Z.A., T.W. McElfresh and A. O'Donnell (1981) "Results of the SDCS (Special Data Collection System) Attenuation Experiment," Teledyne Geotech Report No. SDAC-TR-80-4, Teledyne Geotech, Alexandria, VA.
- Marshall, P.D., R.C. Lilwall and P.J. Warburton (1985) "Body Wave Magnitudes and Locations of French Underground Explosions at the Mururoa Test Site," A.W.R.E. Report No. 0-12/85, HMSO, London.
- Mueller, R.A. and J.R. Murphy (1971) "Seismic Characteristics of Underground Nuclear Detonations," Bull. Seism. Soc. Am., 61, pp. 1675-1692.
- Murphy, J.R. (1981) "P Wave Coupling of Underground Explosions in Various Geologic Media," in Identification of Seismic Sources -- Earthquake or Underground Explosion, Proc. of NATO ASI, E.S. Husebye and S. Mykkeltveit, Editors, Reidel Publishing Co., Dordrecht, Holland, pp. 201-205.
- Murphy, J.R. (1985) "Analyses of Network-Averaged Teleseismic P Wave Spectra from Underground Explosions at NTS and Semipalatinsk," Presentation to DARPA/AFTAC Panel Meeting of 26 February, 1985.
- Stevens, J.L. (1986) "Estimation of Scaler Moments from Explosion-Generated Surface Waves," Bull. Seism. Soc. Am., 76, pp. 123-151.
- von Seggern, D.B. and R.R. Blandford (1972) "Source Time Functions and Spectra for Underground Nuclear Explosions," Geophys. J. R. Astron. Soc., 31, pp. 83-97.

SYNTHETIC P_n / S_n PHASES AND THE FREQUENCY DEPENDENCE OF Q OF OCEANIC LITHOSPHERE

Thomas Sereno and John Orcutt
Institute of Geophysics and Planetary Physics
Scripps Institution of Oceanography, A-025
La Jolla, California 92037

ABSTRACT

It has long been realized that oceanic P_n and S_n phases retain extremely high frequencies even after propagation to teleseismic distances. Estimates of the effective quality factor, Q , indicate a nearly elastic rheology for the oceanic lithosphere. Data collected during the 1983 Ngendei Seismic Experiment in the southwest Pacific are consistent with these observations at high frequencies, but deviate substantially at low frequencies. Spectra of P_n data, when plotted on a logarithmic scale, display an obvious break in slope near a frequency of 1-2 Hz. When Q is estimated from the spectral slope of these events, a much lower value is obtained at frequencies less than 1-2 Hz than at frequencies in excess of 5-10 Hz. While an array of instruments was not available to eliminate the source spectra by the *spectral ratio method*, any of the standard source spectra models would yield this result. The choice of the high frequency fall-off rate and the corner frequency strongly influence the values obtained for Q , but not the observation that Q increases with frequency. Similar observations for travel paths in the northwest Pacific recorded by the Wake Island hydrophone array have also been reported. In order to synthesize more realistic oceanic P_n and S_n wave trains, it now appears that Q should increase with frequency. Wave number integration is conducted in the frequency domain and attenuation is introduced by allowing material velocities to be complex. We have adopted an absorption band rheology with a distribution of relaxation times to implement a frequency dependence of Q into the wave number integration algorithm. An absorption band consistent with published Q values and the Ngendei spectra was used. Synthetic P_n and S_n phases were generated to a frequency of 6.4 Hz on a Cray X-MP computer. The results of the modeling indicate a much better fit of synthetics to data is possible by allowing Q to be a function of frequency.

INTRODUCTION

Oceanic P_n and S_n phases are commonly observed on ocean bottom seismometer (OBS) records in the distance range of 5° to 30°. These are guided phases that

propagate entirely within the oceanic lithosphere and are characterized by an onset velocity of 8.0 km/s, a long reverberatory wave train, and the presence of extremely high frequencies even for regional to teleseismic path lengths. Frequencies as high as 15 Hz for P_n and 20 Hz for S_n have been reported at a distance of 3300 km for travel paths under the western Pacific (Walker, et al., 1983). Walker, et al. (1978) estimated the effective quality factors for P_n and S_n with travel paths in the northwest Pacific for two separate earthquakes yielding P_n values of 3700 ± 200 and 8400 ± 1300 and S_n values of 8500 ± 600 and $19,100 \pm 3700$. More recently, Butler et al. (1985) report a strong frequency dependence of Q_{P_n} and Q_{S_n} between 2 and 20 Hz for travel paths in the northwest Pacific. They were able to use the *spectral ratio method* between pairs of receivers to estimate the quality factors for P_n and S_n . They reported Q values of 300 at 2.5 Hz and 1500 at 17.5 Hz for P_n and for S_n , 500 at 2.5 Hz and 3000 at 22 Hz.

SYNTHETIC P_n AND S_n PHASES

Wave number integration was used to generate complete synthetic seismograms for an oceanic lithosphere model with a constant Q rheology. The velocity structure was chosen on the basis of a refraction study conducted during the 1983 Ngendei Seismic Experiment in the southwest Pacific ($23^\circ 49' S$, $165^\circ 32' W$). The Ngendei site was the location of hole 595B of Deep Sea Drilling Project (DSDP), leg 91. The depth of the oceanic water column at the site is 5.55 km and, from core sample measurements, the sediment thickness is 70 m with a compressional velocity of 1.6 km/s. The model is listed in Table 1 and a single source depth of 15 km was used.

Figure 1 illustrates vertical and radial displacement at the sea floor at a range of 1000 km for a sub-Moho thrust fault. The fault used had a dip of 25° , a rake of 270° , and an azimuth relative to the receiver of 60° . The synthetic radial component oceanic P_n and S_n phases very closely resemble data collected at the Ngendei site. The substantial coda of these phases is modeled as a sum of leaky organ-pipe modes in the oceanic water column and sediment layer. Shear wave resonance is particularly prominent on the horizontal component due to the steep incidence of the rays at the receiver. The 'pulse-like' character of the water reverberations in the synthetic vertical component P_n wave train does not, however, emulate the data. The vertical component coda results predominantly from compressional wave reverberation in the oceanic water column and sediment layer. Due to the low impedance contrast at the ocean-sediment interface for compressional waves, the sediment modes are extremely leaky and die out long before the arrival of the next water multiple.

Figure 2a is the synthetic vertical displacement of Figure 1a after including the OBS instrument response and a source spectrum with f^{-2} amplitude decay and corner

frequency of 0.6 Hz. Figure 2b is the vertical component P_n spectrum. The sharp equally spaced peaks are due to resonance within the oceanic water column. Figure 2c is an example of vertical component data collected at the Ngendei site and Figure 2d is the first 12.8 Hz of its power spectrum. The obvious difference between the two spectra is the relative enrichment of the power at frequencies between 0-2 Hz of the data. The lack of this low frequency energy gives rise to the 'pulse-like' appearance of the synthetic P_n wave train.

ABSORPTION BAND Q

One way to enhance the power level of the low frequencies relative to higher frequencies is to lower the Q . This, however, inhibits the propagation of extremely high frequencies to teleseismic distances required by the data. As an alternative, Q could increase with frequency thereby enhancing the power at frequencies between 0-2 Hz relative to frequencies between 3-5 Hz without severely attenuating frequencies in excess of 15 Hz. To approximate the true frequency dependence of Q in the oceanic lithosphere, we have adopted an absorption band rheology with a distribution of relaxation times. This is incorporated into the wave number integration algorithm (Lundquist and Cormier, 1980) by allowing the complex material velocity to be of the form

$$V_c(\omega) = V_e \left[1 - \frac{1}{\pi Q_m} \ln \frac{1 + \omega^2 \tau_1^2}{1 + \omega^2 \tau_2^2} - i \frac{2}{\pi Q_m} \tan^{-1} \frac{\omega(\tau_1 - \tau_2)}{1 + \omega^2 \tau_1 \tau_2} \right]^{-\frac{1}{2}} \quad (1)$$

where V_e is the 'elastic' velocity, Q_m is the minimum Q , and τ_1 and τ_2 are the low and high frequency relaxation times, respectively. Care must be taken in applying this equation in that the natural log term perturbs the real part of the complex velocity and can cause an unrealistic deviation in travel times. In the limit as this term approaches zero, the familiar expression for Q as a function of frequency for an absorption band rheology is obtained

$$Q^{-1}(\omega) = \frac{2}{\pi Q_m} \tan^{-1} \left[\frac{\omega(\tau_1 - \tau_2)}{1 + \omega^2 \tau_1 \tau_2} \right]. \quad (2)$$

As an example of the effect of an absorption band Q on the spectra we used values for compressional waves of $Q_m = 200$ and $\tau_2 = 0.05$ s resulting in a linear frequency dependence of Q for frequencies greater than about 3.0 Hz. The low frequency relaxation time, τ_1 , was arbitrarily set to 100s, well out of the frequency range of interest. Figure 3a displays curves of the instrument response times a source spectrum with f^{-2} amplitude decay and corner frequency of 0.6 Hz multiplied by $e^{\frac{-\pi f}{Q}}$ for a range of

1000 km, a group velocity of 8 km/s, and varying Q values. The dashed curves represent constant Q values and for the solid curve the absorption band Q was used. Figure 3b displays the same curves to a frequency of 64 Hz. This illustrates that to enhance the low frequency energy of the synthetics without depleting the very high frequencies, Q must increase with frequency.

Synthetic vertical and radial displacement for the Ngendei model with an absorption band rheology in the sub-Moho portion of the lithosphere are shown in Figure 4. While the modeling is not yet complete, the agreement of the synthetic vertical component P_n wave train with the data is greatly enhanced by allowing Q to increase with frequency.

REFERENCES

- Butler, R., C. McCreery, L. N. Frazer, and D. Walker, High-frequency attenuation in the western Pacific, (abstract), *EOS*, 66, p. 305, 1985.
- Lundquist, G., and V. Cormier, Constraints on the absorption band model of Q , *J. Geophys. Res.*, 85, 5244-5256, 1980.
- Sutton, G., C. McCreery, F. Duennebier, and D. Walker, Spectral analyses of high-frequency P_N, S_N phases recorded on ocean bottom seismographs, *Geophys. Res. Lett.*, 5, 745-747, 1978.
- Walker, D., C. McCreery, and G. Sutton, Spectral characteristics of high frequency P_N, S_N phases in the western Pacific, *J. Geophys. Res.*, 88, 4289-4298, 1983.
- Walker, D., C. McCreery, G. Sutton, and F. Duennebier, Spectral analyses of high-frequency P_n and S_n phases observed at great distances in the western Pacific, *Science*, 199, 1333-1335, 1978.

Table 1. Ngendei Model

Layer	V_p , km/s	V_s , km/s	ρ , Mg/m ³	Q_α	Q_β	h, km
1	1.500	0.000	1.0000	50000	---	5.55
2	1.600	0.116	1.0096	200	100	0.07
3	5.000	2.757	2.7000	900	450	0.25
4	5.300	2.923	2.7600	900	450	0.20
5	5.600	3.088	2.8200	900	450	0.20
6	5.900	3.254	2.8800	900	450	0.20
7	6.200	3.419	2.9400	900	450	0.40
8	6.500	3.585	3.0000	900	450	0.70
9	6.800	3.750	3.0600	900	450	4.63
10	8.200	4.650	3.3400	2000	1000	30.0
11	8.225	4.664	3.3450	2000	1000	30.0
12	8.250	4.678	3.3500	2000	1000	30.0
13	8.275	4.693	3.3550	2000	1000	∞

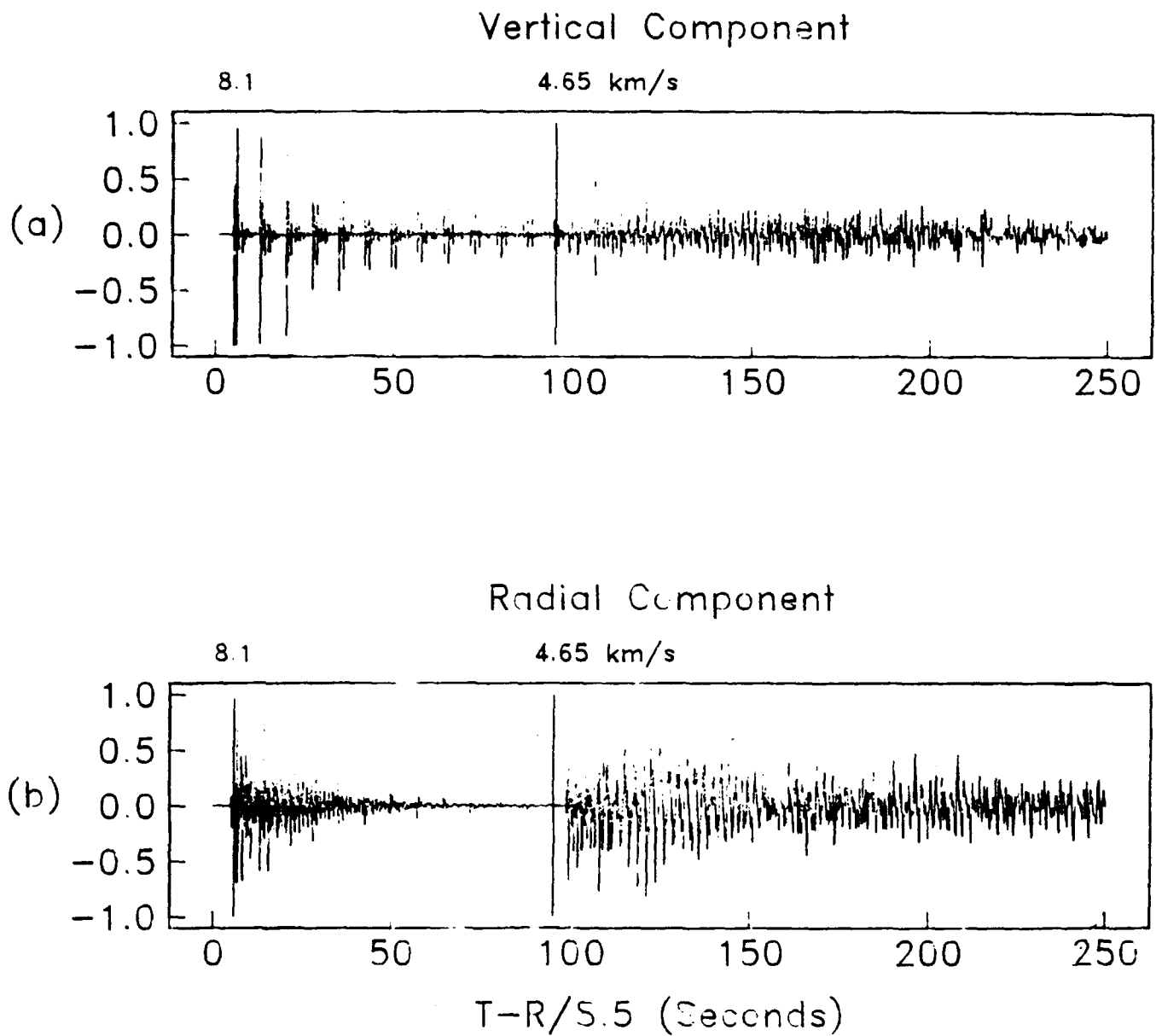


Figure 1. Synthetic P_n/S_n phases computed for the Ngendei structure. (a) Vertical displacement and (b) radial displacement for a thrust fault source at 15.0 km depth at an epicentral range of 1000 km. Velocities of 8.1 and 4.65 km/s are indicated.

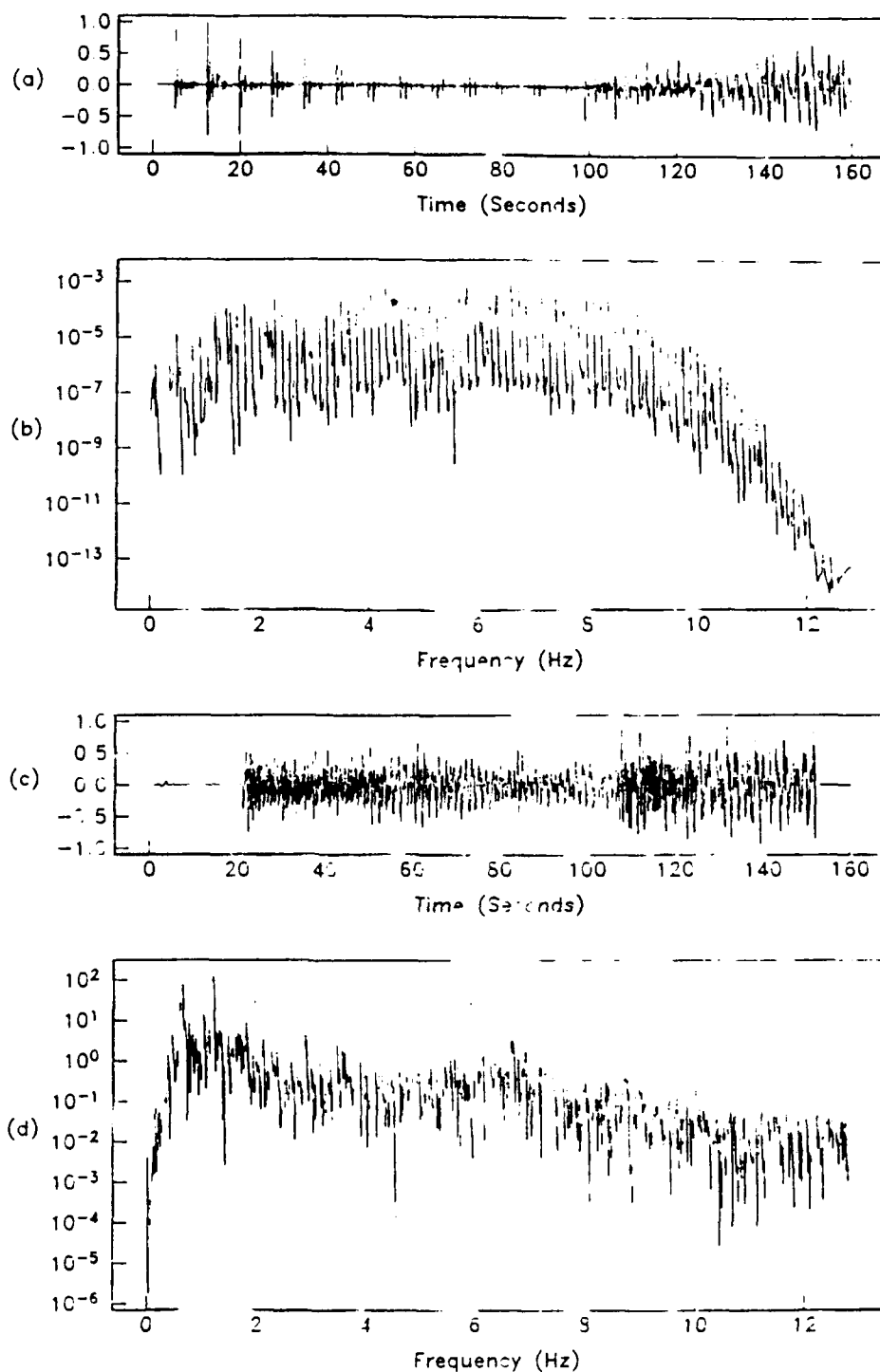


Figure 2. (a) Synthetic vertical component P_n phase of Figure 1a after including the OBS instrument response and a source spectrum with f^{-2} amplitude decay and corner frequency of 0.6 Hz. (b) Power spectrum of the P_n phase in Figure 2a. (c) Vertical component P_n data taken at the Ngendei site. (d) First 12.8 Hz of the data spectrum.

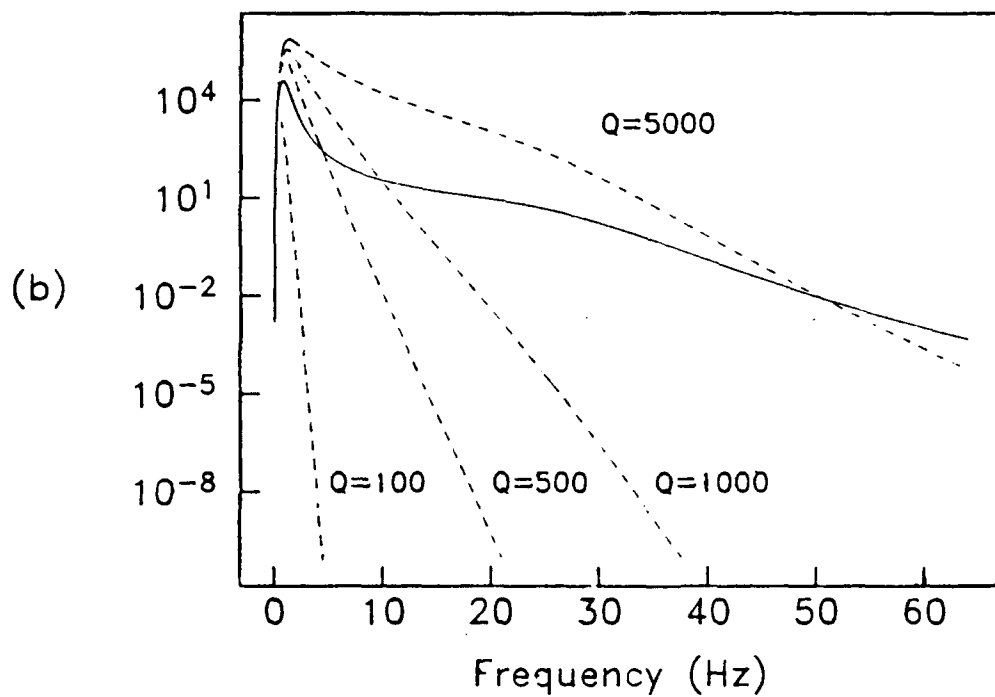
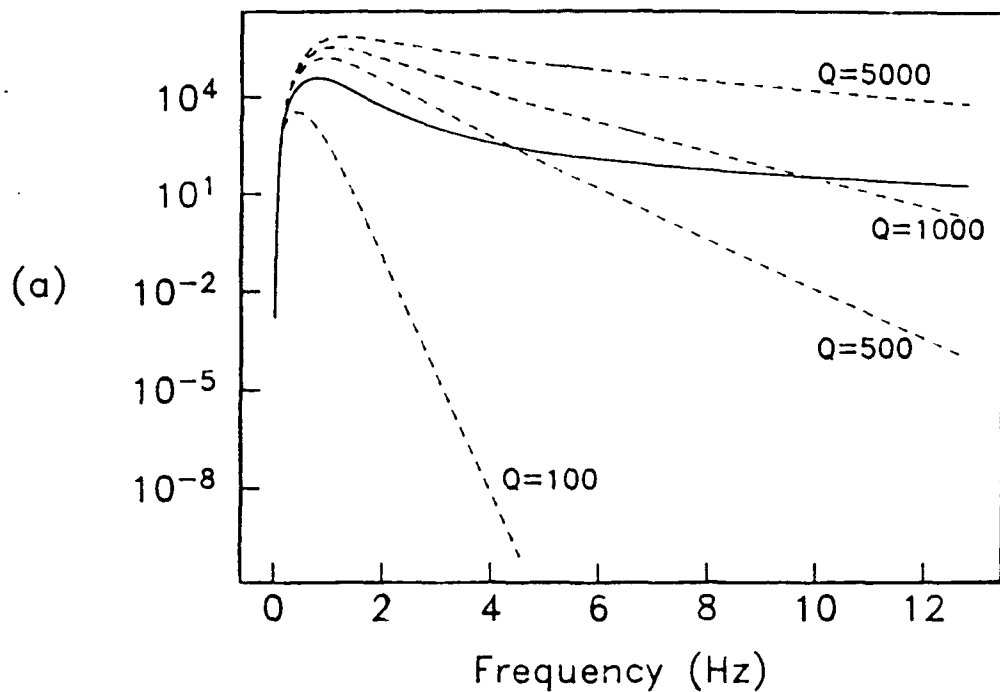


Figure 3. Curves of instrument response times a source spectrum with f^{-2} amplitude decay and corner frequency of 0.6 Hz multiplied by $e^{\frac{-\pi r f}{v Q}}$ for a range of 1000 km, a group velocity of 8 km/s, and varying Q values. The dashed curves are for constant Q and the solid curve represents the result for an absorption band Q model. (a) First 12.8 Hz and (b) 64.0 Hz of the spectrum.

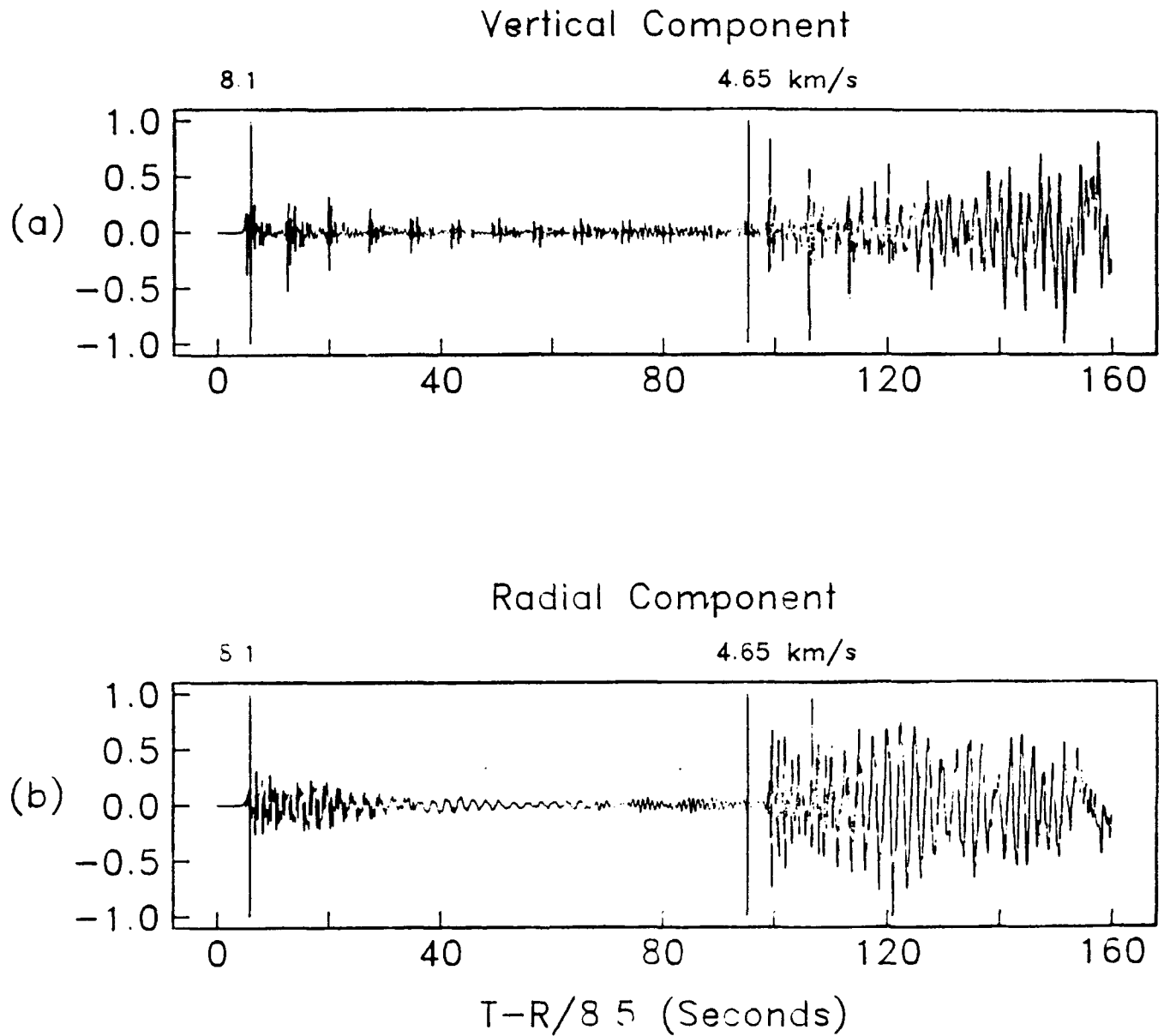


Figure 4. Synthetic P_n / S_n phases computed for the Ngendei structure with an absorption band Q adopted in the mantle portion of the lithosphere. (a) Vertical displacement and (b) radial displacement for a thrust fault source at 15.0 km depth at an epicentral range of 1000 km. Velocities of 8.1 and 4.65 km/s are indicated.

SURFACE WAVE SYNTHESIS FOR LATERALLY HETEROGENOUS SPHERICAL EARTH MODELS

Keiiti Aki, Ta-liang Teng, John Faulkner
Department of Geological Sciences, University of Southern California

INTRODUCTION

The subject matter of our research deals with the improvement on the absolute accuracy concerning the M_s :yield determination. At large epicentral distances, surface waves are the most prominent phase in a seismogram. If they are to be effectively used for treaty monitoring purposes, uniform determination of M_s to an accuracy of 0.1 magnitude unit becomes important. This translates to an absolute determination of surface-wave amplitudes (in time or frequency domain) to an accuracy of better than 25%. Factors entering into any amplitude measurement must include the source effect, the propagation effect, and the recording site effect; each of these effects makes a significant contribution to data scatter. All of these effects are currently under intensive study and these research results should lead to a more accurate yield determination as well as discrimination.

Over the past 12-month contract period, we have accomplished the following tasks with results that have considerably improved our understanding on the propagation of surface waves in a laterally heterogeneous earth. The nature of focusing and defocusing of the surface wavefront has important bearings on the basic analysis of dispersion studies and therefore the structural inversion. Its implication on surface-wave amplitude variations, of course, is the main thrust of this contract research.

GAUSSIAN-BEAM SYNTHESIS OF RAYLEIGH WAVES

For the wave-form synthesis of Rayleigh waves in a laterally heterogeneous Earth, we use the Gaussian beam method originally developed for body waves by Cervený et al. (1982) and modified for surface waves by Yomogida and Aki (1985).

The following is a brief summary of how to make a synthetic seismogram of surface waves by the Gaussian beam approach. First, we specify the phase velocity at mesh points and apply the transformation corresponding to the Mercator projection (Jobert

and Jobert, 1983). Second, we apply the bi-cubic spline interpolation of phase velocity so that we can calculate its first and second derivative at any point. Third, we solve the ray tracing equation and shoot ray paths from a given source to all azimuths at 2° or finer intervals. Fourth, we solve the dynamic ray-tracing equation and determine the spreading and wave-front curvature for each ray. Fifth, we construct the Gaussian beam solution for each ray corresponding to a source function of the Gabor type and sum up the contribution of each Gaussian beam to a particular station. Sixth, we determine the amplitude and arrival time of wave packets using the group velocity data and the kinetic energy integral calculated for the appropriate model structure.

The computer program for the synthesis has been written by K. Yomogida at MIT and was adapted to the USC computer by J. Faulkner. A number of test cases have been run to make sure that the code gives correct results. A world map of Mercator projection has also been digitized that forms the base of reference for the velocity map and for the nuclear test sites and recording stations.

In order to carry out the above steps for ray tracing and synthetic seismogram computations, we first need a world map of phase velocity for each period of interest.

WORLD MAP OF RAYLEIGH-WAVE PHASE VELOCITY

To perform the ray-tracing and Gaussian-beam synthesis, phase velocity, group velocity, and surface-wave energy integral data are needed for the entire region in which waves propagate. Recently, Rosa (personal communication) collected all the existing phase velocity data (published and unpublished) for the period range from 20 to 100 sec. For example, he collected phase velocity at period of 40 sec. for 790 paths.

Rosa compared these ray paths with the regionalized tectonic map of Jordan (1981), and selected those paths which have at least 70% of the total path length lying within one of Jordan's six regions, namely (A) young ocean (0-25 My), (B) intermediate ocean

(25-100 My), (C) old ocean (> 100 My), (P) Phanerozoic platform, (Q) Phanerozoic orogenic zones, and (S) Precambrian shields and platforms. He then computed the mean and the standard error for each region for periods 20, 30, 40, 50, 60, 70, 80, 90, and 98 sec. We assigned these phase velocity values at the center of the $5^\circ \times 5^\circ$ area which is classified to one of the above six regions by Jordan (Fig. 3).

For this preliminary study, we assumed that the group velocity is constant (4.0 km) for all regions and all periods. This affects the arrival time of the wave packet significantly but only slightly the amplitude of individual Gaussian beam solutions.

EXAMPLES OF SURFACE-WAVE RAY MAPS AND THE CORRESPONDING SYNTHETIC RECORDS

Based on Rosa's global phase velocity data, we have computed test cases for a number of surface-wave ray maps and the corresponding Gaussian-beam synthetic seismograms. We have generated ray maps for periods from 20 sec to 90 sec at 10 sec increments. Figures 1-abc give ray maps for 30 sec surface waves originated from Novaya Zemlya, East Kazakh, and China, respectively. It is interesting to see that for an assumed velocity model of mild lateral heterogeneity, intermediate period surface waves can significantly alter their wave paths. Focusing and defocusing regions as well as "transmission corridors" are well displayed that shift themselves with the change of source locations. Unfortunately, because of the nature of the Mercator projection, the path lying near the North Pole cannot be included here. Furthermore, ray paths terminated at the western boundary of the map are not included in the Gaussian-beam synthesis. Therefore, the synthetic seismograms as now presented in Figure 2 have errors in the R1 for eastern U.S. stations (where R1 is missing) and in R2 for western U.S. stations (where R2 is missing). This type of error is being corrected now, which involves a coordinate rotation of the North Pole out of the way to perhaps the equator with an attendant mapping of the global phase velocity distribution onto the new rotated coordinates.

We are currently checking into actual records to see if the ray maps correctly predict the observations.

Figure 1a

Novaya Zemlya $T = 30$ Seconds

$\phi = 40.0^\circ$ $\lambda = 89.0^\circ$

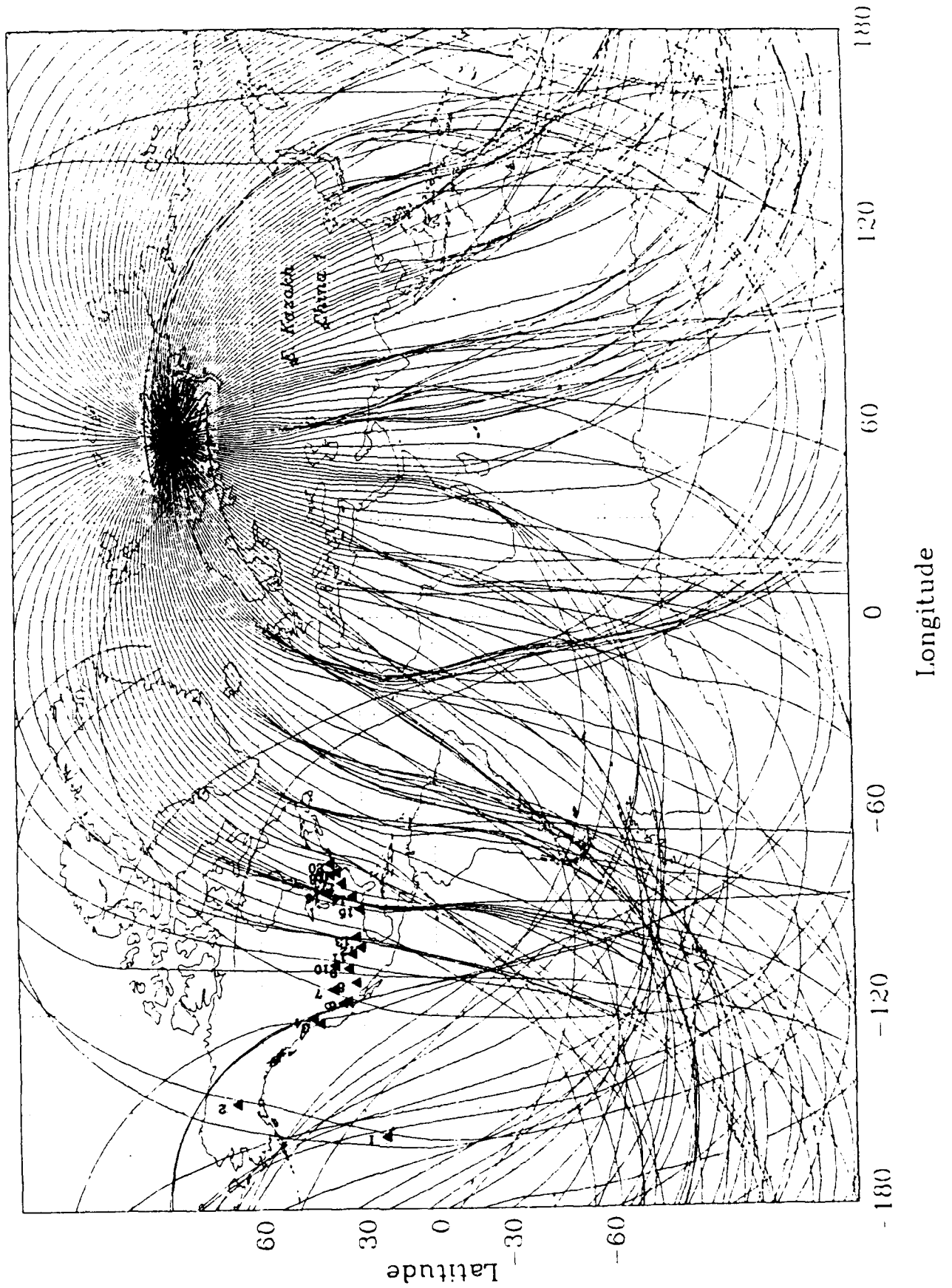


Figure 1b

E Kazakh $T = 30$ Seconds

$\phi = 50.0^\circ$ $\lambda = 78.0^\circ$

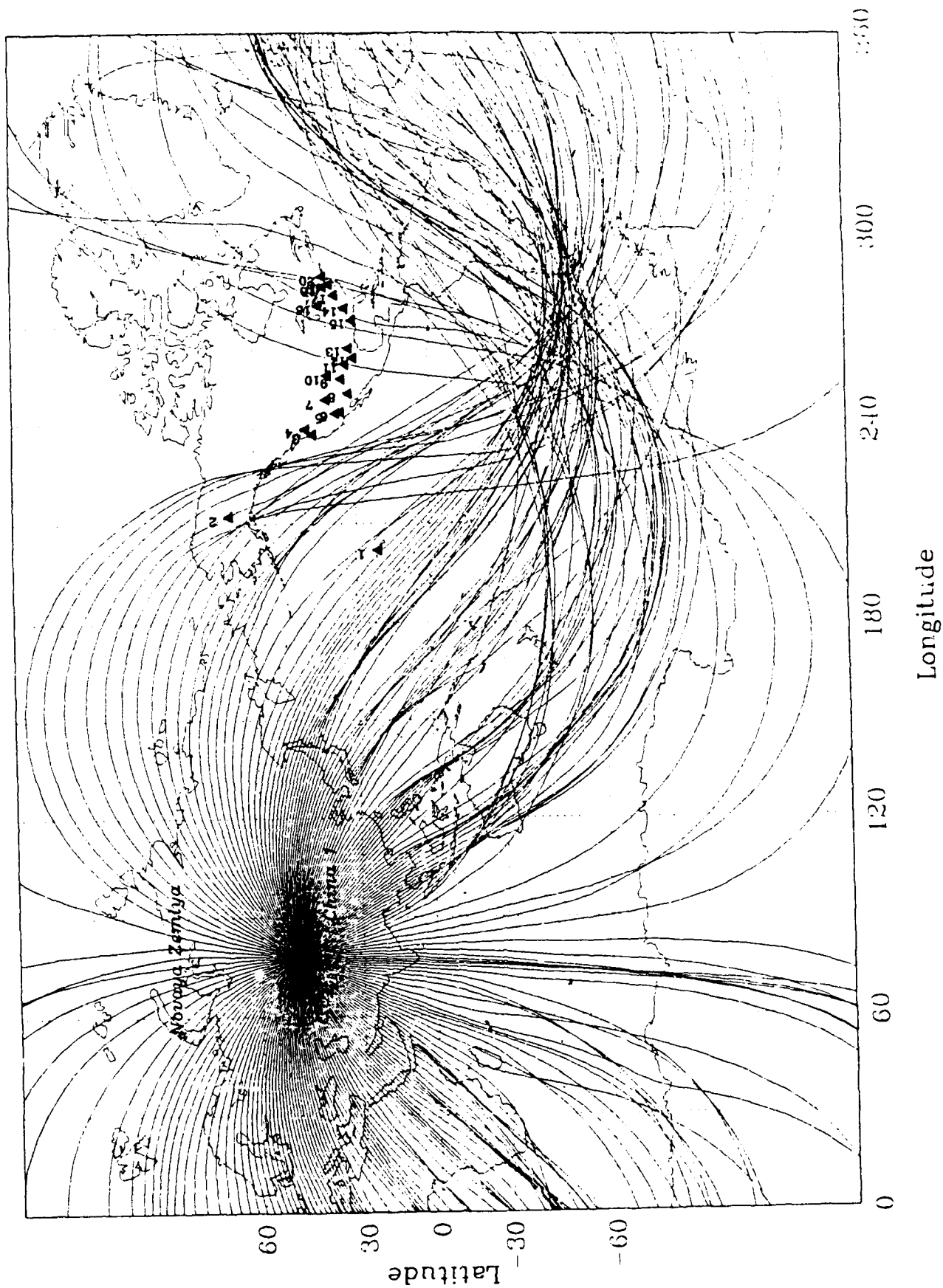


Figure 1c

China $T = 30$ Seconds

$\phi = 40.0^\circ \lambda = 89.0^\circ$

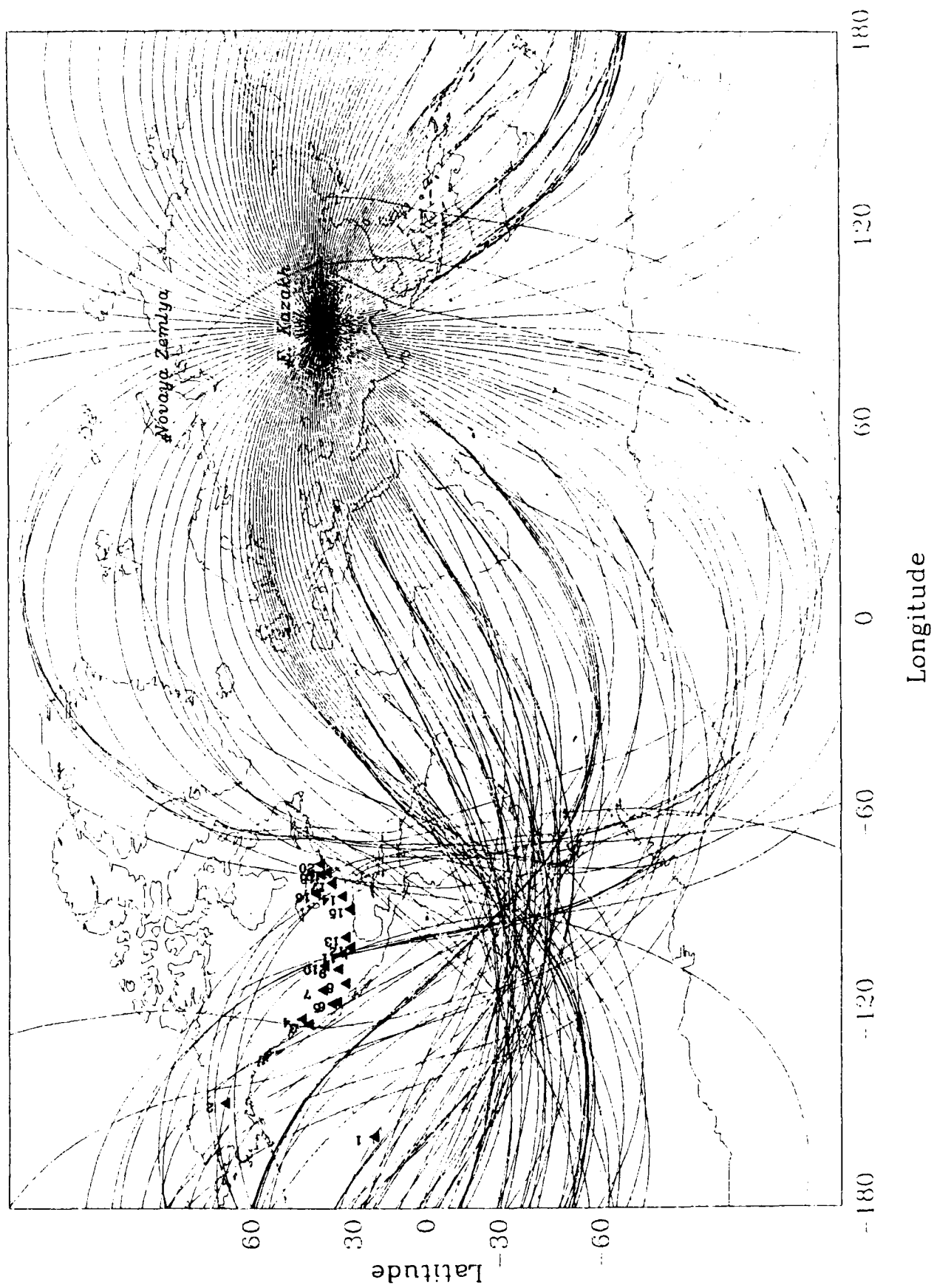
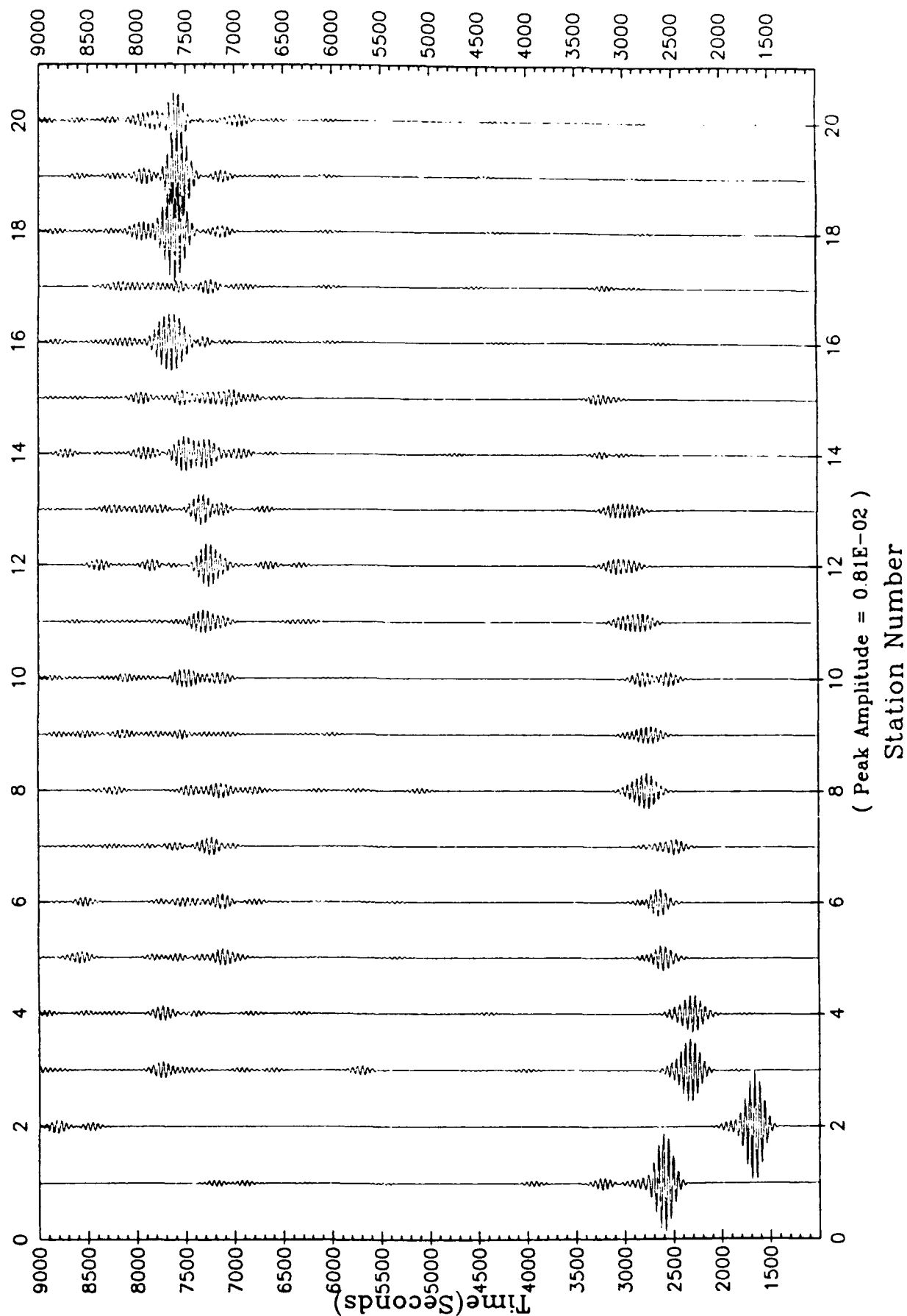


Figure 2

E Kazakh ($\phi = 50^\circ$ $\lambda = 78^\circ$)

($T = 50$ Seconds, $L_0 = 1.0$, $S_0 = 1.0$, $\delta_1 = 2^\circ$, $Q = 1000$)



AFGL / DARPA Seismic Research Symposium

U. S. Air Force Academy

Colorado Springs - 6 - 8 May 1986

Paper tittle : Regional Distribution of apparent attenuation
in the Center of France

Paper authors : M. Campillo - Radiomana

Grant n° 85 0033

The set of seismic data is the one already used in our previous studies on Lg waves (18 quakes with ML between 3.2 and 4.8, within the crust; 22 SP stations of the LDG network).

The method used here is the Algebraic Reconstruction Technic (ART) to build up an image of the Q factor spatial distribution.

The set of propagation paths is presented in Figure 1.

Each point of the image of Q. takes into account all the paths within a distance of 50 km.

In order to apply some confidence criterium on the quality of this Q evaluation we define a confidence index :

$$i c = n_{source} \times l_{rays}$$

where :

n_{source} : is the numbers of different sources which generate the rays

l_{rays} is the length of the ray inside the influence circle divided by the influence radius.

A map of this index is given in Figure 2, where the represented points fit the test of ray length.

As a result, all the blue zones correspond to a high confidence index, and red zones might include systematic bias.

Figure 3 represents a rather simple regional distribution. If one just keeps within high confidence limits, the main regions are defined as :

- Limagne Basin , Forez, Saone valley = weak figure for Q
(between $Q_0 = 180$ and $Q_0 = 240$)
- Limousin = (between $Q_0 = 200$ and $Q_0 = 260$)
- South Parisian basin, Berry, Poitou, North of Massif Central
(between $Q_0 = 300$ and $Q_0 = 440$).

The mean Q_0 value (always computed at $f = 1$ Hz) extracted from these results is : $Q_0 = 290$

Similar to the one obtained by direct Lg measurement (Campillo and al 1984).

We need to extend this Q_0 cartography to other western Europe regions by using other stations and earthquakes.

Conclusion

These results pointed out the importance of graben zones for Lg waves propagation. Nevertheless, at this stage of the study we do not possess yet any separation tool between two types of phenomena which could create attenuation :

- small scale diffraction (or scattering)
- large scale geometrical effect

A study of frequency dependancy for Q should help us in the interpretation of our data.

On the other hand, developpements of numerical simulation methods encourage us to investigate more complex zones in order to interpret the quasi extinction phenomena of Lg waves we have observed along peculiar paths.



Figure 1

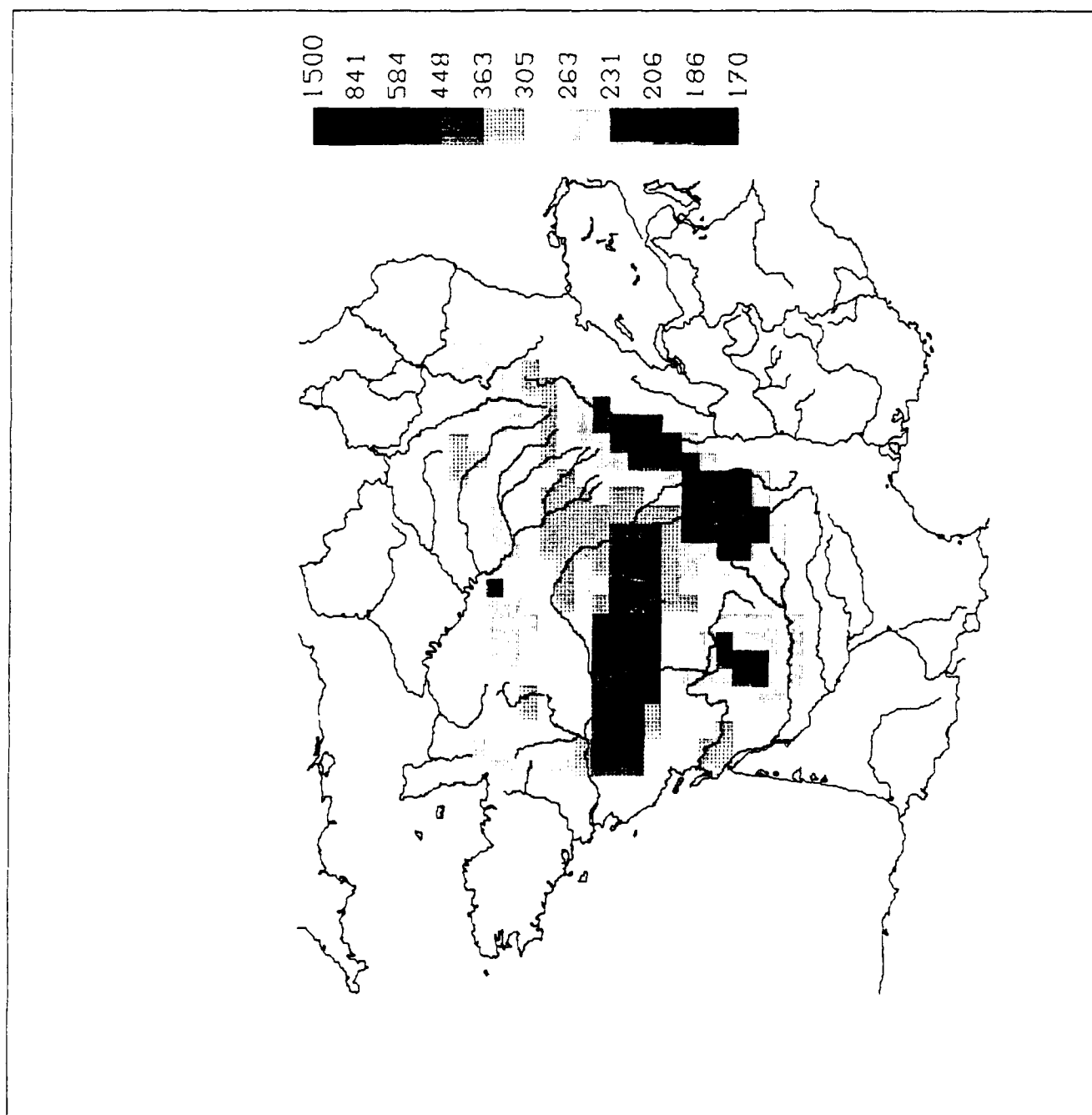


Figure 2

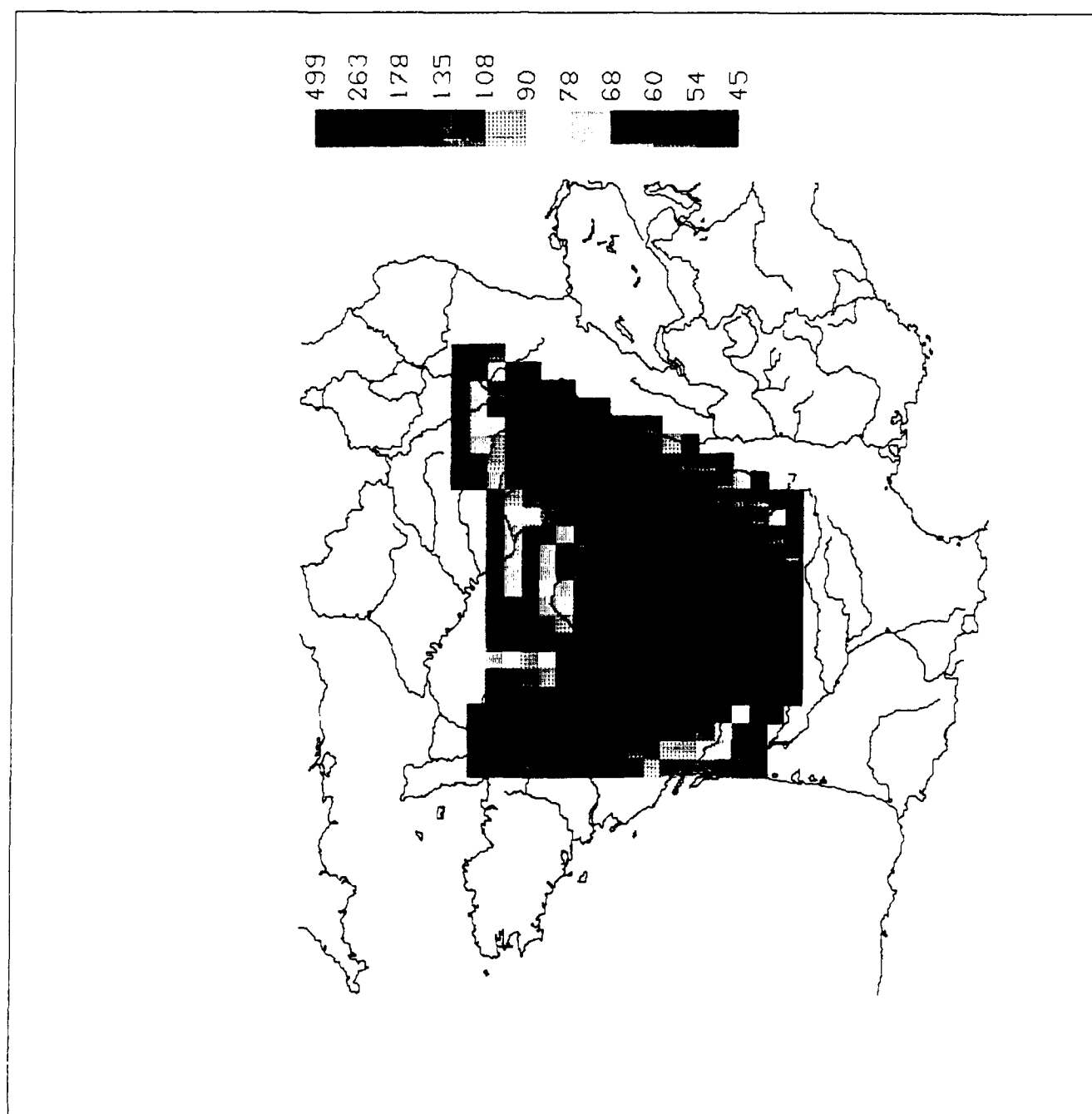


Figure 3

LIST OF ATTENDEES

Monem Abdel-Gawad
Rockwell International Science Center
1049 Camino Dos Rios
Thousand Oaks, CA 91360

Keiiti Aki
Center for Earth Sciences
University of Southern California
University Park
Los Angeles, CA 90089-0741

Ralph Alewine
Geophysical Sciences Division
Defense Advanced Research Projects Agency
1400 Wilson Boulevard
Arlington, VA 22209-2308

Shelton S. Alexander
Geosciences Department
403 Deike Building
The Pennsylvania State University
University Park, PA 16802

Charles B. Archambeau
Cooperative Institute for Research in
Environmental Sciences
University of Colorado
Boulder, CO 80309

Thomas A. Bache Jr.
Science Applications Int'l Corp.
1200 Prospect Street
P.O. Box 2351
La Jolla, CA 92038

Jeff Barker
Woodward-Clyde Consultants
566 El Dorado Street
Pasadena, CA 91101

James Battis
AFGL/LWH
Hanscom AFB, MA 01731-5000

Douglas R. Baumgardt
Signal Analysis and Systems Division
ENSCO, Inc.
5400 Port Royal Road
Springfield, VA 22151

William Best
907 Westwood Drive
Vienna, VA 22180

F. G. Blake
US Dept of Energy/DP 331
Forrestal Building
1000 Independence Ave.
Washington, DC 20585

Robert Blandford
Geophysical Sciences Division
Defense Advanced Research Projects Agency
1400 Wilson Boulevard
Arlington, VA 22209-2308

Michel Bouchon
Universite Scientifique et
Medicale de Grenoble
Laboratoire de Geophysique
Interne et Tectonophysique
I.R.I.G.M.-B.P. 68
38402 St. Martin D'Heres
Cedex FRANCE

Lawrence J. Burdick
Woodward-Clyde Consultants
566 El Dorado Street
Pasadena, CA 91101

Michel Campillo
Societe Radiomana
27, Rue Claude Bernard
75005, Paris, FRANCE

Jerry Carter
Rondout Associates
P.O. Box 224
Stone Ridge, NY 12484

Kin-Yip Chun
Geophysics Division
Physics Department
University of Toronto
Ontario, CANADA M5S 1A7

John Cipar
AFGL/LWH
Hanscom AFB, MA 01731-5000

Vernon F. Cormier
Earth Resources Laboratory
Department of Earth, Atmospheric and
Planetary Sciences
Massachusetts Institute of Technology
42 Carleton Street
Cambridge, MA 02142

Anton M. Dainty
Earth Resources Laboratory
Dept. of Earth, Atmospheric and
Planetary Sciences
Massachusetts Institute of Technology
42 Carleton Street
Cambridge, MA 02142

Steven Day
S-CUBED
3398 Carmel Mountain Road
San Diego, CA 92121

Zoltan A. Der
Teledyne Geotech
P.O. Box 334
Alexandria, VA 22313

H.B. Durham
Sandia National Laboratory
Albuquerque, NM 87185

John F. Ferguson
Center for Lithospheric Studies
The University of Texas at Dallas
P.O. Box 830688
Richardson, TX 75083-0688

Steve Grand
Seismological Laboratory
Division of Geological and Planetary
Sciences
California Institute of Technology
Pasadena, CA 91125

James Hannon
Lawrence Livermore National Laboratory
P.O. Box 808
Livermore, CA 94550

David G. Harkrider
Seismological Laboratory
Division of Geological and Planetary
Sciences
California Institute of Technology
Pasadena, CA 91125

Peter Harjes
Institute for Geophysik
Ruhr University
Bochum
P.O. Box 102148
4630 Bochum 1
FEDERAL REPUBLIC OF GERMANY

David Harris
Lawrence Livermore National Laboratory
P.O. Box 808
Livermore, CA 94550

Thomas Hearn
INSTOC
Snee Hall
Cornell University
Ithaca, NY 14853

Donald V. Helmberger
Seismological Laboratory
Division of Geological and Planetary
Sciences
California Institute of Technology
Pasadena, CA 91125

Anne Suteau-Henson
Science Applications International Corporation
1200 Prospect Street
P.O. Box 2351
La Jolla, CA 92038

Eugene Herrin
Institute for the Study of Earth and Man
Geophysical Laboratory
Southern Methodist University
Dallas, TX 75275

Robert B. Herrmann
Department of Earth and Atmospheric
Sciences
Saint Louis University
Saint Louis, MO 63156

Eystein Husebye
NTNF/NORSAR
P.O. Box 51
N-2007 Kjeller, NORWAY

Lane R. Johnson
Seismographic Station
University of California
Berkeley, CA 94720

Thomas H. Jordan
Department of Earth, Atmospheric and
Planetary Sciences
Massachusetts Institute of Technology
Cambridge, MA 02139

Ann Kerr
Defense Advanced Research Projects Agency
1400 Wilson Boulevard
Arlington, VA 22209-2308

Tormod Kvaerna
NTNF/NORSAR
P.O. Box 51
N-2007 Kjeller, NORWAY

Arthur Lerner-Lam
Lamont-Doherty Geological Observatory
of Columbia University
Palisades, NY 10964

Charles A. Langston
Geosciences Department
403 Deike Building
The Pennsylvania State University
University Park, PA 16802

Thorne Lay
Department of Geological Sciences
1006 C.C. Little Building
University of Michigan
Ann Arbor, MI 48109-1063

William Leith
Lamont-Doherty Geological Observatory
of Columbia University
Palisades, NY 10964

James Lewkowicz
AFGL/LWH
Hanscom AFB, MA 01731-5000

Christopher Lynnes
Department of Geological Sciences
1006 C.C. Little Building
University of Michigan
Ann Arbor, MI 48109-1063

Bernard Massinon
Societe Radiomana
27, Rue Claude Bernard
75005, Paris, FRANCE

Keith L. McLaughlin
Teledyne Geotech
P.O. Box 334
Alexandria, VA 22313

Pierre Mechler
Societe Radiomana
27, Rue Claude Bernard
75005 Paris, FRANCE

Bernard Minster
Science Horizons, Inc.
710 Encinitas Blvd., Suite 101
Encinitas, CA 92024

Brian J. Mitchell
Department of Earth and Atmospheric
Sciences
Saint Louis University
Saint Louis, MO 63156

Jack Murphy
S-CUBED
Reston Geophysics Office
11800 Sunrise Valley Drive
Suite 1212
Reston, VA 22091

Svein Mykkeltveit
NTNF/NORSAR
P.O. Box 51
N-2007 Kjeller, NORWAY

Keith Nakanishi
Lawrence Livermore National Laboratory
P.O. Box 808
Livermore, CA 94550

Francois Navarre
Societe Radiomana
27, Rue Claude Bernard
75005, Paris, FRANCE

Carl Newton
Los Alamos National Laboratory
P.O. Box 1663
Mail Stop C 335
Group ESS3
Los Alamos, NM 87545

Robert North
Earth Physics Branch
Dept. of Energy & Mines
1 Observatory Crescent
Ottawa, Ontario
CANADA, K1A 0Y3

Otto W. Nuttli
Department of Earth and Atmospheric
Sciences
Saint Louis University
Saint Louis, MO 63156

John A. Orcutt
Geological Sciences Division
Univ. of California at San Diego
La Jolla, CA 92038

Frank F. Pilotte
Director of Geophysics
Headquarters Air Force Technical
Applications Center
Patrick AFB, Florida 32925-6001

Paul Pomeroy
Rondout Associates
P.O. Box 224
Stone Ridge, NY 12484

John Prince
AFOSR/NP
410 Bolling AFB, DC 20332-6448

Frode Ringdal
NTNF/NORSAR
P.O. Box 51
N-2007 Kjeller, NORWAY

D. Wilmer Rivers, Jr
Teledyne Geotech
P.O. Box 334
Alexandria, VA 22317

Florence Riviere
Societe Radiomana
27, Rue Claude Bernard
75005, Paris, FRANCE

George H. Rothe
Chief, Research Division
Director of Geophysics
Headquarters Air Force Technical
Applications Center
Patrick AFB, Florida 32925-6001

David Russell
Dept. of Earth & Atmospheric Sciences
St. Louis University
P.O. Box 8099
St. Louis, MO 63156

Alan S. Ryall, Jr.
Center for Seismic Studies
1300 North 17th Street
Suite 1450
Arlington, VA 22209-3871

Charles G. Sammis
Center for Earth Sciences
University of Southern California
University Park
Los Angeles, CA 90089-0741

Stuart Sipkin
Box 25046
Mail Stop 967
Denver Federal Center
Denver, CO 80225

Richard Strelitz
Department of Geology
Duke University
Durham, NC 27701

Brian Stump
Institute for the Study of Earth & Man
Geophysical Laboratory
Southern Methodist University
Dallas, TX 75275

Steve Taylor
Lawrence Livermore National Laboratory
P.O. Box 800
Livermore, CA 94550

Ta-liang Teng
Center for Earth Sciences
University of Southern California
University Park
Los Angeles, CA 90089-0741

Bernhard R. Tittman
Rockwell International Science Center
1049 Camino Dos Rios
P.O. Box 1085
Thousand Oaks, CA 91360

Marios Vassiliou
Rockwell International Science Center
1049 Camino Dos Rios
P.O. Box 1085
Thousand Oaks, CA 91360

Terry C. Wallace
Department of Geosciences
Building #11
University of Arizona
Tucson, AZ 85721

John H. Woodhouse
Hoffman Laboratory
Harvard University
20 Oxford Street
Cambridge, MA 02138